

ABSTRACT

Title of dissertation: An Analytical Investigation of Flapping
Wing Structures for Micro Air Vehicles

Nicholas C. Rosenfeld
Doctor of Philosophy, 2011

Dissertation directed by: Professor Norman M. Wereley
Department of Aerospace Engineering

An analytical model of flapping wing structures for bio-inspired micro air vehicles is presented in this dissertation. Bio-inspired micro air vehicles (MAVs) are based on insects and hummingbirds. These animals have lightweight, flexible wings that undergo large deformations while flapping. Engineering studies have confirmed that deformations can increase the lift of flapping wings. Wing flexibility has been studied through experimental construction-and-evaluation methods and through computational numerical models. Between experimental and numerical methods there is a need for a simple method to model and evaluate the structural dynamics of flexible flapping wings. This dissertation's analytical model addresses this need.

A time-periodic assumed-modes beam analysis of a flapping, flexible wing undergoing linear deformations is developed from a beam analysis of a helicopter blade. The resultant structural model includes bending and torsion degrees of freedom. The model is non-dimensionalized. The ratio of the system's structural natural frequency to wingbeat frequency characterizes its constant stiffness, and the amplitude of flapping motion characterizes its time-periodic stiffness. Current

flapping mechanisms and MAVs are compared to biological fliers on the basis of the characteristic parameters. The beam analysis is extended to develop an plate model of a flapping wing.

The time-periodic stability of the flapping wing model is assessed with Floquet analysis. A flapping-wing stability diagram is developed as a function of the characteristic parameters. The analysis indicates that time-periodic instabilities are more likely for large-amplitude, high-frequency flapping motion. Instabilities associated with the first bending mode dominate the stability diagram. Due to current limitations of flapping mechanisms, instabilities are not likely in current experiments but become more likely at the operating conditions of biological fliers.

The effect of structural design parameters, including wing planform and material stiffness, are assessed with an assumed-modes aeroelastic model. Wing planforms are developed from an empirical model of biological planforms. Non-linearities are described in the effect of membrane thickness on lift generation. Structural couplings due to time-periodic stiffness are identified that can decrease lift generation at certain wingbeat frequencies.

An Analytical Investigation of
Flapping Wing Structures
for Micro Air Vehicles

by

Nicholas C. Rosenfeld

Dissertation submitted to the Faculty of the Graduate School of the
University of Maryland, College Park in partial fulfillment
of the requirements for the degree of
Doctor of Philosophy
2011

Advisory Committee:
Professor Norman M. Wereley, Chair
Professor Inderjit Chopra
Professor Alison Flatau
Assistant Professor J. Sean Humbert
Professor Amr M. Baz

© Copyright by
Nicholas C. Rosenfeld
2011

To my parents for their support
and
to Breinn for her love

Acknowledgements

First and foremost I would like to acknowledge the support and mentorship of my advisor, Dr. Norman Wereley. He graciously invited me into the Alfred Gessow Rotorcraft Center as a young, eager undergraduate research assistant. I couldn't have known that invitation signaled the first step down an academic path that would eventually lead to this dissertation, the culmination of many years at the AGRC. The path was sometimes meandering, but Dr. Wereley was a consistent source of advice, insight and encouragement. He has been a profound influence on my life, and I thank him whole-heartedly.

Thanks are also in order for my dissertation committee, Dr. Inderjit Chopra, Dr. Alison Flatau, Dr. J. Sean Humbert and Dr. Amr Baz, for their comments and suggestions. I would like to acknowledge Dr. Darryll Pines for his early role on my committee, and extend special thanks to Dr. Humbert for taking over Dr. Pines' seat after Dr. Pines' ascension as Dean of the Clark School of Engineering.

My time at the Alfred Gessow Rotorcraft Center was enriched intellectually and personally thanks to interactions with a tremendous group of professors, staff and fellow students. Attempting to properly thank everyone who taught me a lesson (large or small, academic or otherwise), made me see the world in a different light, or shared in misery or laughter is a task that space and my imperfect memory will not allow. In lieu of what would certainly be an incomplete and inadequate list of acknowledgements, I simply say to everyone at the AGRC, past and present: thank you. My days in the student/researcher offices were made brighter by Glen Dimock, Jason Linder, Bill Facey, Jason Pereira, Nick Wilson, Gang Wang, Young-Tai Choi, Jaye Falls and Ben Hein. Outside of the AGRC, I would like to thank Stephen Colodner, Kanishka Gangopadhyay and Carl Vogel, who I met at U. Maryland as undergraduates and who have remained my friends through the entire course of this dissertation.

I would like to acknowledge the Sea-Based Aviation and Aeromechanics Branch at NSWC Carderock, where I have been employed for the past two years while completing my dissertation research. Special thanks go to Dr. David Haas, Dr. Judah Milgram and Dr. Peter Bi for their patience and understanding as I perilously balanced my academic and occupational obligations.

Finally and most importantly I must thank my parents Frank and Daria, my brother Andrew and my beautiful wife Breinn. Their constant love and support have been my strength throughout my academic career and my life. My faith in myself may have wavered, but their faith in me never has. Thank you, deeply and truly.

Table of Contents

List of Tables	viii
List of Figures	ix
List of Nomenclature and Abbreviations	xiii
1 Introduction and Literature Review	1
1.1 Micro Air Vehicles	1
1.1.1 Fixed-Wing Micro Air Vehicles	2
1.1.2 Rotary-Wing Micro Air Vehicles	4
1.1.3 Bird-Like Micro Air Vehicles	5
1.1.4 Unconventional Micro Air Vehicles	9
1.2 Insect-Like Biological Flight	13
1.2.1 Kinematics	16
1.2.2 Aerodynamics	18
1.2.2.1 Early Comprehensive Studies	18
1.2.2.2 Aerodynamic Mechanisms	22
1.2.2.3 Numerical Aerodynamic Modeling	25
1.2.3 Wing Structures	27
1.2.3.1 Deficiencies of Structural Data	30
1.2.3.2 Reversible Airfoils	33
1.2.3.3 Wing Corrugations	36
1.2.3.4 The Pterostigma and Pitch Regulation	38
1.2.3.5 Structural Properties and Distributions	38
1.2.3.6 Inertial and Aerodynamic Loadings	41
1.2.3.7 Indirect Flapping Actuation	43
1.2.4 Hummingbirds	44
1.3 Insect-Like Micro Air Vehicles and Test Stands	46
1.3.1 Flight-Capable Entomopters	47
1.3.2 Entomopter Test Stands	51
1.3.3 Wing Structures	55
1.3.4 Other Flapping-Wing Analyses	62
1.4 Summary	63
1.5 Objective	65
2 Assumed Modes Analysis of a Flapping Wing as a Thin Beam	67
2.1 Introduction	67
2.2 Model Definition	67
2.2.1 Nomenclature	69
2.2.2 Estimation of Physical Properties	71
2.2.3 Aerodynamics	73
2.3 Equations of Motion	74
2.4 Physical Interpretations of Force Loadings	80

2.4.1	Cross-Sectional Inertia	81
2.4.2	Flapping Centrifugal Loadings	82
2.4.3	Feathering Centrifugal Loadings	85
2.4.4	Flapping Inertial Loadings	86
2.4.5	Feathering Inertial Loadings	89
2.4.6	Flap-Feather Coriolis Loadings	90
2.4.7	Feather-Deformation Coriolis Loadings	92
2.4.8	Total Loadings	93
2.5	Assumed Modes Analysis	94
2.6	Non-dimensional Analysis	100
2.6.1	Non-rotational Beam Natural Frequencies	105
2.6.1.1	Torsion Natural Frequency	106
2.6.1.2	Bending Natural Frequency	107
2.6.1.3	Total System Stiffness	111
2.6.2	Comments on Non-dimensional Analysis	115
2.6.2.1	Normalized Cantilever Frequency and Non-rotational Stiffness	116
2.6.2.2	Flapping and Feathering Strokes and Time-Periodic Stiffness	117
2.6.2.3	Comparison of Biological Fliers and Engineering Studies	118
2.7	Summary	121
3	Assumed Modes Linear Time-Periodic Stability	123
3.1	Introduction	123
3.2	Analytical Stability Analyses	124
3.2.1	Development of a Parametric Flapping-Wing Stability Diagram	125
3.2.2	Biological Fliers, MAVs and Test Stands	130
3.2.3	Root Spring Stiffness	132
3.2.4	Uncoupled Bending and Torsion	136
3.3	Floquet Analysis	138
3.3.1	Flapping and Feathering Rotation	139
3.3.2	Additional Modes	140
3.3.3	Root Spring Stiffness	144
3.3.4	Lossy (Damped) Stability	146
3.3.5	Center of Gravity Location	147
3.3.6	Feathering Axis Location	148
3.4	Summary	149
4	Assumed Modes Analysis of a Flapping Wing as a Thin Plate	151
4.1	Introduction	151
4.2	Assumed-Modes Plate Model	151
4.3	Equivalence to Beam Formulation	156
4.4	Finite Element Analysis	158
4.4.1	Approximation of α_{ij} and β_{ij} with Radial Basis Functions . . .	160

4.4.2	Mode Shape Validation	163
4.4.3	Radial Basis Function Interpolation Validation	166
4.4.4	Matrix Calculation Validation	167
4.5	Non-dimensional Analysis	169
4.6	Representative Wing FEM	172
4.6.1	Split-Spar Wing	174
4.6.2	Natural Frequencies of FEM wings	175
4.7	Stability of Plate Wings	176
4.8	Summary	180
5	Parametric Study of an Aeroelastic Flapping Wing	182
5.1	Introduction	182
5.2	Aeroelastic Model	182
5.3	Baseline Wing	184
5.4	Wing Planform Shape	188
5.5	Material Thickness	192
5.5.1	Wing Frame Thickness	192
5.5.2	Wing Membrane Thickness	196
5.6	Forced Flapping at Odd Subharmonics of the the First Natural Fre- quency	198
5.7	Summary	203
6	Concluding Remarks	206
6.1	Summary and Conclusions	206
6.2	Contributions	214
6.3	Recommendations for Future Work	215
A	Natural Frequencies of Beam Wings	219
A.1	Characteristic $(\lambda R)_{\gamma 1}$ of a Uniform Clamped-Free Beam	219
A.2	Characteristic $(\lambda R)_{w1}$ of a Uniform Cantilever-Free Beam	220
A.3	Non-dimensional Mass Moment of Inertia of a Pinned, Uniform Rigid Beam	222
B	Derivation of Root-Spring-Free Bending Modes of a Uniform Beam	224
	Bibliography	230

List of Tables

2.1	Summary of beam frequencies	110
2.2	Summary of characteristic λR s	111
2.3	Non-dimensional flapping parameters of biological fliers and MAVs in hover	118
3.1	Maximum pumping stiffness q and constant stiffness a for uncou- pled second root-spring-free modes as a function of $\omega_{\text{root}}/\omega_{\text{cant}}$. . .	135
4.1	Gauss quadrature points and weights	160
4.2	Plate properties for FEA validation	163
4.3	FEA validation results for a simply supported plate, $b/a = 1/3$	165
4.4	FEA validation results for a simply supported plate, $b/a = 1/4$	165
4.5	RBF interpolation validation results for a simply supported plate . .	167
4.6	Equation-of-motion matrices for simply supported plate	168
4.7	Plate properties for representative wing FEM	172
4.8	Natural frequencies of wing FEMs	175
5.1	Structural properties for baseline wing elements	185
5.2	Lift components on baseline wing undergoing sinusoidal motion . .	188
5.3	Total lift and lift components of bioinspired wing planforms	190
5.4	Results of parametric variation of flapping-wing frame thickness . .	193
5.5	Results of parametric variation of flapping-wing membrane thickness	197
5.6	Frequency response components of a simplified flapping system for different normalized first natural frequencies	202

List of Figures

1.1	Fixed-wing MAVs	3
1.2	Rotary-wing MAVs	4
1.3	A Canada goose in flight	7
1.4	MAV-scale ornithopters	8
1.5	Mock-up of Michelson’s Entomopter	10
1.6	Jones’ flapping-wing–propelled MAV	10
1.7	Time-lapse image of Delft U. Tech. ornicopter rotor	11
1.8	MAV-scale robotic samara	11
1.9	Quad-rotor cyclogyro	12
1.10	Animals using normal hovering flight	15
1.11	Generalized wing motion during normal hovering flight	16
1.12	Components of insect wing motion	16
1.13	Conceptual diagram of clap-and-fling	19
1.14	Cartoon of attached leading-edge vortex on flapping insect wing	23
1.15	Insect wing structure, as seen in a photograph of a dragonfly	28
1.16	Generalized vein geometry and flexion lines of insect wings	29
1.17	Robofly robotic flapping mechanism operating in mineral oil	31
1.18	Reversible torsion and camber in hovering flight	34
1.19	Partial detail of dragonfly wing structure	36
1.20	Diagram of airflow around corrugated wings	36
1.21	Pterostigmas on a common bluetail damselfly	38
1.22	Indirect flight muscle operation	43
1.23	Hummingbird wing structure	45

1.24	A basic Pénaud-type entomopter	48
1.25	Advanced flight-capable entomopters	49
1.26	UC Berkeley Micromechanical Flying Insect (MFI)	52
1.27	Raney and Slominki's vibratory flapping apparatus	53
1.28	Single-degree-of-freedom linkage mechanisms for hover	54
1.29	Single-degree-of-freedom linkage mechanisms for forward flight	55
1.30	Insect-inspired entomopter wings	57
1.31	Harvard Microrobotic Fly wing	58
1.32	Experimental wing configurations used on the Mentor MAV	59
1.33	Example wings from Singh and Chopra's experiments	62
2.1	Coordinate systems for thin-beam analysis	68
2.2	Cross-section of deflected wing	69
2.3	Feathering angle θ versus geometric angle of attack α	70
2.4	Representive wing cross-section	72
2.5	Cross-sectional inertial loadings	81
2.6	Flapping centrifugal loadings, top view	82
2.7	Flapping centrifugal loadings, side view	83
2.8	Feathering centrifugal loadings	85
2.9	Flapping inertial loadings, top view	87
2.10	Flapping inertial loadings, side view	87
2.11	Feathering inertial loadings	89
2.12	Flap-feather Coriolis loadings	91
2.13	Feather-deformation Coriolis loadings	92
3.1	Top view of simplified single-mode, flapping motion.	124

3.2	Strutt diagram of Mathieu equation.	126
3.3	Transformation of Strutt diagram to flapping-wing stability diagram for single cantilever-free bending mode.	127
3.4	Propagation of unforced, undamped tip perturbations in single- mode system at constant $\omega_{\text{cant}}/\omega$	129
3.5	Propagation of unforced, undamped tip perturbations in single- mode system at constant Φ	129
3.6	Stability diagram of a single-mode cantilever beam with approxi- mate parameter ranges of biological fliers and MAV studies	130
3.7	Effect of root spring stiffness on single-mode stability diagram en- velope	132
3.8	Motion of a beam element against centrifugal force arising from beam deflection.	134
3.9	Effect of root spring stiffness on single-mode stability diagram, $\Theta = 0^\circ$	135
3.10	Effect of torsion stiffness on uncoupled two-mode stability diagram, $\Theta = 0^\circ$	138
3.11	Effect of feathering stroke Θ on single-mode stability diagram	140
3.12	Two-mode mode stability diagram, $\Theta = 0^\circ$	141
3.13	Propagation of unforced, undamped tip perturbations in a coupled two-mode system at constant Φ	142
3.14	Additional coupled modes included on flapping stability diagram, $\Theta = 0^\circ$	143
3.15	Effect of feathering stroke Θ on three-mode stability diagram	144
3.16	Effect of root spring stiffness on three-mode bending stability dia- gram, $\Theta = 120^\circ$	145
3.17	Effect of constant damping on three-mode stability diagram, $\Theta = 120^\circ$	147
3.18	Effect of chordwise CG location on three-mode stability diagram, $\Theta = 120^\circ$	148
3.19	Effect of feathering axis location on three-mode stability diagram, $\Theta = 120^\circ$	149

4.1	Coordinate systems for thin plate analysis	153
4.2	Position and numbering of parabolic plate element nodes	158
4.3	Quadrature points on plate element	160
4.4	Example nonuniform plate FEM mesh	161
4.5	Radial basis function interpolation domain	162
4.6	Normal modes of a simply-supported plate from FEA	164
4.7	Comparison of exact and numerically-calculated α_{ij}	166
4.8	Planform view of FEM mesh of straight-spar wing	173
4.9	Normal modes of the straight-spar wing FEM	173
4.10	Planform view of FEM mesh of split-spar wing	174
4.11	Normal modes of the split-spar wing FEM	175
4.12	Comparison of single-mode stability diagrams of plate and beam assumed-modes models	177
4.13	Comparison of three-mode stability diagrams of plate and beam assumed-modes models	178
5.1	FEM of baseline wing	184
5.2	Physical model for baseline FEM	184
5.3	Modes of the baseline FEM	185
5.4	Input flapping and feathering motions for aeroelastic analysis	186
5.5	Comparison of calculated bending moments from validation exer- cise and current implementation	187
5.6	Total lift and lift components of baseline wing subject to sinusoidal motion	187
5.7	Biologically inspired wing planforms	190
5.8	Time history of total lift and lift components of biologically inspired wing planforms	191

5.9	Mean lift versus normalized first natural frequency for Singh's Wing III	194
5.10	Comparison of tip deflections of wings with 0.50 to 1.00× baseline frame thickness	195
5.11	Comparison of lift variations of wings with 0.50 to 1.00× baseline frame thickness	196
5.12	Effect of variation of membrane thickness and equivalent variations of mass and stiffness	198
B.1	Root-spring-free mode shapes of a uniform beam as a function of $\omega_{\text{cant}}/\omega_{\text{root}}$	229

List of Nomenclature and Abbreviations

$A(\tau)$	State-space matrix
$\mathcal{A}, \dots, \mathcal{W}$	Modal coefficient matrices
a	Constant stiffness of Mathieu equation (§ 3.2); Plate length (§ 4.4.2, 4.4.3)
b	Plate width (§ 4.4.2)
$c(x)$	Chord
$EI(x)$	Bending stiffness
$e(x)$	Chordwise center of gravity location
$e_A(x)$	Chordwise centroid location
$e_O(x)$	Offset of elastic axis from feathering axis
\underline{F}	Modal forcing vector
$\underline{GJ}(x)$	Torsional stiffness
\mathbf{I}	Identity matrix
I_b	Inertial mass moment of rigid beam about pinned root
$\hat{i}, \hat{j}, \hat{k}$	Unit coordinate vectors
\mathbf{K}	Non-dimensional stiffness matrix
$k_A(x)$	Polar area radius of gyration
$k_m(x)$	Polar mass radius of gyration
$k_{my}(x), k_{mz}(x)$	Mass radii of gyration parallel and perpendicular to chord
k_{root}	Root torsion spring stiffness
$m(x)$	Mass per unit length
N	Number of assumed modes
$p_x(x), p_y(x), p_z(x)$	Force loading on wing
\mathbf{Q}	Floquet transition matrix
q	Pumping stiffness of Mathieu equation (§ 3.2)
$q_x(x), q_y(x), q_z(x)$	Moment loading on wing
$\tilde{q}(t)$	Modal magnitude
\tilde{R}	Wing radius or length; Scaled support radius of RBF (§ 4.4.1, 4.4.3)
r	Support radius of RBF (§ 4.4.1)
\hat{r}_1, \hat{r}_2	Non-dimensional first and second spanwise moments of wing planform area (§ 5.4)
S	Total wing area of two wings
$S_e(x), S_x(x)$	Mass moments of inertia due to beam tension
$T(x)$	Tension
t	Time
$v(x, t)$	In-plane bending displacement
$w(x, t), w(x, y, t)$	Out-of-plane bending displacement
x, y, z	Rigid-beam coordinates
$\underline{z}(\tau)$	State-space vector

$\alpha_{ij}(x, y), \beta_{ij}(x, y)$	Line integral functions on plate modes
$\gamma(x, t)$	Torsional displacement
η	Non-dimensional chordwise coordinate
Θ	Feathering stroke amplitude (peak-to-peak)
$\theta(t)$	Feathering angle
ξ	Non-dimensional spanwise coordinate
$\rho(x, y)$	Mass per unit area
τ	Non-dimensional time
Φ	Flapping stroke amplitude (peak-to-peak)
$\phi(r)$	Radial basis function (§ 4.4.1)
$\phi(t)$	Flapping angle
$\chi(x), \chi(x, y)$	Non-rotating structural mode shape
ω	Wingbeat frequency
ω_{cant}	Non-rotating bending natural frequency of beam with cantilever-free boundary
ω_{root}	Non-rotating natural frequency of rigid beam with root torsion spring
ω_{tor}	Non-rotating torsion natural frequency of beam with clamped-free boundary

Superscripts and Subscripts

$\dot{\bullet}$	Time derivative
\bullet^*	Non-dimensional time derivative
$\hat{\bullet}$	Non-dimensional distribution
\bullet'	Spatial derivative
\bullet^T	Transpose
\bullet_0	Inertial axes; Characteristic (maximum) value
\bullet_c	Stiffness coefficient of $\cos \theta$
$\bullet_{i'}, \bullet_{j'}, \bullet_{k'}$	Mode number; Matrix index
\bullet_s	Stiffness coefficient of $\sin \theta$
\bullet_v	In-plane bending value
\bullet_w	Out-of-plane bending value
$\bullet_{x'}, \bullet_{y'}, \bullet_{z'}$	Direction in rigid-beam axes
\bullet_γ	Torsion value
\bullet_θ	Feathering axes; Stiffness coefficient of $\hat{\theta}$
\bullet_ϕ	Flapping axes; Stiffness coefficient of $\hat{\phi}$
\bullet_ω	Stiffness coefficient of normalized cantilever frequency

Other Symbols

AR	Aspect ratio, $AR = 4R^2/S$
Re	Reynolds number

Abbreviations

CFD	Computational fluid dynamics
DARPA	Defense Advanced Research Projects Agency
FEA	Finite element analysis
FEM	Finite element model
MAV	Micro air vehicle
MEMS	Microelectromechanical systems
RBF	Radial basis function
SDOF	Single degree of freedom

CHAPTER 1

INTRODUCTION AND LITERATURE REVIEW

1.1 Micro Air Vehicles

Micro air vehicles (MAVs) are a heterogeneous class of aerial robots of very small size. MAVs are a subset of unmanned air vehicles (UAVs). Operational UAVs range in size from man-portable remote-controlled vehicles to full-scale aircraft, with wingspans of two to 100+ ft. MAVs are even smaller, comparable in size to a human hand. The Defense Advanced Research Projects Agency (DARPA) is primarily responsible for the initial interest in, and rapid development of, MAVs. In conjunction with research initiatives, DARPA released a technical report in 1997 laying out conceptual guidelines for MAV sizing, performance and missions [1]. MAVs were defined as aerial vehicles with a maximum dimension no greater than 15 cm. Scaling trends suggested an MAV should have a gross weight of 100 g and a target payload of 20 g. An “over-the-hill” reconnaissance mission was used to set MAVs’ performance goals: an endurance of one hour, a 10-km range and a top speed of 10 to 20 m/s. Additional proposed military applications included reconnaissance, surveillance and communications in urban environments and building/cave interiors; mobile immersion sensing of chemical clouds; and use as flying beacons to aid search-and-rescue missions. Traffic monitoring, fire/rescue operations, wildlife surveys and power-line inspections were identified as potential civilian applications. Regardless of mission, MAVs will operate at Reynolds numbers of 10^3 to 10^5 , a significantly different aerodynamic environment than full-scale aircraft ($Re = 10^7$ to 10^8) [2].

Despite DARPA's wide range of proposed missions, researcher Robert Michelson argues that MAVs may not be best suited to many of them [3]. Citing the effects of adverse aerodynamic environments and questioning the benefits of MAVs versus currently operational UAVs for outdoor missions, Michelson singles out autonomous interior operations as uniquely suited to MAVs, asserting "[t]he mission space for which size really does matter is 'indoors and in confined spaces' where the environment is controlled or at least protected." DARPA called such applications "the most demanding envisioned" because of the technological challenges that must be overcome to give MAVs the "capability to navigate complex shaped passageways, avoid obstacles and relay information" [1]. This dissertation will follow Michelson in considering interior operations to be a primary mission of MAVs. Thus, exceptional maneuverability at low speeds—ideally including hover capability—is deemed of utmost importance for MAVs.

A menagerie of MAVs have emerged in response to DARPA's initiatives. Some are miniaturizations of operational full-scale fixed- and rotary-wing configurations. Others are modeled after the birds and insects that first inspired men to fly. Some resemble neither; novel approaches based on no previous mechanical or biological pattern. The following sections will give overviews of each configuration, saving an in-depth survey of insect flight and insect-like MAVs for last.

1.1.1 Fixed-Wing Micro Air Vehicles

Fixed-wing configurations represent the most technologically mature MAVs. Aided by the availability of off-the-shelf components, early prototypes like the Aerovironment Black Widow [4] (figure 1.1a) and the MLB Trochoid [5] were demonstrating flight performance consistent with DARPA goals by 2000. Other operational fixed-wing MAVs include NRL's MITE [6], several membraneous-



(a) Aerovironment Black Widow



(b) U. Florida 4.5-inch MAV

Figure 1.1: Fixed-wing MAVs.

wing vehicles from the University of Florida [7, 8] (figure 1.1b) and the University of Florida's "bendable-wing" MAV, whose wings can be rolled up for stowage [9]. Numerous experimental and numerical studies of low- Re airfoil and wing design have been performed [10–13]. All fixed-wing MAVs use low aspect ratio wings to maximize wing area for a constrained wingspan, with AR typically between one and two. Current state-of-the-art research is focusing on the benefits of flexible wing structures to MAV applications: static aeroelastic deformations of flexible wings may provide performance enhancements over a range of flight conditions, while active morphing may be used for flight control [7, 8, 14].

Fixed-wing MAVs are best suited for applications requiring long endurance and high cruise speeds, such as DARPA's over-the-hill reconnaissance mission. They are relatively efficient in producing lift at high flight speeds, and the low-aspect ratio wings provide more area to store fuel or fuel cells, mission equipment or payload than other MAV configurations. Fixed-wing designs use separate systems to produce thrust (engine/motor and prop), lift (airfoils) and control forces (control surfaces), significantly decreasing complexity of each subsystem from both a mechanical and a control standpoint. However, they must maintain a high forward velocity for their wings to generate lift and have large turn radii,

making them unsuitable for prolonged applications in confined environments.

1.1.2 Rotary-Wing Micro Air Vehicles

Rotary-wing configurations or micro-rotorcraft, based on helicopters, are an obvious choice for hover-capable MAVs. As with fixed-wing MAVs, initial development of micro-rotorcraft was expedited by the availability of preexisting components, and a number of vehicles have demonstrated controlled flight. Operational rotary-wing MAVs generally appear in two configurations: single-rotor designs with turning vanes, such as the Delft University of Technology XQ-138 [15] (figure 1.2a), the Micro Craft iSTAR [16] and University of Maryland (UMD) TiFlyer [17]; and coaxial-rotor designs, such as the UMD MICOR [18] (figure 1.2b) and active-structure MAV [19], Epson μ FR [20] and Cornerstone Research Group HALO [21]. A quad-rotor design has also been flight-tested by NASA Ames [22]; the same configuration is used by Stanford's three-gram Mesicopter [23] and Daedalus Flight Systems/UMD's Microquad [24]. MAVs' rotors are often shrouded to protect the blades and enhance performance. Drawing from the analytical techniques used for full-scale helicopters, design studies for airfoil and rotor configurations [25–28] as well as shroud geometry [29, 30] have



(a) XQ-138, a shrouded single-rotor configuration



(b) MICOR, a coaxial configuration

Figure 1.2: Rotary-wing MAVs.

been performed for micro-robotcraft.

Most micro-robotcraft use their rotors to provide both lift and thrust, though a ring-wing shroud can augment lift in high-speed forward flight. To reduce the complexity of the rotor system, many rotary-wing MAV designs use fixed-pitch rotors and provide control by directing the rotor downwash via control tabs. Some micro-robotcraft like MICOR, TiFlyer and HALO incorporate traditional control via swashplate. The efficiency of current rotary-wing MAVs, as measured by the figure of merit, is relatively low compared to full-scale helicopters [18, 26, 31]. A rotor with mixed-mode flapping-rotating motion, called an ornicopter, has been proposed as a method of increasing rotor efficiency and is discussed in section 1.1.4.

1.1.3 Bird-Like Micro Air Vehicles

Flapping-wing MAVs generate aerodynamic forces through oscillatory flapping motion of the wing surfaces. Flapping-wing flight is often conceptualized as two regimes, *bird-like* flight and *insect-like* flight, corresponding to the methods of steady flight used by the respective animals. The regimes are generally distinguished by the direction of wing flapping motion. Bird-like flight is characterized by wing motion in a primarily vertical plane. Bird-like flight may be more accurately designated as “fast forward flight” and is associated with high flight velocities. In contrast, insect-like flight is characterized by wing motion in a primarily horizontal plane. Insect-like flight is often considered to be synonymous to a method of hover known as “normal hovering flight.” Despite often being considered separately, the bird-like and insect-like flight regimes are not entirely distinct; rather, they should be viewed as opposing extremes of a continuum of wing motions. In flight, birds and insects alter the orientation of wing motion to generate transient control forces.

In the case of biological fliers, a much clearer distinction between so-called bird-like and insect-like flight can be made by considering the presence of active musculature in the wing. Bird-like fliers have muscles in their wings that allow active control of the shape of the wing (e.g., by extension and retraction). This control is necessary to enhance dissymmetry between the upstrokes and downstrokes in forward flight. Contrarily, insect-like fliers do not have muscles in their wings (in the case of hummingbirds, their muscles cannot actuate a shape change due to a fused wing skeleton). The wings of insect-like fliers have a fixed planform and generate roughly symmetric lift on the upstrokes and downstrokes. However, this distinction is not generally applicable to current MAVs—at present most “bird-like” MAVS lack the ability to actively alter the shape of their wings.

We now consider bird-like flight more in more detail. Birds (excepting hummingbirds) and all bats use bird-like flight. Almost all animals that use bird-like flight are larger than the desired MAV dimensions, many significantly so. Smaller wrens and finches are the only avian bird-like fliers with wingspans less than 20 cm. Bird-like flapping occurs in an approximately vertical plane with secondary forward-and-aft motion. Wing strokes are asymmetric, with the downstroke duration being generally less than the upstroke (i.e., the wings plunge downward faster than they return upward). Wingbeat frequency, stroke and gait may be varied depending on flight condition [32, 33]. The wings pitch about the span during the stroke, but remain relatively horizontal. All bird-like fliers have flexible wing structures—articulated bones covered by feathers in birds or membranes in bats—and musculature by which they actively morph their wings during each wingbeat, as illustrated in figure 1.3. In slow forward flight, bird-like fliers extend their wings fully during the downstroke, generating almost all lift and thrust for the stroke, then pull their wings backward and inward to decrease negative lift during the upstroke. At higher forward flight speeds the wing



Figure 1.3: A Canada goose in flight [34].

planform variation between up- and downstrokes is lessened, and some useful aerodynamic forces are generated on the upstroke. In addition to wing span and sweep, bird-like fliers can actively alter the twist and camber of their wings. The wing surfaces can also flex passively like sails to adapt to the free-stream airflow; in some cases, sets of feathers act as self-deploying flaps.

Besides the impressive adaptability of their wings, bird-like fliers are aided by the time-periodic nature of flapping, causing unsteady stall effects which increase the maximum instantaneous lift coefficient on the downstroke. A bound leading-edge vortex, similar to those seen on delta-wing aircraft, has been recorded on small swifts [35] and may appear on other birds as well. Two recent literature surveys augment biological studies of bird-like flight with engineering analyses to aid MAV development. Shyy, Berg and Ljungqvist [36] focus on kinematics, aerodynamics and power consumption of bird-like flight. Lindhe Norberg [37] reviews structural morphology of bird-like animals with some additional discussion of insect-like and gliding/parachuting flight structures. Videler's *Avian Flight* [32] provides a more in-depth look at the mechanisms of bird-like flight.

Almost none of the adaptability of biological bird-like fliers has been replicated by bird-like vehicles, called ornithopters. In contrast to biological fliers' wide range of wing motions an ornithopter typically has only a single degree of con-

trolled wing motion, vertical flapping motion about the root; cf. the University of Toronto's model and human-sized ornithopters [38], the Aerovironment/Caltech Microbat [39] (figure 1.4a), and the UMD JLMAV [40] as well as commercially available model-scale ornithopters such as the Tim Bird and Cybird. Flapping motion is invariably generated by a four-bar or slider-crank mechanism connected to a driven shaft, which has the effect of fixing the wings' stroke and gait. All ornithopters to date have had fixed planforms. Most ornithopters, and all operable research-based MAVs like the Microbat and JLMAV, have simple wings composed of a stiff leading-edge spar and one or more trailing spars spanned by a torsionally compliant membrane. Wing deformations result in a net positive thrust but little lift; an angled tail is used to point the thrust vector upwards to create usable lift [41]. This design is exceedingly primitive; Alphonse Pénaud was using such a configuration in 1874, illustrated in figure 1.4b [41]. We may thus designate vehicles with a single flapping degree of freedom (typically with a fixed amplitude) and membrane wings with a stiff leading-edge spar as "Pénaud-type ornithopters." DeLaurier notes this configuration is inefficient in creating lift; other ornithopter configurations add fixed cambered airfoils to improve efficiency, but none truly capture biological bird-like flight. DeLaurier himself has developed aerodynamic and aeroelastic analyses of ornithopter flight for large-scale vehicles

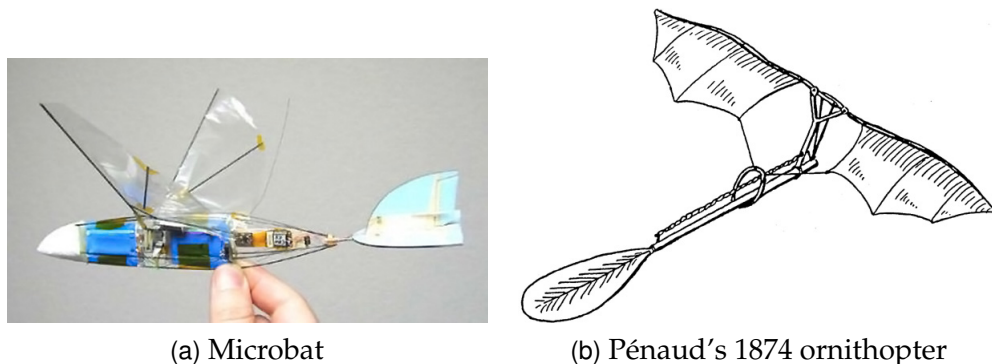


Figure 1.4: MAV-scale ornithopters.

with thick airfoils [38,42–44] but such thick airfoils may not be practical for MAVs.

Interest in MAVs has spurred development of new integrated technologies for ornithopter application. Pornsin-Siriak et al. have used MEMs etching techniques to create wing spars that mimic two-dimensional bone and venation patterns of bats and insects [39]. The same team developed flexible check-valves integral to the wing membrane to allow airflow through the wing on the upstroke, alleviating negative lift without wing morphing [45]. Kim and Han affixed a Macro Fiber Composite (MFC) piezoelectric actuator to a Pénaud-type ornithopter wing to actively induce camber during each downstroke and reported a 20% increase in lift [46]. Kim and Han implemented their system on a commercially available Cybird ornithopter with a wingspan of 99 cm—over six times larger than MAVs.

1.1.4 Unconventional Micro Air Vehicles

Some proposed MAVs do not follow the configurations of previous aircraft or animals. Michelson argues in “Novel Approaches to Miniature Flight Platforms” [3] that MAVs are hindered by “the uncreative tendency towards biomimicry” and suggests designers aim instead for bioinspiration: leveraging knowledge gained from biological fliers without creating exact mechanical copies. Furthermore, he advocates designing vehicles from the start to be energy-efficient via integrated multifunctional structures. As an example Michelson presents his Entomopter design (most closely akin to ornithopters, despite its name), a flapping MAV with two sets of rigid wings at opposite ends of a beam fuselage, as depicted in figure 1.5. The fuselage is designed with a torsional resonance at the wingbeat frequency to enhance the out-of-phase flapping of the two wings. The Entomopter will be powered by a reciprocating chemical muscle (RCM) powered by chemical fuel. The RCM produces byproduct waste gas, which will be used for a variety of different purposes including flow-control over the wings and internal gas bear-

ings. Constructing such a complex MAV appears to be no small task and after more than a decade of research no fully operational Entomopter exists, despite the successful development of four generations of RCMs. The flight of a nonresonant model of the Entomopter powered by a rubber band—essentially a Pénaud-type ornithopter with fore and aft wing pairs—is presented on the Entomopter Project website [47].

Many other bioinspired unconventional MAVs exist. One is Jones’ series of flapping-wing-propelled MAVs, one of which is pictured in figure 1.6 [48]. These MAVs use a fixed airfoil to generate lift, trailed by a pair of vertically plunging Pénaud-type wings which generate thrust alone. The thrust-generating wings flap in opposing directions and pitch freely about a leading-edge hinge, mimicking bird-like flapping. The opposing flapping causes the wings to operate as if they are in ground effect, thereby increasing thrust. The flapping wings have an added benefit of eliminating stall on the primary fixed wing by entraining airflow over it at all flight speeds. Jones has successfully flight-tested controllable prototypes of his design.

Another type of bioinspired designs called ornicopters or rotopters combine the vertically flapped wings of ornithopers with the rotary-wing motion of helicopters. Figure 1.7 shows a time-lapse image of an ornicopter rotor in motion.



Figure 1.5: Mock-up of Michelson’s Entomopter.

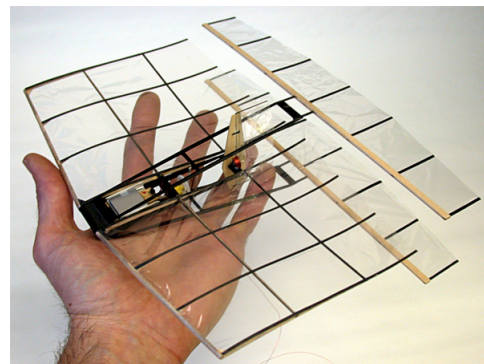


Figure 1.6: Jones’ flapping-wing-propelled MAV.

Vladimir Savov developed the configuration as a means of preventing the main-rotor torque reaction in full-scale single-rotor helicopters, thereby saving power by eliminating anti-torque devices [49]. Forced vertical flapping of the rotor blades cause them to act like ornithopter wings, producing thrust that spins the rotor in addition to lift. Since the rotor shaft is not directly driven there is no reaction torque on the fuselage, though the vertical reaction force from blade flapping would likely be problematic. Researchers at the Delft University of Technology implemented an ornicopter mechanism on a remote-controlled helicopter; flight forces and control authority have been measured on force balances, but free flight has not yet been achieved [50]. MAV research of ornicopters has studied the efficiency gains from a torqueless main rotor, but has also explored a second mode of actuation in which the rotary blade motion is driven. By superimposing higher-harmonic blade flapping onto traditional rotary motion, it is hoped that unsteady aerodynamic effects will improve the low figure of merit of rotary-wing MAVs. Experimental results from UMD's Flotor ornicopter MAV test-stand show improvements in both figure of merit and maximum thrust from superimposed blade flapping [51].

Drawing inspiration from a maple tree's winged seeds, or samaras, yet another type of bioinspired MAV takes the form of a single-bladed rotor, shown in figure 1.8. A biological samara acts as a single-bladed autorotating rotor,

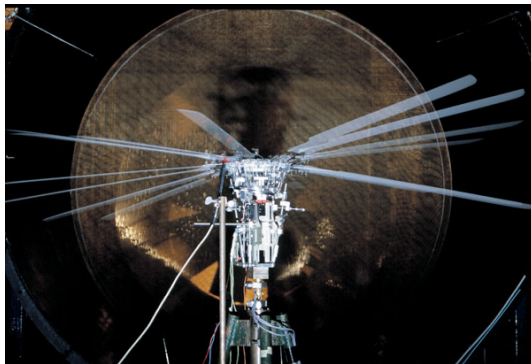


Figure 1.7: Time-lapse image of Delft U. Tech. ornicopter rotor.



Figure 1.8: MAV-scale robotic samara, with natural samara.

generating lift to decrease its rate of descent and increase its dispersal from the parent tree. The robotic samara MAV adds a powered prop to drive the rotor's rotation, thus generating enough lift for sustained hover and flight [52]. In the event of a power loss, the robotic samara autorotates to a safe landing just as a biological samara does. The robotic samara presents a unique challenge for vehicle control. Since the entire MAV structure rotates with the blade, the robotic samara has no fixed reference frame in which to apply a control scheme. This challenge was solved by a novel system that takes advantage of a relationship between the collective pitch of the blade and the MAV's radius of gyration. By altering the blade's pitch and the MAV's rate of rotation (via the prop's throttle) full control of the robotic samara can be achieved [53,54]. Operational robotic samara MAVs have been developed and flown by Ulrich et al. [52–54].

A final unconventional design is not bioinspired, but rather a revisitation of an abandoned full-scale configuration: the cyclogyro (or -giro). Pictured in figure 1.9, the cyclogyro's cycloidal rotors are egg-beater-shaped assemblies with straight blades arranged cylindrically and rotated about the horizontal axis. Periodic pitching of the blades, typically implemented with a four-bar apparatus, creates a net aerodynamic force directed radially outward from the rotor. The direction of the aerodynamic force is controlled by altering the phasing of the

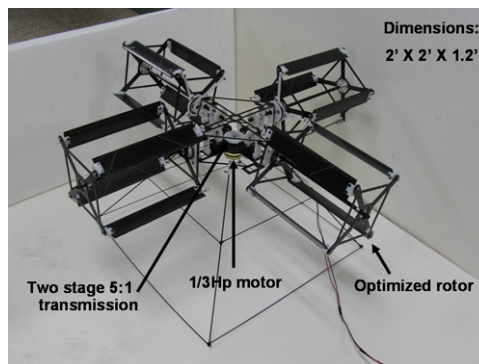


Figure 1.9: Quad-rotor cyclogyro.

blades' pitch. Each airfoil sees a uniform velocity profile across its span—in contrast to helicopters and ornicopters—so the entire blades can be optimized for high efficiency operation. In his brief overview of the cyclogyro, Prouty explains that full-scale cyclogyro research in the 1920s and 30s was halted because of repeated material failures of test rotors, not a fundamental deficiency of the concept [55]. Cycloidal rotors are attractive in MAV applications because they appear to have greater power loadings than conventional rotors [56]. Design studies for MAV-scale cyclogyros have been performed with CFD by Iosilevskii and Levy [57] and with momentum theory by Sirohi, Parsons and Chopra [56]; both teams experimentally validated their studies with test-stand-mounted cycloidal rotors. Prouty notes that cyclogyros operating in high-speed flight (i.e., translational speed on the same order as the blade rotation speed) will need unconventional airfoils and likely require independent blade control (IBC) to optimize lift in both hover and translating flight. This may not be an issue with MAVs, which should have relatively low translational speeds and blade rotation on the order of thousands of RPM. Recently a quad-rotor cyclogyro developed by Benedict, Jarugumilli and Chopra that has demonstrated tethered hover [58], and Benedict et al. have undertaken experimental studies to improve the performance of cycloidal rotors [59–61].

1.2 Insect-Like Biological Flight

The previously discussed MAV configurations all have advantages and disadvantages. Fixed-wing and rotary-wing MAVs leverage available knowledge and technology from full- and model-scale vehicles to achieve quick technological maturation, but fixed-wing MAVs are not suitable for indoor missions and rotary-wing MAVs are significantly less efficient than their full-scale counterparts. Ornithopter MAVs seek to emulate the performance of birds, but are hamstrung

by an inability to yet replicate the morphing structures of avian wings. Instead, ornithopters have remained largely unchanged since before the Wright brothers. It is not improbable that “unconventional” configurations represent the actual future of MAVs: vehicles which neither downsize full-scale vehicles nor exactly emulate nature, but incorporate and synthesize elements of both. There is another attractive configuration that warrants attention: insects and insect-like fliers, which already operate in MAVs’ desired size and performance range. Robin Wootton makes this connection explicit: “insects are past-masters of slow, precise, manoeuvrable flight and hovering—exactly the qualities needed in an MAV” [62]. This section gives an overview of the current knowledge about biological fliers themselves; discussion of MAVs that mimic these creatures is in the following section.

Winged insects constitute an astounding portion of life on the Earth. Over one million species of *Pterygota*, or ancestrally winged insects, have been described (more than any other animal group) and their global biomass exceeds that of humans by an order of magnitude [63, chap. 1]. The diversity and success of insects arises directly from their ability to fly, granting access to a wide array of habitats and resources.* The overwhelming majority of insects are much smaller than MAVs, with typical wingspans on the order of a few millimeters. The largest insects approach the desired size of MAVs: species of butterflies, moths and dragonflies reach wingspans of 10 cm or more. Adult insects’ maximum weight is less than half the projected MAV weight, limited to 40 to 50 g by their respiratory system [63, p. 3], though the flightless larvae of Goliath beetles may exceed 100 g. The heaviest insects are poor fliers; highly aerobatic insects weigh significantly less. For example the *Manduca sexta* hawkmoth,[†] an exceptional flier

**Apterygota*, insects whose ancestors never developed wings, account for less than 0.1% of known living insect species. Natural selection has clearly favored flying insects over non-flying insects.

[†]“Hawkmoth,” “sphinx moth” and “hornworm” are common names for moths in the family Sphingidae. Sphingidae moths are well-known for their agile flight and are common subjects of insect-flight research.

with a wingspan of 10 cm, weighs about 1.5 g [64].

Convergent evolution has driven hummingbirds to approximate insects not only in size and flight method but also in metabolism, diet and behavior [63, pp. 334–336]. Hummingbirds are slightly larger and heavier than comparable aerobic insects. Hummingbird wingspans over 15 cm and weights over 5 g are not uncommon; the giant hummingbird *Patagona gigas* can exceed 24 cm in wingspan and 20 g in weight [65, p. 213].

Considering the diversity of winged insects, it is not surprising that flight kinematics and wing structures vary profoundly among species. This dissertation will focus on so-called “normal hovering flight,” in which a functionally two-winged flier maintains its mid-air position by beating its wings in an approximately horizontal stroke plane [66, 67]. Normal hovering flight is used by animals that generate aerodynamic forces via a single pair of wings (e.g., flies, mosquitoes, beetles, hummingbirds) or two pairs of wings acting in concert as one (bees, wasps, butterflies, moths). The majority of hover-capable animals that have been subjects of aerodynamic study use normal hovering flight; figure 1.10 depicts some examples. Exceptions to normal hovering flight include animals that hover with inclined stroke planes (hoverflies, dragonflies) and functionally four-



(a) White-lined sphinx moth [68]



(b) Rufous hummingbird [69]

Figure 1.10: Animals using normal hovering flight.

winged animals that flap two pairs of wings with a phase differential (dragonflies, grasshoppers, lacewings).

1.2.1 Kinematics

In normal hovering flight, the wings on both sides of the animal's body move symmetrically. The primary motion is flapping rotation, a rotation about the wing base in an approximately horizontal stroke plane as illustrated in figures 1.11 and 1.12. Most animals' flapping stroke amplitude in hover is 120 to 180° [66, 70], and may increase up to 180°+ at maximum loading [71]. Some small insects' wings touch at the end of the upstroke, producing an aerodynamic phenomenon called the Weis-Fogh mechanism or clap-and-fling. Flapping is typically a nearly harmonic, sinusoidal motion [63, p. 91; 70]. In forward flight, the stroke plane

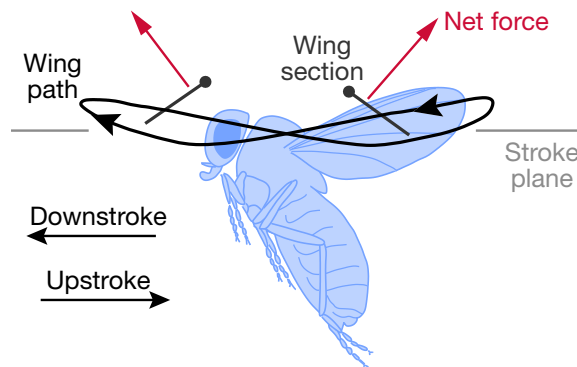


Figure 1.11: Generalized wing motion during normal hovering flight. Modification of original image by Michael H. Dickinson, used with permission.

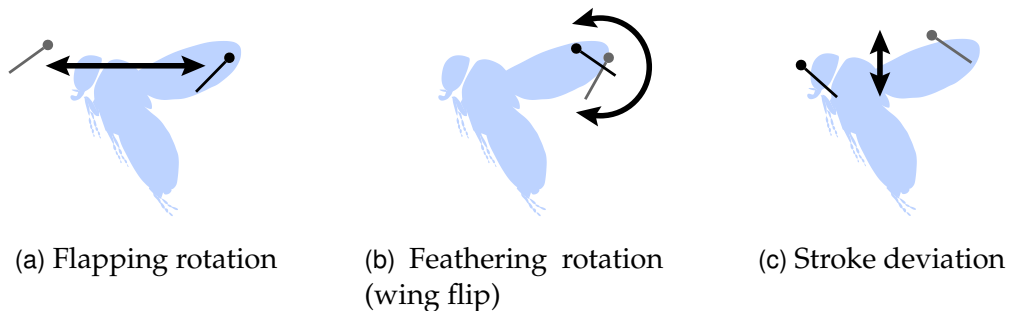


Figure 1.12: Components of insect wing motion.

is tilted forward and the half-strokes become asymmetric [63, p. 95], making the motion more bird-like.

At the end of each half-stroke, the wing undergoes a large-angle rotation about its span often referred to as the wing flip.[‡] In so doing the wing reverses orientation; the upper wing surface during the downstroke becomes the lower surface during the upstroke. The leading edge of the wing, denoted by a dot on the wing section in figure 1.11, is the same during both half-strokes. The angle of incidence between the wing and the stroke plane, or the geometric angle of attack, is relatively constant through the middle of the down- and upstrokes. (In general, this dissertation will prefer the terms “feathering angle” and “feathering rotation” over “geometric angle of attack” when discussing angular motion as opposed to absolute static measures, see section 2.2.1.) The geometric angle of attack of hovering insects at mid-stroke is 30 to 45°; for hummingbirds it is closer to 15° [70]. Insects can alter the timing and extent of the wing flip depending on flight conditions [63, p. 96].

The third component of normal hovering motion is stroke deviation, where the wing moves perpendicular to the stroke plane. This deviation is small with respect to the flapping motion and often varies from wingbeat to wingbeat [63, p. 93]. Stroke deviation may cause the wing tip to trace out shapes such as figures-of-eight (as in figure 1.11), ovals, crescents or more complex paths [70]. Its purpose is not well understood. Wang has suggested that plunging motions in normal hovering flight may induce an upward-directed drag force to help support body weight [72]. (The primary subjects of Wang’s study were dragonflies, functionally four-winged insects that hover with asymmetric wing strokes in a highly inclined stroke plane. She concluded 75% of a dragonfly’s weight is supported by drag

[‡]Perhaps influenced by side projections like figure 1.12, flapping rotation is often termed “translation” and the wing flip termed “rotation”. Such terminology obscures the former’s rotational nature.

forces, with the wings primarily acting like rowing oars.)

1.2.2 Aerodynamics

Our knowledge of insect-like aerodynamic phenomena is far from complete. Application of modern engineering tools and analyses has aided the understanding of insect-like aerodynamics, but the low Reynolds numbers and unsteady nature of the airflow present a significantly different flow regime than aerodynamicists have previously studied. Compounding the difficulties are the small sizes, high wingbeat frequencies and experimental uncooperativeness of insects, which hinder accurate high-resolution measurements of the airflow. These issues have caused aerodynamic phenomena to be overlooked or misunderstood in both theory and experiment [73]. Properly understanding insect flight may require paradigm shifts in thought—Wang has gone so far as questioning the applicability of classical conceptions of lift and drag when studying insect flight [72].

1.2.2.1 *Early Comprehensive Studies*

The earliest attempt at a general aerodynamic analysis of normal hovering flight was undertaken by Weis-Fogh in 1973 [66]. Weis-Fogh developed general equations for the mean quasi-steady lift produced and power consumed by normal-hovering animals in a single wingbeat. He assumed the majority of lift was created by the high-speed flapping rotation during the midstrokes; effects associated with the wing flip were mostly neglected. He applied his lift equation to data of biological fliers from extant literature and his own observations, including 26 species of insects, three species of hummingbirds and one species of bat. The mean lift coefficients necessary to satisfy his equations were generally less than the maximum lift coefficients experimentally measured from biological fliers' wings. Therefore, Weis-Fogh concluded that the aerodynamics of most normal-hovering

animals could be adequately modeled by quasi-steady analyses, with the caveat that unsteady effects must certainly play a role at some points during the stroke. This conclusion was subsequently refuted by Ellington (see below).

The most enduring contribution of Weis-Fogh's study was his identification of the unsteady "clap-and-fling" flight mechanism, proposed to explain anomalously large lift generation by certain small wasps. This mechanism, also called the Weis-Fogh mechanism, theorized that "clapping" the wing surfaces together during the wing flip at the end of the upstroke then "flinging" them apart about the trailing edges eliminates the starting vortices of each wing on the downstroke, as diagrammed in figure 1.13. More precisely, clap-and-fling causes the starting vortex of each wing to manifest as the bound circulation around the opposing wing [74]. Thus, the wings to operate at their full steady-state lift coefficient during the entire downstroke, overcoming the Wagner effect limiting the instantaneous build-up of circulation around an impulsively moving wing. Weis-Fogh calculated that the clap-and-fling mechanism would be available to any animal but would be most efficient for smaller animals (the wasps being studied by Weis-Fogh had wing

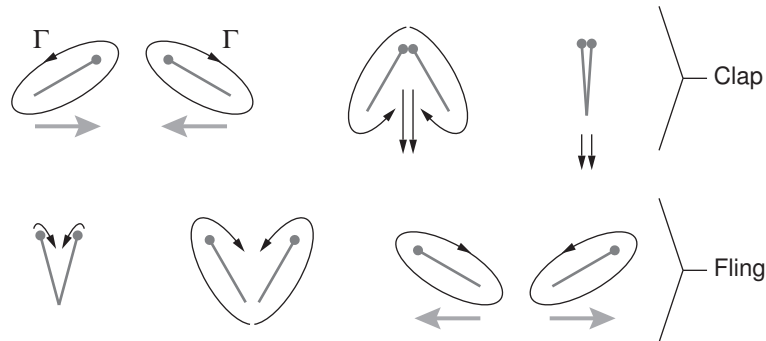


Figure 1.13: Conceptual diagram of clap-and-fling. The clap causes mutual annihilation of the circulations Γ on each wing. Air is forced from between the wings, creating a momentum jet that may provide additional lift [74]. The fling draws air into the widening gap between wings in the correct sense for lift production. The wings separate at the trailing edge; since the net circulation of total system is zero, there is no delay in circulation build-up around either wing. After Weis-Fogh [66] and Sane [73].

lengths less than 1 mm). However, use of clap-and-fling by biological fliers is the exception, not the rule. Additional theoretical and experimental studies of the Weis-Fogh mechanism were undertaken by Lighthill [75] and Maxworthy [76]. Ellington identified several variants of this mechanism: clap-and-peel, partial fling and near fling [74].

Ellington's landmark six-part study in 1984, "The Aerodynamics of Hovering Insect Flight," was the next major attempt at a general analysis of insect aerodynamics in hover, via a comprehensive amalgam of literature review, theory and experiment. Revisiting Weis-Fogh's analysis, Ellington noted deficiencies in both the theory and the experimental data. By applying "new data and a new theory," Ellington reported "the opposite conclusion [of Weis-Fogh] is strongly indicated": unsteady effects play a nonnegligible role in lift production [67]. From his own and other researchers' measurements, he compiled morphological data of 48 individual insects representing 18 species, as well as two species of hummingbird and one species of bat [64]. Using a high-speed film set-up, he recorded the flight of insects and selected 11 sequences that best approximated hover: nine film sequences showed normal hover of eight species of insects, and two sequences showed hoverflies using an inclined stroke plane. The wing kinematics of each sequence were mapped from individual frames of film [70]. Using these kinematics as a starting point for theoretical considerations, Ellington made "deductions" about possible additional aerodynamic mechanisms [74]. These mechanisms included the Wagner effect, virtual-mass effects, leading-edge separation bubbles, delayed stall, clap-and-fling and its variants, and rotational effects of the wing flip. He noted the inapplicability of many classic unsteady airfoil analyses, since their simplifying assumptions—small angle perturbations, large forward velocities, planar wakes—did not hold for normal hovering. In an effort to model the gross influence of unsteady effects on flight forces, Ellington developed a "pulsed actuator disc"

model to calculate the mean lift of each stroke by modifying a momentum-theory actuator disc (as used in propeller and helicopter analyses) with correction terms accounting for spatially and temporally nonuniform circulation [77]. Finally, he applied the experimental data and analytical tools from the previous parts to calculate the lift production and power requirements of insects in his selected hovering sequences, and used the results to reiterate his conclusion that quasi-steady lift alone is inadequate for modeling normal hovering flight [78].

Ellington's papers of 1984 seem to represent a turning point in the investigation of insect aerodynamics. No subsequent study has adopted Weis-Fogh's and Ellington's methodology of developing a general aerodynamic model, then applying it to a data set of diverse biological fliers. We can only speculate as to why this may be, but a key difficulty seems to be measuring the physical wing/air system. As scientists better understand the complex interaction between wing and air, modeling its aerodynamics requires motion and airflow histories at more precise temporal and spatial resolutions than are conveniently available. In fact, measuring instantaneous aerodynamic force distributions on biological fliers' wings is a challenge that has not yet been solved, while coaxing animals to simply fly in a prescribed position or attitude is difficult (many tests on live insects "tether" them in a fixed position, but this can induce unnatural wing motions compared with free flight) [73]. It appears that our modeling of insect aerodynamics currently outstrips our capability to acquire data from insects themselves. Thus, emulating the biological breadth of Weis-Fogh's or Ellington's simplified studies in verifying state-of-the-art aerodynamic models is essentially impossible today. After Ellington's study, most raw quantitative data for insect aerodynamic models comes not from direct measurements of biological fliers, but from scaled mechanical models and computational fluid dynamics (CFD) programs, which offer better resolution [73]. Such models are validated as well as possible against

insects, but this is not an ideal situation since they may not capture all aspects of insect flight. Still, they remain the most viable data source at this time.

1.2.2.2 *Aerodynamic Mechanisms*

In another respect, Ellington's identification of unsteady aerodynamic mechanisms provided a stepping stone for much of the subsequent study of insect aerodynamics. With the understanding that additional aerodynamic mechanisms were necessary to explain insect flight, aerodynamic research since the mid-1980s has focused on identifying and understanding the roles of these mechanisms. In addition to quasi-steady effects, the following mechanisms are considered important: the Wagner effect, virtual mass, clap-and-fling, the leading-edge vortex, wing-wake interaction and the Kramer effect [73,79]. The first three were correctly identified by Ellington: the Wagner and virtual mass effects are well known, especially in helicopter studies [80, ch. 8] and clap-and-fling was discussed earlier. The leading-edge vortex, wing-wake interaction and the Kramer effect will be summarized in turn. The primary source for these summaries is Sane's review of insect aerodynamics [73]. Ansari, Żbikowski and Knowles briefly review the same effects in reference to the modeling of MAV aerodynamics [79]; comparing and contrasting with Sane's review provides some insight about the varying interpretations of the mechanisms. Finally, Wang's review approaches insect aerodynamics as a useful test case for understanding fluid mechanics [81]; while only a small portion specifically pertains to normal hovering flight, it gives a refreshing view from outside the biological and MAV fields and offers provocative alternatives to those fields' conventional wisdom.

The leading-edge vortex (LEV) is a vortical flow structure that extends along the leading-edge of the flapping insect wing. Though its significance was only first guessed by Ellington et al. in 1996 [82], by 2003 it was considered "the single most

important feature of the flows created by insect wings” because of its apparent ability to explain the large lift generated by insect wings [73]. The LEV is a low-pressure vortex that remains stably attached to the top of the wing at the leading edge throughout the flapping stroke, as diagramed in figure 1.14. Its structure breaks down somewhat near the wing tips, where it merges with the tip vortices. The LEV’s effect on flight forces is similar to the delayed-stall effect: the low-pressure vortex creates a suction perpendicular to the wing surface, which increases the stall angle beyond its steady state value. But in contrast to delayed stall, where the vortex continues growing until it sheds with subsequent loss of lift, the attached LEV reaches a stable state and remains on the wing through most of the flapping stroke. Usherwood and Ellington demonstrated the existence of an attached LEV on continuously revolving wings, which implies that the LEV is caused by the rotational flapping motion and is not merely delayed stall operating within the distance of the flapping stroke [84]. The attached LEV in fact appears most similar to the vortices seen on the leading edges of delta-wing aircraft. Ellington et al. identified a strong spanwise velocity in the vortex, and suggested that the vortex’ stability is due to the transportation of air radially towards the wing tips. However, other studies have identified attached LEVs with weaker spanwise components, leading to speculation that the details of the flow structure

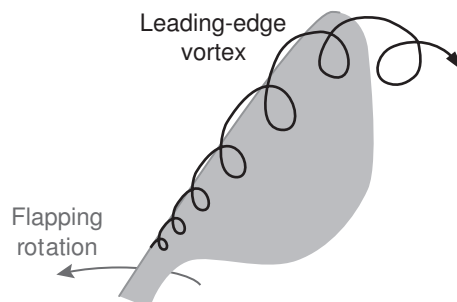


Figure 1.14: Cartoon of attached leading-edge vortex on flapping insect wing. Note spiraling flow structure caused by spanwise air transport. After van den Berg and Ellington [83].

may be Reynolds number dependent [85]. Wang offers an alternative conceptual explanation for the attachment of the LEV, speculating the low root velocity may “pin” the vortex to the wing and prevent shedding [81].

During the wing flip at the end of each half-stroke, an insect wing will shed its wake, undergo a large pitch rotation and reverse direction through the still-advancing newly shed wake. Ansari, Żbikowski and Knowles call this wing–wake interaction “the distinguishing feature of insect-like flapping” [79]. The existence of wing–wake interactions was speculated for some time but their significance, like that of the LEV, was not recognized until the middle of the last decade. Dickinson and his associates first measured gross forces due to wing–wake interactions on robotic models operating in mineral oil: first on a 2-D translational flapper in 1994 [86] then on their Robofly 3-D rotational flapper in 1999 [87]. The data showed large force spikes during the wing flip corresponding to wing–wake interactions visualized with particle image velocimetry. Furthermore, the magnitude of the spikes was highly dependent on the timing of the wing flip, implying that the flip kinematics play a significant role in force production. Since the wing can generate large forces by interacting with, and presumably drawing energy from, its own wake this phenomenon is also known as wake capture. The interaction between the shed wake and reversing wing is an extremely complex fluid-flow problem, and its mechanics are not well understood. Ramamurti and Sandberg’s CFD study concurred that wing–wake interaction causes force peaks [88], but Sun and Tang’s CFD study suggested that the force spikes were caused by the rapid accelerations of the wing, *not* wing–wake interactions [89]. Further particle image velocimetry studies by Dickinson’s research group using the Robofly flapper again showed evidence of wing–wake interactions [90]. Both Sane and Wang agree in their reviews that wing–wake interactions and acceleration effects must both play some role in force-peak production, but that the relative contributions of

each mechanism are not clear at this time [73,81]. Tarascio et al. performed flow visualization on an open-air flapping test stand and identified a complex wake structure in which the returning wing interacts with not just its immediately shed wake, but with a rolled-up wake structure comprised of many previous stroke wakes [91].

The Kramer effect is an alteration in circulation, and hence lift, of a translating wing that is also pitching. In insect studies, it is commonly ascribed to the delay in establishing the trailing-edge Kutta condition on a pitching wing [73]. If the wing continuously changes pitch, the airflow cannot establish the Kutta condition instantaneously and circulation steadily increases or decreases, causing a continual alteration in lift. This lift is proportional to the rate of pitching rotation, so the phenomenon is sometimes called “rotational lift.” In fact, the Kramer effect is a quasi-steady effect that is well-known in helicopter theory: it is exactly the quasi-steady pitch-rate ($\dot{\alpha}$) dependent lift of a thin airfoil; see Leishman [80, p. 430]. Sane and Dickinson experimentally estimated the “rotational lift coefficient”[§] of their Robofly model wing in a mineral-oil tank and reported that the rotational lift coefficients decreased with pitch rate at low frequencies, in conflict with theory showing that the coefficient should be independent of pitch rate. However, using a constant rotational lift coefficient—one consistent with both theory and their own high pitch-rate data—Sane and Dickinson reported good correlation between predicted and measured forces [92].

1.2.2.3 Numerical Aerodynamic Modeling

As a coda to the discussion of flapping-wing aerodynamics, some of the current modeling techniques used to numerically calculate aerodynamic forces on

[§]Sane and Dickinson’s rotational lift coefficient is equivalent to the $\dot{\alpha}$ component of Leishman’s lift coefficient multiplied by half the free-stream velocity and divided by the pitch rate and chord. It is theoretically a constant determined by the nondimensional pitching axis location.

the wing are briefly mentioned; see Ansari, Żbikowski and Knowles [79] for a full historical review. Though the quasi-steady assumption has been refuted for normal hovering flight, Sane and Dickinson developed a “revised” two-dimensional quasi-steady model which included steady translational aerodynamics, added mass effects and the Kramer effect [92]. A blade-element analysis using this model showed good correlation to experimental data obtained from their Robofly flapping mechanism except at the beginning of each half stroke caused by the model’s inability to deal with unsteady wing–wake interactions and/or spanwise flow effects. On the opposite end of the complexity scale are fully three-dimensional CFD codes, from Smith, Wilkin and Williams’ early unsteady panel method in 1996 [93, 94] to more advanced incompressible Navier–Stokes solvers by Liu and Kawachi [95], Ramamurti and Sandberg [88] and Sun and Tang [89].

Most recently, focus has shifted to the development of two-dimensional unsteady analytic aerodynamic models intended to be simple yet accurate enough to provide design data for MAV development. The conceptual framework for such an approach was laid out in Żbikowski’s 2002 paper, where he proposed to “account separately for the bound leading-edge vortex and for the other [non-vortical] part of the flow, then adding both contributions” [96]. To do so, Żbikowski recommended application of helicopter-based aerodynamic methods to account for the non-vortical flow of a rigid wing (i.e., quasi-steady, unsteady and wake-interaction effects) and the Polhamus suction analogy to account for the leading-edge vortex. This method was practically applied by Żbikowski et al. [97]. Extensions to this technique have been introduced by Singh and Chopra [98], who added thin-airfoil aerodynamic effects of linear structural deformations, and by Ansari, Żbikowski and Knowles [99], who introduced a nonlinear aerodynamic formulation.

1.2.3 Wing Structures

Insect wings are lightweight, flexible structures that significantly deform during flight. These deformations presumably affect aerodynamic forces [100]. However, relatively little is known about insect wings' functional morphology, the relationship between their physical form and their functional operation. Wing flexibility is often considered a secondary effect in studies of insect flight. The large majority of aerodynamic studies ignore flexibility by assuming or constructing rigid wings. As recently as 2003, Sane's review of insect aerodynamics did not include any models that accounted for flexibility [73]. Sane cited the incorporation of flexibility as necessary future research.

Direct functional analysis of insects' wings is a difficult task, hindered by insect species' wide range of wing geometries and configurations and by the wings' inherent multifunctionality [101, ch. 4]. Besides their role as airfoils, an insect's wings may be involved in protection, thermoregulation, sexual selection or territorial displays (the latter two encompassing both visual and aural signaling); furthermore, many insects' wings fold and lay flat against the body or under hardened outer wings [102]. For a given insect, differentiation of the wing structures pertinent to flight from those related to other tasks is not obvious, if it is possible at all. As such, there are few analytical models which predict the functionality of a particular feature of the wing structure. Instead much of our understanding comes from simplified conceptual or physical models—imagining the wing as a sail, for example, or using creased paper to demonstrate wing folding—or from increasingly elaborate finite element models that attempt to model the wing as accurately as possible [103].

At the most basic level insect wings are sheets of cuticle membrane supported by veins [63, ch. 2]. The veins, either individually or as linked groups, act as spars in the wing. No musculature exists within the wings; unlike most avian

wings, insect wings are not “active” structures in the sense of having embedded muscular actuators. Insects can only control their wings via actuation at the wing base, where it intersects the thorax. In theory, then, knowledge of the wing’s static geometry and material properties is sufficient to characterize its functional morphology. In practice, the complexity of the vein and membrane structures make such characterizations difficult. The dragonfly shown in figure 1.15 is illustrative of typical insect wings, although it does not use normal hovering flight and is thus not directly within the scope of this dissertation. The wing membrane is a three-dimensional structure with numerous pleats or corrugations [104]. The size and cross-sectional shape of the veins vary between differing veins and along the span of individual veins [102]. Major longitudinal veins are linked and supported by smaller cross-veins. The wing membrane itself varies in thickness and stiffness throughout the wing.

For the remainder of this section, current knowledge of insect functional morphology as pertaining to normal hovering flight is summarized. Significantly more in-depth discussions of insect wing morphology can be found in books by Dudley [63] and Grodnitsky [101], both of whom use evolutionary considerations as a means of exploring wing functionality. Wootton’s review paper of 1992 [102] provides a more succinct summary, albeit one that does not include research from the last two decades.



Figure 1.15: Insect wing structure, as seen in a photograph of a dragonfly [62].

Figure 1.16 represents a generalized insect wing structure, as developed by Wootton in his effort to standardize the nomenclature of wing components [105]. This image is reproduced to present an overview of the functional structure of the wing; the nomenclature itself is unimportant to this dissertation. The three longitudinal veins running parallel to the leading edge (labeled costa, subcosta and radius in figure 1.16a) are typically the largest and thickest veins and act together as a leading-edge spar for the wing, cf. figure 1.15. The remainder of the wing veins are generally oriented at an angle to this leading-edge spar, running outwards and backwards from the leading edge or from the wing root. Insect wings have distinct lines through which they flex during flight and wing folding, as drawn on figure 1.16b. Flexion lines are the regions which primarily deform during flight (the marked claval furrow is also a flexion line). For example, the median flexion line acts as a hinge for the reversible camber of the wing. In contrast, fold lines deform primarily when the wings fold next to the body when not in use. The flexion and fold lines may fall between longitudinal veins or they

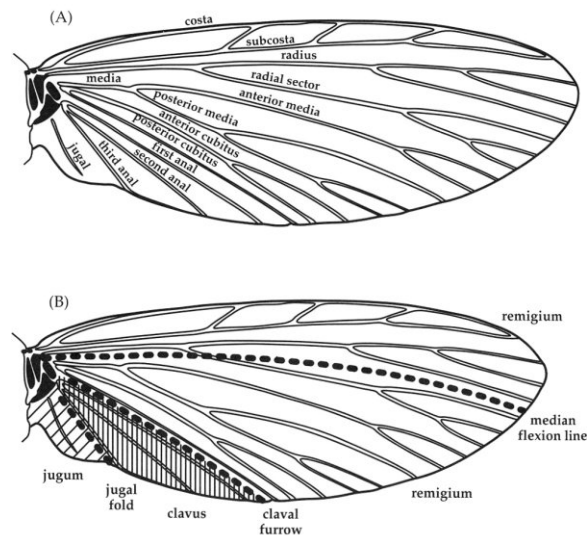


Figure 1.16: Generalized vein geometry and flexion lines of insect wings [63, p. 54]. The top of the wing is the leading edge. Diagram (a) identifies the longitudinal veins of the wing; cross-veins between the longitudinal veins are not drawn. Diagram (b) identifies functional regions and lines of flexion and folding.

may cross longitudinal veins at structurally weakened points. The generalized diagrams in figure 1.16 should not be considered accurate representations of any particular insect. Over the course of a species' evolution, veins may merge, split or disappear; flexion and fold lines may be more or less numerous and can vary in location on the wing. In fact, it is exactly the extreme variability of different insects' wing structures that obscures analyses of functional morphology.

1.2.3.1 Deficiencies of Structural Data in Aerodynamic Modeling

Confounding the deduction of insect wings' aeroelastic functional morphology is biologists' current reliance on numerical and mechanical models—in particular, rigid-wing models—for aerodynamic data sets. As discussed previously, much of the detailed aerodynamic data used in recent insect studies comes not from measurements of insects themselves, but from measurements of scaled physical models or from CFD programs. Many of these studies are performed with rigid non-deforming wings, either to enable the study of pure aerodynamic effects or for simplicity. Dickinson's Robofly, a Reynolds-scaled device that accurately reproduces three-dimensional *Drosophila* (fruit fly) kinematics in mineral oil and is the most advanced mechanical model to date, is typically outfitted with rigid wings [87].[¶] It is not an overstatement to say most of the experimental time-history data of aerodynamic forces on flapping wings used in studies over the past fifteen years have been generated from the rigid-wing Robofly, pictured in figure 1.17. Dickinson's research group has used Robofly to generate data for the study of leading-edge vortices [85], wing-wake interactions [87, 90, 107], wing-wing interactions (i.e., clap-and-fling variants) [108], the Kramer effect [92]

[¶]In an endnote, Dickinson et al. mention that *Drosophila* wings do not twist much in flight, and that flexible wings constructed to mimic their deformations did not evidence much alteration in forces measured on Robofly. However, no design nor force data for the flexible case is given in the paper. Moreso, the effect of deformations of *Drosophila* will likely not be generalizable for all insect wings, especially those which are seen to significantly deform in flight.

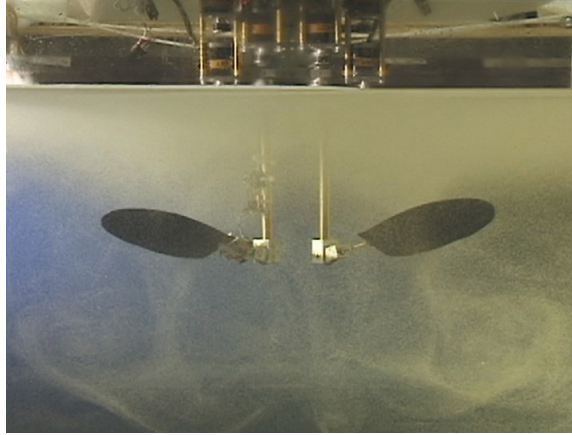


Figure 1.17: Robofly robotic flapping mechanism operating in mineral oil [106]. The oil appears hazy because of seed bubbles for particle image velocimetry.

and the effects of tethering on insect flight [109]. Force data from Robofly has been used to validate CFD codes by Ramamurti and Sandberg [88], Sun and Tang [89] and Sun and Wu [110]; and unsteady analytic aerodynamic models by Żbikowski et al. [97], Ansari, Żbikowski and Knowles [111] and Singh and Chopra [98]. Earlier mechanical-model studies also primarily used rigid wings: e.g., clap-and-fling studies by Spedding and Maxworthy [112] and Sunada et al. [113] and Dickinson's 1994 study of wing-wake effects [86]. Likewise, Wang's 2-D CFD model of dragonfly aerodynamics (which are not mimicked by Robofly) also assumes a rigid wing [114]. Taken together, we see that much of the numerical aerodynamic data on flapping wings comes from rigid-winged systems. This makes deducing aeroelastic functionality of deforming wing structures difficult since there is a lack of suitable data for comparison. The effect of deformations cannot be assessed from wings designed specifically to be non-deformable.

Of course, there are exceptions to the rule of rigid-winged models, though we shall see that these have deficiencies of their own. A partial exception is the Reynolds-scaled flapping mechanism with which Ellington et al. first identified the attached LEV in late 1996 [82]. The 46.5-cm wing on this flapper was a hinged plate, representing the fore and aft wings of a hawkmoth wing pair beating in

concert. The hinge allowed the aft section to rotate relative to the forewing, changing the camber of the total wing system, though neither section of the wing could itself bend or twist [115]. Liu et al.'s subsequent CFD analyses of this model included the hinge degree of freedom [95, 116]. However, aerodynamic force data was not directly measured on the model, so the effect of camber on force generation was unknown; the CFD studies could only be validated by qualitative comparisons with smoke-visualized streamlines on the model, so they too are not a useful source of numerical data on the effect of camber. Also in 1996, Smith incorporated a flexible FEM structure [94] into his previous unsteady aerodynamic panel model of a hawkmoth in forward flight [93], which was validated against tethered hawkmoth force data. Smith's model showed fair correlation to the experimental data, but it is not clear that his analysis is valid for all flight cases. Forward flight—more bird-like than insect-like—will presumably show less dependence on reversible camber deformations and wing-wake interactions during the wing flip than normal hovering flight. Furthermore, Smith's study does not include the then-unknown attached LEV.¹¹ The most recent and advanced non-rigid aerodynamic model was developed by Singh and Chopra for use in MAV design analysis [98]. Singh and Chopra's aerodynamic model incorporates quasi-steady thin-airfoil aerodynamics; the attached LEV; and starting, shed and tip vortices. Wing flexibility is included by linearly superimposing the effects of quasi-steady thin-airfoil deformations of assumed wing structural modes. The rigid aerodynamic model was first validated with Robofly force data, while the full, flexible aeroelastic model was validated with data collected with a custom-made open-air flapping mechanism. This model is a considerable improvement over

¹¹ Still prior to the LEV's identification, Smith extended his forward-flight analysis by including the Polhamus suction analogy to model leading-edge flow separation on outboard portions of the wing during the upstroke [117]. This is similar to the current method of modeling the attached LEV, where the Polhamus suction analogy is applied to the entire wing during up- and downstrokes [96]. Smith's use of the Polhamus analogy came from physical considerations unrelated to the attached LEV, and he did not continue this direction of research.

previous models, but the lack of high-resolution data of flexible wings still makes it difficult to predict the aerodynamic effect of wing deformations on the complex and non-linear wing–wake interaction during wing flip.

We now return to biological insect wings. At least for now, the data collected from live insects and from computational or physical models is insufficient for full quantitative understanding of how a wing’s structural design affects its interaction with the air during flight, and vice versa. Thus, most insights into the relationship of insect wings’ functional morphology on their aerodynamic characteristics are purely qualitative, not to mention speculative, in nature. Images and movies of flying insects show wing deformations, which are interpreted in light of full-scale airplane and helicopter analyses or simply by the researcher’s intuition.

Possible problems with such insights are obvious and manifold: Full-scale and insect-scale airflows have vastly different Reynolds numbers. Normal hovering flight is much more unsteady than airplane and helicopter flight, and direct analogies between them may not hold—to say nothing of the wing flip which has no analogue in full-scale flight. Intuition about such complex phenomena can be misleading or wrong. But when quantitative information is lacking, such qualitative insights are a necessary if non-ideal first step towards understanding aeroelastic functional morphology. A handful of simple analytical models have been developed, which have allowed some basic quantitative analyses of functional morphology. Only recently, thanks to application of FEA, has the prospect of accurate quantitative modeling of insect wings come within reach.

1.2.3.2 *Reversible Airfoils*

The primary study of the insect wings’ functional morphology, vis-à-vis aerodynamics, concerns their role as reversible airfoils. In normal hovering flight

the wings flip over at each half-stroke, operating “upside-down” approximately half the time. The up- and downstrokes produce nearly equal lift, implying the wings’ aerodynamic characteristics are the same whether right-side-up or upside-down. It is therefore inferred that the flexible wing reversibly deforms into oppositely oriented non-symmetric airfoils during successive half-strokes.

In 1981, Wootton systematically identified three general deformation patterns in flapping insect wings: torsion (or twist), camber and transverse bending [100]. Torsion and camber are reversible deformations: they occur in similar but opposite fashions on both the up- and downstrokes as illustrated in figure 1.18. Both are assumed to increase lift during the middle of each half-stroke. (The third type of deformation, transverse bending, is the bending of the outer portion of some insects’ wings a chordwise flexural line. It does not appear to be reversible and occurs during wing upstrokes. Its aerodynamic effects are currently unknown and it is typically neglected from aerodynamic analyses.)

Standard helicopter blade analyses show that spanwise twist is an important feature of well-designed rotary wings [80, sec. 3.3]. Negative twist, where the geometric angle of attack decreases from root to tip, helps to distribute aerodynamic inflow uniformly across the span of the wing in hover, imparting significant efficiency benefits. The observed twist of insect wings show this pattern exactly: the wings reversibly deform with negative twist for both half-strokes, with the

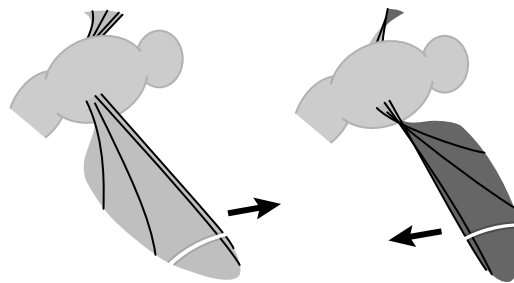


Figure 1.18: Reversible torsion and camber in hovering flight. After Wootton [100].

reversal occurring during the wing flips. This reversal is facilitated by the layout of the wing. The leading-edge vein group is a torsionally compliant spar that shifts the wings' elastic axis forward, while the center of gravity and aerodynamic center of pressure are closer to the mid-chord [100]. Both inertial force and aerodynamic lift create nose-down pitching moments about the elastic axis, passively twisting the wing in the correct sense.

Positive camber lowers an airfoil's zero-lift angle of attack, allowing it to produce greater lift than a uncambered airfoil at any positive angle of attack, provided it does not stall [118, p. 240]. Like twist, the direction of camber reverses during each half-stroke to remain "positive" during both half-strokes in normal hovering flight. Wootton theorized that high pressure on the underside of the wing caused the wing membrane to bow upwards, cambering in a fashion "analogous to the bellying of a sail" [100]. Ennos later proposed that reversible camber is coupled with twisting deformations by the wing's vein morphology [119]. By modeling an insect wing as a leading-edge torsion beam with trailing oblique veins, Ennos derived analytic equations showing that the orientation, divergence and curvature of the trailing veins affected the magnitude and location of maximum camber as well as the geometric angle of attack when the leading-edge beam was twisted. Ennos' analysis remains one of the few closed-form analytic equations describing the function of insect wing structures.

It is important to keep in mind that the aerodynamic effects of insect wing deformations are mostly analyzed by analogy with flight regimes different than normal hovering flight. While researchers have been presenting compelling conceptual arguments why reversible airfoils should be beneficial to insect-like flight, it has only been in the last decade that aerodynamic and aeroelastic studies have begun to confirm that this is indeed the case. As such, understanding of insect wings as reversible airfoils is far from complete. It is worthwhile to note that

reversible structural deformations may have non-aerodynamic benefits as well. For instance, Wootton has suggested a purely structural interpretation of the benefits of wing camber, noting that a cambered plate exhibits additional rigidity from forces applied to its concave side [62]. It is thus possible that reversible camber may be concerned with maintaining wing shape in addition to enhancing aerodynamic effects.

1.2.3.3 Wing Corrugations

The vein and membrane structure of an insect wing is not flat but has corrugations normal to the planform, as in figure 1.19 . In an aerodynamic sense, these corrugations affect the apparent airfoil shape of the wing: they trap small recirculating air bubbles that fill in the cross section of the wing seen by the airflow, as in figure 1.20 [74]. The wing thus acts as an airfoil with a thickness defined by the envelope of the corrugations. It has also been suggested that corrugations near

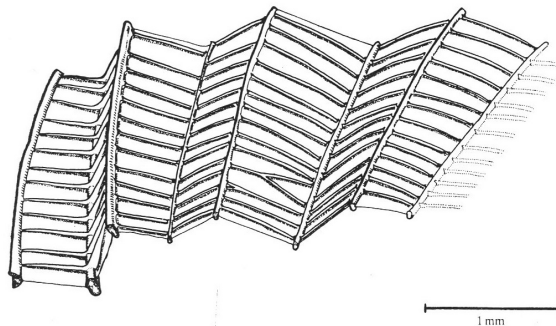


Figure 1.19: Partial detail of dragonfly wing structure [120]. Note the numerous cross-veins between corrugations.

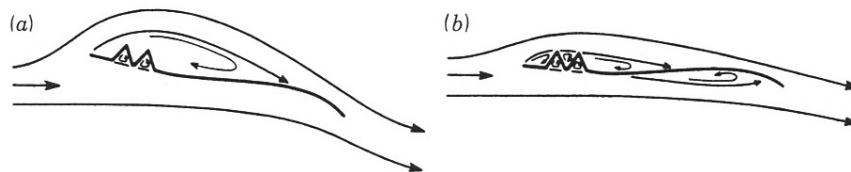


Figure 1.20: Diagram of airflow around corrugated wings [74]. Diagram (a) shows leading-edge trip and attached recirculation. Diagram (b) shows recirculating air bubbles between corrugations.

the wing's leading edge may trip the airflow to help form the LEV.

With regard to structures, corrugations increase the rigidity of wings without imposing a significant weight penalty [104], so long as the corrugations are adequately supported by surrounding structures. Newman and Wootton investigated the role of corrugations in increasing the bending stiffness of dragonfly wings [120]. When reviewing their findings it is important to note that dragonflies do not use normal hovering flight and their wings tend to have more corrugations and more cross-veins than normal-hovering insects (see figure 1.19). Newman and Wootton described the three-dimensional corrugations and cross-veins acting as a series of plate girders to support the dragonfly wing. They also showed that several failure modes of the wing—particularly those in which the top and bottom veins become co-planar, eliminating the stiffness benefits of corrugation—were benign and reversible, allowing the wing to temporarily yield under excessive loadings instead of breaking. Sunada, Zeng and Kawachi investigated the role of corrugations in the torsion stiffness of dragonfly wings, and confirmed its beneficial effect [121]. However, they did not account for modes where the wing deformed; the corrugations were assumed to hold their shape in response to loading. This is exactly the opposite assumption that Ennos used in his model of torsion-camber coupling in normal-hovering flight [119]. Ennos assumed the corrugations would not hold their shape and the membrane's flexibility between the veins would make the wing soft in torsion. Wootton et al. make the same assertion in the introduction to their study of locust wings [122]. With regards to torsional stiffness, the presence and stiffness of the cross-veins appears to be crucial. If the cross-veins are strong enough to support the corrugations (as in dragonflies), the wing is stiffened in torsion. But if the corrugations are not supported (as is likely in normal hovering insects, which have relatively fewer cross-veins) the wing will be soft in torsion.

1.2.3.4 *The Pterostigma and Pitch Regulation*

One of the earliest studies of wing functional morphology with respect to flight characteristics is Norberg's 1972 paper on the role of the pterostigma [123], a dense pigmented spot on the outer leading edge of some orders of insects, such as the damselfly in figure 1.21. While many insects with pterostigmas do not use normal hovering, it is present in the order Hymenoptera which includes normal-hovering bees and wasps. Norberg's study focused on dragonflies for convenience. He located the torsion (elastic) axis of entire dragonfly wings and the chordwise center of gravity for spanwise strips of wing. While the wing's center of gravity was primarily behind the wing's elastic axis, the dense pterostigma shifted it ahead of the elastic axis in the corresponding wing strips. Wind-tunnel tests of anesthetized dragonflies showed that the pterostigma increased the flutter speed of dragonflies in forward flight by counteracting detrimental torsional loads. Norberg speculated that in normal hovering flight, the pterostigma helps to regulate excessive twisting of the wing in response to the wing flip.

1.2.3.5 *Structural Properties and Distributions*

Aside from its analysis, Norberg's study is notable for simply reporting quantitative measurements of insect wings' engineering structural properties. Given the historical focus on the aerodynamics of insect wings and the common assumption of a rigid wing, it is perhaps unsurprising that little data about wings'

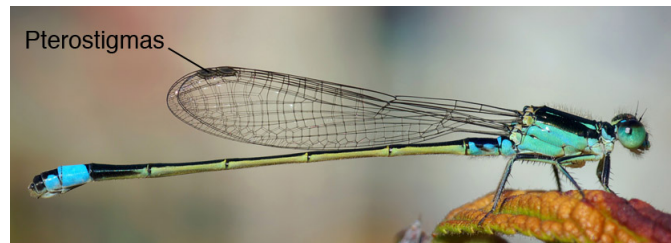


Figure 1.21: Pterostigmas on a common bluetail damselfly [124].

structural properties has been published. Measurements of quantitative properties necessary for structural engineering analyses of wings—bending and torsion stiffness distributions, chordwise locations of the elastic axis and center of gravity, and mode shapes and natural frequencies to name a few—are simply not available for most insects.

Not all wing properties are unknown. It is relatively simple to measure wing planform and mass distributions, and a number of studies provide this data [63, pp. 55–57]. Ellington’s comprehensive aerodynamic study is most useful, characterizing and correlating nondimensional mass and area distributions of various insects’ wings or coupled wing pairs [64]. Wing spanwise mass distribution is biased towards the inboard of the wing, with centers of mass located at 32 to 47% wing radius from the root. Wing area is somewhat more uniformly distributed, with centers of area at 42 to 56% of the radius. The locations of the centers of mass and area are not strongly correlated. Aspect ratios range from 5 to 12.

Simple morphological considerations show that insect wings’ bending stiffness decreases from root to tip: vein diameter and cuticular thickness decrease toward the wing tip, and there is a higher concentration of veins toward the wing root [63, p. 55]. Similarly, bending stiffness decreases from the wing’s leading to trailing edge.

One of the only systematic attempts to quantitatively characterize bending stiffness is Combes and Daniel’s two-part study “Flexural Stiffness in Insect Wings” [125,126]; for full discussion see Combes’ dissertation [127]. In the first part of the study, Combes and Daniel use the static deflection of a clamped wing subject to a point load as a representative measure of bending stiffness and correlate stiffness over sixteen species of insects. They conclude that inter-species variation of bending stiffness in the spanwise direction is proportional to the cube of wing length, while the variation of stiffness in the chordwise direction is proportional

to the square of wing length. Using a plate FEM of a *Manduca sexta* hawkmoth forewing, they confirm that the three veins that constitute the leading edge spar are primarily responsible for the wing's spanwise stiffness. In the second part of the study, Combes and Daniel investigate the spatial distributions of stiffness in *Manduca sexta* hawkmoth and *Aeshna multicolor* dragonfly wings and used their hawkmoth FEM to model dynamic response to sinusoidal flapping. Both hawkmoths and dragonflies had bending stiffnesses that decreased sharply from root to tip, which Combes and Daniel modeled as an exponential function of span. Hawkmoth wings also have exponentially decreasing chordwise stiffness, as do most dragonfly wings. Though this study is useful, it is not without some shortcomings. The torsional stiffnesses and related measurements like the elastic axis location are not measured, nor are any structural dynamic characteristics (e.g., natural frequencies). The hawkmoth wing FEM is relatively crude as well: the wing is assumed to have constant density and thickness, and veins are differentiated from membranes only by a greater Young's modulus.

A handful of other studies provide additional information about wing structural properties, though none are as comprehensive or useful for the study of normal hovering flight as Combes and Daniel's research. Norberg measured and reported the center of gravity and elastic axis distributions along the span of dragonfly wings [123]. Also working with dragonflies, Sunada, Zeng and Kawachi measured the center of gravity and elastic axis distributions; gross bending, torsion and warping rigidities; and nonrotational torsion natural frequencies of their wings [121]. Ennos used Norberg's methodology to measure the center of gravity and elastic axis location of a hoverfly and bluebottle fly, but only illustrates the wing of a hoverfly, a non-normal hovering flyer [128]. Wootton, Smith, Herbert et al. performed an incredibly thorough analysis of the hind wing of the *Schistocerca gregaria* locust, encompassing morphological description, bending

measurements, characterization of material properties and spatial distributions, and detailed three-dimensional FEA [122, 129, 130]. Unfortunately their study is not useful for analyzing structures for normal hovering flight: locust hind wings deform asymmetrically, experience high pressure loads on their underside only and operate almost exclusively in fast forward flight. In a general sense, however, the study explicitly demonstrated the negative effects of oversimplified wing modeling: the FEA portion examined the results of neglecting characteristics like initial camber, vein curvature and vein taper in the static deformation of the wing. More relevant to normal hovering flight but sadly lacking in explanation, Wootton's 2003 survey of structural modeling techniques cites an FEA study to give the the lowest (presumably nonrotational) bending and torsion natural frequencies of a *Manduca sexta* hawkmoth wing pair [103]. The survey indicates a full discussion of the FEA is forthcoming, but as of the date of this dissertation it apparently remains unpublished.

1.2.3.6 *Inertial and Aerodynamic Loadings*

The structural properties of insect wings are essential to understanding how they deform, but equally important are the force loadings on the wings. Insect wings do not have internal musculature, so wing deformations are typically driven by inertial and aerodynamic loads arising from forced flapping motion: inertial forces opposing the acceleration of the wing and aerodynamic forces from the air pressure acting on the wing surface.** There is general agreement that inertial forces play a primary role in effecting the wing flip, perhaps even more than muscular actuation at the wing root [128]. Historically, the relative contributions of inertial and aerodynamic loads during the remainder of the flapping cycle has

**Locusts, mantises and related insects have wings in which camber deformation is coupled to the downstroke motion via static structural couplings, *not* through inertial or aerodynamic forces [122]. This asymmetric coupling does not produce camber on the upstroke. There is no evidence of similar effects in normal-hovering insects.

not been as clear—both types of loadings would tend to cause twist and camber deformations that are consistent with those observed in insect wings. As Combes and Daniel note, many studies have shown that inertial forces are on average higher than aerodynamic forces, but others have reached the opposite conclusion [131]. However, more recent and detailed studies indicate that inertial loads play the dominant role in causing wing deformations, as opposed to aerodynamic loads.

Combes and Daniel's own study measured the instantaneous deflections of a hawkmoth wing flapped in air and in helium (which has 15% the density of air) as a means of quantifying the effects of aerodynamic forces on wing bending [131]; see [127] for full discussion. Fourier analysis of wing deformations at typical wingbeat frequencies showed little difference in the response at the fundamental frequency whether the wing was in air or helium. Higher-harmonic responses—particularly the third harmonic and above—were greater in helium than in air, leading to the conclusion that inertial forces actuate deformations while aerodynamic forces primarily damp the deformations. Using the same hawkmoth FEM described in section 1.2.3.5, Combes and Daniel determined that using numerical damping proportional to the FEM mass matrix was adequate in reproducing aerodynamic damping in a structural model. Combes and Daniel's assumption has been used to justify further research by Mountcastle and Daniel [132] and Thiria and Godoy-Diana have noted their findings were consistent with Combes and Daniel [133].

Though not performed on insect wings, Singh and Chopra's aeroelastic study of flapping MAV wings also indicated inertial forces are primarily responsible for structural deformations [98]. Using Combes and Daniel's study as justification, Singh and Chopra assumed a "loose" coupling between inertial and aerodynamic effects and solved each independently and iteratively. Inertial loads and their

deformations were first estimated for a vacuum chamber case, then aerodynamic loads were calculated for the deformed wing and used as a correction for a subsequent inertial calculation, repeating until convergence. Using the bending moment at the wing root as an indicative measure of loading, Singh and Chopra reported that inertial loads governed the deformations of the wing, but also concluded aerodynamics could not be neglected for a fully accurate analysis.

1.2.3.7 Indirect Flapping Actuation

Most species of insects, including all normal-hovering insects, do not have flight muscles directly connected to their wings [63, pp. 42–45]. Instead indirect flight musculature connects to a dorsal exoskeletal plate called the notum and drives the wings by leverage. The flight musculature consists of perpendicularly oriented muscles as drawn in figure 1.22. During the upstroke, the dorsoventral muscles contract, pulling the notum downwards and causing the wing to flap upwards about flexible pivots. During the downstroke, dorsal longitudinal muscles oriented along the length of the body (i.e., perpendicular to the page in figure 1.22) contract. In so doing, their cross-sectional area expands, forcing the notum up and the wings down. Feathering rotation and other wing controls are actuated by additional sets of muscles (not shown) that alter the position and orientation of the

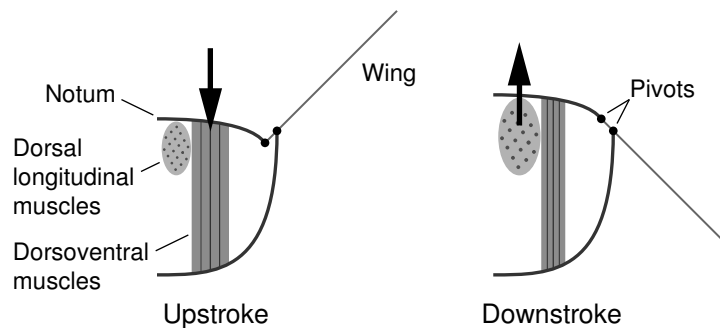


Figure 1.22: Cross-sectional diagram of a half-thorax illustrating indirect flight muscle operation.

pivots.

Some orders of insects have evolved unique, asynchronous flight muscles that are specialized for high-speed wing motion. Asynchronous flight muscles contract and release several times in response to a single nerve impulse [134]. (This is contrasted to the synchronous muscles found in all other animals, in which single nerve impulse is synchronized to a single muscle contraction.) Asynchronous musculature allows insects to perform steady, high frequency flapping motion—literally, faster than thought—with greater efficiency and power output than achievable with synchronous muscle. Most normal hovering insects are in orders with asynchronous flight muscles, though butterflies and moths are not. The steady oscillatory character of asynchronous muscle actuation has led to speculation that insects’ flight structures may be “tuned” with respect to the wingbeat frequency to increase efficiency.

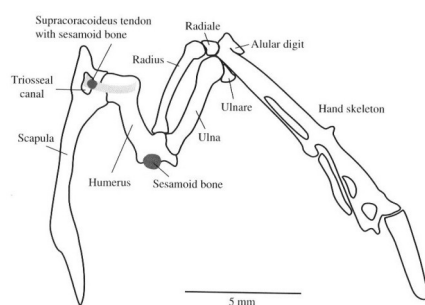
1.2.4 Hummingbirds

A brief account of hummingbirds, focusing on their wing structures, will conclude the discussion of biological flight. Hummingbirds fly in a manner similar to insects—particularly the aerobatic hawkmoths, which share hummingbirds’ propensity for feeding on flower nectar while hovering—and their wing kinematics follow the normal-hovering motions described in section 1.2.1. Broad analogies can be made between hummingbirds’ wing structures and the wings of insects. It is generally taken as given that findings and inferences about the function of insect wings apply to hummingbirds. Still, we must remember that birds and insects are divergent groups overall, belonging to separate phyla in the animal kingdom. It is not unreasonable to expect some differences between hummingbirds and insects despite their convergent evolution. Recent aerodynamic measurements suggest that hummingbirds differ from insects in the ratio of force production between

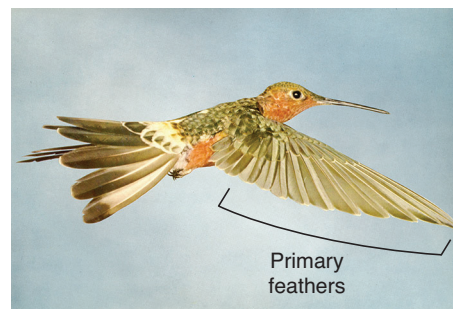
down- and upstrokes [135]. For the present, we must be content to describe the anatomy of hummingbird wings as a means of differentiating them from insects.

Like all birds, hummingbirds' wings are built on a skeletal frame to which is attached muscles, flesh and feathers. Unlike all other birds, hummingbirds cannot extend or bend their wings: the unique skeletomuscular configuration, depicted in figure 1.23a, only allows rotation about the shoulder and axial rotation of the wrist while the elbow is immobile [32, sec. 2.2.3]. The hand bones are fused and represent over 80% of the wing skeleton's length. Ten primary feathers attached to the fused hand comprise the majority of the wing area, as seen in figure 1.23b. They extend radially outward and backward from the hand skeleton. The feathers consist of a central shaft, from which radiate tiny barbs making up the feathery vanes. The barbs of one feather interlock with the adjacent feather, forming a coherent surface where the vanes overlap.

The structural analogies between insect and hummingbird wings can thus be expressed. The hand skeleton and the shafts of the first few feathers play the same role as the leading-edge veins in insects; the remaining feather shafts are similar to insects' trailing radial veins; and the overlapping feather vanes act as the wing membrane does. Since the majority of a hummingbird's wing is made of feathers attached to the fused hand bones, the wing has a constant shape like



(a) Wing skeleton [32, p. 32]



(b) Primaries of a giant hummingbird [65, pl. 40]

Figure 1.23: Hummingbird wing structure.

insects' wings. In contrast to most insects, hummingbird flapping muscles attach directly to the wing structure. The muscles that typically extend the wings are modified to actuate the large rotations necessary for normal hovering flight.

1.3 Insect-Like Micro Air Vehicles and Test Stands

Interest in insect-like MAVs has blossomed as a consequence of general MAV research initiatives. We may generically call these vehicles entomopters, that is “insect-winged,” after the fashion of “bird-winged” ornithopters.^{††} Indeed, insects have informed our vision of MAVs' achievable capabilities—their performance, maneuverability and size—just as birds influenced early conceptions of full-scale flight for aviation pioneers. It is only a minor exaggeration to say the objective of MAV research is the creation of a robotic flying insect: certainly an MAV matching the size and flight performance of a hawkmoth would be considered an unqualified success.

Engineers must overcome fundamental deficiencies in understanding insect-like flight and design before such a machine can be realized. Entomopters are at the very earliest stages of infancy. In order to create working entomopters we must understand both the principles of insect flight and how to embody those principles in MAVs. The preceding section on biological fliers mentioned some obstacles to the former. Regarding the latter, the difficult task is to properly mimic or approximate the already-known features of insect flight. This dual lack of knowledge presents an intriguing opportunity: development of entomopters may inform, augment and enhance biological understanding of insect flight. Ground-up construction of insect-like machines could provide novel insights about insects that are obscured in top-down studies of biological beings.

From a mechanisms perspective, a current challenge is capturing the kine-

^{††}Though contrast Michelson's capital-*E* Entomopter, which uses vertical bird-like strokes.

matics of insect wings: not only approximating the motions described in section 1.2.1 at the proper frequencies, but also altering them in response to flight conditions—changing the kinematics “on the fly,” as it were. A related difficulty is miniaturization: making the components necessary for flapping (and all other systems) small and light enough for practical implementation. In short, mimicking insect wing motions has proven difficult in and of itself; doing so at MAV scales even moreso. The few extant flight-capable entomopters use simplified kinematics, while more complex systems are almost exclusively bulkier bench-top test stands. It is typically understood that practical entomopters must exploit state-of-the-art and next-generation materials like smart composites and MEMS to achieve their desired size.

1.3.1 Flight-Capable Entomopters

The simplest way to make a hover-capable entomopter is to take a Pénaud-type ornithopter (see figure 1.4) and rotate it nose-up. Such a configuration lacks a true feathering degree of freedom at the wing root. The wing flip is approximated by torsional compliance of the membrane wings in response to inertial and aerodynamic loads, albeit at smaller magnitudes than the kinematic wing flip of insects.

This is a surprisingly good first attempt at normal hovering flight. Pénaud-type ornithopters are effective at producing horizontal thrust, but the vertical (lift) forces cancel on the up- and downstrokes. A rotated “Pénaud-type entomopter,” then, produces upward thrust with little side force: exactly what is required for hovering. It is not difficult to construct a rudimentary Pénaud-type entomopter from off-the-shelf materials; an example is the entomopter pictured in figure 1.24, which was built at the University of Maryland and uses a four-bar flapping mechanism driven by a cell-phone motor. At the time of writing, all flight-capable

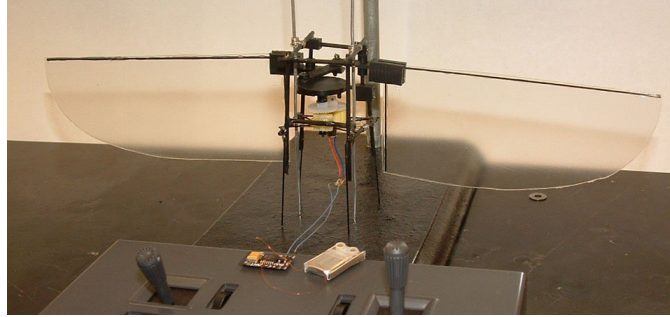


Figure 1.24: A basic Pénaud-type entomopter, tethered to guide wires.

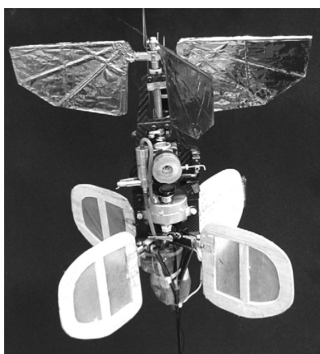
entomopters have used a variation of a Pénaud-type design. I will briefly touch on two notable examples.

The SRI International/University of Toronto Mentor was the first entomopter to demonstrate controlled free flight in hover and translation [136]. The Mentor uses a unique four-wing configuration, shown in figure 1.25a, to enhance lift by exploiting clap-and-fling. The opposing wings are arranged in an X-configuration, with each bar flapping in a 76° horizontal arc at the root. Additional structural flexibility causes the wings' tips and trailing edges to sweep out arcs approaching 90° . The cross-bars flap in opposing directions, nearly striking at the end of each stroke in an approximation of clap-and-fling. The four lower control fins orient the vehicle by directing its downwash. An operator pilots the Mentor by radio-control while onboard gyros and electronics augment stability. The Mentor is significantly larger than the target MAV size: the pictured vehicle with an internal combustion engine has a 36-cm wingspan and weighs 580 g; a later version with a NiCd battery and brushless motor weighs 440 g. The internal-combustion Mentor has flown in hover for one minute while the electric Mentor is able to achieve continuous hover for 20 seconds. The internal-combustion Mentor can achieve translational speeds of 3 m/s when tilted 15° from vertical, but greater tilts cause instabilities.

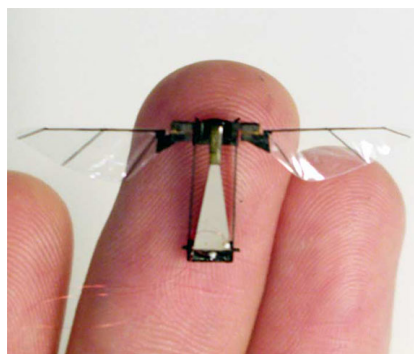
At the opposite end of the size range the Harvard Microrobotic Fly is the smallest entomopter to demonstrate tethered flight [137]. Figure 1.25b shows the

60-mg, 3-cm MAV consisting of an airframe, piezo bimorph actuator, bioinspired transmission and wings. The triangular cantilever piezo bimorph bends at high frequency to drive the transmission, which uses leverage to flap the wings in the same manner as an insect notum (cf. figure 1.22). The driving frequency of the piezo is tuned to the structural natural frequency of the wing system so the system operates in resonance. The wings are functionally rigid, but a compliant joint at the root allows feathering rotation in response to inertial and aerodynamic forces. Mechanical stops limit the flapping and feathering strokes to 100°. Restrained by vertical guide wires and using an offboard power source, the Harvard Microrobotic Fly achieved lift-off with a measured thrust-to-weight ratio of 2:1. The MAV is intended to receive ongoing modifications towards the final goal of an autonomous vehicle with a projected 120 mg weight.

Most recently AeroVironment's bio-inspired Nano Air Vehicle (NAV), shown in figure 1.25c, has demonstrated controlled free flight and hover for a vehicle of comparable size to hummingbirds [138]. The successful flight of the NAV, which has a wingspan of 16 cm and a weight of 19 g, was announced in February 2011. At the date of this dissertation, fall 2011, published documentation of the NAV is limited to non-technical press releases [138,139]. The NAV is controlled using only



(a) SRI/U. Toronto Mentor



(b) Harvard Microrobotic Fly



(c) AeroVironment NAV

Figure 1.25: Advanced flight-capable entomopters.

two flapping wings without auxiliary control surfaces, which suggests that the wings have more degrees of freedom than a Pénaud-type entomopter. The NAV has demonstrated continuing flight for eight minutes, as well as transition from hover to forward flight.

If Pénaud-type entomopters are successful in flight, why consider more complex configurations? Pénaud-type vehicles' advantage is their simplicity: with a single degree of motion, the flapping mechanism can be compact and lightweight. But as a consequence they only produce thrust perpendicular to the flapping plane. Moreover, if the flapping amplitude is fixed as is typical of most Pénaud-type vehicles (either by the driving mechanism itself or by mechanical stops) the amount of thrust is governed by the wingbeat frequency via the throttle—a flapping-wing analogue of a fixed-pitch propellor. A separate system is required to direct the thrust and provide control. Using fins to direct the downwash in hover, like the Mentor MAV does, is the obvious solution but one which carries penalties. The weight and size of the fins are non-trivial, and control nonlinearities will arise if the fins move out of the downwash (I suspect such nonlinearities contributed to the Mentor's instabilities when it was tilted for translational flight).

Contrast this to the articulation of insect wings: in addition to flapping, insects have feathering and stroke deviation degrees of freedom. The amplitude and phasing of each degree of freedom can be changed independently and near-instantaneously. This gives insects immediate command over the magnitude and direction of their wings' thrust vector without supplemental control surfaces. If entomopters achieve similar command of their wing kinematics, the size and weight savings may offset the simplicity of a Mentor-like configuration. Bio-inspired kinematic control should provide performance gains as well; direct control over the aerodynamic forces affords exceptional maneuverability to some insects. The benefits for normal hovering flight are less clear, but the increased control

authority will likely improve efficiency by granting fine control over aerodynamic effects like the leading-edge vortex and wing-wake interaction. The recent success of the Aerovironment Nano Air Vehicle has demonstrated the feasibility of controlling insect-like entomopters using only flapping wings, but the exact methods of control have not been published at the time of this dissertation.

1.3.2 Entomopter Test Stands

Development of more complex flapping mechanisms is currently relegated to bench-top test stands, where they can be designed and evaluated without concern for their size and weight. Unlike the test stands used for biological research, which are typically Reynolds-scaled to accurately duplicate insect kinematics at low frequencies, engineering test stands function at MAVs' operational wingbeat frequencies while loosely approximating insect kinematics. But even freed from the constraint of being flightworthy, most test stands cannot replicate insects' ability to adapt their kinematics in flight. Instead they physically constrain and couple the flapping and feathering rotations. Still, they are necessary and useful stepping-stones towards more elaborate vehicles, and some test-stands are already demonstrating degrees of insect-like kinematic control.

University of California Berkeley's long-running Micromechanical Flying Insect (MFI) project currently straddles the line between test stand and entomopter [140–144]. The MFI, shown in figure 1.26, is designed as a flight-capable entomopter. At-scale airframes and flapping actuators have been built and evaluated on test stands, but the MFI has not yet achieved lift-off (however, the Harvard Microrobotic Fly is an offshoot of MFI research). The MFI's flapping actuation is uniquely advanced and is the most successful attempt at approaching insect-like levels of kinematic control. Each wing is actuated by two independent piezo bimorphs connected to the wing through four-bar mechanisms. A composite-

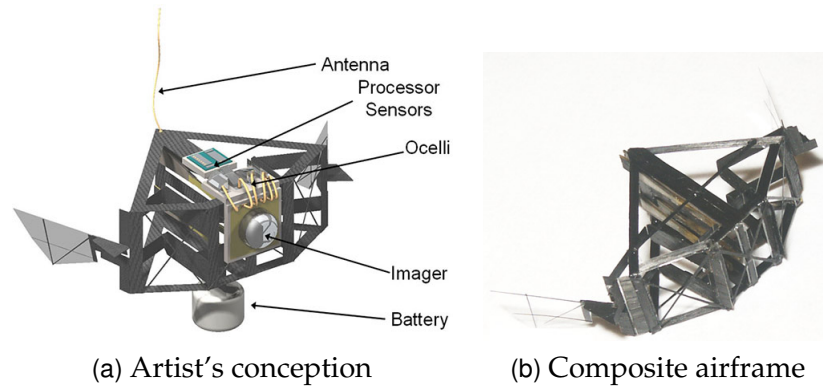


Figure 1.26: UC Berkeley Micromechanical Flying Insect (MFI) [145].

flexture transmission links one four-bar to the leading edge of the wing and the other to the trailing edge. This configuration allows independent flapping rotation of the leading and trailing edges of the wing. By prescribing a time-lag on the trailing edge relative to the leading edge's flapping position, the MFI can control the feathering angle of its wing. More importantly, the control inputs to the driving piezos can be altered during operation. This means the MFI should be able to adapt its kinematics and direct its thrust in flight, though a demonstration of this capability has not yet appeared in the literature.

Raney and Slominski's "vibratory flapping apparatus" takes a different approach to mimicking biological control by replicating the skeletomuscular arrangement of a hummingbird shoulder [146]. In hummingbirds, the wing skeleton interfaces with the body at the shoulder joint. Two muscles attach to the wing outboard of the shoulder at opposing downward diagonals while a flexible tendon attaches from above; muscles and tendon form an upside-down Y arrangement. The vibratory flapping apparatus in figure 1.27 uses a spring in place of the tendon and two electrodynamic shakers in place of muscles. The two-dimensional trajectory of the wing (in flapping and stroke deviation degrees of freedom) can be prescribed via the oscillatory waveforms of the shakers. Raney and Slominski demonstrated circular, oval and figure-of-eight tip trajectories with the apparatus

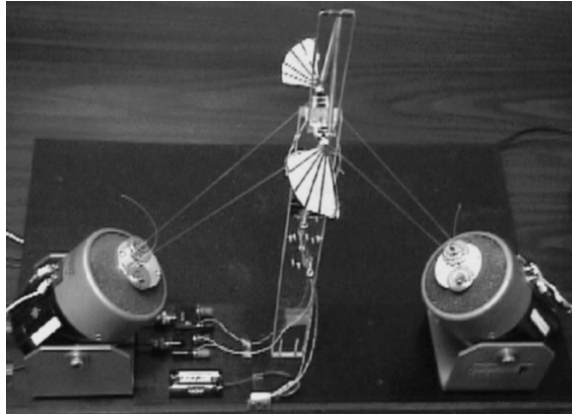


Figure 1.27: Raney and Slominki's vibratory flapping apparatus.

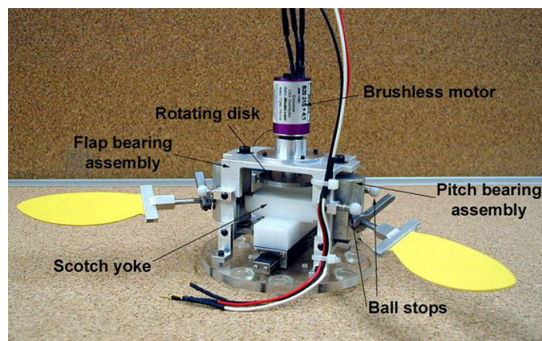
and were able to transition between them in as little as four wingbeats. However, the feathering degree of freedom was uncontrolled. No attempt was made to scale the flapping apparatus to a flightworthy size.

We now come to a broad category of test stands that we may designate as single-degree-of-freedom (SDOF) linkage mechanisms. They are characterized by the use of physical linkages to transform a driven one-degree-of-freedom motion—typically a rotating motor shaft—into reciprocating wing motion. Pénaud-type configurations with their planar flapping are the simplest such mechanisms. More intricate examples, a sample of which are pictured in figures 1.28 and 1.29, couple feathering and/or stroke-deviation with the flapping motion. By better mimicking insect-like kinematics, these additional coupled motions can potentially generate greater thrust than Pénaud-type mechanisms. Like Pénaud-type designs, the appeal of SDOF mechanisms is their (relative) simplicity. The flapping motions are wholly defined by their linkage geometries, and their single-input actuations are easy to implement and control. But if used in a flying entomopter, they will have the same deficiency as Pénaud-type entomopters: the invariant flapping motion generates thrust in a fixed direction, so steering the vehicle will require supplemental control surfaces.

The wing path defined by any SDOF linkage mechanism is invariable during

operation. But the wing path *can* be altered by physically swapping out components of the mechanism for pieces of different geometry. This makes SDOF mechanisms useful for reproducing steady-state flight regimes, like normal hovering or fast forward flight. Hovering kinematics with different feathering amplitudes, for example, can be compared by exchanging a few pieces of a well-designed SDOF mechanism.

The test stands in figure 1.28 approximate normal hovering flight. Wing motions are symmetric on the up- and downstrokes, and large-amplitude changes in feathering angle occur intermittently at the end of the flapping strokes. Singh and Chopra’s test stand uses a scotch yoke to generate planar flapping, while feathering is set by a bi-stable cam assembly that is switched by contact with ball stops [98]. It is capable of a flapping stroke of 80° and geometric angles of attack of 30 to 45° at a wingbeat frequency of 12 Hz. This test stand was employed for Singh and Chopra’s aeroelastic studies, see pp. 32, 42. Żbikowski, Galiński and Pedersen’s test stand is somewhat more complex, using a four-bar Watt’s mechanism modified with auxiliary springs and elastic couplings to generate a figure-of-eight wingtip path [147, 148]. A coupled Geneva wheel mechanism effects intermittent feathering rotation. This test stand can achieve a 90° flapping stroke at a frequency of 20 Hz (its geometric angle of attack is not reported).



(a) Singh and Chopra



(b) Żbikowski et al.

Figure 1.28: Single-degree-of-freedom linkage mechanisms for hover.

Figure 1.29 shows some test stands which approximate forward flight (i.e., more like ornithopters than entomopters). Wing motions are typically asymmetric on the up- and downstrokes, and changes in feathering angle are often not intermittent, if they are controlled at all. Banala and Agrawal’s is simplest, using a five-bar mechanism to generate an asymmetric figure-of-eight motion with continuous feathering [149]. Its approximation of insect kinematics is not very good, particularly with respect to the feathering angle on the upstroke. McIntosh, Agrawal and Khan’s flapper uses a four-bar mechanism for P enaud-type ornithopter motion, but adds a follower–guide mechanism to feather the wings vertically on the upstroke [150]. This arrangement is designed to alleviate negative lift on the upstroke in forward flight. Nguyen et al.’s mechanism is a basic P enaud-type design with a torsion hinge allowing the wing to passively feather in response to inertial and aerodynamic loads [151]. It is primarily a demonstrator for the authors’ unimorph lightweight piezo-composite actuator (LIPCA), which is used instead of the rotary motor common to most SDOF mechanisms. Many other SDOF linkage test stands can be found in the literature.

1.3.3 Wing Structures

When constructing entomopters, engineers have mostly focused on the kinematics and actuation of wing motion. Less thought has been given to the wings’

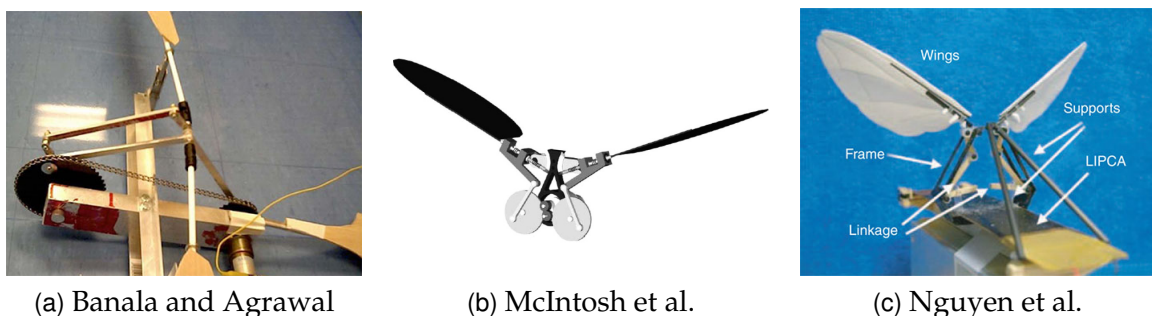


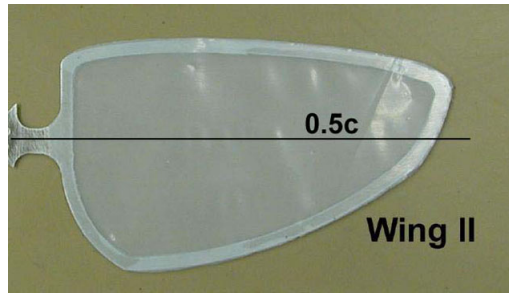
Figure 1.29: Single-degree-of-freedom linkage mechanisms for forward flight.

structural design, particularly their structural dynamics. This is hardly unexpected. The structural (and structural dynamic) properties of insects themselves are unclear, providing little guidance to designers.

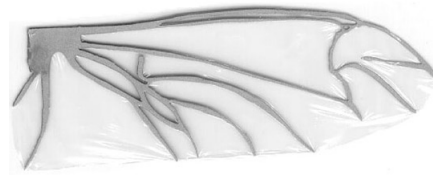
As such, there is no coherent design philosophy consistently applied to entomopter wings. In the simplest cases, wings are constructed with seemingly little regard for their structural properties. Their geometries are planned, they are built with convenient materials and attached to a flapping mechanism to operate however they will. More commonly, qualitative experiment-based methods are implemented: many wings of various geometries and materials are constructed and evaluated on a flapping test rig, or an initial guesstimate configuration is iteratively modified. Rarely are wings manufactured to any quantitative design specification (e.g., a target natural frequency). Indeed, we can currently only speculate which design parameters should be specified, let alone estimate beneficial values.

However, one common trend can be identified in the design of entomopter wings: geometric approximation of insect wing features. Though structural properties of insect wings may be unknown, their shapes are readily determined. Engineers can copy or modify them at need. This is frequently seen in the planforms of entomopter wings, which are often modeled on a particular insect. More elaborate designs—such as those from Pornsin-Sirirak et al. [39], Shang et al. [152], Tanaka, Matsumoto and Shimoyama [153], and Tanaka and Wood [154]—emulate venation patterns, flexion lines or three-dimensional geometry. Figure 1.30 illustrates some examples of biological imitation.

The degree to which entomopter wings should reproduce insect wings is a matter of discretion. On one hand we wish to exploit the knowledge embodied by animals; this is the crux of bioinspired design. On the other, it is unproductive to blindly copy natural forms whose behaviors are not understood. That is the



(a) Aluminum frame, mylar membrane



(b) Titanium alloy frame, parylene-C membrane

Figure 1.30: Insect-inspired entomopter wings. Both are metal frames spanned by plastic membranes. Singh and Chopra (a) approximate the planform of a fruit fly [98]. Pornsin-Sirirak et al. (b) project the major venation of a beetle as a two-dimensional frame [39].

very essence of “the uncreative tendency towards biomimicry” that Michelson warns against. Evolution has optimized insects’ wings according to the biological requirements of each species; their structures manifest functionalities—and *compromises* of functionality—that would be unnecessary and perhaps detrimental to entomopters conceived for other roles. Faithfully imitating insects’ forms in entomopters without understanding their practical significance may result in a mismatch of functionality. Instead, we should learn from nature what functionalities would be beneficial to entomopters, then design MAVs to incorporate those functions. For example, we should not strive to exactly duplicate insects’ wings, but from them glean advantageous wing deformations for normal hovering flight and give entomopters wings that deform in the same fashion. In some cases this may lead to copying insects’ forms, but in others it may not.

I will now survey selected examples of entomopter wing structures. Attention is given to cases where an underlying design philosophy has been clearly elucidated and to cases where the wings’ structural properties are particularly well-documented.

The wing structures of the Harvard Microrobotic Fly were designed in part using a priori specifications for the wing’s rotational natural frequency [137]. This

appears to be the only case so far where an entomopter wing was designed to specification from its earliest stages. However, the design criteria was chosen to ensure the *rigidity* of the wing. As noted earlier, the Harvard Microrobotic Fly uses a compliant joint to allow passive rotation rotation. The joint is parallel to the leading edge spar; in figure 1.31 it is hidden within the joint stop, which limits the maximum angle of feathering rotation. It was desired that the wing itself be functionally rigid in torsion, so that the feathering rotation was quasi-static. Thus, the carbon-fiber and polyester wing's torsion frequency was required to be sufficient higher than the wingbeat frequency. Using a CAD model, the first torsion natural frequency of 250 Hz was determined to be adequate to ensure rigidity during operation at the 110 Hz wingbeat frequency. The wing's size and planform are copied from a hoverfly wing.

The design procedure of the Mentor's wings exemplifies the more common experimental method. The Mentor team chose a "pragmatic design methodology" of constructing and evaluating trial wings to hone in on a final design after concluding that development of an unsteady aeroelastic design algorithm would be prohibitively prolonged [155, p. 4-1]. Bilyk's dissertation [155] gives a detailed description of the first two years of the wing design program, but subsequent developments are only briefly discussed in an overview of the eight-year Mentor project [136]. Figure 1.32 shows three stages of wing iterations: BAT-12 is the result of Bilyk's initial design study, BIRIB-04 is a later development, and Webwing SF-

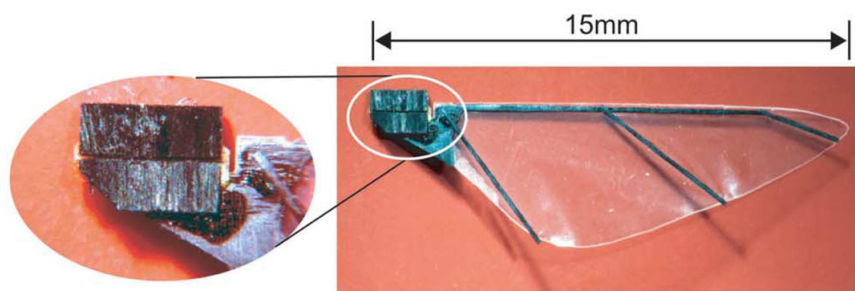


Figure 1.31: Harvard Microrobotic Fly wing, with detail of joint stop.

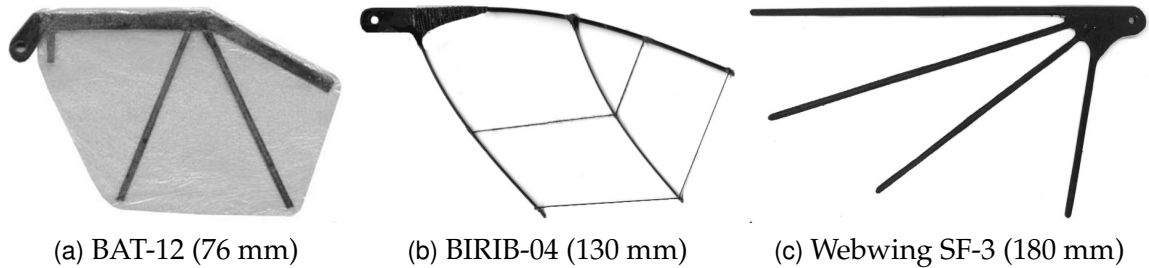


Figure 1.32: Experimental wing configurations used on the Mentor MAV. The semispan, measured from central axis to wingtip, is given in parentheses.

3 is the final operational wing of the battery-powered Mentor. These iterations embody different structural and geometric design strategies. The size of the wings increases with each iteration: the 180-mm Webwing SF-3 final design is 50 mm longer than the preceding BIRIB-04, which in turn was 54 mm longer than its BAT-12 predecessor.

Each wing in figure 1.32 represents a family of related wings; Bilyk’s dissertation includes “Blue” and “Desertcamo” families preceding the BAT family. The design process within each family was evolutionary: evaluating variant wings with slightly different structural and geometric layouts gave an intuitive, qualitative feel for optimizing within the family. This follows the team’s stated pragmatic design philosophy. But the jump between families appears revolutionary; moreover, the justifications behind the configurational alterations are not well explained. The spar geometry of the wing families, for example: the BAT family is based on bats’ finger bones with trailing spars radiating from a “palm” at mid-span, while the BIRIB has a single trailing spar from the root and the mid-span, and the Webwing’s spars radiate from the root. No explanation is given *why* the spar layouts were thus changed. It is indicated that the Webwing family was developed to enable construction of consistent wings using pre-preg carbon fibers, in contrast to the hand-built BAT and BIRIB wings. Thus, the differences between BIRIB and Webwing configurations may be partially due to manufacturing concerns.^{‡‡} On

^{‡‡}The Webwing’s layout is most akin to the much earlier Desertcamo family that preceded

the whole there is little indication how the intuition gleaned from experiments on one family was exploited in subsequent families, or if it was applicable to subsequent families at all. The overall impression is that each wing family represented a wholly new design—starting essentially from scratch—which was then systematically optimized by the experimental methodology.

Sadly, the Mentor publications do not offer much quantitative data of the structural designs of the trial wings. The BAT family of wings is the most well-represented. Bilyk’s dissertation reports the mass and area of every BAT-series wing, and the location of the centers of mass and area. Additionally, representative values of bending and torsional stiffness for each wing were calculated from the deflection caused by a point load at an arbitrary spanwise location. Bilyk attempted to characterize the BAT wings’ performance as functions of nondimensional parameters in hopes of gaining better understanding of design trade-offs than was offered by “the intuition obtained from the trial-and-error process of wing testing” [155, appx. F]. This attempt was not successful; Bilyk suspected that the stiffness estimates were not sufficiently accurate. Much less data has been published for the later BIRIB and Webwing families. The overview paper reports the leading edge spar geometries and materials of selected wings, but no additional specifications are given.

The Mentor program does provide some design guidelines for wings, albeit mostly qualitative in nature. For example, the team found the Mentor’s flight performance was more profoundly influenced by variations of the leading edge spar’s bending stiffness than by variations of the wing planform. The spar’s

the BAT wings. The Desertcamo family was rejected because the prototype BAT-01 had a more promising thrust-to-power ratio. In the absence of explanation in the Mentor review paper, we can only make conjectures about the reasons for this reversion. One possibility is that when first implementing carbon fiber pre-preg construction, the Mentor team reverted to a simple early geometry. But an alternate possibility is that the promising performance of the BAT-01 wing did not reflect the appropriateness of the family in general, and later experiments led the team back to a previously abandoned design. If the latter is the case, this presents an argument against the experimental design method, since an outlier test may lead the design in the wrong direction.

bending stiffness was experimentally optimized so the wing tips almost touched during the clap-and-fling. The wings were made flexible enough to sweep out a maximum arc but not so flexible as to hit one another, which would increase power consumption and noise. Also, in the words of the Mentor team, a “degree of slackness” was allowed when the membrane was attached to the frame, causing a nonlinear torsional stiffness that increases with greater deformations. Oddly, the review paper omits a very important design trend in the Mentor wing families: the consistent increase of wing radius with each new family. Wing radius strongly affects the mean lift of a flapping wing [78], and it is not clear from the published discussion how much of the performance gains arose from improvements in structural design, and how much arose from the simple lengthening of the wings.

Like the Mentor team, Singh and Chopra also used an experimental design methodology, though on a less extensive scale [98, 156]. Since Singh and Chopra’s research was focused on aeroelastic analysis instead of operational optimization, their wing design went through many fewer iterations and variations than the Mentor’s. Variations on two basic frame-and-membrane configurations were developed: scaled fruit fly planforms and rectangular planforms. All the wings had the same radius and mean chord. The fruit fly wings were constructed with thin aluminum frames and Mylar membranes. “Wing II,” shown in figure 1.30a, feathered about the 50%-chord axis and had a closed frame. “Wing III,” in figure 1.33a, feathered about the 20%-chord axis and had a frame that was open along the trailing edge. Wing III consistently achieved greater thrust than Wing II for the same flapping motion, which Singh and Chopra ascribed to greater rotational lift (i.e., Kramer effect) from the more-forward feathering axis. The later rectangular series were constructed from composites next in an effort to decrease wing weight and, thus, inertial power requirements. The rectangular geometry shown in figure 1.33b was chosen to simplify construction, using either

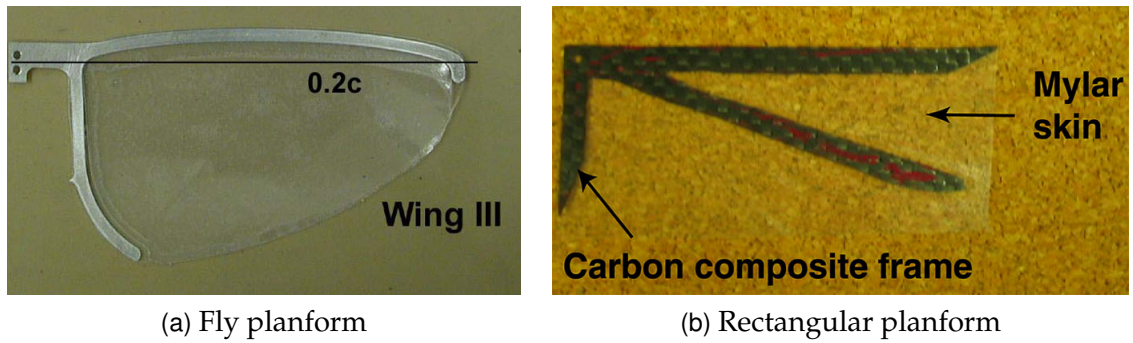


Figure 1.33: Example wings from Singh and Chopra's experiments.

carbon composite or fiberglass frames and mylar or RC Microlite membranes. The feathering axis for all the rectangular wings was moved forward to 10% chord.

Singh and Chopra's study is notable for reporting the first nonrotational natural frequency of each trial wing, determined from the wings' impulse response. This appears to be the only study which reports the wings' natural frequency or, indeed, any quantitative data characterizing the structural dynamics of an MAV wing. Together with thrust and power graphs over the range of flapping frequencies, this allows an estimation of the dynamic stiffness of the wing. A schematic diagram is given of Wing III (on which most of the aeroelastic analysis was focused), from which could be derived estimates of the wing area and centers of mass and area. However, scant quantitative structural data for the other wings is given particularly for the rectangular wing series.

1.3.4 Other Flapping-Wing Analyses

Concurrent with the research performed for this dissertation, several research programs have begun to focus on the aerodynamic and aeroelastic effects of wing flexibility for flapping-wing flight. Shyy et al. [157] provides an overview of recent aeroelastic modeling efforts, with a focus on the work of Aono, Chimakurthi et al. [158, 159], as a part of a general survey of flapping-wing aerodynamics. In general, the aeroelastic analyses are complex numerical methods which couple computa-

tional fluid dynamics (CFD) with computational structural dynamics (CSD). Such analyses are shown to provide good agreement with experimental measurements. The aeroelastic numerical analyses confirm the beneficial effects of flexibility for flapping-wing aerodynamics.

As flapping-wing MAV technology matures and flight-capable MAVs are developed, detailed models of insect-like flight dynamics are necessary to develop suitable control and stability analyses. To this end, Orłowski and Girard developed an analytical model of insect-like MAV flight dynamics which considers the effects of six-degree-of-freedom wing motion (flapping, feathering and stroke deviation for each wing) in addition to the standard six degrees of freedom associated with rigid-body flight [160]. The wings were modeled as rigid structure, which comprised 5.7% of the mass of the total MAV. Despite accounting for only a small portion of the vehicle's mass, Orłowski and Girard concluded that wing effects cause appreciable changes in the qualitative and quantitative nature of flight dynamics when compared to a standard model that neglects wing effects. Therefore, modeling wing motion is important for understanding insect-like flight dynamics. The analytical framework used by Orłowski and Girard to model rigid-wing dynamics is compatible with the flexible-wing structural dynamic model presented in this dissertation, suggesting that the two analyses can be combined in the future.

1.4 Summary

Insects and insect-like animals are attractive models for micro air vehicles. In particular, large hawkmoths and hummingbirds are maneuverable and hover-capable fliers with wingspans near DARPA's target for MAVs. Study of these animals will yield knowledge that can be applied to MAV design. Hawkmoths and hummingbirds use normal hovering flight, in which the wings undergo large-

angle oscillatory flapping and pitching rotations at frequencies of 10 Hz or more. These animals' wings are lightweight and flexible structures that experience substantial deformations during flight. The airflow associated with normal hovering flight is significantly different than those of full-scale airplanes and helicopters, and only within the last fifteen years have we begun to identify and understand its major aerodynamic mechanisms.

Reversible deformations during normal hovering flight cause nose-down twist and positive camber of biological fliers' wings, properties that enhance lift in rotary-winged helicopters. However, the effect of wing flexibility has been largely ignored in aerodynamic studies, and the majority of analytical and physical models of normal hovering flight neglect flexibility altogether. Therefore it is impossible to definitively conclude that twist and camber, or any structural deformations for that matter, act analogously in normal hovering flight as in more well-known fixed- and rotary-wing regimes. There is a clear need for engineers to better understand the structural and aeroelastic operation of flexible flapping wings at a basic level.

At present, a number of factors hinder such basic understanding. The first is the complexity of the biological wings—small, delicate, intricate and multi-functional structures that often confound simple analysis. Biological complexity has led engineers and biologists to construct analogues of insects for basic research, studying not the animals directly but mechanical approximations of them. This leads to the second factor: current mechanical devices cannot replicate the wingbeat amplitudes and frequencies of biological fliers. This dissertation shows that the wingbeat amplitudes and frequencies are fundamental parameters characterizing the time-periodic structural dynamics of the flapping wing. It is reasonable to assume that as MAV technology progresses mechanical systems will approach biological ranges of actuation, but current technology cannot physically

evaluate how those future structural systems will act. The final factor hindering our understanding is simply a lack of quantitative measurements of structural properties for either biological or mechanical wings. Only a few instances of data for bending stiffnesses, natural frequencies and elastic axis and center of gravity locations are reported for flapping wings; more detailed data is often wholly unavailable. With little quantitative data on which to base design analysis, most flapping MAV wings are designed using experimental trial-and-error methods.

Despite these difficulties, recent research indicates a possible bright spot for the study of flapping wing structures. Biologists have speculated that inertial loads play a greater role in causing wing deformations than aerodynamic loads. This speculation is borne out by the few recent studies that account for structural flexibility. A particularly promising finding by Combes and Daniel, the only researchers to experimentally evaluate the effect of air density on biological wing deformations, concludes that the effect of aerodynamics on flapping wing deformations can be approximated by the addition of damping to a structural model. This suggests that, on a preliminary level at least, flapping wing flexibility can be modeled by purely structural methods, allowing analysis separate from aerodynamic considerations.

1.5 Objective

The objective of this research is the development and application of an analytic structural model of a flexible flapping wing. The analytic model will capture the effects of general design variables, such as mass and stiffness distributions, on the structural dynamics of the wing. This analytic model is developed to address a gap in current modeling and design capability with regards to flexible flapping wings.

The current state-of-the-art for design and evaluation of flexible flapping

wings can be generalized into two broad regimes. On one hand, physical wings for flapping-wing mechanisms are typically designed by construction-and-evaluation methods, in which many design iterations are built and experimentally tested. This design method is efficacious for developing wings for any particular in-hand mechanism, but not suitable for predicting or optimizing the performance of wing structures. On the other hand, ever-more-complex coupled CFD/FEM models of flapping wings (particularly biological wings) are being developed to study flexible wings. These computational models are very useful for comprehensive, detailed examination of a particular wing, but are resource-intensive to set-up and solve and are difficult to draw generalized knowledge from. The analytic structural model developed in this dissertation provides a middle-ground between these two options. The structural model is then applied to examine the time-periodic stability of flapping wing systems for operating conditions that are beyond the current capabilities of experimental flapping mechanisms, as well as interpreting results from a FEM-based aeroelastic code.

CHAPTER 2

ASSUMED MODES ANALYSIS OF A FLAPPING WING AS A THIN BEAM

2.1 Introduction

This chapter presents the derivation and non-dimensionalization of the equations of motion of an elastic wing structure undergoing bending and torsional deformations. The wing loadings are derived for a thin beam undergoing arbitrary flapping and feathering motions. The derived blade loadings are used to create the matrix assumed-modes equations of motion. By enforcing time-periodic flapping and feathering, the equations of motion are non-dimensionalized as functions of the flapping and feathering frequencies and amplitudes. The chapter concludes with commentary and insights on the non-dimensional flapping-wing equations of motion. The derivation and non-dimensionalization of the flapping wing model was published in part by Rosenfeld and Wereley [161].

2.2 Model Definition

In order to create a simple analytical model, we assume that the bending and torsion loads of the wing are carried through the leading-edge spar. Combes and Daniel [125] show that this is a good assumption for bending deformations, while Ennos' study [119] implies it is adequate for torsion deformations. The leading-edge spar is modeled as a thin beam. We assume the wing is symmetric across the

cross-sectional thickness and has no initial twist. The wing has a length or radius R and a chord distribution $c(x)$.

The motion of the rigid wing is described by a prescribed feathering rotation $\phi(t)$ and a prescribed flapping rotation $\theta(t)$ as shown in figure 2.1. The flapping angle ϕ describes the wing's rotation within the stroke plane, while the feathering angle θ describes the rotation of the wing along its spanwise axis. ϕ and θ are defined positive in the directions illustrated. Both $\phi(t)$ and $\theta(t)$ are periodic functions of time with a frequency ω . $\phi(t)$ has a stroke (i.e., peak-to-peak) amplitude of Φ and a median value of $\phi = 0$, while $\theta(t)$ has a stroke amplitude of Θ and a median value of $\theta = \pi/2$.

We define several coordinate axes, also seen in figure 2.1. First are the fixed inertial axes, designated by the vectors $(\underline{i}_0, \underline{j}_0, \underline{k}_0)$. The flapping axes $(\underline{i}_\phi, \underline{j}_\phi, \underline{k}_\phi)$ rotate about the inertial \underline{k}_0 axis with the flapping angle ϕ . In turn, the feathering axes $(\underline{i}_\theta, \underline{j}_\theta, \underline{k}_\theta)$ rotate about the flapping \underline{i}_ϕ axis with the feathering angle θ . The inertial, flapping and feathering coordinate systems are coincident at their origin. The wing's elastic axis lies some offset distance e_O ahead of the axis of feathering

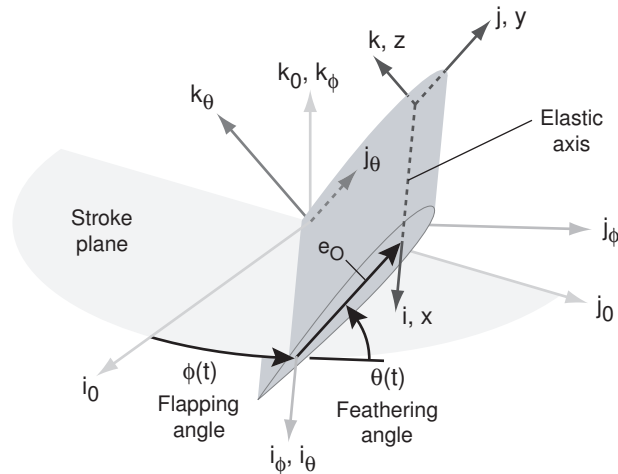


Figure 2.1: Coordinate systems for thin beam analysis, shown with respect to a rigid wing. Not to scale.

rotation. We define the rigid-beam axes $(\underline{i}, \underline{j}, \underline{k})$ with their origin at the root of the elastic axis (i.e., at $e_{Oj\theta}$) and oriented parallel to the feathering axes. Positions in the rigid-beam coordinates are denoted by the triplet (x, y, z) .

Deformations of the wing are measured in the rigid-beam coordinate system as in figure 2.2. The wing is allowed to undergo bending within the plane of the wing v , bending out of the plane of the wing w and torsion about the elastic axis γ . Positive deformations are as illustrated. Also shown are the locations of the cross-section's center of gravity e and area centroid e_A , both measured positive forward of the elastic axis.

This flapping-wing beam model is a generalization of the rotating beam models used to analyze helicopter rotor blades. The helicopter-blade system is recovered for the case of constant positive flapping rate, $\dot{\phi}(t) = C > 0$, and small feathering angle $\theta(t)$.

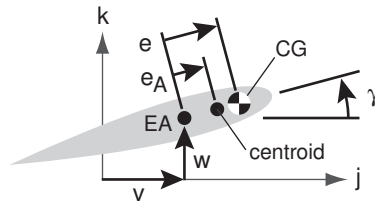


Figure 2.2: Cross-section of deflected wing, shown in rigid-beam coordinate frame. Not to scale.

2.2.1 Nomenclature

The model on which this analysis is based is a synthesis of biological modeling of insects and engineering modeling of rotating beams—specifically, helicopter blades. We attempt to respect the terminology and symbolic conventions of both fields. Since biological models were derived from aeronautical engineering analyses, there is already significant overlap of both fields' lexicons. However, there is a disheartening lack of standardization for biological kinematic nomenclature, with

only a few key symbols and terms being constant across all studies (the universal use ϕ to represent flapping angle is one of the exceptions).

In the interest of clarity when combining the fields, we chose a slightly less common terminology and nomenclature to refer to the angle of incidence of the wing measured from the stroke plane. In biological nomenclature, this angle is typically called the “geometric angle of attack” α , where “geometric” is occasionally discarded. The measurement of α is not standardized. Many studies measure α as an absolute value from different origins for alternating half-strokes, as in figure 2.3; others choose a fixed reference angle (as θ is measured in figure 2.3); still others measure from a vertical reference line. Furthermore, the biological use of *angle of attack* and α conflicts with the engineering convention of measuring angle of attack from the free-stream velocity vector. To eliminate these confusions and conflicts we adopt the alternate term “feathering angle,” which is gaining use MAV studies [146, 150, 151]. Following the convention of Raney and Slominski, we designate the feathering angle as θ (some biological studies use θ to represent the angle of stroke deviation). It is referenced so the feathering angle of a wing traveling nose-forward for counter-clockwise flapping (i.e., rotating in the same direction as a helicopter rotor) is $\theta = 0^\circ$. This nomenclature has the advantage of giving θ a similar meaning to helicopter studies, where θ is the blade pitch angle, while retaining the engineering convention that α designates aerodynamic angles

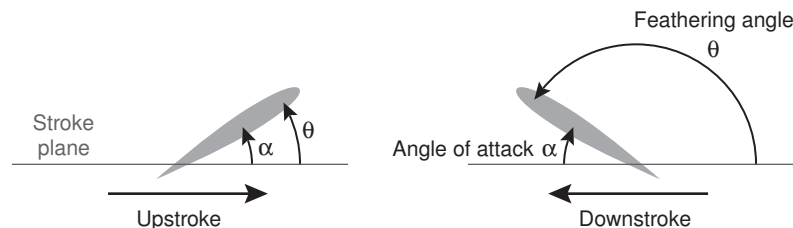


Figure 2.3: Measurement of feathering angle θ versus geometric angle of attack α . Both wings have the same measured geometric angle of attack α , despite their different orientations. Side view of wing, not to scale.

of attack only.

While the kinematics of the wing use biological nomenclature, the nomenclature for beam structures and deformations is taken from Houbolt and Brooks' study of helicopter blades [162], from which the engineering analysis of this chapter is derived. Houbolt and Brooks' nomenclature is standard for helicopter analysis. The only change we make is to use γ to represent the elastic torsion deformation of the wing. Houbolt and Brooks designate elastic torsion as ϕ , which conflicts with the standard biological nomenclature for flapping angle. Helicopter analyses typically designate elastic torsion deformations as θ with an additional subscript (e.g., θ_e in Johnson [163]). We instead chose γ for differentiation from feathering angle θ without the use of subscripts.

2.2.2 Estimation of Physical Properties

Before deriving the equations of motion, we need estimates for the structural properties of the wing. We require measurements of the center of gravity offset e , the centroid offset e_A , the rotational offset e_O of the cross-section, as well as the mass radii of gyration in the chord-wise and thickness directions k_{my} and k_{mz} , and the area polar radius of gyration k_A , all measured from the elastic axis. As noted previously, scant quantitative information from biological studies exist on which to base these values. Norberg's study [123] indicates some values for e and e_A , but no published information gives insight into reasonable values for the radii of gyration. Dudley [63, p. 62] suggests that the center of gravity is near the axis of feathering rotation to decrease inertial torques.

A representative model of a wing cross-section has been created to calculate general dimensions for use in this study. The initial geometry is chosen to approximate Norberg's illustrated locations of the EA and CG locations of dragonfly wings. Denoting the wing chord as c , the average location of the elastic

axis of the forewing of a dragonfly is $0.21c$ behind the leading edge of the wing and the location of the center of gravity is $0.31c$ behind the leading edge. The representative wing is modeled as two rectangular sections: a large section of length $0.42c$ with its front at the leading edge of the wing and a thinner trailing section extending for the remaining $0.58c$ as shown in figure 2.4. Locating the position of the elastic axis on an arbitrary area such as the cross-section in figure 2.4 is not straightforward. For simplicity, we approximate the elastic axis' location as coincident with the centroid of the thick leading section by assuming the thinner trailing section will not carry large out-of-plane shear loads. Assuming the wing is of uniform density, the trailing section must be 0.181 times as thick as the leading section to locate the CG at $0.31c$ behind the leading edge.

We select the exact thicknesses of the sections to match data from hawkmoth wings measured by Combes [127, chap. 4]. The mean physical parameters of the measured hawkmoth wings were a planform area of 774 mm^2 , a radius of 52.2 mm and a mass of 44.3 mg . The mean chord is calculated as 14.8 mm and the mean mass per unit length is 0.852 mg/mm . Combes reports the average density of hawkmoth wings as 0.5 mg/mm^3 [127, p. 108]. The thicknesses of the leading and trailing sections must be $1.48 \times 10^{-2} c$ and $2.7 \times 10^{-3} c$, respectively, for the representative model to have the same mean mass per unit length as the hawkmoth wings for a section of mean chord. The maximum wing thickness is approximately 1.5% of the chord, which is reasonable for a thin airfoil. The representative physical

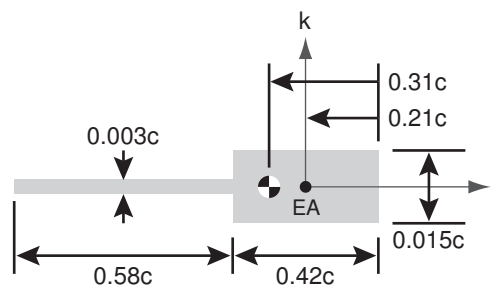


Figure 2.4: Representative wing cross-section. Not to scale.

properties are then calculated as

$$e = -0.10c \quad (2.1)$$

$$e_A = -0.10c \quad (2.2)$$

$$e_O = -e = 0.10c \quad (2.3)$$

$$k_{my}^2 = 0.068c^2 \quad (2.4)$$

$$k_{mz}^2 = 1.5 \times 10^{-5} c^2 \quad (2.5)$$

$$k_A^2 = 0.068c^2 \quad (2.6)$$

e and e_A are negative to indicate that they lie behind the elastic axis. The elastic axis offset e_O is set as $-e$ so that the CG is coincident with the feathering axis i_θ per Dudley.

2.2.3 Aerodynamics

Aerodynamic forces on the wing are not explicitly included in the structural model. Biological researchers including Ellington [78] and Ennos [164] have contended that inertial and elastic forces play the primary role in causing wing deformations, with aerodynamic forces being secondary. Recent experimental tests on insect wings and complementary FEA by Combes and Daniel [131] and numerical aeroelastic models by Singh and Chopra [98] indicate an even stronger conclusion: aerodynamic forces play very little role in determining wing deformations. Combes and Daniel concluded aerodynamic forces primarily provide damping to the wing structure, and the structural dynamics can be adequately calculated from a damped structural model without inclusion of aerodynamic terms. They approximated the aerodynamic damping as viscous damping proportional to the model's mass matrix. We follow this approach by using a structural, rather than aeroelastic, model of the wing. The model is derived for an undamped

system (damping is added for some analysis cases in chapter 3.) Note that aerodynamic forces are implicitly included in the model derivation by the external force distributions and may be expanded given a suitable analytic aerodynamic model accounting for the influence of wing deformations.

2.3 Equations of Motion

The derivation of the equations of motion is based on the linear methodology presented in Houbolt and Brooks' study of helicopter blades [162]. This methodology facilitates linear decomposition of the wing dynamics via an assumed-modes method to simplify analysis. When applied to helicopter blades, Houbolt and Brooks' linear analysis does not include nonlinear flap-torsion nor flap-lag Coriolis couplings [165] when compared to the nonlinear analysis of Hodges and Dowell [166]. ("Flap" bending by helicopter convention is structurally equivalent to our out-of-plane bending with respect to the airfoil, while "lag" bending is equivalent to in-plane bending.) Furthermore, this analysis has assumed that the structural deflections are small enough to be modeled linearly; if larger deflections occur, a non-linear model is necessary. Being aware of these deficiencies, we proceed with the analysis .

We begin with an untwisted beam element of width dx at a radial position x_i . The equilibrium equations of this beam element in torsion, out-of-plane bending and in-plane bending respectively are

$$-\left[(GJ + Tk_A^2)\gamma'\right]' - Te_A w'' + q_y v' - q_z w' - q_x = 0 \quad (2.7)$$

$$(EI_z w'' - Te_A \gamma)'' - (Tw')' + q_y' - p_z = 0 \quad (2.8)$$

$$(EI_y v'' - Te_A)'' - (Tv')' + q_z' - p_y = 0 \quad (2.9)$$

The force loadings p_y and p_z act upon the beam element in the $+\underline{j}$ and $+\underline{k}$ directions. The moment loadings q_x , q_y and q_z act at the elastic axis in the $+\underline{i}$, $-\underline{j}$ and $+\underline{k}$ directions, respectively. The centrifugal tension T is defined by

$$T' = -p_x \quad (2.10)$$

where p_x is the force loading acting in the $+\underline{i}$ direction. The beam loadings p_x , p_y , p_z , q_x , q_y and q_z include inertial forces arising from the prescribed rotations ϕ and θ and external forces acting on the beam.

To derive the inertial loadings, the acceleration acting on a differential volume at a generic point P on the wing is derived in the beam-fixed coordinate system. The accelerations are integrated over the cross-section to give the loadings on a differential section of the wing. Consider a differential volume of size (dx, dy, dz) located at a point P on the undeformed beam. The position vector of P in the rigid-beam coordinates is

$$\underline{P} = \begin{Bmatrix} x \\ y \\ z \end{Bmatrix} \quad (2.11)$$

The beam is allowed to deform in in-plane bending v , out-of-plane bending w and torsion γ as shown in figure 2.2. If the angle γ is small, the deformed position of the point P , denoted as P_1 , is

$$P_1 = \begin{Bmatrix} x - v'y - w'z \\ y + v - z\gamma \\ z + w + y\gamma \end{Bmatrix} = \begin{Bmatrix} P_{1x} \\ P_{1y} \\ P_{1z} \end{Bmatrix}$$

The rigid-beam axes lie parallel to, and a distance e_{Oj} ahead of, the θ -axes. The

deformed position of point P in the θ -axes is

$$\underline{P}_\theta = \begin{pmatrix} x - v'y - w'z \\ y + v - z\gamma + e_O \\ z + w + y\gamma \end{pmatrix}$$

We calculate the acceleration at the deformed point P_1 by transforming the position vector into the inertial 0-axes, taking the second time derivative and transforming back into the θ -axes. The transformation matrices from the inertial axes to the θ -axes and vice versa are

$$\mathbf{T}_{\theta 0} = \begin{bmatrix} \cos \phi & \sin \phi & 0 \\ -\cos \theta \sin \phi & \cos \theta \cos \phi & \sin \theta \\ \sin \theta \sin \phi & -\sin \theta \cos \phi & \cos \theta \end{bmatrix} \quad (2.12)$$

$$\mathbf{T}_{0\theta} = \mathbf{T}_{\theta 0}^\top \quad (2.13)$$

and the acceleration vector \underline{a} in the beam-fixed frame is

$$\underline{a} = \mathbf{T}_{\theta 0} \frac{\partial^2}{\partial t^2} (\mathbf{T}_{0\theta} \underline{P}_\theta) = \begin{pmatrix} a_x \\ a_y \\ a_z \end{pmatrix} \quad (2.14)$$

The components of the acceleration vector are

$$\begin{aligned}
a_x = & \ddot{\phi} \left[\sin(\theta)w - \cos(\theta)(v + e_O) \right] - \dot{\phi}^2 x \\
& + 2\dot{\phi}\dot{\theta} \left[\cos(\theta)w + \sin(\theta)(v + e_O) \right] + 2\dot{\phi} \left[\sin(\theta)\dot{w} - \cos(\theta)\dot{v} \right] \\
& + y \left\{ -\ddot{v}'\gamma + \ddot{\phi} \left[\sin(\theta) - \cos(\theta) \right] + \dot{\phi}^2 v' + 2\dot{\phi}\dot{\theta} \left[\cos(\theta)\gamma + \sin(\theta) \right] \right. \\
& + 2\dot{\phi} \sin(\theta)\dot{\gamma} \left. \right\} + z \left\{ -\ddot{w}' + \ddot{\phi} \left[\cos(\theta)\gamma + \sin(\theta) \right] + \dot{\phi}^2 w' \right. \\
& \left. - 2\dot{\phi}\dot{\theta} \left[\sin(\theta)\gamma - \cos(\theta) \right] + 2\dot{\phi} \cos(\theta)\dot{\gamma} \right\} \tag{2.15}
\end{aligned}$$

$$\begin{aligned}
a_y = & \ddot{v} + \ddot{\phi} \cos(\theta)x - \ddot{\theta}w + \dot{\phi}^2 \cos(\theta) \left[\sin(\theta)w - \cos(\theta)(v + e_O) \right] \\
& - \dot{\theta}^2(v + e_O) - 2\dot{\theta}\dot{w} + y \left\{ -\ddot{\phi} \cos(\theta)v' - \ddot{\theta}\gamma \right. \\
& + \dot{\phi}^2 \cos(\theta) \left[\sin(\theta)\gamma - \cos(\theta) \right] - \dot{\theta}^2 - 2\dot{\phi} \cos(\theta)v' - 2\dot{\theta}\dot{\gamma} \left. \right\} \\
& + z \left\{ -\ddot{\gamma} - \ddot{\phi} \cos(\theta)w' - \ddot{\theta} + \dot{\phi}^2 \cos(\theta) \left[\cos(\theta)\gamma + \sin(\theta) \right] \right. \\
& \left. + \dot{\theta}^2\gamma - 2\dot{\phi} \cos(\theta)\dot{w}' \right\} \tag{2.16}
\end{aligned}$$

$$\begin{aligned}
a_z = & \ddot{w} - \ddot{\phi} \sin(\theta)x + \ddot{\theta}(v + e_O) - \dot{\phi}^2 \sin(\theta) \left[\sin(\theta)w - \cos(\theta)(v + e_O) \right] \\
& - \dot{\theta}^2 w + 2\dot{\theta}\dot{v} + y \left\{ \ddot{\gamma} + \ddot{\phi} \sin(\theta)v' + \ddot{\theta} - \dot{\phi}^2 \sin(\theta) \left[\sin(\theta)\gamma - \cos(\theta) \right] \right. \\
& \left. - \dot{\theta}^2\gamma + 2\dot{\phi} \sin(\theta)\dot{v}' \right\} + z \left\{ \ddot{\phi} \sin(\theta)w' - \ddot{\theta}\gamma \right. \\
& \left. - \dot{\phi}^2 \sin(\theta) \left[\cos(\theta)\gamma + \sin(\theta) \right] - \dot{\theta}^2 + 2\dot{\phi} \sin(\theta)\dot{w}' - 2\dot{\theta}\dot{\gamma} \right\} \tag{2.17}
\end{aligned}$$

Integrating the accelerations over the beam cross-sections gives the force and moment loadings for the beam at the elastic axis. The beam density ρ may vary over the cross-section. Since the beam is symmetric about the chordwise axis, terms multiplied by z integrate to zero. The forces p and moments q are given

by

$$\begin{aligned}
p_x &= - \int_y \int_z a_x \rho \, dz \, dy \\
p_y &= L_y - \int_y \int_z a_y \rho \, dz \, dy \\
p_z &= L_z - \int_y \int_z a_z \rho \, dz \, dy \\
q_x &= M - \int_y \int_z \left[-a_y(P_{1z} - w) + a_z(P_{1y} - v) \right] \rho \, dz \, dy \\
q_y &= - \int_y \int_z \left[-a_x(P_{1z} - w) \right] \rho \, dz \, dy \\
q_z &= - \int_y \int_z \left[-a_x(P_{1y} - v) \right] \rho \, dz \, dy
\end{aligned}$$

L_y , L_z and M are the external loadings acting at the elastic axis, including all aerodynamic forces. The resultant equations, with all second-order functions of deformation variables removed, are:

$$\begin{aligned}
p_x &= m e \ddot{v}' + m \ddot{\phi} \left[\cos(\theta)(e_O + e + v) - \sin(\theta)(w + e\gamma) \right] \\
&+ m \dot{\phi}^2 (x - e v') - 2m \dot{\phi} \dot{\theta} \left[\sin(\theta)(e_O + e + v) + \cos(\theta)(w + e\gamma) \right] \\
&+ 2m \dot{\phi} \left[\cos(\theta) \dot{v} - \sin(\theta)(\dot{w} + e\dot{\gamma}) \right] \tag{2.18}
\end{aligned}$$

$$\begin{aligned}
p_y &= L_y - m \ddot{v} - m \ddot{\phi} \cos(\theta)(x - e v') + m \ddot{\theta}(w + e\gamma) \\
&+ m \dot{\phi}^2 \cos(\theta) \left[\cos(\theta)(e_O + e + v) - \sin(\theta)(w + e\gamma) \right] \\
&+ m \dot{\theta}^2 (e_O + e + v) + 2m e \dot{\phi} \cos(\theta) \dot{v}' + 2m \dot{\theta}(\dot{w} + e\dot{\gamma}) \tag{2.19}
\end{aligned}$$

$$\begin{aligned}
p_z &= L_z - m(\ddot{w} + e\ddot{\gamma}) + m \ddot{\phi} \sin(\theta)(x - e v') - m \ddot{\theta}(e_O + e + v) \\
&- m \dot{\phi}^2 \sin(\theta) \left[\cos(\theta)(e_O + e + v) - \sin(\theta)(w + e\gamma) \right] \\
&+ m \dot{\theta}^2 (w + e\gamma) - 2m e \dot{\phi} \sin(\theta) \dot{v}' - 2m \dot{\theta} \dot{v} \tag{2.20}
\end{aligned}$$

$$\begin{aligned}
q_x = & M - me\ddot{w} - mk_m^2\ddot{\gamma} + me\ddot{\phi} \left[\sin(\theta)x + \cos(\theta)x\gamma \right] \\
& - m\ddot{\phi} \left[k_{my}^2 \sin(\theta)v' + k_{mz}^2 \cos(\theta)w' \right] - me\ddot{\theta}(e_O + v) - mk_m^2\ddot{\theta} \\
& + me\dot{\phi}^2 \left[\sin^2(\theta)w - \cos^2(\theta)e_O\gamma - \sin(\theta)\cos(\theta)(e_O + v) \right] \\
& + m(k_{my}^2 - k_{mz}^2)\dot{\phi}^2 \left\{ \left[\sin^2(\theta) - \cos^2(\theta) \right] \gamma - \sin(\theta)\cos(\theta) \right\} \\
& + me\dot{\theta}^2(w - e_O\gamma) - 2m\dot{\phi} \left[k_{my}^2 \sin(\theta)v' + k_{mz}^2 \cos(\theta)w' \right] - 2me\dot{\theta}\dot{v} \quad (2.21)
\end{aligned}$$

$$\begin{aligned}
q_y = & -mk_{mz}^2\ddot{w}' - me\dot{\phi}\cos(\theta)e_O\gamma + mk_{mz}^2\ddot{\phi}\sin(\theta) - m(k_{my}^2 - k_{mz}^2)\ddot{\phi}\cos(\theta)\gamma \\
& - me\dot{\phi}^2x\gamma + mk_{mz}^2\dot{\phi}^2w' + 2me\dot{\phi}\dot{\theta}\sin(\theta)e_O\gamma \\
& + 2m(k_{my}^2 - k_{mz}^2)\dot{\phi}\dot{\theta}\sin(\theta)\gamma + 2mk_{mz}^2\dot{\phi}\dot{\theta}\cos(\theta) + 2mk_{mz}^2\dot{\phi}\cos(\theta)\dot{\gamma} \quad (2.22)
\end{aligned}$$

$$\begin{aligned}
q_z = & -mk_{my}^2\ddot{v}' - me\dot{\phi} \left[\cos(\theta)(e_O + v) - \sin(\theta)w \right] \\
& + m(k_{my}^2 - k_{mz}^2)\ddot{\phi}\sin(\theta)\gamma - mk_{my}^2\ddot{\phi}\cos(\theta) - me\dot{\phi}^2x + mk_{my}^2\dot{\phi}^2v' \\
& + 2me\dot{\phi}\dot{\theta} \left[\sin(\theta)(e_O + v) + \cos(\theta)w \right] + 2m(k_{my}^2 - k_{mz}^2)\dot{\phi}\dot{\theta}\cos(\theta)\gamma \\
& + 2mk_{my}^2\dot{\phi}\dot{\theta}\sin(\theta) - 2me\dot{\phi} \left[\cos(\theta)\dot{v} - \sin(\theta)\dot{w} \right] + 2mk_{my}^2\dot{\phi}\sin(\theta)\dot{\gamma} \quad (2.23)
\end{aligned}$$

In the preceding equations, $k_m = \sqrt{k_{my}^2 + k_{mz}^2}$ is the polar radius of gyration.

The forces and moments of equations 2.18–2.23 are simplified by performing order-of-magnitude analysis. Orders of magnitude are assigned to each term: m , x , ϕ and θ are $O(1)$; v , w , γ , e and e_O are $O(\epsilon)$. The squared radii of gyration k_{my}^2 and k_{mz}^2 are $O(\epsilon^2)$ and $O(\epsilon^5)$, respectively. This implies $k_m^2 = k_{my}^2 + k_{mz}^2 \approx k_{my}^2$; the cross-section's polar radius of gyration is approximately equal to its chordwise radius of gyration. We simplify the loadings using the following metrics. In p_x terms of $O(1)$ and constant terms of $O(\epsilon)$ are retained. In p_y and p_z all terms of $O(1)$ and $O(\epsilon)$, as well as terms of $O(\epsilon^2)$ which are functions of γ are retained. In q_x all terms of $O(\epsilon)$ and $O(\epsilon^2)$ as well as terms of $O(\epsilon^3)$ which are functions of γ are retained. In q_y all terms of $O(\epsilon^2)$ and $O(\epsilon^3)$ are retained. In q_z , terms of $O(\epsilon)$ and

constant terms of $O(\epsilon^2)$ are retained. The resulting expressions are

$$p_x = m\dot{\phi}^2 x + m(e_O + e)\ddot{\phi} \cos(\theta) - 2m(e_O + e)\dot{\phi}\dot{\theta} \sin(\theta) \quad (2.24)$$

$$\begin{aligned} p_y = & L_y - m\ddot{v} - m\ddot{\phi} \cos(\theta)x + m\ddot{\theta}(w + e\gamma) \\ & + m\dot{\phi}^2 \cos(\theta) \left[\cos(\theta)(e_O + e + v) - \sin(\theta)(w + e\gamma) \right] \\ & + m\dot{\theta}^2(e_O + e + v) + 2m\dot{\theta}(\dot{w} + e\dot{\gamma}) \end{aligned} \quad (2.25)$$

$$\begin{aligned} p_z = & L_z - m(\ddot{w} + e\dot{\gamma}) + m\ddot{\phi} \sin(\theta)x - m\ddot{\theta}(e_O + e + v) \\ & - m\dot{\phi}^2 \sin(\theta) \left[\cos(\theta)(e_O + e + v) - \sin(\theta)(w + e\gamma) \right] \\ & + m\dot{\theta}^2(w + e\gamma) - 2m\dot{\theta}\dot{v} \end{aligned} \quad (2.26)$$

$$\begin{aligned} q_x = & M - me\ddot{w} - mk_m^2 \dot{\gamma} + me\ddot{\phi}x \left[\sin(\theta) + \cos(\theta)\gamma \right] - me\ddot{\theta}(e_O + v) \\ & - mk_m^2 \ddot{\theta} + me\dot{\phi}^2 \left[\sin^2(\theta)w - \cos^2(\theta)e_O\gamma - \sin(\theta)\cos(\theta)(e_O + v) \right] \\ & + mk_m^2 \dot{\phi}^2 \left\{ \left[\sin^2(\theta) - \cos^2(\theta) \right] \gamma - \sin(\theta)\cos(\theta) \right\} \\ & + me\dot{\theta}^2(w - e_O\gamma) - 2me\dot{\theta}\dot{v} \end{aligned} \quad (2.27)$$

$$q_y = -me\dot{\phi}^2 x \gamma - m(e_O e + k_m^2)\ddot{\phi} \cos(\theta)\gamma + 2m(e_O e + k_m^2)\dot{\phi}\dot{\theta} \sin(\theta)\gamma \quad (2.28)$$

$$q_z = -me\dot{\phi}^2 x - m(e_O e + k_m^2)\ddot{\phi} \cos(\theta) + 2m(e_O e + k_m^2)\dot{\phi}\dot{\theta} \sin(\theta) \quad (2.29)$$

2.4 Physical Interpretations of Force Loadings

The cross-sectional force and moment loadings from Eqs. 2.24–2.29 are derived from an order-of-magnitude analysis applied to the integrated inertial forces across the beam's cross-section. This derivation implicitly accounts for the various inertial, centrifugal and Coriolis loadings; no *a priori* physical insight into individual component forces is necessary. We would like to understand these component effects in their own right. In this section the component loadings

are individually derived to furnish this insight, and also as a confirmation of the preceding analysis.

For clarity and simplicity, the cross-sectional mass distribution is modeled in this section as a point mass. The mass radius of gyration will therefore equal the magnitude of the CG offset, so $k_m^2 = e^2$. Higher-order effects are neglected; only terms appearing in the simplified loadings of Eqs. 2.24–2.29 are derived.

Beam loadings are defined along the rigid-beam coordinate axes. Recall that the rigid-beam axes are parallel to the feathering axes by definition. Also recall that the moment loadings q_x and q_z are defined positive in the \underline{i} and \underline{k} directions by the right-hand-rule, but q_y is positive in the $-\underline{j}$ direction.

2.4.1 Cross-Sectional Inertia

The inertia of the beam cross section resists structural deformations with a force proportional to the acceleration of the deformations v , w and γ . Figure 2.5 shows the deformation accelerations in the feathering coordinate system. For small γ , the inertial force loadings resisting deformations are

$$p_y = -m\ddot{v}$$

$$p_z = -m(\ddot{w} + e\ddot{\gamma})$$

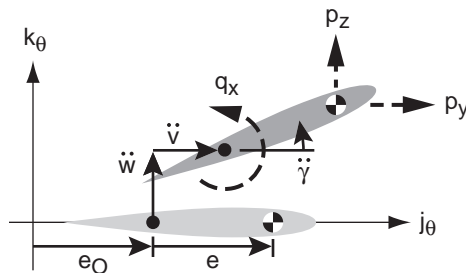


Figure 2.5: Inertial resistance of airfoil cross-section to deformations shown from the side in the feathering coordinate frame. Undeformed position shown in light gray, deformed position in dark gray. Dashed arrows indicate positive loadings.

The torsional loading q_x is taken about the deformed elastic axis position and is equal to

$$\begin{aligned} q_x &= -e\gamma p_y + ep_z \\ &= \underbrace{me\gamma\ddot{v}}_{\text{2nd-order}} - me\ddot{w} - me^2\ddot{\gamma} \end{aligned}$$

The marked second-order term is a non-linear function of deformation variables and is neglected in our linear model. Comparing the inertial q_x terms with Eq. 2.27 confirms that the point-mass analysis gives $k_m^2 = e^2$. Since no forces act out of the cross-sectional plane,

$$p_x = q_y = q_z = 0$$

2.4.2 Flapping Centrifugal Loadings

Like helicopter rotors, flapping wings are stiffened by centrifugal force. In flapping wings, centrifugal loadings are a primary source of system periodicity. Figure 2.6 shows the instantaneous flapping centrifugal force acting on the cross-section at radial position x , drawn in the flapping coordinate frame. The magni-

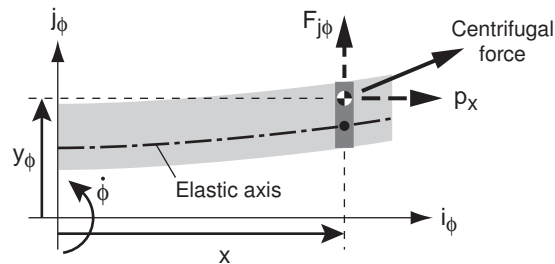


Figure 2.6: Centrifugal force components due to flapping rotation $\dot{\phi}$ acting on a beam element, shown from the top in the flapping coordinate frame. The flapping rotation acts at the coordinate origin.

tudes of the components p_x and $F_{j\phi}$ are proportional to the distances x and y_ϕ :

$$p_x = m\dot{\phi}^2 x$$

$$F_{j\phi} = m\dot{\phi}^2 y_\phi$$

The length y_ϕ is a function of the feathering angle θ and the beam displacements, as shown in figure 2.7a:

$$y_\phi = (e_O + e + v) \cos(\theta) - (w + e\gamma) \sin(\theta)$$

The force loadings p_y and p_z , shown in figure 2.7b are equal to

$$\begin{aligned} p_y &= \cos(\theta) F_{j\phi} \\ &= m\dot{\phi}^2 \cos(\theta) \left[(e_O + e + v) \cos(\theta) - (w + e\gamma) \sin(\theta) \right] \\ p_z &= -\sin(\theta) F_{j\phi} \\ &= -m\dot{\phi}^2 \sin(\theta) \left[(e_O + e + v) \cos(\theta) - (w + e\gamma) \sin(\theta) \right] \end{aligned}$$

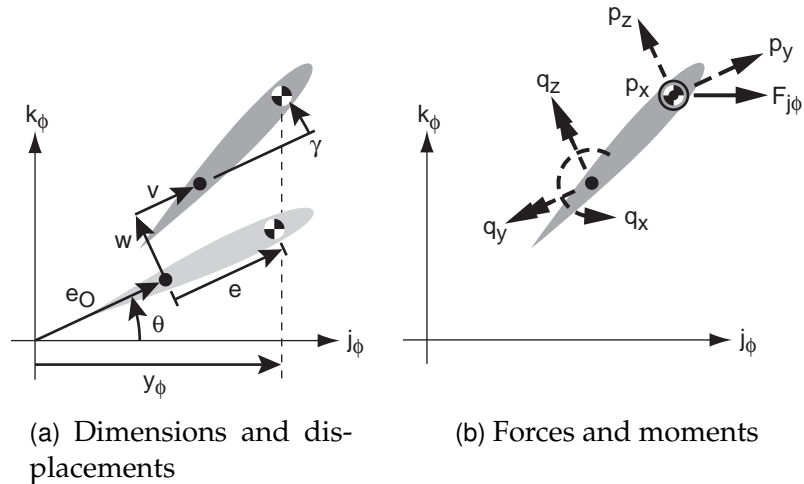


Figure 2.7: Force components due to prescribed flapping motion $\phi(t)$ acting on an airfoil cross-section, shown from the side in the flapping coordinate frame. Rigid beam position shown in light gray, displaced position shown in dark gray.

The torsional loading q_x is equal to

$$\begin{aligned}
 q_x &= -e\gamma p_y + ep_z \\
 &= m\dot{\phi}^2 \left[-e\gamma(e_O + e + \underbrace{v}_{\text{2nd-order}}) \cos^2(\theta) + \underbrace{e\gamma(w + e\gamma) \sin(\theta) \cos(\theta)}_{\text{2nd-order}} \right. \\
 &\quad \left. - e(e_O + e + v) \sin(\theta) \cos(\theta) + e(w + e\gamma) \sin^2(\theta) \right] \tag{2.30}
 \end{aligned}$$

Again, the marked second-order functions of displacement variables are neglected. Rearranging yields

$$\begin{aligned}
 q_x &= me\dot{\phi}^2 \left[\sin^2(\theta)w - \cos^2(\theta)e_O\gamma - \sin(\theta) \cos(\theta)(e_O + v) \right] \\
 &\quad + me^2\dot{\phi}^2 \left\{ \left[\sin^2(\theta) - \cos^2(\theta) \right] \gamma - \sin(\theta) \cos(\theta) \right\} \tag{2.31}
 \end{aligned}$$

Examining Eq. 2.31 reveals that the dependence of q_x on v and w arises from the p_z term in Eq. 2.30. The primary effect of v and w on q_x is to change the *magnitude of the centrifugal force*. In contrast, most of the dependence of q_x on γ comes from the $e\gamma$ term multiplying p_y in Eq. 2.30. The primary effect of γ on q_x is to change the *moment arm* about which the centrifugal force acts. This effect of γ on torque is used later to account for important forcing terms which would otherwise be neglected.

The moment loadings q_y and q_z are functions of the force p_x . These loadings are:

$$\begin{aligned}
 q_y &= -e\gamma p_x \\
 &= -me\dot{\phi}^2 x \gamma \\
 q_z &= -ep_x \\
 &= -me\dot{\phi}^2 x
 \end{aligned}$$

Again, note the influence of γ on the moment arm for q_y .

2.4.3 Feathering Centrifugal Loadings

The prescribed velocity of feathering rotation $\dot{\theta}$ imparts a centrifugal force on the beam in the plane of the cross-section, as shown in figure 2.8. The component loadings of feathering centrifugal force are proportional to y_θ and z

$$\begin{aligned} p_y &= m\dot{\theta}^2 y_\theta \\ &= m\dot{\theta}^2 (e_O + e + v) \\ p_z &= m\dot{\theta}^2 z \\ &= m\dot{\theta}^2 (w + e\gamma) \end{aligned}$$

The torsional moment q_x is

$$\begin{aligned} q_x &= -e\gamma p_y + e p_z \\ &= m\dot{\theta}^2 \left[-e\gamma (e_O + e + \underbrace{v}_{\text{2nd-order}}) + e(w + e\gamma) \right] \\ &= m e \dot{\theta}^2 (w - e_O \gamma) \end{aligned}$$

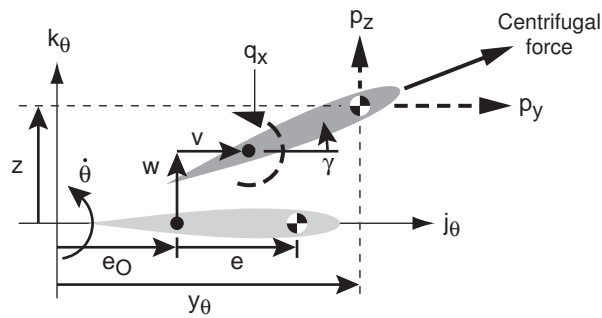


Figure 2.8: Centrifugal force components due to feathering rotation $\dot{\theta}$ acting on an airfoil cross-section, shown in a side view of the flapping coordinate frame. The feathering rotation acts at the coordinate origin.

The second-order term is neglected as usual. Again, the dependence of the centrifugal feathering component of q_x on γ is due to a change in the moment arm of the p_y component. Since no forces act outside of the cross-sectional plane,

$$p_x = q_y = q_z = 0$$

2.4.4 Flapping Inertial Loadings

The time-periodic prescribed flapping motion gives rise to inertial forces which resist the flapping accelerations. The inertial forces are proportional in magnitude to the rotational acceleration $\ddot{\phi}$. The associated *force* loadings are derived for the rigid-beam position. This is justified for the p_y and p_z loadings because the order-of-magnitude analysis shows that the variation of flapping inertial loadings due to deformations is small. In the case of p_x , recall that p_x is the differential beam tension force (see Eq. 2.34). The tension force acts primarily as a stiffness term in the equations of motion; thus, any dependency of p_x on the displacements will manifest as non-linear stiffness terms in the equations of motion and is neglected.

However, in calculating the associated *moment* loadings q_x , q_y and q_z , we assume that the torsional deformation γ exists. Recall that, with respect to moment loadings, the primary influence of γ was to change the moment arm by which the force loadings acted. Using a non-zero γ for the calculation of the present moment loadings will account for important terms in q_x and q_y .

The inertial force resisting flapping accelerations is shown in the flapping coordinate system in figure 2.9. The component forces p_x and $F_{j\phi}$ are proportional

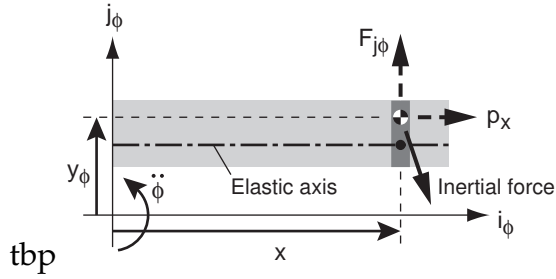


Figure 2.9: Inertial force components resisting flapping acceleration $\ddot{\phi}$ acting on a beam element, shown in a top view of the flapping coordinate frame. The flapping acceleration acts at the coordinate origin

to the distances y_ϕ and x

$$p_x = m\ddot{\phi}y_\phi$$

$$F_{j\phi} = -m\ddot{\phi}x$$

The length y_ϕ is shown in figure 2.10a and is equal to $y_\phi = (e_O + e) \cos(\theta)$ so that

$$p_x = m\ddot{\phi}(e_O + e) \cos(\theta)$$

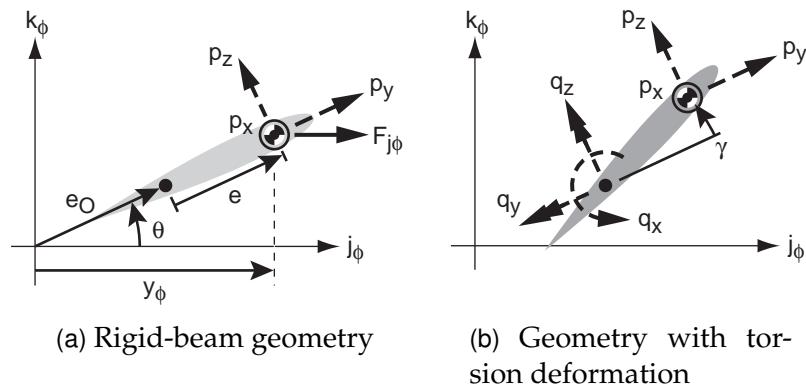


Figure 2.10: Forces resisting flapping acceleration $\ddot{\phi}$ acting on beam cross-section, shown in the side view of the flapping coordinate frame. Force loadings are derived from the rigid geometry in (a). Moment loadings are derived from the deflected geometry in (b) using forces derived from (a).

The force loadings p_y and p_z are equal to

$$\begin{aligned}
 p_y &= \cos(\theta)F_{j\phi} \\
 &= -m\ddot{\phi} \cos(\theta)x \\
 p_z &= -\sin(\theta)F_{j\phi} \\
 &= m\ddot{\phi} \sin(\theta)x
 \end{aligned}$$

When calculating moment loadings, we assume that the force loadings act at the deflected CG location shown in figure 2.10b. The q_x loading is

$$\begin{aligned}
 q_x &= -e\gamma p_y + ep_z \\
 &= me\ddot{\phi}x \left[\cos(\theta)\gamma + \sin(\theta) \right]
 \end{aligned}$$

The term $me\ddot{\phi}x \cos(\theta)\gamma$ is order ϵ^2 and is thus a significant component of q_x , but it would have been neglected had only the rigid beam been used for the derivation.

The remaining moment loadings are

$$\begin{aligned}
 q_y &= -e\gamma p_x \\
 &= -me_Oe\ddot{\phi} \cos(\theta)\gamma - me^2\ddot{\phi} \cos(\theta)\gamma \\
 q_z &= -ep_x \\
 &= -me_Oe\ddot{\phi} \cos(\theta) - me^2\ddot{\phi} \cos(\theta)
 \end{aligned}$$

Again, if we had assumed that $\gamma = 0$ then $q_y = 0$, which would lead to mismatched coupling terms in the equations of motion.

2.4.5 Feathering Inertial Loadings

The time-periodic feathering rotation $\ddot{\theta}$ gives rise to inertial loadings opposing the feathering acceleration. These loadings are derived for a cross section undergoing displacements v , w and γ as shown in figure 2.11. The component force loadings p_y and p_z are proportional to the distances z and y_θ

$$\begin{aligned} p_y &= m\ddot{\theta}z \\ &= m\ddot{\theta}(w + e\gamma) \\ p_z &= -m\ddot{\theta}y_\theta \\ &= -m\ddot{\theta}(e_0 + e + v) \end{aligned}$$

and the moment loading q_x is

$$\begin{aligned} q_x &= -e\gamma p_y + e p_z \\ &= m\ddot{\theta} \left[\underbrace{-e\gamma(w + e\gamma)}_{\text{2nd-order}} - e(e_0 + e + v) \right] \\ &= -me\ddot{\theta}(e_0 + v) - me^2\ddot{\theta} \end{aligned}$$

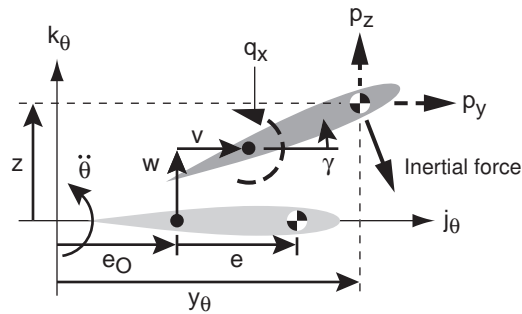


Figure 2.11: Inertial force resisting feathering acceleration $\ddot{\theta}$, shown in a side view of the feathering coordinate frame. The feathering acceleration acts at the coordinate origin.

As usual the second-order function of deformation variables is neglected. Since no forces act outside of the cross-sectional plane,

$$p_x = q_y = q_z = 0$$

2.4.6 Flap-Feather Coriolis Loadings

Coriolis forces arise when a mass in a rotating frame experiences additional motion within the plane of rotation. The Coriolis force acts perpendicularly to the velocity of the mass relative to the rotating frame: a mass with a velocity tangential to the frame's rotation will experience a Coriolis force in the radial direction, while a mass with a radial velocity will experience a tangential Coriolis force.

Three types of Coriolis forces can arise in this flapping-feathering model. The first is flap-feather Coriolis loadings, in which prescribed feathering motion induces a velocity relative to the rotating flapping frame. The second is feather-deformation Coriolis loadings, in which the motion of the deforming wing acts relative to the rotating feathering frame. The third is flap-deformation Coriolis loadings, in which the motion of the deforming wing acts relative to the rotating flapping frame. Flap-deformation effects are small according to the order-of-magnitude analysis, so their derivation is not included. For a given cross-section, the Coriolis force is proportional to twice the cross sectional mass, the frame's rotational velocity and the cross-sectional mass' velocity relative to the rotating frame.

In deriving the flap-feather Coriolis force loadings, the wing is assumed to be rigid, but the moment loadings are derived for a torsionally deformed wing (as in figure 2.10, but note that $p_y = p_z = q_x = 0$ for flap-feather Coriolis loadings). This is the same methodology used to derive the flapping inertial loadings.

The flap-feather Coriolis force is shown in figure 2.12. The velocity \dot{y}_ϕ is a

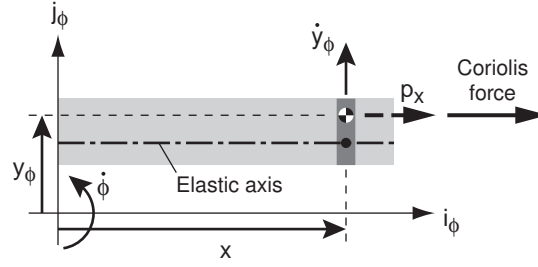


Figure 2.12: Coriolis loadings on a rigid beam due to the interaction of flapping velocity $\dot{\phi}$ and feathering velocity $\dot{\theta}$ (through \dot{y}_ϕ), shown in a top view of the flapping coordinate frame.

function of the prescribed feathering velocity $\dot{\theta}$. Note that $\dot{y}_\phi > 0$ causes a Coriolis force acting outward in the radial direction. This force is equal to p_x :

$$p_x = 2m\dot{\phi}\dot{y}_\phi$$

Figure 2.10a shows that $y_\phi = (e_O + e) \cos(\theta)$, so the time derivative of y_ϕ is

$$\dot{y}_\phi = -(e_O + e) \sin(\theta)\dot{\theta}$$

and the flap-feather Coriolis force is

$$p_x = -2m(e_O + e)\dot{\phi}\dot{\theta} \sin(\theta)$$

Recalling that γ is assumed to exist for calculation of moment loadings, q_y and q_z are

$$\begin{aligned} q_y &= -e\gamma p_x \\ &= 2me_O e \dot{\phi} \dot{\theta} \sin(\theta) \gamma + 2me^2 \dot{\phi} \dot{\theta} \sin(\theta) \gamma \\ q_z &= -e p_x \\ &= 2me_O e \dot{\phi} \dot{\theta} \sin(\theta) + 2me^2 \dot{\phi} \dot{\theta} \sin(\theta) \end{aligned}$$

Since no forces act within the cross-sectional plane,

$$p_y = p_z = q_x = 0$$

2.4.7 Feather-Deformation Coriolis Loadings

The feather-deformation Coriolis loadings arise from the motion of a wing cross-section in the rotating feathering frame. This motion gives rise to both radial and tangential components of Coriolis force acting in the plane of the cross-section, as shown in figure 2.13. The force components are proportional to the perpendicular motions: the radial Coriolis force is proportional to $(\dot{w} + e\dot{\gamma})$ and the tangential Coriolis force is proportional to \dot{v} . The force components p_y and p_z are

$$p_y = 2m\dot{\theta}(\dot{w} + e\dot{\gamma})$$

$$p_z = -2m\dot{\theta}\dot{v}$$

and the moment loading q_x is

$$\begin{aligned} q_x &= -e\gamma p_y + e p_z \\ &= \underbrace{-2me\dot{\theta}(\dot{w} + e\dot{\gamma})\gamma}_{\text{2nd-order}} - 2me\dot{\theta}\dot{v} \end{aligned}$$

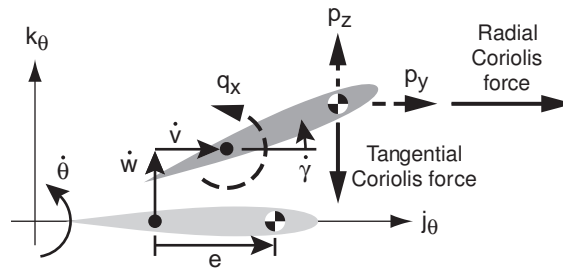


Figure 2.13: Coriolis loadings due to the interaction of feathering velocity $\dot{\theta}$ and beam deformations, shown in a side view of the feathering coordinate frame.

Once again, the second-order function of deformation variables is neglected. Since no forces act outside of the cross-sectional plane,

$$p_x = q_y = q_z = 0$$

2.4.8 Total Loadings

Summing the physically derived inertial, centrifugal and Coriolis loadings to the total force and moment loadings acting on a beam element at a radial position x and including the external in-plane force and moment loadings L_y , L_z and M give the following loadings:

$$\begin{aligned}
 p_x = & \underbrace{m\dot{\phi}^2 x}_{\text{centrifugal flapping}} + \underbrace{m(e_O + e)\ddot{\phi} \cos(\theta)}_{\text{inertial flapping}} - \underbrace{2m(e_O + e)\dot{\phi}\dot{\theta} \sin(\theta)}_{\text{flap-feather Coriolis}} \\
 p_y = & \underbrace{L_y}_{\text{external load}} - \underbrace{m\ddot{w}}_{\text{blade inertia}} - \underbrace{m\dot{\phi} \cos(\theta)x}_{\text{inertial flapping}} + \underbrace{m\ddot{\theta}(w + e\gamma)}_{\text{inertial feathering}} \\
 & + \underbrace{m\dot{\phi}^2 \cos(\theta) [\cos(\theta)(e_O + e + v) - \sin(\theta)(w + e\gamma)]}_{\text{centrifugal flapping}} \\
 & + \underbrace{m\dot{\theta}^2(e_O + e + v)}_{\text{centrifugal feathering}} + \underbrace{2m\dot{\theta}(\dot{w} + e\dot{\gamma})}_{\text{feather-deformation Coriolis}} \\
 p_z = & \underbrace{L_z}_{\text{external load}} - \underbrace{m(\ddot{w} + e\ddot{\gamma})}_{\text{blade inertia}} + \underbrace{m\dot{\phi} \sin(\theta)x}_{\text{inertial flapping}} - \underbrace{m\ddot{\theta}(e_O + e + v)}_{\text{inertial feathering}} \\
 & - \underbrace{m\dot{\phi}^2 \sin(\theta) [\cos(\theta)(e_O + e + v) - \sin(\theta)(w + e\gamma)]}_{\text{centrifugal flapping}} \\
 & + \underbrace{m\dot{\theta}^2(w + e\gamma)}_{\text{centrifugal feathering}} - \underbrace{2m\dot{\theta}\dot{v}}_{\text{feather-deformation Coriolis}}
 \end{aligned}$$

$$\begin{aligned}
q_x = & \underbrace{M}_{\text{external load}} - \underbrace{me(\ddot{w} + e\ddot{\gamma})}_{\text{blade inertia}} + \underbrace{me\ddot{\phi}x[\sin(\theta) + \cos(\theta)\gamma]}_{\text{inertial flapping}} - \underbrace{me\ddot{\theta}(e_O + e + v)}_{\text{inertial feathering}} \\
& + \underbrace{me\dot{\phi}^2[\sin^2(\theta)(w + e\gamma) - \cos^2(\theta)(e_O + e)\gamma - \sin(\theta)\cos(\theta)(e_O + e + v)]}_{\text{centrifugal flapping}} \\
& + \underbrace{me\dot{\theta}^2(w - e_O\gamma)}_{\text{centrifugal feathering}} - \underbrace{2me\dot{\theta}\dot{v}}_{\text{feather-deformation Coriolis}} \\
q_y = & \underbrace{-me\dot{\phi}^2x\gamma}_{\text{centrifugal flapping}} - \underbrace{m(e_Oe + e^2)\ddot{\phi}\cos(\theta)\gamma}_{\text{inertial flapping}} + \underbrace{2m(e_Oe + e^2)\dot{\phi}\dot{\theta}\sin(\theta)\gamma}_{\text{flap-feather Coriolis}} \\
q_z = & \underbrace{-me\dot{\phi}^2x}_{\text{centrifugal flapping}} - \underbrace{m(e_Oe + e^2)\ddot{\phi}\cos(\theta)}_{\text{inertial flapping}} + \underbrace{2m(e_Oe + e^2)\dot{\phi}\dot{\theta}\sin(\theta)}_{\text{flap-feather Coriolis}}
\end{aligned}$$

The physically derived loadings above are identical those derived from the order-of-magnitude analysis (Eqs. 2.24–2.29) for the assumption that the cross-sectional mass distribution is a point mass (i.e., $k_m^2 = e^2$). This validates the previous analysis.

2.5 Assumed Modes Analysis

Resuming our derivation of the flapping equations of motion, we return to the equilibrium equations of a beam section Eqs. 2.7–2.9, restated here:

$$\begin{aligned}
- \left[(GJ + Tk_A^2)\gamma' \right]' - Te_A w'' + q_y v' - q_z w' - q_x &= 0 \\
(EI_z w'' - Te_A \gamma)'' - (Tw')' + q_y' - p_z &= 0 \\
(EI_y v'' - Te_A)'' - (Tv')' + q_z' - p_y &= 0
\end{aligned}$$

Centrifugal tension T is a function of the prescribed flapping and feathering rotations ϕ and θ . This dependence is made explicit by defining mass moments

S_x and S_e

$$S_x = \int_x^R mx dx \quad (2.32)$$

$$S_e = \int_x^R m(e_O + e) dx \quad (2.33)$$

and writing T as a function of these mass moments and the prescribed rotations

$$\begin{aligned} T &= - \int_R^x p_x dx = \int_x^R p_x dx \\ &= \dot{\phi}^2 S_x + \left[\ddot{\phi} \cos(\theta) - 2\dot{\phi}\dot{\theta} \sin(\theta) \right] S_e \end{aligned} \quad (2.34)$$

The equations of motion are solved by applying a modified Galerkin assumed-modes analysis as described by Houbolt and Brooks [162]. The displacements are approximated by the summation of the first N non-rotational modes

$$\gamma(x, t) = \sum_{i=1}^{N_\gamma} \chi_{\gamma i}(x) q_{\gamma i}(t) = \underline{\chi}_\gamma^T(x) \underline{q}_\gamma(t) \quad (2.35)$$

$$w(x, t) = \sum_{j=1}^{N_w} \chi_{w j}(x) q_{w j}(t) = \underline{\chi}_w^T(x) \underline{q}_w(t) \quad (2.36)$$

$$v(x, t) = \sum_{k=1}^{N_v} \chi_{v k}(x) q_{v k}(t) = \underline{\chi}_v^T(x) \underline{q}_v(t) \quad (2.37)$$

where $\chi(x)$ are the assumed mode shapes and $q(t)$ are the time-varying modal magnitudes.

We apply a Galerkin method modified by including forcing boundary terms in the equations in order to form the equations of motion. In the classic Galerkin method, assumed modes must satisfy both geometric and forcing boundary conditions. The modified Galerkin method relaxes these restrictions so assumed modes need only satisfy geometric boundary conditions. The resulting equations are equivalent to those formed by the Rayleigh-Ritz method. The modified Galerkin

equations are

$$\begin{aligned}
\int_0^R \chi_{\gamma i} D_\gamma(v, w, \gamma) dx + \chi_{\gamma i} Q \Big|_0^R &= 0 & i = 1, \dots, N_\gamma \\
\int_0^R \chi_{w j} D_w(v, w, \gamma) dx + \chi'_{w j} M_y \Big|_0^R + \chi_{w j} V_z \Big|_0^R &= 0 & j = 1, \dots, N_w \\
\int_0^R \chi_{v k} D_v(v, w, \gamma) dx + \chi'_{v k} M_z \Big|_0^R + \chi_{v k} V_y \Big|_0^R &= 0 & k = 1, \dots, N_v
\end{aligned}$$

D_γ , D_w and D_v are the left-hand sides of Eqs. 2.7–2.9, respectively, and the forcing functions are

$$\begin{aligned}
Q &= (GJ + Tk_A^2)\gamma' \\
M_y &= EI_z w'' - Te_A \gamma + \delta(x)k_{\text{root}} w'(x) \\
M_z &= EI_y v'' - Te_A \\
V_z &= -M'_y + Tw' - q_y \\
V_y &= -M'_z + Tv' - q_z
\end{aligned}$$

The term $\delta(x)k_{\text{root}} w'(x)$ represents a torsional root spring of stiffness k_{root} acting on the out-of-plane displacement mode. The Dirac delta distribution $\delta(x)$ indicates that this term exists only at $x = 0$ and is zero elsewhere. Note that this term will also be zero for a cantilever boundary condition, since $w'(0) \equiv 0$ for a cantilever beam.

Substituting the expressions for D_γ , D_w and D_v and using integration by parts to eliminate the boundary terms, the equations are

$$\int_0^R \left[\chi'_{\gamma i} (GJ + Tk_A^2)\gamma' - \chi_{\gamma i} (Te_A w'' - q_y v' + q_z w' + q_x) \right] dx = 0,$$

$$i = 1, \dots, N_\gamma \quad (2.38)$$

$$\int_0^R \left[\chi''_{wj} (EI_z w'' - Te_A \gamma) + \chi'_{wj} (T w' - q_y) - \chi_{wj} p_z \right] dx + \chi'_{wj}(0) \left(k_{\text{root}} w'(0) \right) = 0, \\ j = 1, \dots, N_w \quad (2.39)$$

$$\int_0^R \left[\chi''_{vk} (EI_y v'' - Te_A) + \chi'_{vk} (T v' - q_z) - \chi_{vk} p_y \right] dx = 0, \quad k = 1, \dots, N_v \quad (2.40)$$

The integrands must equal zero for every assumed mode for the equations to be true.

A matrix equation is formed for the modal magnitude vectors \underline{q}_v , \underline{q}_w and \underline{q}_γ by substituting the simplified force and moment equations Eqs. 2.24–2.29 and the modal summation equations Eqs. 2.35–2.37 into the modified Galerkin equations Eqs. 2.38–2.40 and setting the integrands equal to zero. Rearranging forcing terms

to the right-hand side, the full matrix equation is

$$\begin{aligned}
& \begin{bmatrix} \mathbf{A} & \mathbf{B} & \mathbf{0} \\ \mathbf{B}^T & \mathbf{C} & \mathbf{0} \\ \mathbf{0} & \mathbf{0} & \mathbf{D} \end{bmatrix} \begin{Bmatrix} \underline{\ddot{q}}_\gamma \\ \underline{\ddot{q}}_w \\ \underline{\ddot{q}}_v \end{Bmatrix} + 2\dot{\theta} \begin{bmatrix} \mathbf{0} & \mathbf{0} & \mathbf{E} \\ \mathbf{0} & \mathbf{0} & \mathbf{F} \\ -\mathbf{E}^T & -\mathbf{F}^T & \mathbf{0} \end{bmatrix} \begin{Bmatrix} \underline{\dot{q}}_\gamma \\ \underline{\dot{q}}_w \\ \underline{\dot{q}}_v \end{Bmatrix} + \begin{pmatrix} \begin{bmatrix} \mathcal{G} & \mathbf{0} & \mathbf{0} \\ \mathbf{0} & \mathcal{H} & \mathbf{0} \\ \mathbf{0} & \mathbf{0} & \mathcal{I} \end{bmatrix} \\ \\ \\ \end{pmatrix} \\
& - \ddot{\phi} \cos \theta \begin{bmatrix} \mathcal{J} - \mathcal{K} & -\mathcal{L} + \mathcal{M} & \mathbf{0} \\ (-\mathcal{L} + \mathcal{M})^T & -\mathcal{N} & \mathbf{0} \\ \mathbf{0} & \mathbf{0} & -\mathcal{P} \end{bmatrix} + \ddot{\theta} \begin{bmatrix} \mathbf{0} & \mathbf{0} & \mathbf{E} \\ \mathbf{0} & \mathbf{0} & \mathbf{F} \\ -\mathbf{E}^T & -\mathbf{F}^T & \mathbf{0} \end{bmatrix} \\
& + \phi^2 \begin{bmatrix} \mathcal{Q} & \mathcal{R} - \mathcal{S} & \mathbf{0} \\ (\mathcal{R} - \mathcal{S})^T & \mathcal{T} & \mathbf{0} \\ \mathbf{0} & \mathbf{0} & \mathcal{U} \end{bmatrix} - \phi^2 \sin^2 \theta \begin{bmatrix} \mathbf{A} & \mathbf{B} & \mathbf{0} \\ \mathbf{B}^T & \mathbf{C} & \mathbf{0} \\ \mathbf{0} & \mathbf{0} & \mathbf{0} \end{bmatrix} \\
& + \phi^2 \cos^2 \theta \begin{bmatrix} \mathbf{A} + \mathcal{V} & \mathbf{0} & \mathbf{0} \\ \mathbf{0} & \mathbf{0} & \mathbf{0} \\ \mathbf{0} & \mathbf{0} & \mathbf{D} \end{bmatrix} + \phi^2 \sin \theta \cos \theta \begin{bmatrix} \mathbf{0} & \mathbf{0} & \mathbf{E} \\ \mathbf{0} & \mathbf{0} & \mathbf{F} \\ \mathbf{E}^T & \mathbf{F}^T & \mathbf{0} \end{bmatrix} \\
& - \dot{\theta}^2 \begin{bmatrix} -\mathcal{V} & \mathbf{B} & \mathbf{0} \\ \mathbf{B}^T & \mathbf{C} & \mathbf{0} \\ \mathbf{0} & \mathbf{0} & \mathbf{D} \end{bmatrix} + 2\phi\dot{\theta} \sin \theta \begin{bmatrix} -\mathcal{K} & -\mathcal{L} + \mathcal{M} & \mathbf{0} \\ (-\mathcal{L} + \mathcal{M})^T & -\mathcal{N} & \mathbf{0} \\ \mathbf{0} & \mathbf{0} & -\mathcal{P} \end{bmatrix} \\
& + k_{\text{root}} \begin{pmatrix} \begin{bmatrix} \mathbf{0} & \mathbf{0} & \mathbf{0} \\ \mathbf{0} & \mathcal{W} & \mathbf{0} \\ \mathbf{0} & \mathbf{0} & \mathbf{0} \end{bmatrix} \\ \\ \\ \end{pmatrix} \begin{Bmatrix} \underline{q}_\gamma \\ \underline{q}_w \\ \underline{q}_v \end{Bmatrix} \\
& = \left\{ \begin{array}{l} \underline{E}_{\gamma\mathcal{A}} + \ddot{\phi} \sin \theta \underline{E}_{\gamma\mathcal{B}} - \ddot{\theta} \underline{E}_{\gamma\mathcal{C}} - \phi^2 \sin \theta \cos \theta \underline{E}_{\gamma\mathcal{C}} \\ \underline{E}_{w\mathcal{A}} + \ddot{\phi} \sin \theta \underline{E}_{w\mathcal{B}} - \ddot{\theta} \underline{E}_{w\mathcal{C}} - \phi^2 \sin \theta \cos \theta \underline{E}_{w\mathcal{C}} \\ \left(\begin{array}{l} \underline{E}_{v\mathcal{A}} - \ddot{\phi} \cos \theta (\underline{E}_{v\mathcal{B}} + \underline{E}_{v\mathcal{C}} - \underline{E}_{v\mathcal{D}}) + \phi^2 (\underline{E}_{v\mathcal{E}} - \underline{E}_{v\mathcal{F}}) \\ + \phi^2 \cos^2 \theta \underline{E}_{v\mathcal{G}} + \dot{\theta}^2 \underline{E}_{v\mathcal{G}} + 2\phi\dot{\theta} \sin \theta (\underline{E}_{v\mathcal{C}} - \underline{E}_{v\mathcal{D}}) \end{array} \right) \end{array} \right\} \quad (2.41)
\end{aligned}$$

The integral matrix entries are

$$\begin{aligned}
\mathcal{A}_{ij} = \mathcal{A}_{ji} &= \int_0^R m k_m^2 \chi_{\gamma i} \chi_{\gamma j} dx & \mathcal{B}_{ij} &= \int_0^R m e \chi_{\gamma i} \chi_{w j} dx \\
\mathcal{C}_{ij} = \mathcal{C}_{ji} &= \int_0^R m \chi_{w i} \chi_{w j} dx & \mathcal{D}_{ij} = \mathcal{D}_{ji} &= \int_0^R m \chi_{v i} \chi_{v j} dx \\
\mathcal{E}_{ij} &= \int_0^R m e \chi_{\gamma i} \chi_{v j} dx & \mathcal{F}_{ij} &= \int_0^R m \chi_{w i} \chi_{v j} dx \\
\mathcal{G}_{ij} = \mathcal{G}_{ji} &= \int_0^R G J \chi'_{\gamma i} \chi'_{\gamma j} dx & \mathcal{H}_{ij} = \mathcal{H}_{ji} &= \int_0^R E I_z \chi''_{w i} \chi''_{w j} dx \\
\mathcal{I}_{ij} = \mathcal{I}_{ji} &= \int_0^R E I_y \chi''_{v i} \chi''_{v j} dx & \mathcal{J}_{ij} = \mathcal{J}_{ji} &= \int_0^R m e x \chi_{\gamma i} \chi_{\gamma j} dx \\
\mathcal{K}_{ij} = \mathcal{K}_{ji} &= \int_0^R k_A^2 S_e \chi'_{\gamma i} \chi'_{\gamma j} dx & \mathcal{L}_{ij} &= \int_0^R m (e_{Oe} + k_m^2) \chi_{\gamma i} \chi'_{w j} dx \\
\mathcal{M}_{ij} &= \int_0^R e_A S_e \chi_{\gamma i} \chi''_{w j} dx & \mathcal{N}_{ij} = \mathcal{N}_{ji} &= \int_0^R S_e \chi'_{w i} \chi'_{w j} dx \\
\mathcal{P}_{ij} = \mathcal{P}_{ji} &= \int_0^R S_e \chi'_{v i} \chi'_{v j} dx & \mathcal{Q}_{ij} = \mathcal{Q}_{ji} &= \int_0^R k_A^2 S_x \chi'_{\gamma i} \chi'_{\gamma j} dx \\
\mathcal{R}_{ij} &= \int_0^R m e x \chi_{\gamma i} \chi'_{w j} dx & \mathcal{S}_{ij} &= \int_0^R e_A S_x \chi_{\gamma i} \chi''_{w j} dx \\
\mathcal{T}_{ij} = \mathcal{T}_{ji} &= \int_0^R S_x \chi'_{w i} \chi'_{w j} dx & \mathcal{U}_{ij} = \mathcal{U}_{ji} &= \int_0^R S_x \chi'_{v i} \chi'_{v j} dx \\
\mathcal{V}_{ij} = \mathcal{V}_{ji} &= \int_0^R m e_{Oe} \chi_{\gamma i} \chi_{\gamma j} dx & \mathcal{W}_{ij} = \mathcal{W}_{ji} &= \chi'_{w i}(0) \chi'_{w j}(0)
\end{aligned}$$

and the forcing vector entries are

$$\begin{aligned}
F_{\gamma\mathcal{A}i} &= \int_0^R M\chi_{\gamma i} dx & F_{\gamma\mathcal{B}i} &= \int_0^R mex\chi_{\gamma i} dx \\
F_{\gamma\mathcal{C}i} &= \int_0^R m(e_O e + k_m^2)\chi_{\gamma i} dx & F_{w\mathcal{A}i} &= \int_0^R L_z\chi_{wi} dx \\
F_{w\mathcal{B}i} &= \int_0^R mx\chi_{wi} dx & F_{w\mathcal{C}i} &= \int_0^R m(e_O + e)\chi_{wi} dx \\
F_{v\mathcal{A}i} &= \int_0^R L_y\chi_{vi} dx & F_{v\mathcal{B}i} &= \int_0^R mx\chi_{vi} dx \\
F_{v\mathcal{C}i} &= \int_0^R m(e_O e + k_m^2)\chi'_{vi} dx & F_{v\mathcal{D}i} &= \int_0^R e_A S_e \chi''_{vi} dx \\
F_{v\mathcal{E}i} &= \int_0^R e_A S_x \chi''_{vi} dx & F_{v\mathcal{F}i} &= \int_0^R mex\chi'_{vi} dx \\
F_{v\mathcal{G}i} &= \int_0^R m(e_O + e)\chi_{vi} dx & &
\end{aligned}$$

where the mass moments S_x and S_e are defined in Eqs. 2.32–2.33. Note that if the CG is coincident with the feathering axis—as we assumed for our estimated wing properties—then $e_O = -e$ and \mathcal{K} , \mathcal{M} , \mathcal{N} and \mathcal{P} are zero matrices.

2.6 Non-dimensional Analysis

The linear, time-periodic matrix equations of the flapping-wing deformations given in Eq. 2.41 are the basis of our time-periodic structural stability analysis. This study focuses on out-of-plane bending and torsion deformations only, so we consider a reduced system with no in-plane deformations, $v = 0$. (However, the following non-dimensionalization and stability analyses can be extended to include this additional deformation.) In order to develop a scalable stability analysis, the system of equations is non-dimensionalized with respect to characteristic parameters: the system's non-dimensional non-rotating natural frequencies and the stroke amplitudes of the prescribed rigid-beam rotations. We begin with the

reduced out-of-plane-bending/torsion equations:

$$\begin{aligned}
& \begin{bmatrix} \mathbf{A} & \mathbf{B} \\ \mathbf{B}^T & \mathbf{C} \end{bmatrix} \begin{Bmatrix} \ddot{q}_\gamma \\ \ddot{q}_w \end{Bmatrix} + \left(\begin{bmatrix} \mathbf{G} & \mathbf{0} \\ \mathbf{0} & \mathcal{H} \end{bmatrix} - \ddot{\phi} \cos \theta \begin{bmatrix} \mathcal{J} - \mathcal{K} & -\mathcal{L} + \mathcal{M} \\ (-\mathcal{L} + \mathcal{M})^T & -\mathcal{N} \end{bmatrix} \right. \\
& + \ddot{\phi}^2 \begin{bmatrix} \mathcal{Q} & \mathcal{R} - \mathcal{S} \\ (\mathcal{R} - \mathcal{S})^T & \mathcal{T} \end{bmatrix} - \ddot{\phi}^2 \sin^2 \theta \begin{bmatrix} \mathbf{A} & \mathbf{B} \\ \mathbf{B}^T & \mathbf{C} \end{bmatrix} \\
& + \ddot{\phi}^2 \cos^2 \theta \begin{bmatrix} \mathbf{A} + \mathcal{V} & \mathbf{0} \\ \mathbf{0} & \mathbf{0} \end{bmatrix} - \ddot{\theta}^2 \begin{bmatrix} -\mathcal{V} & \mathbf{B} \\ \mathbf{B}^T & \mathbf{C} \end{bmatrix} \\
& \left. + 2\ddot{\phi}\dot{\theta} \sin \theta \begin{bmatrix} -\mathcal{K} & -\mathcal{L} + \mathcal{M} \\ (-\mathcal{L} + \mathcal{M})^T & -\mathcal{N} \end{bmatrix} + k_{\text{root}} \begin{bmatrix} 0 & 0 \\ 0 & \mathcal{W} \end{bmatrix} \right) \begin{Bmatrix} q_\gamma \\ q_w \end{Bmatrix} \\
& = \begin{Bmatrix} \underline{E}_{\gamma A} \\ \underline{E}_{w A} \end{Bmatrix} + \ddot{\phi} \sin \theta \begin{Bmatrix} \underline{E}_{\gamma B} \\ \underline{E}_{w B} \end{Bmatrix} - \ddot{\theta} \begin{Bmatrix} \underline{E}_{\gamma C} \\ \underline{E}_{w C} \end{Bmatrix} - \ddot{\phi}^2 \sin \theta \cos \theta \begin{Bmatrix} \underline{E}_{\gamma C} \\ \underline{E}_{w C} \end{Bmatrix} \quad (2.42)
\end{aligned}$$

Non-dimensional length and time variables ξ and τ are introduced:

$$\xi = x/R \quad (2.43)$$

$$\tau = \omega t \quad (2.44)$$

so that $0 \leq \xi \leq 1$. Non-dimensional structural distributions, denoted by a hatted variable, are defined as follows. Length distributions (including bending mode shapes) are non-dimensionalized with respect to the beam radius R :

$$\hat{\chi}_{wi}(\xi) = \chi_{wi}(\xi R)/R$$

$$\hat{c}(\xi) = c(\xi R)/R, \text{ etc.} \dots$$

while the torsion mode shapes retain their value in radians

$$\hat{\chi}_{\gamma i}(\xi) = \chi_{\gamma i}(\xi R)$$

Mass and stiffness distributions are non-dimensionalized by the maximum distributional values, e.g. $m_0 = \max(m)$ and $EI_{z0} = \max(EI_z)$:

$$\hat{m}(\xi) = m(\xi R)/m_0$$

$$\widehat{EI}_z(\xi) = EI_z(\xi R)/EI_{z0}, \text{ etc. } \dots$$

All non-dimensional structural distributions are non-dimensional in both value and argument. The mass and stiffness distributions \hat{m} , \widehat{EI}_z and \widehat{GJ} have a minimum value of 0 and a maximum value of 1.

Flapping and feathering rotation distributions are non-dimensionalized by their respective amplitudes. For formality, the prescribed rotation distributions $\hat{\phi}$ and $\hat{\theta}$ are separately defined for zero stroke amplitudes.

$$\hat{\phi}(\tau) = \begin{cases} \phi(\frac{\tau}{\omega})/(\Phi/2) & \Phi \neq 0 \\ 0 & \Phi = 0 \end{cases} \quad (2.45)$$

$$\hat{\theta}(\tau) = \begin{cases} \theta(\frac{\tau}{\omega})/(\Theta/2) & \Theta \neq 0 \\ 0 & \Theta = 0 \end{cases} \quad (2.46)$$

The flapping rotation ϕ has a median value of 0, so $\hat{\phi}$ will range between $-1 \leq \hat{\phi} \leq 1$. The feathering rotation θ has a median value of $\pi/2$, so $\hat{\theta}$ will range between $-1 \leq \hat{\theta} - \pi/\Theta \leq 1$.

Finally, we non-dimensionalize the external force and moment using the

previously defined characteristic mass, length and time measures:

$$\hat{M}(\xi) = M(\xi R)/(m_0 R^3 \omega^2) \quad (2.47)$$

$$\hat{L}_z(\xi) = L_z(\xi R)/(m_0 R^2 \omega^2) \quad (2.48)$$

We now substitute the above non-dimensional definitions into the flapping equation of motion Eq. 2.42. We find that all of the matrices and vectors—with the exception of the stiffness matrices \mathcal{G} , \mathcal{H} and \mathcal{W} —are multiplied by the dimensional factor $m_0 R^3 \omega^2$. Dividing both sides by this factor gives us non-dimensional flap-torsion equations of motion of the form

$$\begin{aligned} & \begin{bmatrix} \hat{\mathcal{A}} & \hat{\mathcal{B}} \\ \hat{\mathcal{B}}^\top & \hat{\mathcal{C}} \end{bmatrix} \begin{Bmatrix} \hat{q}_\gamma \\ \hat{q}_w \end{Bmatrix} + \left(\begin{bmatrix} \frac{GJ_0}{m_0 R^4 \omega^2} \hat{\mathcal{G}} & \mathbf{0} \\ \mathbf{0} & \frac{EI_{z0}}{m_0 R^4 \omega^2} \hat{\mathcal{H}} \end{bmatrix} + \frac{k_{\text{root}}}{m_0 R^3 \omega^2} \begin{bmatrix} 0 & 0 \\ 0 & \hat{\mathcal{W}} \end{bmatrix} \right. \\ & - \frac{\Phi^{**}}{2} \hat{\phi} \cos \theta \begin{bmatrix} \hat{\mathcal{J}} - \hat{\mathcal{K}} & -\hat{\mathcal{L}} + \hat{\mathcal{M}} \\ (-\hat{\mathcal{L}} + \hat{\mathcal{M}})^\top & -\hat{\mathcal{N}} \end{bmatrix} + \frac{\Phi^2}{4} \hat{\phi}^2 \begin{bmatrix} \hat{\mathcal{Q}} & \hat{\mathcal{R}} - \hat{\mathcal{S}} \\ (\hat{\mathcal{R}} - \hat{\mathcal{S}})^\top & \hat{\mathcal{T}} \end{bmatrix} \\ & - \frac{\Phi^2}{4} \hat{\phi}^2 \sin^2 \theta \begin{bmatrix} \hat{\mathcal{A}} & \hat{\mathcal{B}} \\ \hat{\mathcal{B}}^\top & \hat{\mathcal{C}} \end{bmatrix} + \frac{\Phi^2}{4} \hat{\phi}^2 \cos^2 \theta \begin{bmatrix} \hat{\mathcal{A}} + \hat{\mathcal{V}} & \mathbf{0} \\ \mathbf{0} & \mathbf{0} \end{bmatrix} \\ & \left. - \frac{\Theta^2}{4} \hat{\theta}^2 \begin{bmatrix} -\hat{\mathcal{V}} & \hat{\mathcal{B}} \\ \hat{\mathcal{B}}^\top & \hat{\mathcal{C}} \end{bmatrix} + \frac{\Phi \Theta}{2} \hat{\phi} \hat{\theta} \sin \theta \begin{bmatrix} -\hat{\mathcal{K}} & -\hat{\mathcal{L}} + \hat{\mathcal{M}} \\ (-\hat{\mathcal{L}} + \hat{\mathcal{M}})^\top & -\hat{\mathcal{N}} \end{bmatrix} \right) \begin{Bmatrix} q_\gamma \\ q_w \end{Bmatrix} \\ & = \begin{Bmatrix} \hat{\mathcal{L}}_{\gamma A} \\ \hat{\mathcal{L}}_{w A} \end{Bmatrix} + \frac{\Phi}{2} \hat{\phi} \sin \theta \begin{Bmatrix} \hat{\mathcal{L}}_{\gamma B} \\ \hat{\mathcal{L}}_{w B} \end{Bmatrix} - \frac{\Theta}{2} \hat{\theta} \begin{Bmatrix} \hat{\mathcal{L}}_{\gamma C} \\ \hat{\mathcal{L}}_{w C} \end{Bmatrix} - \frac{\Phi^2}{4} \hat{\phi}^2 \sin \theta \cos \theta \begin{Bmatrix} \hat{\mathcal{L}}_{\gamma C} \\ \hat{\mathcal{L}}_{w C} \end{Bmatrix} \quad (2.49) \end{aligned}$$

The non-dimensional matrix entries are defined as

$$\begin{aligned}
\hat{\mathcal{A}}_{ij} = \hat{\mathcal{A}}_{ji} &= \int_0^1 \hat{m} \hat{k}_m^2 \hat{\chi}_{\gamma i} \hat{\chi}_{\gamma j} d\zeta & \hat{\mathcal{B}}_{ij} &= \int_0^1 \hat{m} \hat{e} \hat{\chi}_{\gamma i} \hat{\chi}_{w j} d\zeta \\
\hat{\mathcal{C}}_{ij} = \hat{\mathcal{C}}_{ji} &= \int_0^1 \hat{m} \hat{\chi}_{w i} \hat{\chi}_{w j} d\zeta & \hat{\mathcal{G}}_{ij} = \hat{\mathcal{G}}_{ji} &= \int_0^1 \widehat{GJ} \hat{\chi}'_{\gamma i} \hat{\chi}'_{\gamma j} d\zeta \\
\hat{\mathcal{H}}_{ij} = \hat{\mathcal{H}}_{ji} &= \int_0^1 \widehat{EI}_z \hat{\chi}''_{w i} \hat{\chi}''_{w j} d\zeta & \hat{\mathcal{J}}_{ij} = \hat{\mathcal{J}}_{ji} &= \int_0^1 \hat{m} \hat{e} \zeta \hat{\chi}_{\gamma i} \hat{\chi}_{\gamma j} d\zeta \\
\hat{\mathcal{K}}_{ij} = \hat{\mathcal{K}}_{ji} &= \int_0^1 \hat{k}_A^2 \hat{S}_e \hat{\chi}'_{\gamma i} \hat{\chi}'_{\gamma j} d\zeta & \hat{\mathcal{L}}_{ij} &= \int_0^1 \hat{m} (\hat{e}_O \hat{e} + \hat{k}_m^2) \hat{\chi}_{\gamma i} \hat{\chi}'_{w j} d\zeta \\
\hat{\mathcal{M}}_{ij} &= \int_0^1 \hat{e}_A \hat{S}_e \hat{\chi}_{\gamma i} \hat{\chi}'_{w j} d\zeta & \hat{\mathcal{N}}_{ij} = \hat{\mathcal{N}}_{ji} &= \int_0^1 \hat{S}_e \hat{\chi}'_{w i} \hat{\chi}'_{w j} d\zeta \\
\hat{\mathcal{Q}}_{ij} = \hat{\mathcal{Q}}_{ji} &= \int_0^1 \hat{k}_A^2 \hat{S}_x \hat{\chi}'_{\gamma i} \hat{\chi}'_{\gamma j} d\zeta & \hat{\mathcal{R}}_{ij} &= \int_0^1 \hat{m} \hat{e} \zeta \hat{\chi}_{\gamma i} \hat{\chi}'_{w j} d\zeta \\
\hat{\mathcal{S}}_{ij} &= \int_0^1 \hat{e}_A \hat{S}_x \hat{\chi}_{\gamma i} \hat{\chi}''_{w j} d\zeta & \hat{\mathcal{T}}_{ij} = \hat{\mathcal{T}}_{ji} &= \int_0^1 \hat{S}_x \hat{\chi}'_{w i} \hat{\chi}'_{w j} d\zeta \\
\hat{\mathcal{V}}_{ij} = \hat{\mathcal{V}}_{ji} &= \int_0^1 \hat{m} \hat{e}_O \hat{e} \hat{\chi}_{\gamma i} \hat{\chi}_{\gamma j} d\zeta & \hat{\mathcal{W}}_{ij} = \hat{\mathcal{W}}_{ji} &= \hat{\chi}'_{w i}(0) \hat{\chi}'_{w j}(0)
\end{aligned}$$

and the non-dimensional forcing vector entries are defined as

$$\begin{aligned}
\hat{F}_{\gamma Ai} &= \int_0^1 \hat{M} \hat{\chi}_{\gamma i} d\zeta & \hat{F}_{\gamma Bi} &= \int_0^1 \hat{m} \hat{e} \zeta \hat{\chi}_{\gamma i} d\zeta \\
\hat{F}_{\gamma Ci} &= \int_0^1 \hat{m} (\hat{e}_O \hat{e} + \hat{k}_m^2) \hat{\chi}_{\gamma i} d\zeta & \hat{F}_{w Ai} &= \int_0^1 \hat{L}_z \hat{\chi}_{w i} d\zeta \\
\hat{F}_{w Bi} &= \int_0^1 \hat{m} \zeta \hat{\chi}_{w i} d\zeta & \hat{F}_{w Ci} &= \int_0^1 \hat{m} (\hat{e}_O + \hat{e}) \hat{\chi}_{w i} d\zeta
\end{aligned}$$

where the non-dimensional mass moments are

$$\begin{aligned}
\hat{S}_x &= \int_{\zeta}^1 \hat{m} \zeta d\zeta \\
\hat{S}_e &= \int_{\zeta}^1 \hat{m} (\hat{e}_O + \hat{e}) d\zeta
\end{aligned}$$

2.6.1 Non-rotational Beam Natural Frequencies

The matrix equation of Eq. 2.49 can be fully non-dimensionalized by multiplying the equation by the inverted mass matrix,

$$\begin{bmatrix} \hat{\mathcal{A}} & \hat{\mathcal{B}} \\ \hat{\mathcal{B}}^T & \hat{\mathcal{C}} \end{bmatrix}^{-1}$$

Additional manipulation is necessary to explicitly parameterize the equation in terms of the system's non-rotating structural frequencies. The non-rotational stiffness of the beam is a function of the beam's bending stiffness EI_{z0} , torsion stiffness GJ_0 and root spring stiffness k_{root} . We wish to parameterize the equation of motion with respect to three uncoupled, non-rotational frequencies of the beam: ω_{cant} , the *first bending natural frequency* of the beam when attached with cantilever-free boundary conditions; ω_{tor} , the *first torsion natural frequency* of the beam when attached with clamped-free boundary conditions; and ω_{root} , the *rigid natural frequency* of the pinned beam due to the root spring.

The total non-rotational structural stiffness matrix is

$$\frac{1}{\omega^2} \begin{bmatrix} \frac{GJ_0}{m_0 R^4} \hat{\mathcal{G}} & \mathbf{0} \\ \mathbf{0} & \frac{EI_{z0}}{m_0 R^4} \hat{\mathcal{H}} + \frac{k_{\text{root}}}{m_0 R^3} \hat{\mathcal{W}} \end{bmatrix}$$

which can be non-dimensionalized by premultiplying by the inverted mass matrix:

$$\begin{aligned} & \frac{1}{\omega^2} \begin{bmatrix} \hat{\mathcal{A}} & \hat{\mathcal{B}} \\ \hat{\mathcal{B}}^T & \hat{\mathcal{C}} \end{bmatrix}^{-1} \begin{bmatrix} \frac{GJ_0}{m_0 R^4} \hat{\mathcal{G}} & \mathbf{0} \\ \mathbf{0} & \frac{EI_{z0}}{m_0 R^4} \hat{\mathcal{H}} + \frac{k_{\text{root}}}{m_0 R^3} \hat{\mathcal{W}} \end{bmatrix} \\ &= \frac{1}{\omega^2} \begin{bmatrix} \mathbf{I} & \hat{\mathcal{A}}^{-1} \hat{\mathcal{B}} \\ \hat{\mathcal{C}}^{-1} \hat{\mathcal{B}}^T & \mathbf{I} \end{bmatrix}^{-1} \begin{bmatrix} \frac{GJ_0}{m_0 R^4} \hat{\mathcal{A}}^{-1} \hat{\mathcal{G}} & \mathbf{0} \\ \mathbf{0} & \hat{\mathcal{C}}^{-1} \left(\frac{EI_{z0}}{m_0 R^4} \hat{\mathcal{H}} + \frac{k_{\text{root}}}{m_0 R^3} \hat{\mathcal{W}} \right) \end{bmatrix} \quad (2.50) \end{aligned}$$

2.6.1.1 Torsion Natural Frequency

We first consider the term $GJ_0/(m_0R^4)\widehat{\mathcal{A}}^{-1}\widehat{\mathcal{G}}$, which represents the torsional stiffness of the beam. The natural frequencies of the uncoupled torsion mode are given by

$$\omega_{\gamma i}^2 = (\lambda R)_{\gamma i}^2 \frac{GJ_0}{m_0R^4} \quad i = 1, \dots, N_\gamma \quad (2.51)$$

where $(\lambda R)_{\gamma i}$ is a characteristic parameter for the i th mode which is a function of the beam structure and boundary conditions. For the first torsion mode of a general assumed-modes system, this parameter is the minimum eigenvalue of $\widehat{\mathcal{A}}^{-1}\widehat{\mathcal{G}}$:

$$(\lambda R)_{\gamma 1}^2 = \text{eig}(\widehat{\mathcal{A}}^{-1}\widehat{\mathcal{G}})_{\min} \quad (2.52)$$

See appendix A.1 for demonstration of Eq. 2.52 for the case of a uniform beam.

We now define ω_{tor} as the first torsion frequency of our modeled beam subject to a clamped-free boundary condition. We do this in order to use ω_{tor} as a characteristic measure of torsion strain stiffness in comparing different beams—by selecting a particular, known boundary condition, we ensure that ω_{tor} will only be a function of the beam mass distribution \widehat{m} and torsional stiffness distribution \widehat{G} when comparing different beams. This additional definition is somewhat unnecessary for the torsion modes, where we shall only look at beams with clamped-free torsion boundaries. However it will be vitally important for the bending modes, where we will compare beams with different boundary conditions. We therefore include the definition of ω_{tor} here as a useful analogy:

$$\omega_{\text{tor}}^2 = (\lambda R)_{\text{tor}}^2 \frac{GJ_0}{m_0R^4} \quad (2.53)$$

where

$$(\lambda R)_{\text{tor}}^2 = \text{eig}(\widehat{\mathcal{A}}^{-1}\widehat{\mathcal{G}})_{\min} \Big|_{\text{clamped-free}} \quad (2.54)$$

It is then easy to see that

$$\frac{GJ_0}{m_0R^4} \widehat{\mathcal{A}}^{-1} \widehat{\mathcal{G}} = \frac{\omega_{\text{tor}}^2}{(\lambda R)_{\text{tor}}^2} \widehat{\mathcal{A}}^{-1} \widehat{\mathcal{G}} \quad (2.55)$$

2.6.1.2 Bending Natural Frequency

We now consider the term

$$\widehat{\mathcal{C}}^{-1} \left(\frac{EI_{z0}}{m_0R^4} \widehat{\mathcal{H}} + \frac{k_{\text{root}}}{m_0R^3} \widehat{\mathcal{W}} \right)$$

which represents the combined out-of-plane bending stiffness of the beam resulting from both the beam's strain stiffness and the root spring stiffness. We begin by removing the ratio EI_{z0}/m_0R^4 from inside the parentheses:

$$\frac{EI_{z0}}{m_0R^4} \widehat{\mathcal{C}}^{-1} \left(\widehat{\mathcal{H}} + \frac{k_{\text{root}}R}{EI_{z0}} \widehat{\mathcal{W}} \right) \quad (2.56)$$

By analogy to the previous analysis, we can write the first natural frequency of the beam in bending as

$$\omega_1^2 = \text{eig} \left[\widehat{\mathcal{C}}^{-1} \left(\widehat{\mathcal{H}} + \frac{k_{\text{root}}R}{EI_{z0}} \widehat{\mathcal{W}} \right) \right]_{\min} \frac{EI_{z0}}{m_0R^4} \quad (2.57)$$

The natural frequency ω_1 is due to the combined effects of strain stiffness and root spring stiffness. It is *not* equivalent to ω_{cant} or ω_{root} except in special cases presented below:

CANTILEVER BEAM. Consider a root spring k_{root} that is infinitely stiff so that there is no change in slope at the root: $w'(0) = 0$. In this case, the system reduces to a cantilever beam. Since $\widehat{\mathcal{W}}$ is solely a function of the root slope, $\widehat{\mathcal{W}} = \mathbf{0}$ and

the natural frequencies are

$$\omega_1^2 = \text{eig}(\widehat{\mathcal{C}}^{-1}\widehat{\mathcal{H}})_{\min} \frac{EI_{z0}}{m_0R^4} \Big|_{\text{cantilever-free}} \quad (2.58)$$

where we explicitly note that the system is being evaluated with cantilever-free boundary conditions. The i th natural frequency of a cantilever beam is similarly given as

$$\omega_{wi}^2 = (\lambda R)_{wi}^4 \frac{EI_{z0}}{m_0R^4} \quad i = 1, \dots, N_w \quad (2.59)$$

Thus, the minimum eigenvalue of the right-hand term of Eq. 2.58 corresponds to the first natural frequency of the cantilever-free system, $\omega_{w1} = \omega_{\text{cant}}$. (See appendix A.2 for a demonstration that $\text{eig}(\widehat{\mathcal{C}}^{-1}\widehat{\mathcal{H}})_{\min} = (\lambda R)_{w1}^4$ with a uniform beam.) We therefore define ω_{cant} as

$$\omega_{\text{cant}}^2 = (\lambda R)_{\text{cant}}^4 \frac{EI_{z0}}{m_0R^4} \quad (2.60)$$

where

$$(\lambda R)_{\text{cant}}^4 = \text{eig}(\widehat{\mathcal{C}}^{-1}\widehat{\mathcal{H}})_{\min} \Big|_{\text{cantilever-free}} \quad (2.61)$$

We see that the system's first natural frequency is the first natural frequency of a cantilever beam

$$\omega_1^2 = \omega_{\text{cant}}^2 \quad (2.62)$$

as expected. Since there is no root spring stiffness contribution, ω_{cant} characterizes the bending strain stiffness of the beam.

RIGID BEAM WITH SPRING. Consider a pinned beam with infinite bending stiffness EI_{z0} so that the beam is rigid with no curvature, $w''(x) = 0$. In this case, the system reduces to a rigid beam with a root spring. Since $\widehat{\mathcal{H}}$ is a function of beam

curvature w'' , $\widehat{\mathcal{H}} = \mathbf{0}$ and the natural frequency is

$$\begin{aligned}\omega_1^2 &= \text{eig}\left(\frac{k_{\text{root}}R}{EI_{z0}}\widehat{\mathcal{C}}^{-1}\widehat{\mathcal{W}}\right)_{\min} \frac{EI_{z0}}{m_0R^4} \\ &= \text{eig}(\widehat{\mathcal{C}}^{-1}\widehat{\mathcal{W}})_{\min} \frac{k_{\text{root}}}{m_0R^3} \Big|_{\text{rigid, pinned-free}}\end{aligned}\quad (2.63)$$

The natural frequency of a pinned rigid beam with a spring is

$$\begin{aligned}\omega_{\text{root}}^2 &= \frac{k_{\text{root}}}{I_b} \\ &= \frac{k_{\text{root}}}{\widehat{I}_b m_0 R^3}\end{aligned}\quad (2.64)$$

where \widehat{I}_b , the non-dimensional mass moment of inertia of the rigid beam about the pin, is equal to

$$\widehat{I}_b = \int_0^1 \widehat{m} \zeta^2 d\zeta \quad (2.65)$$

Once again, the minimum eigenvalue is $\text{eig}(\widehat{\mathcal{C}}^{-1}\widehat{\mathcal{W}})_{\min} = 1/\widehat{I}_b$. See appendix A.3 for a demonstration with a uniform beam. So, the system's natural frequency is the natural frequency of a pinned rigid beam with a root spring

$$\omega_1^2 = \omega_{\text{root}}^2 \quad (2.66)$$

as expected. Since there is no strain stiffness contribution, ω_{root} characterizes the root spring stiffness.

Dividing Eq. 2.64 by Eq. 2.60 gives a ratio of the natural frequency of a rigid beam with a root spring over the natural frequency of a cantilevered beam

$$\left(\frac{\omega_{\text{root}}}{\omega_{\text{cant}}}\right)^2 = \frac{1}{(\lambda R)_{\text{cant}}^4 \widehat{I}_b} \frac{k_{\text{root}}R}{EI_{z0}} \quad (2.67)$$

The natural frequency of the beam in bending from Eq. 2.68 can now be rewritten

as

$$\omega_1^2 = \text{eig} \left[\widehat{\mathcal{C}}^{-1} \left(\widehat{\mathcal{H}} + \left(\frac{\omega_{\text{root}}}{\omega_{\text{cant}}} \right)^2 (\lambda R)_{\text{cant}}^4 \hat{I}_b \widehat{\mathcal{W}} \right) \right]_{\min} \frac{EI_{z0}}{m_0 R^4} \quad (2.68)$$

The non-dimensional expression $(\omega_{\text{root}}/\omega_{\text{cant}})^2$ characterizes the ratio of the root spring stiffness to the bending strain stiffness of the system. Note that the term $(\lambda R)_{\text{cant}}^4$ is approximated as $\text{eig}(\widehat{\mathcal{C}}^{-1}\widehat{\mathcal{H}})_{\min}$ where $\widehat{\mathcal{C}}$ and $\widehat{\mathcal{H}}$ are assembled using *cantilever-free* modes, even if the modeled system is not itself cantilever-free. In other words, the matrices $\widehat{\mathcal{C}}$ and $\widehat{\mathcal{H}}$ used to calculate $(\lambda R)_{\text{cant}}^4$ are *different* than those used in the matrix equation itself *unless we are modeling a cantilever-free system*.

By analogy to previous derivations, we can define a characteristic parameter $(\lambda R)_1$ that gives the frequency of the first root-spring-free bending mode as

$$(\lambda R)_1^4 = \text{eig} \left[\widehat{\mathcal{C}}^{-1} \left(\widehat{\mathcal{H}} + \left(\frac{\omega_{\text{root}}}{\omega_{\text{cant}}} \right)^2 (\lambda R)_{\text{cant}}^4 \hat{I}_b \widehat{\mathcal{W}} \right) \right]_{\min} \quad (2.69)$$

so that

$$\omega_1^2 = (\lambda R)_1^4 \frac{EI_{z0}}{m_0 R^4} \quad (2.70)$$

(c.f. Eq. 2.60). Tables 2.1 and 2.2 summarize the various natural frequency definitions we have developed. Table 2.1 gives the nomenclature for the various frequencies, the definitions in terms of characteristic λR s and beam properties, and

Table 2.1: Summary of beam frequencies.

Name	Symbol	Definition	Mode Shape
Torsion frequency	ω_{tor}	$\omega_{\text{tor}}^2 = (\lambda R)_{\text{tor}}^2 \frac{GJ_0}{m_0 R^2}$	
Cantilever frequency	ω_{cant}	$\omega_{\text{cant}}^2 = (\lambda R)_{\text{cant}}^4 \frac{EI_{z0}}{m_0 R^4}$	
Root spring frequency	ω_{root}	$\omega_{\text{root}}^2 = \frac{k_{\text{root}}}{\hat{I}_b m_0 R^3}$	
First natural frequency	ω_1	$\omega_1^2 = (\lambda R)_1^4 \frac{EI_{z0}}{m_0 R^4}$	

Table 2.2: Summary of characteristic λR s.

Symbol	Definition	Modal B.C. in matrices
$(\lambda R)_{\text{tor}}$	$(\lambda R)_{\text{tor}}^2 = \text{eig}(\widehat{\mathcal{A}}^{-1}\widehat{\mathcal{G}})_{\text{min}}$	Clamped-free
$(\lambda R)_{\text{cant}}$	$(\lambda R)_{\text{cant}}^4 = \text{eig}(\widehat{\mathcal{C}}^{-1}\widehat{\mathcal{H}})_{\text{min}}$	Cantilever-free
$(\lambda R)_1$	$(\lambda R)_1^4 = \text{eig}\left[\widehat{\mathcal{C}}^{-1}\left(\widehat{\mathcal{H}} + \left(\frac{\omega_{\text{root}}}{\omega_{\text{cant}}}\right)^2 (\lambda R)_{\text{cant}}^4 \hat{I}_b \widehat{\mathcal{W}}\right)\right]_{\text{min}}$	Root-spring-free

depictions of the modes and boundary conditions associated with each frequency. Table 2.2 gives the nomenclature for the characteristic λR s, their definitions as minimum eigenvalues of assumed-modes matrices and the boundary conditions of the assumed modes used for calculating those matrices.

As a final note, the bending modes for the assumed-modes model must be calculated so that they are valid for the root-spring boundary conditions. Appendix B presents the derivation of the mode shapes for an arbitrary root spring, where the relative stiffness of the root spring is measured by the ratio $\omega_{\text{root}}/\omega_{\text{cant}}$.

2.6.1.3 Total System Stiffness

Returning to Eq. 2.50, the matrix on the right-hand side can be written as

$$\begin{aligned}
 & \begin{bmatrix} \frac{GJ_0}{m_0R^2} \widehat{\mathcal{A}}^{-1} \widehat{\mathcal{G}} & \mathbf{0} \\ \mathbf{0} & \widehat{\mathcal{C}}^{-1} \left(\frac{EI_{z0}}{m_0R^4} \widehat{\mathcal{H}} + \frac{k_{\text{root}}}{m_0R^3} \widehat{\mathcal{W}} \right) \end{bmatrix} \\
 & = \begin{bmatrix} \frac{\omega_{\text{tor}}^2}{(\lambda R)_{\text{tor}}^2} \widehat{\mathcal{A}}^{-1} \widehat{\mathcal{G}} & \mathbf{0} \\ \mathbf{0} & \frac{\omega_1^2}{(\lambda R)_1^4} \widehat{\mathcal{C}}^{-1} \left(\widehat{\mathcal{H}} + \left(\frac{\omega_{\text{root}}}{\omega_{\text{cant}}} \right)^2 (\lambda R)_{\text{cant}}^4 \hat{I}_b \widehat{\mathcal{W}} \right) \end{bmatrix} \quad (2.71)
 \end{aligned}$$

We continue by writing the torsion frequency ω_{tor} as a function of the first cantilever frequency ω_{cant}

$$\omega_{\text{tor}}^2 = \left(\frac{\omega_{\text{tor}}}{\omega_{\text{cant}}} \right)^2 \omega_{\text{cant}}^2 \quad (2.72)$$

and similarly, the first bending frequency ω_1 as a function of the first cantilever frequency

$$\begin{aligned}\omega_1^2 &= \left(\frac{\omega_1}{\omega_{\text{cant}}} \right)^2 \omega_{\text{cant}}^2 \\ &= \frac{(\lambda R)_1^4}{(\lambda R)_{\text{cant}}^4} \omega_{\text{cant}}^2\end{aligned}\quad (2.73)$$

This results in a final form:

$$\begin{aligned}& \begin{bmatrix} \frac{GJ_0}{m_0 R^2} \widehat{\mathcal{A}}^{-1} \widehat{\mathcal{G}} & \mathbf{0} \\ \mathbf{0} & \widehat{\mathcal{C}}^{-1} \left(\frac{EI_{z0}}{m_0 R^4} \widehat{\mathcal{H}} + \frac{k_{\text{root}}}{m_0 R^3} \widehat{\mathcal{W}} \right) \end{bmatrix} \\ &= \omega_{\text{cant}}^2 \begin{bmatrix} \left(\frac{\omega_{\text{tor}}}{\omega_{\text{cant}}} \right)^2 \frac{1}{(\lambda R)_{\text{tor}}^2} \widehat{\mathcal{A}}^{-1} \widehat{\mathcal{G}} & \mathbf{0} \\ \mathbf{0} & \frac{1}{(\lambda R)_{\text{cant}}^4} \widehat{\mathcal{C}}^{-1} \left(\widehat{\mathcal{H}} + \left(\frac{\omega_{\text{root}}}{\omega_{\text{cant}}} \right)^2 (\lambda R)_{\text{cant}}^4 \widehat{I}_b \widehat{\mathcal{W}} \right) \end{bmatrix}\end{aligned}\quad (2.74)$$

The result of the manipulations is a matrix explicitly written so that it is proportional to the square of the first natural frequency of the beam with cantilever-free boundary conditions, ω_{cant} . The relative contribution of the torsion strain stiffness on the total system is a function of the ratio $\omega_{\text{tor}}/\omega_{\text{cant}}$. Likewise, the relative contribution of the root spring stiffness on the total system is a function of the ratio $\omega_{\text{root}}/\omega_{\text{cant}}$. Moreover, these frequency ratios are independent, so that the relative root spring stiffness can be varied while holding the relative torsion strain stiffness constant or vice versa. All the other terms in the above matrix are functions of the non-dimensional property distributions of the beam: \widehat{m} , \widehat{EI}_z , \widehat{GJ} , etc. The preceding manipulations provide us convenient, non-dimensional control over the contributions of various stiffnesses in the system and will give us a powerful tool for analyzing the stability effects of these stiffnesses.

Multiplying Eq. 2.49 by the inverse mass matrix and using the relationships

of Eqs. 2.50 and 2.74, the final non-dimensional bending-torsion equation is:

$$\begin{aligned}
& \begin{Bmatrix} \tilde{q}_\gamma^{**} \\ \tilde{q}_w^{**} \end{Bmatrix} + \left[\left(\frac{\omega_{\text{cant}}}{\omega} \right)^2 K_\omega - \Phi \hat{\phi}^{**} \cos \theta K_{\phi c}^{**} + \Phi^2 \hat{\phi}^{*2} K_{\phi^2}^{**} - \Phi^2 \hat{\phi}^{*2} \sin^2 \theta K_{\phi^2 s^2}^{**} \right. \\
& \left. + \Phi^2 \hat{\phi}^{*2} \cos^2 \theta K_{\phi^2 c^2}^{**} - \Theta^2 \hat{\theta}^{*2} K_{\theta^2}^{**} + \Phi \Theta \hat{\phi}^{*} \hat{\theta}^{*} \sin \theta K_{\phi \theta s}^{**} \right] \begin{Bmatrix} \tilde{q}_\gamma \\ \tilde{q}_w \end{Bmatrix} \\
& = \underline{F}_{ext} + \Phi \hat{\phi}^{**} \sin \theta \underline{F}_{\phi s}^{**} - \Theta \hat{\theta}^{**} \underline{F}_{\theta}^{**} - \Phi^2 \hat{\phi}^{*2} \sin \theta \cos \theta \underline{F}_{\phi^2 s c}^{**} \quad (2.75)
\end{aligned}$$

The stiffness matrices in Eq. 2.75 are

$$\begin{aligned}
\mathbf{K}_\omega &= \begin{bmatrix} \mathbf{I} & \hat{\mathbf{A}}^{-1}\hat{\mathbf{B}} \\ \hat{\mathbf{C}}^{-1}\hat{\mathbf{B}}^\top & \mathbf{I} \end{bmatrix}^{-1} \times \\
&\quad \begin{bmatrix} \frac{1}{(\lambda R)_{\text{tor}}^2} \left(\frac{\omega_{\text{tor}}}{\omega_{\text{cant}}} \right)^2 \hat{\mathbf{A}}^{-1}\hat{\mathbf{G}} & \mathbf{0} \\ \mathbf{0} & \frac{1}{(\lambda R)_{\text{cant}}^4} \hat{\mathbf{C}}^{-1} \left(\hat{\mathcal{H}} + \left(\frac{\omega_{\text{root}}}{\omega_{\text{cant}}} \right)^2 (\lambda R)_{\text{cant}}^4 \hat{I}_b \hat{\mathcal{W}} \right) \end{bmatrix} \\
\mathbf{K}_{\phi^c}^{**} &= \frac{1}{2} \begin{bmatrix} \hat{\mathbf{A}} & \hat{\mathbf{B}} \\ \hat{\mathbf{B}}^\top & \hat{\mathbf{C}} \end{bmatrix}^{-1} \begin{bmatrix} \hat{\mathcal{J}} - \hat{\mathcal{K}} & -\hat{\mathcal{L}} + \hat{\mathcal{M}} \\ (-\hat{\mathcal{L}} + \hat{\mathcal{M}})^\top & -\hat{\mathcal{N}} \end{bmatrix} \\
\mathbf{K}_{\phi^2}^{*2} &= \frac{1}{4} \begin{bmatrix} \hat{\mathbf{A}} & \hat{\mathbf{B}} \\ \hat{\mathbf{B}}^\top & \hat{\mathbf{C}} \end{bmatrix}^{-1} \begin{bmatrix} \hat{\mathcal{Q}} & \hat{\mathcal{R}} - \hat{\mathcal{S}} \\ (\hat{\mathcal{R}} - \hat{\mathcal{S}})^\top & \hat{\mathcal{T}} \end{bmatrix} \\
\mathbf{K}_{\phi^2 s^2}^{*2} &= \frac{1}{4} \mathbf{I} \\
\mathbf{K}_{\phi^2 c^2}^{*2} &= \frac{1}{4} \begin{bmatrix} \hat{\mathbf{A}} & \hat{\mathbf{B}} \\ \hat{\mathbf{B}}^\top & \hat{\mathbf{C}} \end{bmatrix}^{-1} \begin{bmatrix} \hat{\mathcal{A}} + \hat{\mathcal{V}} & \mathbf{0} \\ \mathbf{0} & \mathbf{0} \end{bmatrix} \\
\mathbf{K}_{\theta^2}^{*2} &= \frac{1}{4} \begin{bmatrix} \hat{\mathbf{A}} & \hat{\mathbf{B}} \\ \hat{\mathbf{B}}^\top & \hat{\mathbf{C}} \end{bmatrix}^{-1} \begin{bmatrix} -\hat{\mathcal{V}} & \hat{\mathcal{B}} \\ \hat{\mathcal{B}}^\top & \hat{\mathcal{C}} \end{bmatrix} \\
\mathbf{K}_{\phi\theta s}^{**} &= \frac{1}{2} \begin{bmatrix} \hat{\mathbf{A}} & \hat{\mathbf{B}} \\ \hat{\mathbf{B}}^\top & \hat{\mathbf{C}} \end{bmatrix}^{-1} \begin{bmatrix} -\hat{\mathcal{K}} & -\hat{\mathcal{L}} + \hat{\mathcal{M}} \\ (-\hat{\mathcal{L}} + \hat{\mathcal{M}})^\top & -\hat{\mathcal{N}} \end{bmatrix}
\end{aligned}$$

and the forcing vectors are

$$\begin{aligned}\tilde{F}_{ext} &= \begin{bmatrix} \hat{\mathcal{A}} & \hat{\mathcal{B}} \\ \hat{\mathcal{B}}^T & \hat{\mathcal{C}} \end{bmatrix}^{-1} \begin{Bmatrix} \hat{E}_{\gamma A} \\ \hat{E}_{wA} \end{Bmatrix} \\ \tilde{F}_{\phi^s}^{**} &= \frac{1}{2} \begin{bmatrix} \hat{\mathcal{A}} & \hat{\mathcal{B}} \\ \hat{\mathcal{B}}^T & \hat{\mathcal{C}} \end{bmatrix}^{-1} \begin{Bmatrix} \hat{E}_{\gamma B} \\ \hat{E}_{wB} \end{Bmatrix} \\ \tilde{F}_{\theta}^{**} &= \frac{1}{2} \begin{bmatrix} \hat{\mathcal{A}} & \hat{\mathcal{B}} \\ \hat{\mathcal{B}}^T & \hat{\mathcal{C}} \end{bmatrix}^{-1} \begin{Bmatrix} \hat{E}_{\gamma C} \\ \hat{E}_{wC} \end{Bmatrix} \\ \tilde{F}_{\phi^2 sc}^* &= \frac{1}{4} \begin{bmatrix} \hat{\mathcal{A}} & \hat{\mathcal{B}} \\ \hat{\mathcal{B}}^T & \hat{\mathcal{C}} \end{bmatrix}^{-1} \begin{Bmatrix} \hat{E}_{\gamma C} \\ \hat{E}_{wC} \end{Bmatrix}\end{aligned}$$

To aid numerical calculation of these matrices, note that the matrix $K_{\theta^2}^*$ and the forcing vector $\tilde{F}_{\phi^2 sc}^*$ can be calculated as

$$\begin{aligned}K_{\theta^2}^* &= K_{\phi^2 s^2}^* - K_{\phi^2 c^2}^* \\ \tilde{F}_{\phi^2 sc}^* &= \tilde{F}_{\theta}^{**}/2\end{aligned}$$

2.6.2 Comments on Non-dimensional Analysis

We now examine the non-dimensional system equation Eq. 2.75. The stiffnesses of the system can be categorized as constant, non-rotational stiffnesses or as time-periodic rotational stiffnesses. The former are expressed by the leading stiffness term $(\omega_{\text{cant}}/\omega)^2 K_{\omega}$, the latter by the remaining stiffness terms. The non-rotational stiffnesses are inherent to the structure of the wing system, arising either from the strain stiffness of the wing or from stiffness within the boundary condition. In contrast, the rotational stiffnesses arise from inertial loadings as the wing rotates. They are time-periodic in our flapping-wing system because the

flapping motions are time-periodic. We will now define the normalized cantilever frequency $\omega_{\text{cant}}/\omega$ and the flapping and feathering strokes Φ and Θ as characteristic non-dimensional parameters of the system's stiffness, respectively expressing the magnitude of the constant and time-periodic stiffnesses of the system.

2.6.2.1 Normalized Cantilever Frequency and Non-rotational Stiffness

We begin by writing out in full the expression of the non-rotational stiffness term:

$$\left(\frac{\omega_{\text{cant}}}{\omega}\right)^2 \mathbf{K}_\omega = \left(\frac{\omega_{\text{cant}}}{\omega}\right)^2 \begin{bmatrix} \mathbf{I} & \widehat{\mathbf{A}}^{-1} \widehat{\mathbf{B}} \\ \widehat{\mathbf{C}}^{-1} \widehat{\mathbf{B}}^T & \mathbf{I} \end{bmatrix}^{-1} \times \begin{bmatrix} \frac{1}{(\lambda R)_{\text{tor}}^2} \left(\frac{\omega_{\text{tor}}}{\omega_{\text{cant}}}\right)^2 \widehat{\mathbf{A}}^{-1} \widehat{\mathbf{G}} & \mathbf{0} \\ \mathbf{0} & \frac{1}{(\lambda R)_{\text{cant}}^4} \widehat{\mathbf{C}}^{-1} \left(\widehat{\mathbf{H}} + \left(\frac{\omega_{\text{root}}}{\omega_{\text{cant}}}\right)^2 (\lambda R)_{\text{cant}}^4 \hat{I}_b \widehat{\mathbf{W}} \right) \end{bmatrix}$$

This term represents the non-rotational stiffness of the wing structure subject to forcing at a prescribed frequency ω and its magnitude is proportional to the square of our characteristic parameter, the normalized cantilever frequency $\omega_{\text{cant}}/\omega$; such a relationship is expected from the basic theory of structural dynamics [167]. A number of considerations influenced the choice of the cantilever frequency as the characteristic parameter. First, with regards to the first bending frequency of the root-spring-free beam ω_1 , we note that ω_1 will vary depending on the the root spring stiffness, meaning that two structurally identical beams will have different ω_1 if the root spring stiffnesses are different. Characterizing with respect to ω_1 would therefore obscure the effect of the root spring on stability. The first cantilever frequency ω_{cant} represents the system at a convenient ideal case* so characterizing with respect to ω_{cant} allows us to compare with a known idealized system. Further-

*I.e., one in which the root spring is infinitely stiff

more, many previous analyses of flapping wing structures have assumed that the wings have a cantilever boundary condition, so that characterizing with respect to ω_{cant} is convenient for examining these studies. Second, with regards to the first torsion frequency of the beam ω_{tor} , we simply note that the torsion frequencies of wing will be higher than the bending frequencies and thus chose the lower of these frequencies

Recall that the frequency ω_{cant} is a measure of the bending strain stiffness of the beam. The torsion strain stiffness is measured by ω_{tor} , so the relative torsion strain stiffness is set through the frequency ratio $\omega_{\text{tor}}/\omega_{\text{cant}}$. Similarly, the root spring stiffness is measured by ω_{root} and the relative root spring stiffness is set through the frequency ratio $\omega_{\text{root}}/\omega_{\text{cant}}$. The premultiplying matrix

$$\begin{bmatrix} I & \hat{\mathcal{A}}^{-1}\hat{\mathcal{B}} \\ \hat{\mathcal{C}}^{-1}\hat{\mathcal{B}}^T & I \end{bmatrix}^{-1}$$

expresses bending/torsion modal coupling through the beam's CG offset.

2.6.2.2 *Flapping and Feathering Strokes and Time-Periodic Stiffness*

The remaining stiffness terms are time-periodic inertial stiffnesses arising from the prescribed motion of the flapping wing. The magnitudes of these stiffnesses are functions of the flapping and feathering stroke amplitudes Φ and Θ , while the time-variations are due to the rotational distributions $\hat{\phi}$ and $\hat{\theta}$. (The trigonometric functions of the dimensional feathering angle, $\sin \theta$ and $\cos \theta$, are functions of both Θ and $\hat{\theta}$ and thus affect both the magnitude and time-variation of the stiffnesses). This is a notable finding: the relative magnitudes of time-periodic inertial stiffnesses are dependent on the total *angle* of rotational motion but are independent of the *frequency* at which the motion occurs.

2.6.2.3 Comparison of Biological Fliers and Engineering Studies

By using our defined non-dimensional characteristic parameters, we can present scalable analyses for flapping systems. Flapping systems with identical structural and rotational non-dimensional distributions will have matched non-rotational strain stiffness if they have equal normalized cantilever frequencies $\omega_{\text{cant}}/\omega$. Likewise, these systems will have matched inertial (i.e., periodic) stiffnesses if they have equal flapping and feathering amplitudes Φ and Θ .

We can apply this knowledge to evaluate the effectiveness of current flapping-wing mechanisms in mimicking biological fliers. Table 2.3 compares biological fliers in hover, MAVs and flapping test-stands for a simplified case of no feathering rotation $\Theta = 0$ and no torsional deformations $\gamma = 0$ (a full analysis of this case appears in the following section). Furthermore, we assume that any measured structural natural frequencies in the literature is equivalent to the cantilevered frequency ω_{cant} : a good assumption, since almost all computational and experimental studies have used cantilever boundary conditions.

The flapping strokes of biological fliers sweep out large arcs of 110 to 190°, with greater flapping strokes associated with greater loadings [71]. Unfortunately, there are no experimental data of the normalized cantilever frequency $\omega_{\text{cant}}/\omega$

Table 2.3: Non-dimensional flapping parameters of biological fliers and MAVs in hover.

	Φ [deg]	$\omega_{\text{cant}}/\omega$
Insects [66]	110–180	—
<i>Manduca sexta</i> [103, 168]	115–120	1.15–1.55
Hummingbirds [71]	120–190	—
Mentor MAV (Zdunich et al.) [136]	76	—
Robofly (Dickenson et al.) [87, 169]	60–180	$\gg 1$
U. Maryland testbed (Singh & Chopra) [98]	80	.8–5.2
Cranfield U. testbed (Żbikowski et al.) [147]	90	—
NASA Langley testbed (Raney & Slominski) [146]	45	~ 1

for biological fliers available. The sole datum in literature is derived from a FEM analysis of a *Manduca sexta* hawkmoth wing, indicating that the flapping frequency is slightly below the first non-rotating flap frequency. We can understand why biological fliers would tend towards large flapping strokes and relatively low normalized bending frequencies by examining Ellington's expression for the quasi-steady portion of lift generated by normal hovering flight [78, Eqn. 11]. Among other factors, this equation shows that the mean lift is a function of flapping stroke, wing radius, wing area S and mean flapping velocity (i.e., ω):

$$(L_{q-s})_{mean} \propto \Phi^2 R^2 S \omega^2$$

Larger flapping strokes obviously produce greater lift. Likewise, higher flapping frequencies ω also produce greater lift, so lowering ω_{cant}/ω is important. A second consideration also plays a role in lowering ω_{cant}/ω : for a driving mechanism of fixed power, increasing the flapping frequency of the wing requires decreasing the wing's inertia and mass (Singh experienced this effect with his flapping test stand, where heavy wings could not be tested at high flapping frequencies [156, pp. 66–67]). For a given material, m_0 can be lowered by scaling the wing's cross-section; m_0 will decrease proportionally with ct , where c is the chord and t is the wing thickness. However, the bending stiffness EI_{z0} will decrease proportionally with ct^3 ; furthermore, a significant decrease of chord will adversely affect lift via smaller wing area S . Thus, lower wing weight is best achieved through decreased thickness, which lowers EI_{z0} more than m_0 . Recalling that

$$\omega_{cant}^2 \propto \frac{EI_{z0}}{m_0 R^4}$$

and noting that decreasing wing radius R will adversely affect lift, we see that lowering wing weight will lower ω_{cant} —more reason for operating at low ratios of

$\omega_{\text{cant}}/\omega$. Ellington's expression for the rotational portion of lift [78, Eqn. 17] gives the proportionality

$$(L_{\text{rot}})_{\text{mean}} \propto \frac{\Phi R^2 S \omega^2}{AR} \propto \Phi S^2 \omega^2$$

for which the above considerations also hold.

Only the Reynolds-scaled Robofly testbed is capable of matching the flapping stroke Φ , and therefore the inertial stiffnesses, of biological fliers. As with biological fliers, there is little data available for $\omega_{\text{cant}}/\omega$ of man-made engineering apparatuses. The only experimental data from which $\omega_{\text{cant}}/\omega$ can be quantitatively computed are from the University of Maryland flapping testbed—the most flexible wing tested had values similar to insects, but most experiments were performed at $\omega_{\text{cant}}/\omega$ of two to five. Composite wings on the NASA testbed were operated near resonance of the rotational natural frequency by tuning the flapping frequency via feedback from a wing-mounted strain sensor. The Robofly testbed is typically outfitted with a functionally rigid wing, so $\omega_{\text{cant}}/\omega$ is very large.

Taken together, and even accounting for our considerable simplifications, it is clear that no man-made MAV or test-stand has yet produced data that is structurally similar to biological systems. No current open-air flapping mechanism can achieve biological fliers' flapping stroke Φ (Robofly operates in mineral oil). Development of mechanisms capable of $120^\circ \leq \Phi \leq 180^\circ$ will allow matching of inertial stiffnesses. The lack of detailed, extensive measurements of biological wings' natural frequencies is the obvious hurdle in matching $\omega_{\text{cant}}/\omega$ ratios—once target values are established, materials and manufacturing techniques should be assessed for constructing MAV wings.

2.7 Summary

The linear assumed-modes matrix equations of motion of a flapping wing were developed for a wing modeled as a thin elastic beam undergoing bending and torsion motions. The blade loadings and equations of motion were developed by using an extension of Houbolt and Brooks' helicopter-blade methodology that included time-dependent flapping and feathering angles. The resulting wing loadings were then re-derived by physical considerations by considering the separate inertial, centrifugal and Coriolis forces acting on the wing. The loads calculated from these two derivations were shown to be equivalent, validating the analyses.

The blade loadings were then used to generate the assumed-modes matrix equations of motion. In order to model insect-like wing structures, the wing root is assumed to have a pinned boundary condition and a root spring. The ideal cantilever boundary condition can be recovered from this model by assuming a root spring of infinite stiffness.

By assuming prescribed, time-periodic flapping and feathering motions, the equations of motion were non-dimensionalized for insect-like flapping. The nondimensional parameters which characterized the system were identified:

- $\omega_{\text{cant}}/\omega$: Natural bending frequency of the wing (assuming cantilever boundary conditions) divided by wingbeat frequency, or "normalized cantilever frequency." Characterizes the magnitude of the constant structural stiffness of the wing structure.
- Φ, Θ : Stroke amplitudes of the flapping and feathering motions. Characterize the magnitudes of the time-periodic stiffnesses of the system.
- $\omega_{\text{tor}}/\omega_{\text{cant}}$: Natural torsional frequency of the wing divided by natural bending frequency of the wing (assuming cantilever boundary conditions). Characterizes non-rotational torsion stiffness relative to non-rotational bending

stiffness.

- $\omega_{\text{root}}/\omega_{\text{cant}}$: Natural frequency of a rigid wing with a root-spring boundary divided by natural bending frequency of the wing (assuming cantilever boundary conditions). Characterizes the root spring stiffness relative to the wing's structural stiffness.

Non-dimensionalization reveals that, for a given wing structure experiencing time-periodic insect-like motion, the magnitude of the constant stiffness is a function of the wingbeat *frequency* only. Conversely, the magnitudes of the time-periodic stiffnesses are functions of the flapping and feathering *stroke amplitudes* only. This independence has not been previously identified.

Using the characteristic values of the normalized cantilever frequency and the flapping and feathering amplitudes, biological fliers were compared with mechanical MAVs and flapping-wing test stands. MAVs and test stands were found to have lower stroke amplitudes than biological fliers, indicating relatively lower time-periodic stiffnesses. MAVs and test stands were also found to have higher normalized cantilever frequency than biological fliers, indicating relatively greater constant stiffnesses. This indicates that MAV research to date has resulted in physical models in which time-periodic stiffness effects will be relatively small compared to the biological fliers on which they are based. Possible consequences of this dissimilarity will be addressed in subsequent chapters.

CHAPTER 3

ASSUMED MODES LINEAR TIME-PERIODIC STABILITY

3.1 Introduction

A time-periodic system can experience instabilities for certain combinations of constant and periodic stiffness magnitudes. These instabilities arise directly from the time-periodic nature of the system. The time-periodic flapping wing equation of motion, which was developed in the previous chapter, is analyzed for instabilities in this chapter. The stability of the flapping wing system is characterized as a function of the normalized cantilever frequency (representing the constant stiffness magnitude) and the flapping stroke (representing the time-periodic stiffness magnitude). The stability of the system is examined with respect to various system and modeling parameters, including number and coupling of assumed modes, root spring stiffness, feathering stroke amplitude, and other structural parameters. Mechanical systems, including MAVs and test stands, are compared with biological fliers regarding the respective instability regions. The flapping-wing stability analysis and results were published in part by Rosenfeld and Wereley [161].

3.2 Analytical Stability Analyses

We first develop a parametric stability analysis of a flapping wing for a reduced case of Eq. 2.75. The feathering angle is fixed at $\theta = \pi/2$ and the wing is assumed rigid in torsion, $\gamma = 0$. The wing is thus oriented with its chord pointing nose-up as it flaps in the horizontal plane and it deforms only by bending within the plane of rotation (i.e., equivalent to elastic blade lag in helicopter analysis). The bending deformation is modeled by a single assumed mode, $w(x, t) = \chi_{w1}(x)q_{w1}(t)$. A diagram of this case is shown in figure 3.1, and the reduced non-dimensional equation of motion is

$$\ddot{q}_{w1} + \left[(\omega_{\text{cant}}/\omega)^2 K_\omega + \Phi^2 \hat{\phi}^2 (K_{\phi^2}^* - K_{\phi^2 s^2}^*) \right] q_{w1} = 0 \quad (3.1)$$

where the scalar stiffnesses are

$$K_\omega = \frac{1}{(\lambda R)_{\text{cant}}^4 \hat{\mathcal{C}}_{11}} \left[\hat{\mathcal{H}}_{11} + \left(\frac{\omega_{\text{root}}}{\omega_{\text{cant}}} \right)^2 (\lambda R)_{\text{cant}}^4 \hat{I}_b \hat{\mathcal{W}}_{11} \right] \quad (3.2)$$

$$K_{\phi^2}^* = \hat{\mathcal{T}}_{11} / (4 \hat{\mathcal{C}}_{11}) \quad (3.3)$$

$$K_{\phi^2 s^2}^* = 1/4 \quad (3.4)$$

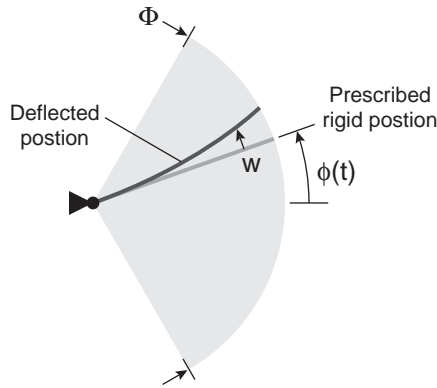


Figure 3.1: Top view of simplified single-mode, flapping motion. The deflection $w(x, t)$ is in the plane of flapping rotation $\phi(t)$.

Comparing Eq. 3.1 with the standard equation for helicopter lag [163] shows that $\Phi^2 \hat{\phi}^2 K_{\phi^2}^*$ is the centrifugal stiffness while $\Phi^2 \hat{\phi}^2 K_{\phi^2 s^2}^*$ is the centrifugal relaxation.

The equation is further simplified by prescribing harmonic flapping rotation, $\hat{\phi} = \cos \tau$. For this case, Eq. 3.1 becomes a time-periodic scalar Mathieu equation [170] with the form

$$q_{w1}^{**} + (a - 2q \cos 2\tau) q_{w1} = 0 \quad (3.5)$$

The parameters a and q characterize the periodicity of the Mathieu equation. The constant stiffness a is the mean stiffness of the system and the pumping stiffness q is the amplitude of the time-periodic component of stiffness. Constant and pumping stiffness are functions of the physical system parameters $\omega_{\text{cant}}/\omega$ and Φ :

$$a = (\omega_{\text{cant}}/\omega)^2 K_{\omega} + \Phi^2 (K_{\phi^2}^* - .25)/2 \quad (3.6)$$

$$q = \Phi^2 (K_{\phi^2}^* - .25)/4 \quad (3.7)$$

3.2.1 Development of a Parametric Flapping-Wing Stability Diagram

The parametric stability analysis of flapping MAV wings can now be developed from the Mathieu equation in Eq. 3.5. The scalar Mathieu equation is a classic time-periodic equation; its stability is well known and can be represented graphically on a Strutt diagram as a function of the stiffness parameters a and q , as shown in figure 3.2. The stability boundaries of the Mathieu equation are given by a set of Mathieu functions, corresponding to lines of marginally-stable values of (q, a) . Mathieu functions are known analytically, allowing us to create figure 3.2 as the exact, analytical stability diagram of the Mathieu equation.

The Strutt diagram in figure 3.2 is ideal for analyzing the general Mathieu equation, but we desire a flapping-wing stability diagram in terms of our physical

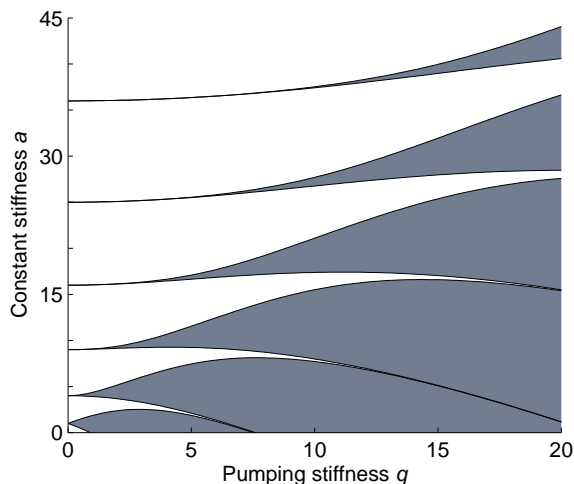


Figure 3.2: Strutt diagram of Mathieu equation. Shaded areas are unstable, black lines are stability boundaries calculated by Mathieu functions.

system parameters, $\omega_{\text{cant}}/\omega$ and Φ . Using the relationships in Eqs. 3.6–3.7, the Strutt diagram can be transformed into a new stability diagram showing the effects of independent variations of $\omega_{\text{cant}}/\omega$ and Φ . Equations 3.2–3.3 show that the stiffnesses K_ω and K_{ϕ^2} are functions of the root spring frequency ratio $\omega_{\text{root}}/\omega_{\text{cant}}$: explicitly in K_ω and implicitly in both since the mode shape used to calculate $\hat{\mathcal{C}}_{11}$, $\hat{\mathcal{H}}_{11}$, etc. changes with $\omega_{\text{root}}/\omega_{\text{cant}}$. For this example, we choose $\omega_{\text{root}}/\omega_{\text{cant}} = \infty$, or cantilever-free boundary conditions.

We need to transform the Strutt diagram over the values of (q, a) associated with physical parameter ranges of interest. The normalized cantilever frequency range is selected as $0 \leq \omega_{\text{cant}}/\omega \leq 4$ —we shall see that parametric instabilities are unlikely at above this range—and the flapping stroke range as $0 \leq \Phi \leq \pi$ radians. Recalling that $\hat{\mathcal{W}} = \mathbf{0}$ for the cantilever boundary condition, Eq. 2.61 can be used to show that $K_\omega = 1$. K_{ϕ^2} for the cantilever wing is 0.298, so the variation of q and a to be small as a function of Φ . This represents a small influence of periodic inertial stiffness on the single-mode cantilever model.

Figure 3.3 depicts how a Strutt diagram is transformed into a stability diagram in terms of the non-dimensional parameters $\omega_{\text{cant}}/\omega$ and Φ . Figures 3.3a–

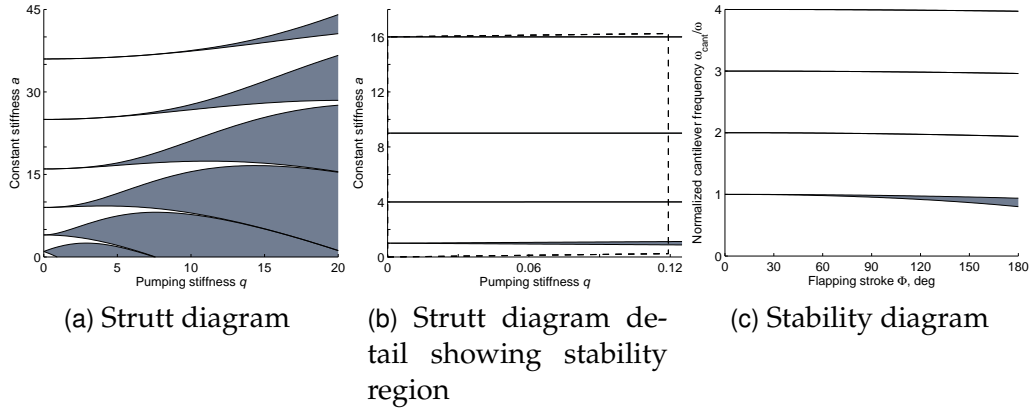


Figure 3.3: Transformation of Strutt diagram to flapping-wing stability diagram for single cantilever-free bending mode, $\Theta = 0^\circ$.

3.3b show the Strutt diagram. The first redraws figure 3.2 for reference, while the second shows a detail view with a dashed line enclosing the region on (q, a) corresponding to $0 \leq \Phi \leq \pi$ and $0 \leq \omega_{\text{cant}}/\omega \leq 4$ for the cantilever-free beam. By inverting Eqs. 3.6–3.7, we calculate the Mathieu functions bounding the unstable regions as functions of $(\Phi, \omega_{\text{cant}}/\omega)$, resulting in the flapping-wing stability diagram for the enclosed region shown in figure 3.3c.

We now examine the stability diagram in figure 3.3c more thoroughly. Combinations of parameters resulting in parametric instabilities are the shaded areas bounded by the dark lines of the transformed Mathieu functions. Only to the lowermost Mathieu functions enclose a significant region of instability on this diagram; the Mathieu functions at higher $\omega_{\text{cant}}/\omega$ are essentially zero-thickness lines of marginal stability. This is a typical trend: parametric instabilities decrease at higher normalized cantilever frequencies. The unstable regions appear relatively benign, occupying only a small portion of the diagram. We will see that the unstable regions are larger when we do not make the simplifications used for this initial stability diagram: inclusion of additional modeled bending and torsion modes will increase their size, as will a non-zero feathering stroke Θ .

The vertical axis of the stability diagram is the normalized cantilever fre-

quency $\omega_{\text{cant}}/\omega$, which represents the magnitude of the relative non-rotational structural stiffness of the wing, including both strain stiffness and root-spring stiffness, if present. For any particular wing, the physical non-rotational stiffness is fixed, so increasing $\omega_{\text{cant}}/\omega$ is equivalent to decreasing the flapping frequency ω : as the wing moves more slowly, the stiffness of the structure increases relative to the effects of motion. The horizontal axis is the flapping stroke Φ written in degrees for convenience, which represents the magnitude of the inertial stiffness of the beam arising from rotational motion. Moving vertically on the stability diagram is equivalent to changing the *constant* stiffness of the system, while moving horizontally is generally equivalent to changing the *time-periodic* stiffness of the system. (More precisely, some—but not all—of the rotational stiffnesses will change the time-averaged mean stiffness of the system, so Φ and also Θ will affect the constant stiffness of the system, c.f. Eq. 3.6. However, these effects are secondary to the effect of $\omega_{\text{cant}}/\omega$.) Time-periodic structural effects will be most pronounced at low $\omega_{\text{cant}}/\omega$ and high Φ , where constant stiffness will be lowest and time-periodic stiffness will be highest. In section 2.6.2.3, we showed that operating at low $\omega_{\text{cant}}/\omega$ and high Φ would maximize quasi-steady lift for normal hovering flight. We expect the wings of biological fliers and flapping MAVs which efficiently generate lift will likely experience time-periodic structural effects.

We use this simple case to illustrate the effect of flapping stroke Φ and normalized cantilever frequency $\omega_{\text{cant}}/\omega$ on the propagation of unforced, undamped instabilities in the time domain. We propagate an initial tip deflection of $\hat{w} = .01$ with an explicit Runge-Kutta ODE solver [171] implemented on Fortran 95 for various system parameters. Figure 3.4 shows the effect of varying Φ —the measure of the system’s time-periodic inertial stiffness—as $\omega_{\text{cant}}/\omega$ and strain stiffness is held constant. Each alternating white and gray band is, respectively, a downstroke and upstroke of the wing. Since $\omega_{\text{cant}}/\omega$ is fixed, all of these time-plots represent

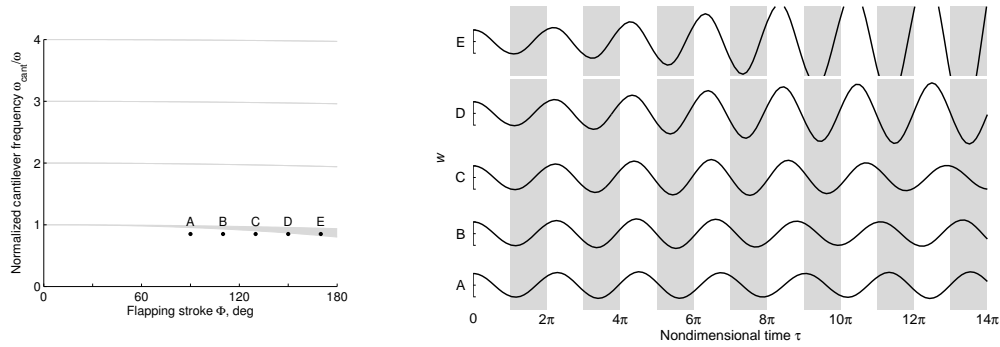


Figure 3.4: Propagation of unforced, undamped tip perturbations \hat{w} in single-mode system, $\omega_{cant}/\omega = .85$, $90^\circ \leq \Phi \leq 170^\circ$

a wing flapped at a constant frequency. As Φ increases, so does the natural frequency of the rotating wing, as can be seen by comparing the crests and troughs of tip deformation plots. When the rotating natural frequency approaches a harmonic of the flapping frequency, as in case E, parametric instabilities occur. Case D is close to, but not in, the region of instability; the deformations initially grow but the system is stable overall. It must be stressed that these instabilities are *not* caused by inertial forcing of the beam. Since we are considering a homogeneous system, forcing does not play a role in these instabilities. Rather, they are wholly the result of the *periodic inertial stiffnesses* arising from the flapping rotation.

Similar results are seen when ω_{cant}/ω is varied at a fixed Φ , as in figure 3.5. Here, strain stiffness changes with ω_{cant}/ω as inertial stiffness is held constant.

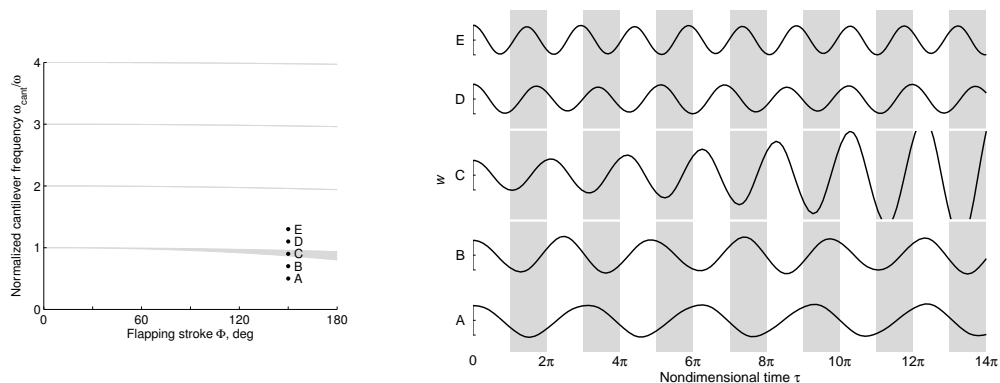


Figure 3.5: Propagation of unforced, undamped tip perturbations \hat{w} in single-mode system, $.5 \leq \omega_{cant}/\omega \leq 1.3$, $\Phi = 150^\circ$

The wing's rotating natural frequency increases with $\omega_{\text{cant}}/\omega$. As before, parametric instabilities occur when the wing's rotating natural frequency is near a harmonic of the flapping frequency. However in contrast to figure 3.4, these plots represent wings flapped at different frequencies. If we assume a constant ω_{cant} for a given wing, the dimensional time t corresponding to one period of non-dimensional time τ is proportional to $\omega_{\text{cant}}/\omega$. Finally, note that the single-mode system is more sensitive to changes of its constant strain stiffness than its time-periodic inertial stiffness, hence the more pronounced change in the rotating natural frequency with $\omega_{\text{cant}}/\omega$ than with Φ .

3.2.2 Biological Fliers, MAVs and Test Stands

The single-mode cantilever stability diagram is redrawn in figure 3.6 with overlays of the approximate parameter ranges of biological fliers, MAVs and test

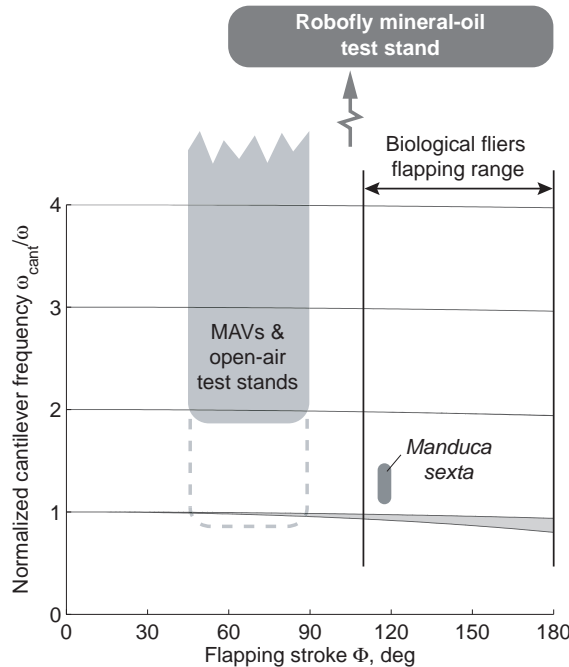


Figure 3.6: Stability diagram of a single-mode cantilever beam with approximate parameter ranges of biological fliers and MAV studies, $\Theta = 0^\circ$. Shaded “MAVs & test stands” area shows range of typically-constructed MAV wings, dashed line encloses normalized cantilever frequencies of Singh’s light-weight Wing VI [156].

stands given in table 2.3. First, we look at the operational range of MAVs and open-air test stands. It was noted earlier that all operational open-air mechanisms have been unable to deliver large-stroke flapping motions at the desired flapping frequencies, instead limited to $\Phi \leq 90^\circ$. The illustrated $\omega_{\text{cant}}/\omega$ range comes from the sole available source, Singh's flapping testbed. Almost all of Singh's tests were performed at $\omega_{\text{cant}}/\omega > 2$. However "Wing VI," which had both the lowest cantilever frequency and lowest mass of all the tested wings [156, p. 69], operated down to $\omega_{\text{cant}}/\omega \approx 0.8$. ("Wing IX" is recorded as having a similarly-low cantilever frequency, but data for flapping frequency ω was not reported.) The wing construction and flapping actuation methods used by Singh were typical of current MAV research, so we do not expect other open-air experiments to have significantly different $\omega_{\text{cant}}/\omega$ values. In contrast to the open-air test stands, the Robofly operates at Reynolds-scaled frequencies in mineral oil, allowing a series of slow-speed stepper motors to achieve a wide range of flapping strokes. Robofly is used for fluid mechanics studies and is fitted with functionally-rigid wings; combined with the low Reynolds-scaled flapping frequencies, this means Robofly's normalized cantilever frequencies are certainly above the range of the stability diagram. Between the open-air studies and the mineral-oil Robofly, we see that parametrically-unstable regions exist in a very small part of the range explored by current mechanical flapping studies. Biological fliers, however, use greater flapping strokes and, as discussed previously, efficient lift production should drive biological fliers to operate at low $\omega_{\text{cant}}/\omega$. The *Manduca sexta* hawkmoth, the only biological flier for which $\omega_{\text{cant}}/\omega$ can be numerically calculated, operates closer to the region of instability than most current flapping mechanisms reach. Though the recorded hovering values of *Manduca sexta*'s flapping stroke are given as approximately 120° , it is probable that it could use larger strokes to increase lift for heavy loading conditions.

3.2.3 Root Spring Stiffness

Earlier, we chose to develop the flapping-wing stability diagram using a cantilever boundary condition, which is equivalent to an infinitely-stiff root spring or $\omega_{\text{root}}/\omega_{\text{cant}} = \infty$. We now revisit this choice by examining effect of different values of root-spring stiffness on the stability diagram. The root-spring stiffness changes the diagram by altering the stiffnesses K_ω and K_{ϕ^2} , which will alter the range of stiffness parameters (q, a) corresponding to the ranges of interest of $(\Phi, \omega_{\text{cant}}/\omega)$ (Eqs. 3.6–3.7).

Figure 3.7 shows a detail view of the Strutt diagram, on which have been marked the regions corresponding the our stability diagram as $\omega_{\text{root}}/\omega_{\text{cant}}$ decreases from ∞ to 0.5. Before continuing, it must be noted that some of the trends seen in this simplified case (i.e., single modeled bending mode, no feathering rotation) do not carry through to more complex models. These differences are mostly because the current case approaches a single rigid-body mode as $\omega_{\text{root}}/\omega_{\text{cant}} \rightarrow 0$. We will begin by discussing the trends that are generalizable from this case, then discuss those that are not in the following paragraph. From figure 3.7, we see that

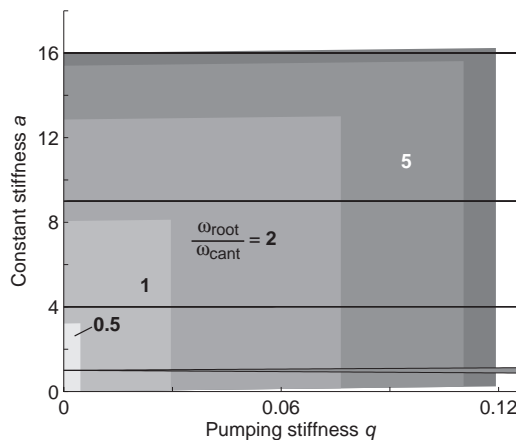


Figure 3.7: Effect of root spring stiffness on single-mode stability diagram envelope, shown on detail view of Strutt diagram. Shaded regions correspond to $0 \leq \omega_{\text{cant}}/\omega \leq 4$ and $0 \leq \Phi \leq \pi$ for various $\omega_{\text{root}}/\omega_{\text{cant}}$.

the maximum constant stiffness a of the enclosed region decreases with decreasing $\omega_{\text{root}}/\omega_{\text{cant}}$. This makes sense physically: by decreasing $\omega_{\text{root}}/\omega_{\text{cant}}$, we decrease the root spring stiffness relative to the wing's bending strain stiffness. Since the bending strain stiffness is constant for a given wing and $\omega_{\text{cant}}/\omega$, the root spring stiffness must decrease, hence the total non-rotational system is less stiff and a is lower. This is true for any modeled system.

There are two trends unique to this single-mode, non-feathering model which appear on figure 3.7 as $\omega_{\text{root}}/\omega_{\text{cant}}$ approaches zero: first, that the maximum constant stiffness a of the enclosed regions goes to zero and second, that the maximum pumping (i.e., time-periodic) stiffness q decreases monotonically to zero. We shall address each separately. Constant stiffness a approaches zero for this case because the sole modeled root-spring-free mode approaches a rigid beam, which has no strain stiffness, while the root-spring stiffness also approaches zero. Thus, the total constant stiffness approaches the stiffness of a rigid pinned-free beam, which is zero. Additional modeled root-spring-free bending modes will approach pinned-free bending modes, which will retain some strain stiffness as $\omega_{\text{root}}/\omega_{\text{cant}}$ approaches zero. Pumping stiffness q decreases monotonically to zero because the system approaches a rigid beam with deformation motion completely *within the plane of forced rotation* $\phi(t)$. Recall that the periodic stiffness of this simplified system is equivalent to centrifugal stiffness in the zero-offset helicopter lag case. Centrifugal stiffness occurs because the bending deflections of the beam decrease the radial position of the wing elements, performing work against the centrifugal force field (i.e., increasing the system's potential energy), as shown in figure 3.8a. In contrast, rigid deflections do no work against the centrifugal force field as in figure 3.8b, thus no centrifugal stiffness and no time-periodic stiffness component of the model. Again, additional models modes will not approach the rigid-beam mode and will retain some centrifugal stiffness (moreso,

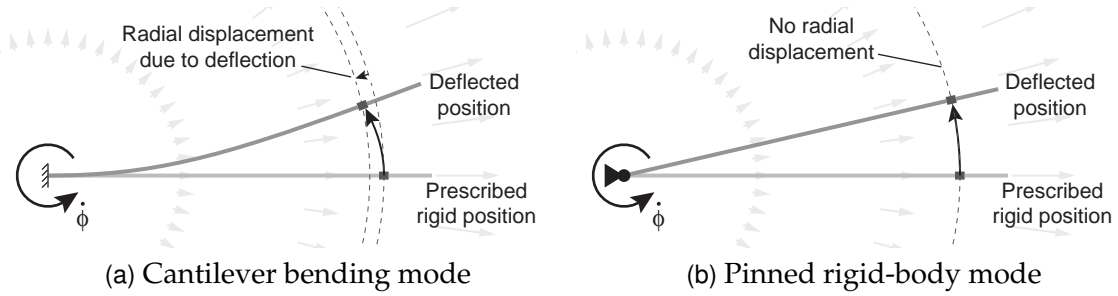


Figure 3.8: Motion of a beam element against centrifugal force arising from beam deflection, shown in top view of flapping frame. Gray background arrows show the magnitude and direction of the centrifugal force field due to flapping rotation, $m\dot{\phi}^2 x^2$

these stiffnesses may not constantly decrease, see below). Alternately, a non-zero feathering angle would cause rigid-beam deflections to partially act out of the flapping plane, which would cause work to be done against the centrifugal force field. This would also retain some centrifugal stiffness.

As a demonstration that pumping stiffness q and constant stiffness a will not generally approach zero as $\omega_{\text{root}}/\omega_{\text{cant}}$ approaches zero, let us consider the second bending mode as if it were uncoupled from the first bending mode. (In reality this is not the case, since the bending modes will be coupled through off-diagonal entries in the $K_{\phi^2}^*$ matrix.) We construct q and a as before, using K_{ω} and $K_{\phi^2}^*$ calculated from Eqs. 3.2–3.3 using the second root-spring-free bending mode (i.e., with \mathcal{C}_{22} , \mathcal{H}_{22} , etc.). The maximum values of q and a for our stability diagram, corresponding to the uncoupled second mode as a function of $\omega_{\text{root}}/\omega_{\text{cant}}$, are given in table 3.1. As we asserted before, constant stiffness a steadily decreases with $\omega_{\text{root}}/\omega_{\text{cant}}$, but does not approach zero. Pumping stiffness q first decreases with $\omega_{\text{root}}/\omega_{\text{cant}}$ but then increases, with a minimum somewhere between $1 < \omega_{\text{root}}/\omega_{\text{cant}} < 2$. This demonstration does not have any strict physical meaning, since we are considering an uncoupled mode of a system that is coupled in reality; it is merely a quick illustration that some of the $\omega_{\text{root}}/\omega_{\text{cant}}$ trends in the simplified single-mode model do not hold for higher modes.

Table 3.1: Maximum pumping stiffness q and constant stiffness a for uncoupled second root-spring-free modes as a function of $\omega_{\text{root}}/\omega_{\text{cant}}$.

$\omega_{\text{root}}/\omega_{\text{cant}}$	$q(\pi, 4)$	$a(\pi, 4)$
∞	3.38	635
5	3.33	612
2	3.23	530
1	3.22	421
0.5	3.28	349
0	3.33	314

Returning to the stability diagrams themselves, figure 3.9 shows the effect of root spring stiffness on the single-mode, flapping-only stability diagram. The first five stability diagrams correspond to the five shaded regions in figure 3.7 while the last shows $\omega_{\text{root}}/\omega_{\text{cant}} = .05$, which is nearly equivalent to a pinned-free system. The *contraction* of the stability diagram region on the Strutt diagram manifests as an *expansion* of the plotted region on the stability diagrams themselves: we can

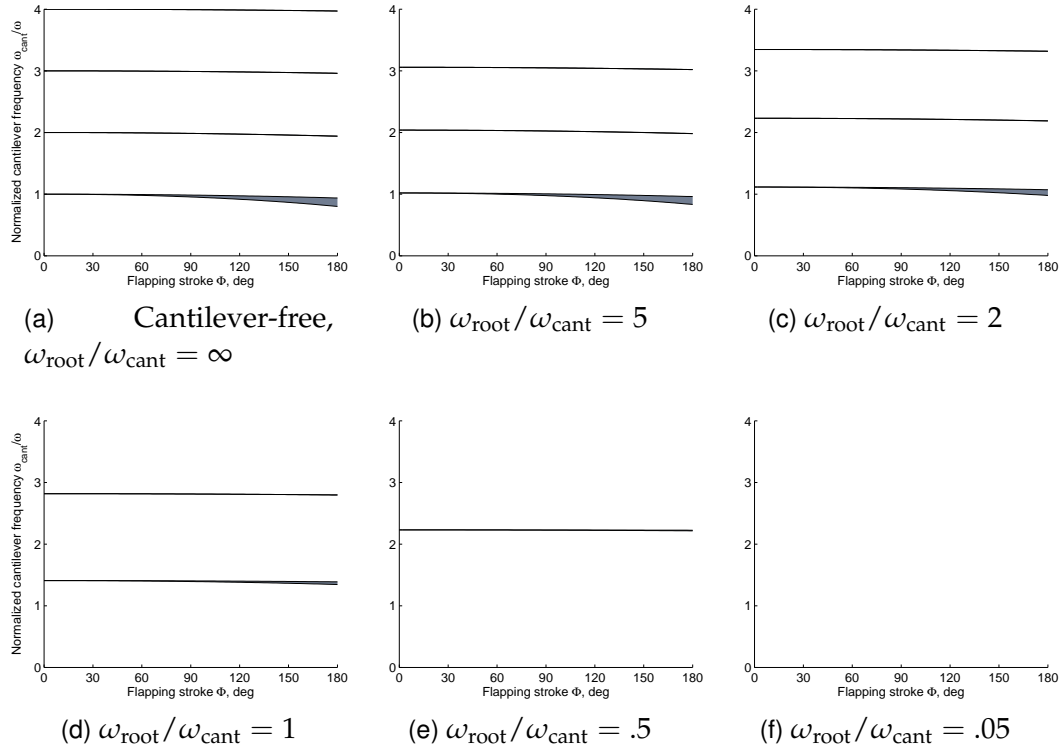


Figure 3.9: Effect of root spring stiffness on single-mode stability diagram, $\Theta = 0^\circ$.

see that as $\omega_{\text{root}}/\omega_{\text{cant}}$ decreases, instability plot “zooms in” toward the origin. It is most notable on the vertical axis, where the instability regions spread apart to higher normalized cantilever frequencies. This means that at lower root spring stiffnesses, instabilities will be encountered at higher $\omega_{\text{cant}}/\omega$, that is, at *lower* flapping frequencies ω . Again, this is physically intuitive: reducing the stiffness of the total system will cause instability effects to manifest at lower actuation frequencies. The effect is not as apparent on the vertical axis, since our simplified model had a relatively small dependence on time-periodic stiffness to begin with. As before, the apparent ability to eliminate instabilities by decreasing $\omega_{\text{cant}}/\omega$ is unique to this simplified model. We will see that decreasing $\omega_{\text{cant}}/\omega$ will result in larger unstable regions on more complex analyses.

3.2.4 Uncoupled Bending and Torsion

In general the analytic, single-mode stability analyses that we have applied thus far cannot be directly extended to deal with multiple modes. However, if we consider a single bending mode and a single torsion mode that are structurally uncoupled, the system is equivalent to two separate single-mode equations, from which we can generate the stability diagram via transformations of Mathieu functions as above. We now allow a nonzero torsion deformation γ , but continue to hold the feathering angle constant at $\theta = \pi/2$. If both bending and torsion deformations are modeled by a single assumed mode, the homogeneous matrix equation of motion is

$$\begin{Bmatrix} q_{\gamma 1}^{**} \\ q_{w 1}^{**} \end{Bmatrix} + \left[(\omega_{\text{cant}}/\omega)^2 \mathbf{K}_{\omega} + \Phi^2 \hat{\phi}^{*2} (\mathbf{K}_{\phi^2}^{*} - \mathbf{K}_{\phi^2 s^2}^{*}) \right] \begin{Bmatrix} q_{\gamma 1} \\ q_{w 1} \end{Bmatrix} = \underline{0} \quad (3.8)$$

The matrices \mathbf{K}_{ω} and $\mathbf{K}_{\phi^2}^{*}$ will be diagonal and the degrees of freedom will be uncoupled if the wing’s center of gravity and area centroid are coincident with its

elastic axis: $\hat{e} = \hat{e}_A = 0$. This will be the case if the wing is symmetric along its chord as well as along its thickness. (The matrix $K_{\phi^2 s^2}$ is always diagonal.) In order to calculate K_ω and K_{ϕ^2} , it is necessary to know the squared non-dimensional mass and area moments \hat{k}_m^2 and \hat{k}_A^2 . We use values calculated from the representative wing developed in section 2.2.2. Using Eqs. 2.4–2.6, the non-dimensional values will be $\hat{k}_m^2 = \hat{k}_A^2 = .068\hat{c}^2$ (recall that $\hat{k}_m^2 \approx \hat{k}_{my}^2$). We select the non-dimensional chord as $\hat{c} = 1/4$ so the wing has the same aspect ratio as a single hummingbird wing, based on Chai and Millard’s measurements of $AR \approx 8^*$ [71].

The characteristic parameter defining the torsion-mode stiffness is the non-rotating natural frequency ratio of the first clamped-free torsion mode to the first cantilever-free bending mode, $\omega_{\text{tor}}/\omega_{\text{cant}}$. We look to a FEA of an insect wing to estimate a reasonable baseline value of this ratio; Wootton et al.’s FEA of a hawkmoth wing calculated the first non-rotational bending frequency as 31 Hz and the first non-rotational torsional frequency as 88 Hz [103]. We therefore choose the ratio $\omega_{\text{tor}}/\omega_{\text{cant}} = 2.84$ as our baseline. The analytical stability plot of the uncoupled two-mode stability diagram using the baseline $\omega_{\text{tor}}/\omega_{\text{cant}}$ is shown in figure 3.10b. The other diagrams of figure 3.12 show the baseline $\omega_{\text{tor}}/\omega_{\text{cant}} \pm 1$ for comparison. The uncoupled torsion modes appear as thin lines that hardly vary position with flapping stroke Φ . This indicates that time-period stiffnesses have relatively little effect on the torsion instabilities. The effect of torsion frequency ratio $\omega_{\text{tor}}/\omega_{\text{cant}}$ can be easily seen in figure 3.12—as $\omega_{\text{tor}}/\omega_{\text{cant}}$ increases, the torsion instabilities become packed closer together. This is very similar to the effect of the root-spring frequency $\omega_{\text{root}}/\omega_{\text{cant}}$ discussed above: a smaller torsion frequency ratio $\omega_{\text{tor}}/\omega_{\text{cant}}$ indicates a smaller relative non-rotational torsion stiffness, which has the effect of “zooming in” the region

*Chai and Millard measured AR with respect to the span and area of both wings. Therefore, their reported AR are twice the value that would be calculated for a single wing. Note also that selecting $\hat{c} = 1/4$ results in a slightly more slender wing than the hawkmoth measurements from which the representative wing was derived in section 2.2.2, which have $\hat{c} = .28$

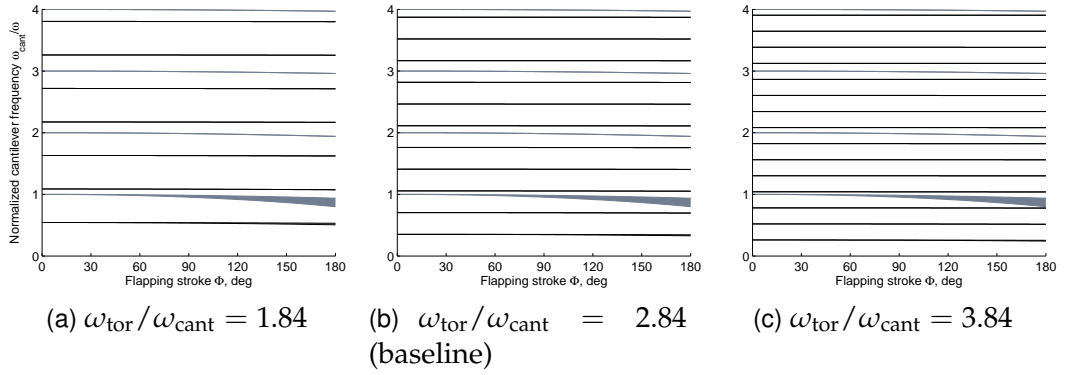


Figure 3.10: Effect of torsion stiffness on uncoupled two-mode stability diagram, $\Theta = 0^\circ$. Gray regions are cantilever-free bending instability regions, black lines enclose clamped-free torsion instability regions.

of the Strutt diagram that is transformed into the stability diagram.

3.3 Floquet Analysis

All of the previous stability diagrams were constructed by transformation of the analytic Mathieu functions. This transformation was possible because our simplified analytical models were equivalent to scalar Mathieu equations. The introduction of coupled modes and feathering rotation $\theta(t)$ will break this equivalency, with the result being that we cannot construct exact, analytic stability boundaries for more complex models. Instead, the stability diagrams of these more complex models must be evaluated numerically on a discrete mesh of $(\Phi, \omega_{\text{cant}}/\omega)$. We use Floquet analysis to evaluate the stability of the linear, time-periodic system at each discrete mesh point [170]. At any particular point $(\Phi, \omega_{\text{cant}}/\omega)$, the matrix equation of motion Eq. 2.75 is transformed into a state-space form

$$\dot{\mathbf{z}}^*(\tau) = \mathbf{A}(\Phi, \omega_{\text{cant}}/\omega, \tau) \mathbf{z}(\tau) \quad (3.9)$$

where the time-periodic state-space matrix \mathbf{A} is a function of the system parameters. This equation is integrated over one period $0 \leq \tau \leq 2\pi$ to construct a time-

independent transition matrix \mathbf{Q} that transfers the state-space vector one period into the future. The integration is performed by the Runge-Kutta ODE solver used to construct the tip deflection figures 3.4 and 3.5.

$$\underline{z}(\tau + 2\pi) = \mathbf{Q}(\Phi, \omega_{\text{cant}}/\omega) \underline{z}(\tau) \quad (3.10)$$

The system at point $(\Phi, \omega_{\text{cant}}/\omega)$ is considered unstable if the eigenvalues of $\mathbf{Q}(\Phi, \omega_{\text{cant}}/\omega)$ satisfy

$$\max \left| \text{eig}(\mathbf{Q}) \right| > 1 + \epsilon \quad (3.11)$$

where ϵ is a small safety factor to account for numerical errors in the time integration and is set at $\epsilon = 10^{-5}$.

3.3.1 Flapping and Feathering Rotation

Before adding higher-frequency torsion and bending modes to the model, we examine the effect of feathering stroke amplitude Θ on the single-mode stability diagram, shown in figure 3.11. In each diagram, Θ is held constant while Φ and $\omega_{\text{cant}}/\omega$ vary. Figure 3.11a redraws the previously considered $\Theta = 0^\circ$ case with analytic stability boundaries, while the remaining figures are numerically generated. The instability regions at higher $\omega_{\text{cant}}/\omega$ are so thin as to often fall between the numerical grid. The general shapes of the unstable regions are similar at all magnitudes of Θ , but the size of the unstable regions increases with increasing Θ . For larger feathering strokes, the unstable regions associated with the bending-mode instability extend to higher Φ and $\omega_{\text{cant}}/\omega$ than at lower strokes. The shaded region extending from the origin as Θ increases appears to be an additional bending parametric instability affecting systems with low total stiffnesses (i.e., where both non-rotational and flapping stiffnesses are relatively small) associated with feathering-induced periodic stiffnesses.

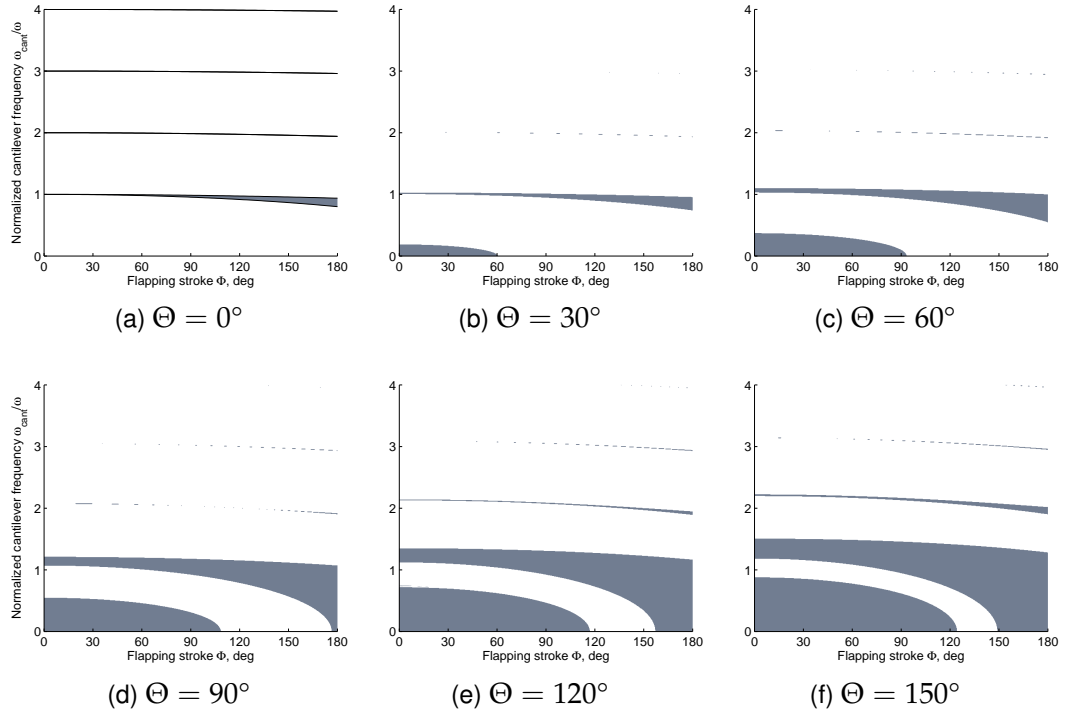


Figure 3.11: Effect of feathering stroke Θ on single-mode stability diagram.

Though our model is still relatively crude, figure 3.11 already indicates that structures undergoing insect-like flapping and feathering should not be operated at low $\omega_{\text{cant}}/\omega$ because of parametric instabilities. For example, if our representative system has a feathering stroke of $\Theta = 150^\circ$, much of the region $\omega_{\text{cant}}/\omega < 1.5$ is unstable. Therefore, flapping frequencies greater than 2/3rds of the lowest non-rotational bending frequency should be avoided for this structure.

3.3.2 Additional Modes

We now add higher-frequency structural modes to the system, beginning with the first torsion mode. For the special case with no feathering rotation and the CG and the centroid coinciding with the elastic axis ($\hat{e} = \hat{e}_A = 0$), the bending and torsion modes are uncoupled and the modal equations of motion reduce to two uncoupled scalar Mathieu equations. We may apply the analytic transformation

of the Strutt diagram separately for each mode and develop an exact stability diagram by overlaying the instability regions, as in figure 3.12a. In this diagram, gray regions are the previously derived bending instability regions while the black lines are the boundaries of the torsion-mode instabilities. As with the bending-associated instability regions, the torsion regions at higher $\omega_{\text{cant}}/\omega$ are essentially zero-width lines of marginal stability. Figure 3.12b shows the stability diagram of the same system generated numerically by Floquet analysis. Again, only the lowest instability regions are thick enough to show up on the mesh. Setting \hat{e} and \hat{e}_A to their nonzero baseline values couples the bending and torsion modes; the resulting matrix equation of motion cannot be solved analytically. Figure 3.12c shows the numerically generated stability diagram of the coupled case. The additional shaded areas—e.g., the horizontal spike near $\omega_{\text{cant}}/\omega = .45$ —arise from bending-torsion modal couplings.

The simple, coupled two-mode system allows comparison of the different types of instability regions in the time domain. In figure 3.13, the flapping stroke is held constant at $\Phi = 150^\circ$ while $\omega_{\text{cant}}/\omega$ is varied to create systems with bending, torsion or coupled bending-torsion instabilities. At each point, two time plots are created: one propagating an initial tip bending deformation of $\hat{w} = .01$ and one propagating an initial tip torsion deformation of $\hat{\gamma} = .01$. Cases E and F show

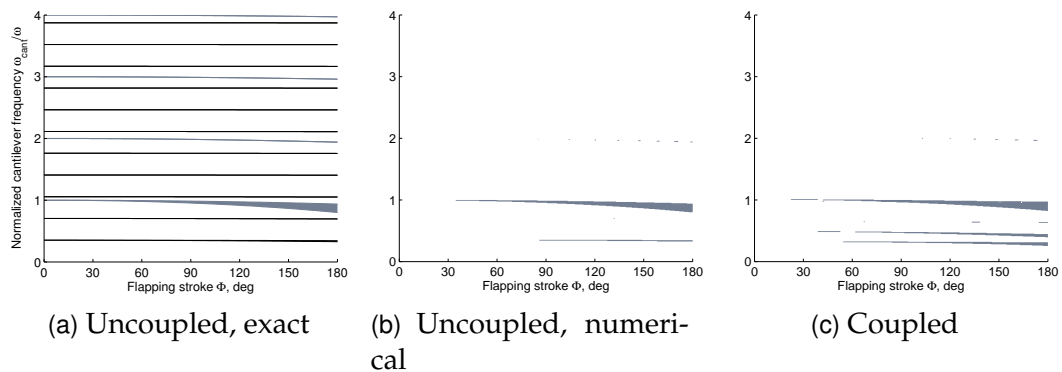


Figure 3.12: Two-mode mode stability diagram, $\Theta = 0^\circ$.

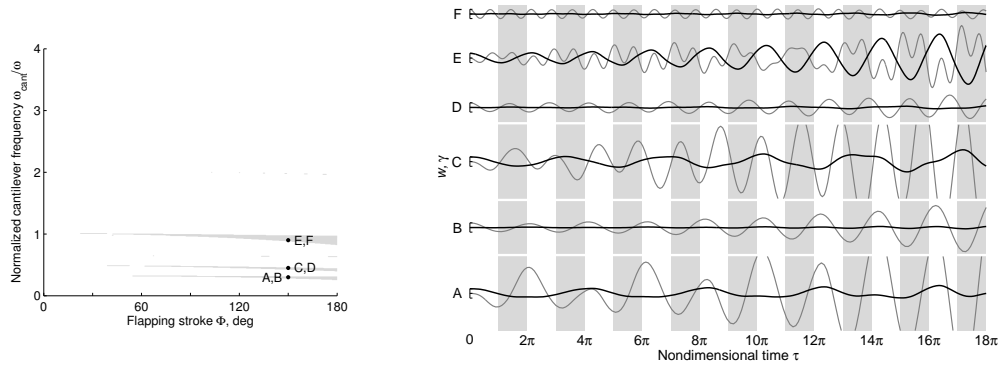


Figure 3.13: Propagation of unforced, undamped tip perturbations \hat{w} (black line) and $\hat{\gamma}$ (gray line) in coupled two-mode system, $.3 \leq \omega_{cant}/\omega \leq .9$, $\Phi = 150^\circ$.

a system unstable in bending. Case E, with an initial tip deformation, clearly shows the bending natural frequency is near the first harmonic of the flapping frequency, causing the instability. The coupled torsion deformation grows with bending, but has an additional frequency component at its own nature frequency, 2.84 times higher than the bending frequency. Case F shows that the initial torsion deformation does not immediately cause the bending deformation to grow quickly, indicating that bending deformations affect torsion more than torsion deformations affect bending. However, the bending deformation is present and will eventually go unstable. Cases A and B show a system unstable in torsion. In these cases, it is the torsion deformation frequency that is near the flapping frequency (recall that lower ω_{cant}/ω corresponds to less dimensional time per period of τ). Both cases clearly go unstable; in case A, the additional frequency component in the bending deformations at $1/2.84$ of the torsion frequency is visible. Cases C and D show a system unstable in coupled bending-torsion. As with case F, we see in case D that the initial tip torsion weakly affects the bending deformations. Case C shows the clearer result. Neither bending nor torsion deformations have a frequency near the flapping frequency, which is characteristic of a coupled instability.

Figure 3.14 shows the stability diagram for the non-feathering, flapping-

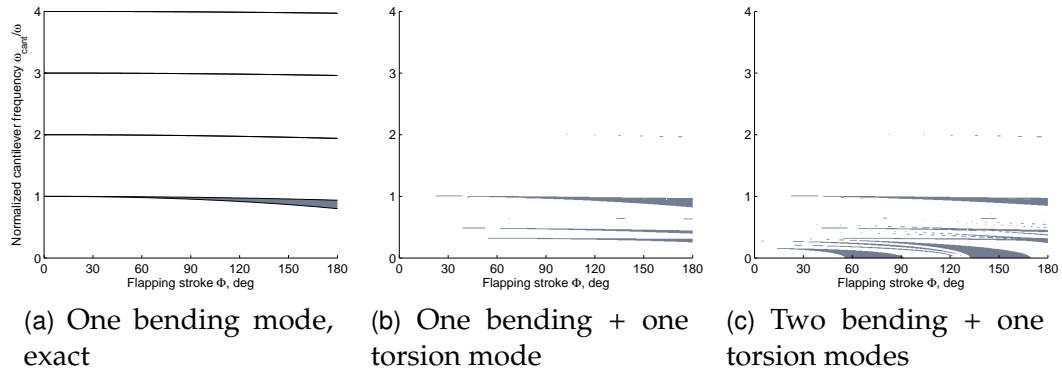


Figure 3.14: Additional coupled modes included on flapping stability diagram, $\Theta = 0^\circ$.

wing model as progressively higher coupled modes are included. The leftmost diagram is again the exact single mode case, the middle diagram adds the first torsion mode ($\omega_{\text{tor}}/\omega_{\text{cant}} = 2.84$) and the rightmost adds the second bending mode ($\omega_{w2}/\omega_{w1} = 6.27$). The instability regions associated with higher-frequency modes primarily manifest at *lower* values of $\omega_{\text{cant}}/\omega_w$. These are regions where the first-bending-mode instabilities already dominate the diagram for non-zero feathering strokes. Recalling that parametric instabilities decrease at higher normalized cantilever frequencies, we can expect that the instability regions associated with these higher modes will be relatively benign at higher $\omega_{\text{cant}}/\omega_w$. Thus, we should expect the parametric instabilities associated with the first bending mode to continue to dominate the system even when higher modes are modeled.

This expectation is borne out when non-zero feathering rotation is applied to the three-mode model. Figure 3.15 shows the effect of increasing feathering stroke on the three-mode model's stability diagrams. Comparing this to the corresponding single-mode diagrams of figure 3.11, shows that the diagrams are practically identical at higher normalized cantilever frequencies, i.e. $\omega_{\text{cant}}/\omega_w > 1.5$. The instabilities associated with higher-frequency structural modes grow (note the nearly horizontal spike at $\omega_{\text{cant}}/\omega_w \approx .6$, which is a torsion-associated region)

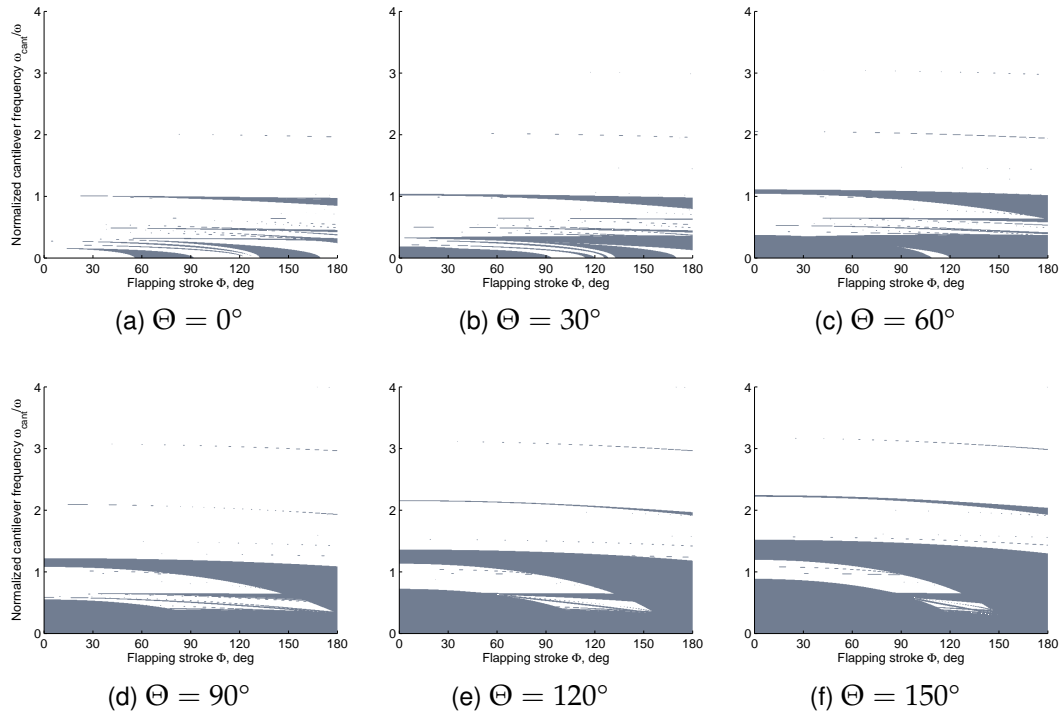


Figure 3.15: Effect of feathering stroke Θ on three-mode stability diagram.

and coalesce. But, these additional regions of instability largely act in regions where the single-mode model already indicated that operation is inadvisable. This suggests that adequate guidelines for avoiding parametric instabilities may be generated with models containing only a few low-frequency modes, but more research is necessary to confirm such a generalization.

3.3.3 Root Spring Stiffness

We now reexamine the effect of root-spring stiffness for a system with multiple modes and feathering rotation. Figure 3.16 shows the stability diagram for a feathering, three-mode system as a function of root-spring stiffness. The two bending modes are modeled with root-spring-free boundary conditions. Using the exact, single-mode diagrams in figure 3.9 as a comparison, we see again that decreasing $\omega_{\text{root}}/\omega_{\text{cant}}$ causes a “zoom-in” effect with respect to the first-mode

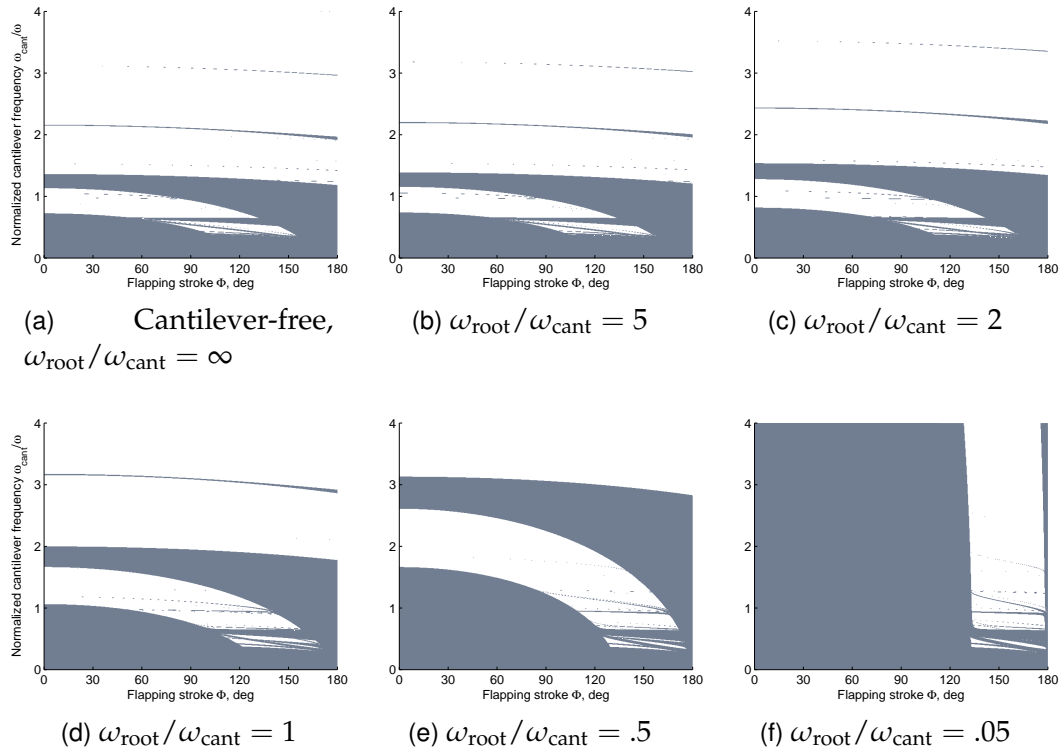


Figure 3.16: Effect of root spring stiffness on three-mode bending stability diagram, $\Theta = 120^\circ$.

bending instabilities. With smaller $\omega_{\text{root}}/\omega_{\text{cant}}$, the instability regions associated with the first bending mode move higher and increase in width. This includes the instability region in the lower-left corner, previously identified as an effect of feathering-induced periodic stiffnesses, which eventually fills the majority of the diagram in figure 3.16f. In contrast, note that the instability regions associated with higher modes remain at the bottom of the diagram for all values of $\omega_{\text{root}}/\omega_{\text{cant}}$. From these plots, we can conclude that low values of $\omega_{\text{root}}/\omega_{\text{cant}}$ should be avoided. This is already the case for most MAVs and test stands, which use clamped boundaries at the wing root. In general, it seems advisable to allow as little deviation from this clamped boundary condition as possible.

3.3.4 Lossy (Damped) Stability

Combes and Daniel [131] concluded that aerodynamic forces on a flapping wing primarily add damping to the system. Damping is included in our non-dimensional equations of motion by adding a linear viscous damping matrix $2\zeta I$ multiplying the modal velocity terms. We choose viscous damping as valid for the linear, small-deflection structural model considered in this study. Combes and Daniel report using a “mass damping factor” of 10 resulted in a good match between their FEM and their experimental data at a wingbeat frequency of 26 Hz [126]. Assuming this indicates a damping matrix of the form αM where $\alpha = 10$, the equivalent damping can be approximated as follows. The equivalence between the linear damping ζ and the mass damping α is

$$\zeta = \frac{\alpha}{2\omega_n} = \frac{\alpha}{2\omega_{\text{cant}}} \quad (3.12)$$

where ω_n is the natural frequency of an appropriate n th mode, in radians/second. For our case, we are concerned with the first cantilever bending mode, so we set $\omega_n = \omega_{\text{cant}}$. Combes and Daniel do not report the natural frequencies of their FEM, so ω_{cant} for their model must be estimated. Wootton et al., using their own FEM, report the first natural frequency of a hawkmoth wing as 31 Hz, as compared to hawkmoth wingbeat frequencies of 21 to 27 Hz [103]. If $\omega_{\text{cant}} = 31$ Hz is substituted into Eq. 3.12 with $\alpha = 10$, the linear damping is $\zeta = 0.026$. While this is a reasonable value, it is perhaps not wise to assume that Wootton et al.’s FEM is equivalent to Combes and Daniel’s FEM. Instead, we may only assume that Combes and Daniel’s FEM has a first natural frequency greater than or equal to the wingbeat frequency $\omega_{\text{cant}} \geq 26$ Hz (equivalent to $\omega_{\text{cant}}/\omega \geq 1$). This relationship bounds the linear damping to $\zeta \leq 0.030$. An extreme value of $\zeta = 0.030$ may then be chosen as a upper bound for Combes and Daniel’s damping.

Figure 3.17 shows the undamped, flapping and feathering three-mode model along with a slightly damped and significantly damped system. As damping is increased, the thin outlying regions of instability disappear while the large regions slightly shrink. But even with damping as high as $\zeta = .10$, the general shape and size of the instability regions at low $\omega_{\text{cant}}/\omega$ —the area our stability tests indicate should be avoided—remain unchanged. We can also note that the instability regions associated with higher-frequency modes tend to be eliminated with damping, again lending credence that perhaps only a small number of modes are necessary to model time-periodic stability of flapping wings.

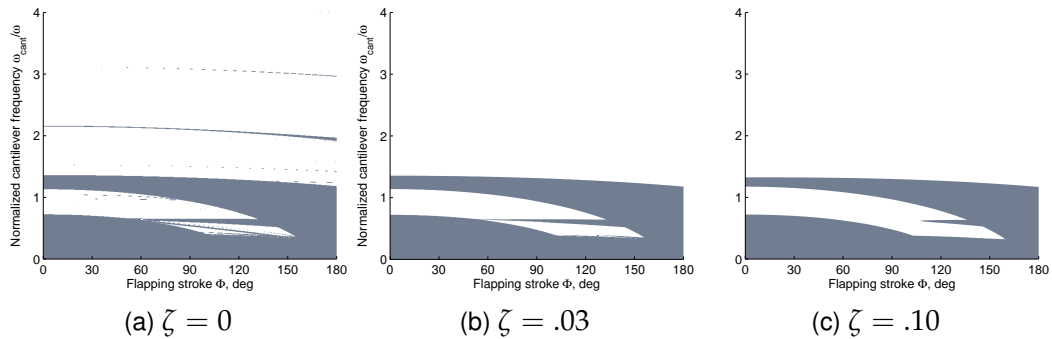


Figure 3.17: Effect of constant damping on three-mode stability diagram, $\Theta = 120^\circ$.

3.3.5 Center of Gravity Location

We now return to the undamped model. In rotary wing systems such as helicopters, the chordwise location of center of gravity significantly affects system stability [163]. It is therefore instructive to examine the effects of CG on flapping wing system stability. For the baseline stability diagram, redrawn in figure 3.18a, the baseline CG is 10% chord behind the elastic axis. Figure 3.18b shows the effect of moving the CG forward to the EA; figure 3.18c moves the CG an additional 10% chord forward. For our model, the CG location does not appear to greatly affect the instability regions associated with the first bending mode, which dominate

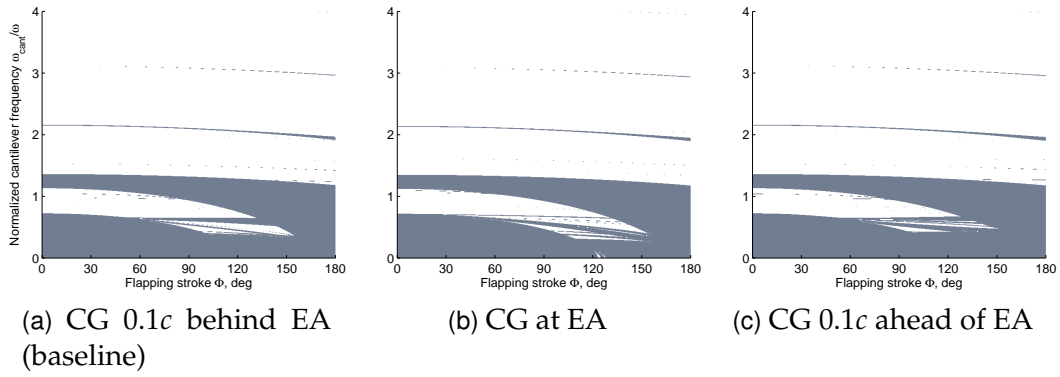


Figure 3.18: Effect of chordwise CG location on three-mode stability diagram, $\Theta = 120^\circ$.

the diagrams. The CG location does affect the higher-mode instability regions, seen by comparing the areas of $60^\circ \leq \Phi \leq 150^\circ$, $\omega_{w1}/\omega < 2/3$. Notably, the horizontal spike (near $\omega_{w1}/\omega = .6$) corresponding to a torsion instability diminishes when the CG coincides with the EA, while the diagonal spike directly below corresponding to a coupled bending-torsion instability strengthens. When the CG is ahead of the EA, both these regions seem equally thick. However, we again see that these changes do not affect the overall character of the stability diagram.

3.3.6 Feathering Axis Location

The elastic axis offset distance \hat{e}_O was chosen so that the CG is coincident with the feathering axis \hat{i}_θ , in order to reduce inertial torques during feathering rotation. We assess whether this selection has any effect on stability by changing the offset distance. The baseline diagram is given in figure 3.19b, while figure 3.19a and 3.19c move the axis of rotation $\pm 10\%$ chord from the CG along the chord. The effect on stability diagrams is negligible; data comparison shows that figures 3.19a and 3.19c each differ from the baseline case over only .2% of the plotted range, primarily in subtle shifts of higher-mode instability regions. Small changes of \hat{e}_O

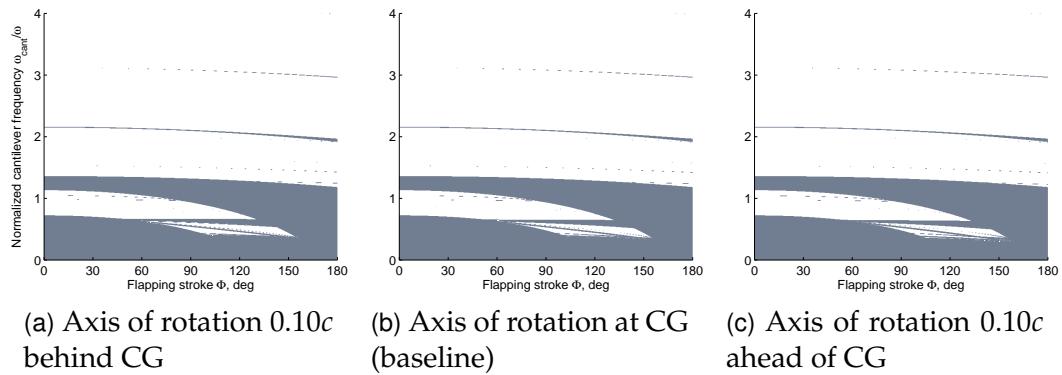


Figure 3.19: Effect of feathering axis location on three-mode stability diagram, $\Theta = 120^\circ$.

appear to have almost no effect on system stability.

3.4 Summary

A parametric stability analysis for a flapping-wing structure was developed in this chapter. By modeling the flapping-wing system with a single-degree-of-freedom (SDOF) bending mode undergoing sinusoidal flapping, the resulting time-periodic scalar equation of motion is shown to be equivalent to the Mathieu equation. Using this equivalence, the stability boundaries of the simplified wing system as functions of the characteristic non-dimensional parameters (normalized cantilever frequency and flapping stroke) can be solved exactly by transformation of the Mathieu functions. A stability diagram plotting regions of instability of a flapping wing as a function of normalized cantilever frequency and flapping stroke was derived from a transformation of the Strutt diagram.

Using the simplified SDOF model, it was demonstrated that parametric instabilities occur when a combination of constant and time-periodic stiffness cause the wing's rotational natural frequency to approach an even harmonic of the flapping frequency. In general, systems with relatively low constant stiffness (i.e., low normalized cantilever frequency) and high time-periodic stiffness (i.e., high

flapping stroke) are more likely to experience parametric instabilities. This region corresponds to biological fliers. In contrast, MAVs and mechanical test stands tend to have lower flapping strokes and higher normalized cantilever frequencies, and thus operate in regions where parametric instabilities are unlikely. This suggests that as mechanical systems approach the operating conditions of biological fliers, the possibility of encountering parametric instabilities becomes greater than they currently are.

The transformed Mathieu functions can be used to calculate the exact stability boundaries for SDOF systems or uncoupled multi-mode systems undergoing flapping rotation. Exact stability solutions were calculated for an SDOF system for a range of root-spring stiffnesses, and for uncoupled two-degree-of-freedom bending–torsion system. In order to analyze systems with multiple coupled elastic modes or systems with non-zero feathering rotation, it is necessary to numerically calculate system stability using the Floquet method.

For multi-mode models, it is found that regions of instability exist which are associated with each individual mode. Additional “coupled” instability regions exist due to the interaction of two (or possibly more) modes. In general the instability regions associated with the first bending mode dominate the system, except at low values of normalized natural frequency ($\omega_{\text{cant}}/\omega < 1$), where higher-mode instabilities may be strong. Studies were performed to examine the effect of operational and structural parameters on regions of instabilities. It is found that increases in feathering angle exacerbate instabilities, as do decreases in root-spring stiffness (that latter greatly so). Damping of the system slightly decreases the instability regions, but does not eliminate them completely. The chordwise location of the wing’s center-of-gravity and elastic axis do not significantly alter the instability regions.

CHAPTER 4

ASSUMED MODES ANALYSIS OF A FLAPPING WING AS A THIN PLATE

4.1 Introduction

In chapter 2, the flapping-wing equations of motion were derived by modeling the wing structure as a thin beam. This modeling assumption was justified by biological studies that indicated that the wing's leading-edge spar carries most bending and torsion loads for biological fliers. However, the validity of the thin-wing assumption warrants further consideration, because the wings of biological fliers and MAVs typically have low aspect ratios. In this chapter, the assumed-modes equations of motion are re-derived for a flapping wing modeled as a two-dimensional plate. The plate equations of motion are non-dimensionalized and their stability is analyzed in the same manner as the thin-beam equations of chapters 2 and 3. Assumed modes for input into the plate model are generated using a commercial finite element analysis (FEA) code. The results are compared to the thin-beam model in order to identify any differences or discrepancies between the two modeling methods.

4.2 Assumed-Modes Plate Model

The equations of motion of a wing are derived using Banerjee and Kane's assumed-modes analysis of a plate undergoing large motion [172]. Their analysis

assumes a plate undergoing large rigid-body translations and rotations while simultaneously experiencing small, linear deformations relative to the rigid-body position. The displacements are modeled as the sum of the non-rotational modes of the plate; Banerjee and Kane suggest that the modes be determined by finite element analysis (FEA) of the plate.

The full equation of motion as given by Banerjee and Kane for the i th mode (retaining most of their original notation) is

$$\begin{aligned}
& \sum_{j=1}^N \left\{ \mathcal{E}_{3ij} \ddot{q}_j + (\omega_1 \mathcal{E}_{2ij} - \omega_2 \mathcal{E}_{1ij}) \dot{q}_j + \left[\lambda_{ij} - (\dot{v}_1 + \omega_2 v_3 - \omega_3 v_2) \mathcal{C}_{ij} \right. \right. \\
& \quad - (\omega_1 \omega_2 - \dot{\omega}_3) \mathcal{C}_{2ij} + (\omega_2^2 + \omega_3^2) \mathcal{C}_{1ij} - (\dot{v}_2 + \omega_3 v_1 - \omega_1 v_3) \mathcal{D}_{ij} \\
& \quad - (\dot{\omega}_3 + \omega_1 \omega_2) \mathcal{D}_{1ij} + (\omega_3^2 + \omega_1^2) \mathcal{D}_{2ij} + (\dot{\omega}_1 + \omega_2 \omega_3) \mathcal{E}_{2ij} \\
& \quad \left. \left. + (\omega_3 \omega_1 - \dot{\omega}_2) \mathcal{E}_{1ij} - (\omega_1^2 + \omega_2^2) \mathcal{E}_{3ij} \right] q_j \right\} \\
& = -(\dot{v}_3 + \omega_1 v_2 - \omega_2 v_1) \mathcal{A}_i - (\dot{\omega}_1 + \omega_2 \omega_3) \mathcal{B}_{2i} - (\omega_3 \omega_1 - \dot{\omega}_2) \mathcal{B}_{1i} \quad (4.1)
\end{aligned}$$

Here, the terms \mathcal{A} – \mathcal{E} are integer functions of the mode shapes, λ_{ij} is an element of the non-rotational modal stiffness matrix (as calculated by FEA) and v and ω are elements of the respective translational rotational velocity vectors of the plate's rigid body motion as measured in the plate-fixed coordinate system.

We wish to apply Banerjee and Kane's equation of motion to the time-periodic system shown in figure 4.1. The inertial axes, flapping and feathering axes are defined identically to the assumed-modes beam model of previous chapters. As before, the rigid-body coordinate system $(\underline{i}, \underline{j}, \underline{k})$ is parallel to the feathering axes and lies an offset distance e_O ahead of the axis of feathering rotation. In contrast to the beam model, where the \underline{i} axis was defined as the elastic axis of the wing, we here define the \underline{i} axis so that it coincides with the rearmost point of the wing finite element model (FEM). This slight change is more convenient for defining the FEM

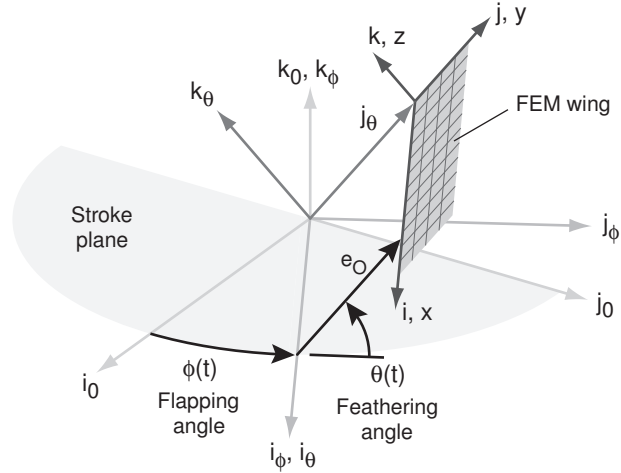


Figure 4.1: Coordinate systems for thin plate analysis. Not to scale.

and reflects that the location of the FEM's elastic axis is unknown beforehand.

There is no translational motion in the flapping system of figure 4.1 so all velocities $v = 0$ in the equation of motion Eq. 4.1. The rotations ω_1, ω_2 and ω_3 in Eq. 4.1 are equivalent to the rotational velocity of the feathering θ -axes as measured along $\underline{i}_\theta, \underline{j}_\theta$ and \underline{k}_θ , respectively:

$$\begin{Bmatrix} \omega_1 \\ \omega_2 \\ \omega_3 \end{Bmatrix} = \begin{Bmatrix} \dot{\theta} \\ \dot{\phi} \sin \theta \\ \dot{\phi} \cos \theta \end{Bmatrix} \quad (4.2)$$

Substituting Eq. 4.2 into Eq. 4.1 and setting all v terms equal to zero results in a

flapping-wing-specific equation:

$$\begin{aligned}
& \sum_{j=1}^N \left\{ \mathcal{E}_{3ij} \ddot{q}_j + \left[\dot{\theta} \mathcal{E}_{2ij} - \dot{\phi} \sin(\theta) \mathcal{E}_{1ij} \right] \dot{q}_j + \left[\lambda_{ij} - \ddot{\phi} \cos(\theta) (\mathcal{D}_{1ij} - \mathcal{C}_{2ij}) \right. \right. \\
& \quad - \ddot{\phi} \sin(\theta) \mathcal{E}_{1ij} + \dot{\phi}^2 \mathcal{C}_{1ij} - \dot{\phi}^2 \sin^2(\theta) \mathcal{E}_{3ij} + \dot{\phi}^2 \cos^2(\theta) \mathcal{D}_{2ij} \\
& \quad \left. \left. + \dot{\phi}^2 \sin(\theta) \cos(\theta) \mathcal{E}_{2ij} + \ddot{\theta} \mathcal{E}_{2ij} - \dot{\theta}^2 (\mathcal{E}_{3ij} - \mathcal{D}_{2ij}) - 2\dot{\phi}\dot{\theta} \sin(\theta) \mathcal{C}_{2ij} \right] q_j \right\} \\
& \quad = \ddot{\phi} \sin(\theta) \mathcal{B}_{1i} - \left[\ddot{\theta} + \dot{\phi}^2 \sin(\theta) \cos(\theta) \right] \mathcal{B}_{2i} \quad (4.3)
\end{aligned}$$

The terms \mathcal{B} through \mathcal{E} in Eq. 4.3 are integrals over the plate surface S :

$$\mathcal{B}_{1i} = \iint_S x_\theta \chi_{wi} \rho \, dx \, dy \quad (4.4)$$

$$\mathcal{B}_{2i} = \iint_S y_\theta \chi_{wi} \rho \, dx \, dy \quad (4.5)$$

$$\mathcal{C}_{1ij} = \iint_S x_\theta \alpha_{ij} \rho \, dx \, dy \quad (4.6)$$

$$\mathcal{C}_{2ij} = \iint_S y_\theta \alpha_{ij} \rho \, dx \, dy \quad (4.7)$$

$$\mathcal{D}_{1ij} = \iint_S x_\theta \beta_{ij} \rho \, dx \, dy \quad (4.8)$$

$$\mathcal{D}_{2ij} = \iint_S y_\theta \beta_{ij} \rho \, dx \, dy \quad (4.9)$$

$$\mathcal{E}_{1ij} = \iint_S \chi_{wi} \chi_{uj} \rho \, dx \, dy \quad (4.10)$$

$$\mathcal{E}_{2ij} = \iint_S \chi_{wi} \chi_{vj} \rho \, dx \, dy \quad (4.11)$$

$$\mathcal{E}_{3ij} = \iint_S \chi_{wi} \chi_{wj} \rho \, dx \, dy \quad (4.12)$$

The mass per unit area of the plate is ρ . The terms x_θ and y_θ are the distances from the origin of the feathering axes measured in the \underline{i}_θ and \underline{j}_θ directions and χ_{ui} ,

χ_{vi} and χ_{wi} are the displacements of the i th non-rotational mode in the \underline{i} , \underline{j} and \underline{k} directions. The functions α_{ij} and β_{ij} are line integrals across the plate:

$$\alpha_{ij}(x, y) = \int_0^x \left[\frac{\partial}{\partial x} \chi_{vi}(\sigma, y) \frac{\partial}{\partial x} \chi_{vj}(\sigma, y) + \frac{\partial}{\partial x} \chi_{wi}(\sigma, y) \frac{\partial}{\partial x} \chi_{wj}(\sigma, y) \right] d\sigma$$

$$\beta_{ij}(x, y) = \int_0^y \left[\frac{\partial}{\partial y} \chi_{ui}(x, \sigma) \frac{\partial}{\partial y} \chi_{uj}(x, \sigma) + \frac{\partial}{\partial y} \chi_{wi}(x, \sigma) \frac{\partial}{\partial y} \chi_{wj}(x, \sigma) \right] d\sigma$$

The above equations can be simplified further by assuming that the wing is relatively stiff in the plane of the wing, such that a linear model will not deform in the \underline{i} and \underline{j} directions. This assumption is justified later in section 4.6 by inspection of the numerically-calculated mode shapes. By this assumption, the modal deformations χ_u and χ_v will be $\chi_u = \chi_v = 0$ for all modes. Thus the integrals $\mathcal{E}_{1ij} = \mathcal{E}_{2ij} = 0$ and α_{ij} and β_{ij} simplify to

$$\alpha_{ij}(x, y) = \int_0^x \frac{\partial}{\partial x} \chi_{wi}(\sigma, y) \frac{\partial}{\partial x} \chi_{wj}(\sigma, y) d\sigma \quad (4.13)$$

$$\beta_{ij}(x, y) = \int_0^y \frac{\partial}{\partial y} \chi_{wi}(x, \sigma) \frac{\partial}{\partial y} \chi_{wj}(x, \sigma) d\sigma \quad (4.14)$$

Applying these simplifications to Eq. 4.3 and evaluating the equation for all assumed modes gives the matrix equation of motion

$$\begin{aligned} \mathcal{E}_3 \ddot{\underline{q}} + \left[\mathbf{\Lambda} - \ddot{\phi} \cos(\theta) (\mathcal{D}_1 - \mathcal{C}_2) + \dot{\phi}^2 \mathcal{C}_1 - \dot{\phi}^2 \sin^2(\theta) \mathcal{E}_3 \right. \\ \left. + \dot{\phi}^2 \cos^2(\theta) \mathcal{D}_2 - \dot{\theta}^2 (\mathcal{E}_3 - \mathcal{D}_2) - 2 \dot{\phi} \dot{\theta} \sin(\theta) \mathcal{C}_2 \right] \underline{q} \\ = \ddot{\phi} \sin(\theta) \mathcal{B}_1 - \left[\ddot{\theta} + \dot{\phi}^2 \sin(\theta) \cos(\theta) \right] \mathcal{B}_2 \end{aligned} \quad (4.15)$$

It stands for us now to calculate the mode shapes and numerically evaluate the integral matrices in Eq. 4.15, as explained in section 4.4.

4.3 Equivalence to Beam Formulation

The equivalence of the assumed-modes plate equation to the beam equation formulated in the previous chapters can be demonstrated by considering a rectangular plate with a small width, such that the plate properties and mode shapes do not vary with y . In this case, $\chi_{wi}(x, y) = \chi_{wi}(x)$ and $\partial\chi_{wi}/\partial y = 0$. Furthermore let us assume, as we did for the beam bending analysis in section 3.2, that the plate is modeled by a single mode and the feathering angle is fixed at $\theta = \pi/2$. For these assumptions, the homogenous form of Eq. 4.15 reduces to

$$\mathcal{E}_{311} \ddot{q}_1 + \left[\lambda_{11} + \dot{\phi}^2 (\mathcal{C}_{111} - \mathcal{E}_{311}) \right] q_1 = 0 \quad (4.16)$$

This is the dimensional form of the non-dimensional bending-only equation, Eq. 3.1 on page 124. It is trivial to show that the square of the first non-rotating bending frequency is the modal stiffness λ_{11} divided by the modal mass \mathcal{E}_{311} . The equivalence of the term \mathcal{C}_{111} can be shown by integrating over the width of the plate

$$\begin{aligned} \mathcal{C}_{111} &= \iint_S x_\theta \left[\int_0^x \frac{\partial}{\partial x} \chi_{w1}(\sigma, y) \frac{\partial}{\partial x} \chi_{w1}(\sigma, y) d\sigma \right] \rho dx dy \\ &= \int_0^R x_\theta \left[\int_0^x \frac{d}{dx} \chi_{w1}(\sigma) \frac{d}{dx} \chi_{w1}(\sigma) d\sigma \right] m dx \end{aligned}$$

and switching the order of integration:

$$\mathcal{C}_{111} = \int_0^R \left[\int_x^R m x_\theta dx \right] \frac{d}{dx} \chi_{w1}(\sigma) \frac{d}{dx} \chi_{w1}(\sigma) d\sigma \quad (4.17)$$

Since $x_\theta = x$, the bracketed term in Eq. 4.17 is the mass moment S_x (Eq. 2.32, p. 95) and \mathcal{C}_{111} is equivalent to \mathcal{T}_{11} as defined on page 99.

General equivalences between the equations of motion of the beam formulation and plate formulation can be determined by inspection of the bending-torsion

beam equation Eq. 2.42 (p. 101) and the plate equation Eq. 4.15:

$$\begin{aligned}
 \Lambda &\equiv \begin{bmatrix} \mathcal{G} & 0 \\ 0 & \mathcal{H} + k_{\text{root}}\mathcal{W} \end{bmatrix} \\
 \mathcal{C}_1 &\equiv \begin{bmatrix} \mathcal{Q} & \mathcal{R} - \mathcal{S} \\ (\mathcal{R} - \mathcal{S})^T & \mathcal{T} \end{bmatrix} \\
 \mathcal{C}_2 &\equiv \begin{bmatrix} \mathcal{K} & \mathcal{L} - \mathcal{M} \\ (\mathcal{L} - \mathcal{M})^T & \mathcal{N} \end{bmatrix} \\
 \mathcal{D}_1 &\equiv \begin{bmatrix} \mathcal{J} & 0 \\ 0 & 0 \end{bmatrix} \\
 \mathcal{D}_2 &\equiv \begin{bmatrix} \mathcal{A} + \mathcal{V} & 0 \\ 0 & 0 \end{bmatrix} \\
 \mathcal{E}_3 &\equiv \begin{bmatrix} \mathcal{A} & \mathcal{B} \\ \mathcal{B}^T & \mathcal{C} \end{bmatrix} \\
 \mathcal{B}_1 &\equiv \begin{Bmatrix} \underline{F}_{\gamma\mathcal{B}} \\ \underline{F}_{w\mathcal{B}} \end{Bmatrix} \\
 \mathcal{B}_2 &\equiv \begin{Bmatrix} \underline{F}_{\gamma\mathcal{C}} \\ \underline{F}_{w\mathcal{C}} \end{Bmatrix}
 \end{aligned}$$

where the matrices on the right-hand side of the equations are defined on page 99. Note that these general equivalences hold, but that differences in selection of assumed mode shapes will alter the exact forms of the matrices. For example, using FEA to identify the normal mode shapes of a given plate will eliminate the coupling matrices \mathcal{B} in the modal mass matrix \mathcal{E}_3 ; in fact, \mathcal{E}_3 will be strictly diagonal.

4.4 Finite Element Analysis

The assumed mode shapes are calculated using the FEA applications of the I-DEAS 11 NX program. This program allows for easy definitions of layouts and materials for finite element models (FEM), automatic mesh generation and normal mode solutions. All FEMs are created using 8-node parabolic plate elements [173] as shown in figure 4.2. The mapping/shape functions N_i for the element are given by

$$f(\xi, \eta) = \sum_{i=1}^8 N_i(\xi, \eta) (f_{node})_i = \underline{N}^T \underline{f}_{node} \quad (4.18)$$

$$\underline{N}(\xi, \eta) = \frac{1}{4} \begin{Bmatrix} -(1+\xi)(1-\eta)(1-\xi+\eta) \\ 2(1+\xi)(1+\eta)(1-\eta) \\ -(1+\xi)(1+\eta)(1-\xi-\eta) \\ 2(1+\xi)(1-\xi)(1+\eta) \\ -(1-\xi)(1+\eta)(1+\xi-\eta) \\ 2(1-\xi)(1+\eta)(1-\eta) \\ -(1-\xi)(1-\eta)(1+\xi+\eta) \\ 2(1+\xi)(1-\xi)(1-\eta) \end{Bmatrix} \quad (4.19)$$

where f is the function over the surface of the element and $(f_{node})_i$ is the function value at the i th node. Each node has three translational degrees of freedom ($u, v,$

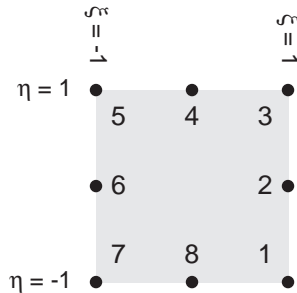


Figure 4.2: Position and numbering of parabolic plate element nodes.

w) and three rotational degrees of freedom ($\gamma_x, \gamma_y, \gamma_z$), so that the 8-node element has 48 degrees of freedom.

The I-DEAS mesh-generation FEA application outputs the nodal positions (x, y, z) for the mesh, the connectivity vector for each element and the density ρ of each element. The normal mode FEA solution outputs the nodal displacements ($u, v, w, \gamma_x, \gamma_y, \gamma_z$) for each normal mode, the modal masses of each mode (which are the diagonal entries of the matrix \mathcal{E}_3) and the natural frequency ω_i for the mode. Since the modes are normal for this linear model the off-diagonal modal masses are zero, $\mathcal{E}_{3ij} = \mathcal{E}_{3ji} = 0, i \neq j$. The entries of the diagonal modal stiffness matrix Λ can be calculated by $\lambda_{ii} = \omega_i^2 \mathcal{E}_{3ii}$ but, as we shall see, non-dimensionalization of the equations of motion makes this calculation unnecessary.

The surface integrals in Eqs. 4.4–4.12 are evaluated by summing the integrals over the surfaces of the individual elements. The elemental surface integrals are in turn approximated by Gaussian quadrature, in which an integral of a function f is approximated by the weighted summation of that function evaluated at points known as quadrature points.

$$\begin{aligned} \iint_{\text{Element}} f(x, y) dx dy &= \int_{-1}^1 \int_{-1}^1 f(\xi, \eta) \det \mathbf{J}(\xi, \eta) d\xi d\eta \\ &\approx \sum_i \sum_j f(\xi_i, \eta_j) \det \mathbf{J}(\xi_i, \eta_j) W_i W_j \end{aligned} \quad (4.20)$$

The Jacobian matrix \mathbf{J} of the mapping $(x, y) \rightarrow (\xi, \eta)$ is equal to

$$\mathbf{J}(\xi, \eta) = \begin{bmatrix} \frac{\partial x}{\partial \xi} & \frac{\partial x}{\partial \eta} \\ \frac{\partial y}{\partial \xi} & \frac{\partial y}{\partial \eta} \end{bmatrix} \quad (4.21)$$

The 5-point quadrature points and weights used in this study are listed in table 4.1 and depicted in figure 4.3.

Table 4.1: 5×5 Gauss quadrature points and weights.

ξ_i, η_j	W_i, W_j
0	0.568889
± 0.538469	0.478629
± 0.906180	0.236927

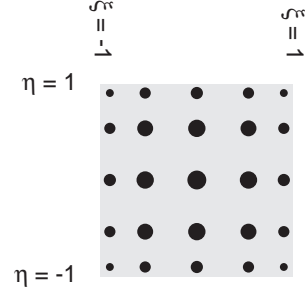


Figure 4.3: Quadrature points on plate element. Areas of circles are proportional to $W_i W_j$

4.4.1 Approximation of α_{ij} and β_{ij} with Radial Basis Functions

The modal displacements χ_w can easily be calculated at the quadrature points on an element-by-element basis in order to evaluate the surface integrals. Calculating the functions α_{ij} and β_{ij} (Eqs. 4.13–4.14) is not so simple, because they require line integrals to be evaluated over several elements. Banerjee and Kane suggest evaluating the surface integrals Eqs. 4.6–4.9 by using integration by parts to eliminate α_{ij} and β_{ij} , and they demonstrate the technique for a uniform rectangular plate [172]. Unfortunately, creating an integration-by-parts solution for a general nonuniform, nonrectangular plate is prohibitively difficult, so we choose to evaluate α_{ij} and β_{ij} directly. At this time, we note that the spatial derivatives $\partial\chi_w/\partial x$ and $\partial\chi_w/\partial y$ in the integrands of α_{ij} and β_{ij} are given by the rotation angles from the FEA:

$$\partial\chi_w/\partial x = -\gamma_y$$

$$\partial\chi_w/\partial y = \gamma_x$$

Exactly evaluating α_{ij} and β_{ij} would require finding all of the elements along the line of integration and numerically solving a line integral of over each individual element. This procedure would be additionally complicated for a general

mesh because of the nonuniform orientation of the automatically-generated grids, as illustrated by figure 4.4.* Instead, we would like to eliminate the need to identify and integrate over individual elements. One possibility is using the nodal data to construct a spline approximation of the integrands over the entire plate surface and integrating the spline to find α_{ij} and β_{ij} . But calculating an accurate spline over the entire surface is numerically expensive for large data sets. As an alternative, we use radial basis functions (RBFs) to generate local approximations of the integrands on the fly.

Radial basis functions are typically used in meshless finite volume methods, in which a volume is modeled by distributed, unconnected nodes [174]. As opposed to meshed FEA methods in which nodes' influences on one another are determined by the element connectivity, meshless methods use the proximity of nodes to weight their influence. Much of the background and analysis of RBFs is beyond the scope of this thesis; we are merely interested in their use to approximate a function from the distributed nodes of a nonuniform FEM mesh. The key feature of RBFs (more specifically, RBFs with compact support) is that they have a finite neighborhood of influence, or support. This allows local approximation of a function without considering the entire FEM domain.

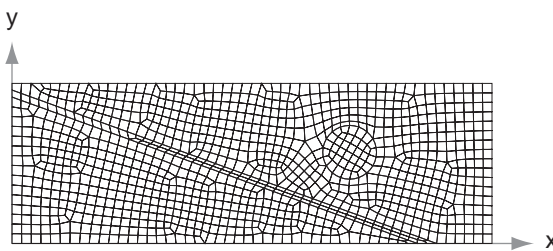


Figure 4.4: Example nonuniform plate FEM mesh. Mesh created by manually partitioning plate area, then applying I-DEAS' automatic mesh-generation routine.

*The rectangular plate in figure 4.4 has been manually partitioned to generate the nonuniform grid. A rectangular plate would normally be meshed with uniform rectangular elements. However, use of nonuniform materials (e.g., spars vs. membranes) or nonrectangular geometries will lead to similarly nonuniform meshes.

Radial basis functions ϕ have the form $\phi(r)$, where r is the positive distance measured between points of interest [175]. In this thesis, we choose the RBF

$$\phi(r) = \begin{cases} (1-r)^4(4r+1) & 0 \leq r \leq 1 \\ 0 & r > 1 \end{cases} \quad (4.22)$$

The support radius of this RBF is $r = 1$, but it can be arbitrarily scaled to some radius R by taking $\phi(r) = \phi(r/R)$. For some N nodes, a function f at a point $\underline{x}_0 = (x_0, y_0)$ is given as a weighted sum of RBFs

$$f(\underline{x}_0) = \sum_{i=1}^N a_i \phi(\|\underline{x}_i - \underline{x}_0\|) \quad (4.23)$$

where $\|\underline{x}_i - \underline{x}_0\|$ is the distance between \underline{x}_0 and the i th node \underline{x}_i .

Interpolation at a general point \underline{x}_0 is performed as follows. First, the N nodes within the interpolation support radius R are identified, as shown in figure 4.5. The unknown coefficients a_i are solved with Eq. 4.23 by creating a system of linear equations for the known nodal function values $f(\underline{x}_j)$, $j = 1, \dots, N$. Once these coefficients are known, Eq. 4.23 is used to interpolate the function value $f(\underline{x}_0)$. By calculating the RBFs between the fixed FEM nodes prior to interpolation, significant computational overhead is saved, making this interpolation method relatively time-efficient.

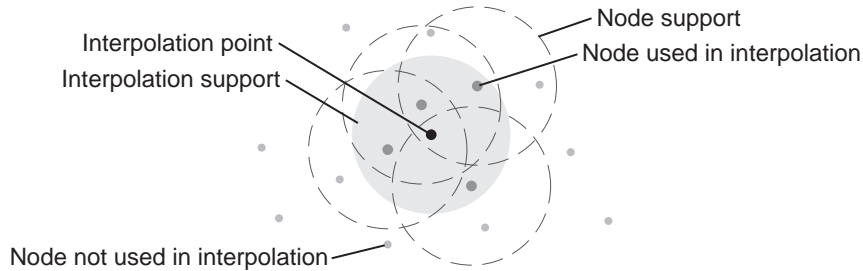


Figure 4.5: Radial basis function interpolation domain.

For the calculation of α_{ij} , then, the integrand $(\partial\chi_{wi}/\partial x)(\partial\chi_{wj}/\partial x) = \gamma_{yi} \gamma_{yj}$ is approximated using the RBF interpolation at any points needed for the numerical integration; β_{ij} is calculated similarly. Validation of this method and discussion of the selection of the support radius R is postponed to section 4.4.3.

4.4.2 Mode Shape Validation

The FEM output from the I-DEAS 11 NX program was validated by calculating the mode shapes of a uniform isotropic rectangular plate of length a and width b with simply-supported boundaries on all edges. This boundary condition was selected because the mode shapes and natural frequencies are known exactly [176, p. 44] and are given for any integers m and n by

$$\chi_{wmn}(x, y) = \sin\left(\frac{m\pi x}{a}\right) \sin\left(\frac{n\pi y}{b}\right) \quad (4.24)$$

$$\omega_{mn} = \sqrt{\frac{D}{\rho} \left[\left(\frac{m\pi}{a}\right)^2 + \left(\frac{n\pi}{b}\right)^2 \right]} \quad (4.25)$$

In Eq. 4.25, the flexural rigidity D is $D = Et^3/12(1 - \nu^2)$ where E is the Young's modulus, t is plate thickness and ν is Poisson's ratio; and ρ is the mass per unit area of the plate. Table 4.2 gives the properties of the plate used for validation.

The FEA output was validated by comparing the modal displacements χ_w predicted at the nodes of a FEM to the exact displacements at the same location

Table 4.2: Plate properties for FEA validation.

Property	Value
E	2×10^5 MPa
t	.5 mm
ν	.3
ρ	4 kg/m ²
a	100 mm
b/a	1/4, 1/3

as calculated by Eq. 4.24. The plate was modeled and meshed using the I-DEAS program and the first ten natural modes were calculated and saved. The integers m, n corresponding to the ten lowest exact natural frequencies were selected using Eq. 4.25 and the exact modal displacements were calculated. The FEA and exact data of χ_w may differ by a scale factor, so the FEA modes were scaled so that the mean value of χ_w^2 over all the node points was equal to the mean value of χ_w^2 of the corresponding exact mode. The mean and standard deviation of the difference of the scaled FEA data from the exact data (i.e., $\chi_w \text{ error} = (\chi_w)_{\text{exact}} - (\chi_w)_{\text{FEM}}$) provide measures of the quality of the FEA results. Additionally, the natural frequencies calculated from the FEA were checked against the exact frequencies from Eq. 4.25.

Two plates were used in the FEM validation having width-to-length ratios of $1/3$ and $1/4$ respectively. Four meshes were automatically generated for each plate with nominal element lengths of $5, 3\frac{1}{3}, 2$ and 1 mm. The 2-mm element (corresponding to a 50×17 -element mesh on the $1/3$ plate and a 50×13 -element mesh on the $1/4$ plate) was selected as sufficiently fine to resolve the mode shapes. Figure 4.6 shows the first six modes of the $1/3$ plate. Tables 4.3 and 4.4 give the

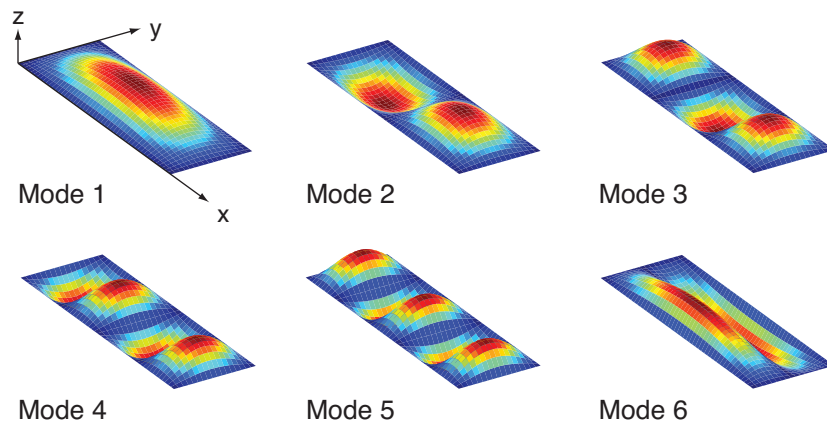


Figure 4.6: Normal modes of a simply-supported plate from FEA; $b/a = 1/3$, 50×17 rectangular mesh. Element color is proportional to the magnitude of displacement at the element centroid.

results of the validation with the 2-mm element. For reference, the maximum magnitude of the exact mode shapes of Eq. 4.24 is $|\chi_w| = 1$ mm for all modes. The FEA under-predicts the exact natural frequency within 0.3% for all cases and within 0.15% for the first five modes. The mean error in the FEA modes χ_w is at least a factor of 10^{-6} smaller than the maximum modal displacement in all cases and the standard deviation of the FEA modal errors is approximately a factor of 10^{-5} smaller than the maximum modal magnitude.

Table 4.3: FEA validation results for a simply supported plate, $b/a = 1/3$.

Mode (m, n)	Exact ω_{mn} [Hz]	FEA ω_{mn} error	Mean χ_w error [mm]	STD χ_w error [mm]
1 (1,1)	1188	-.035%	1.26×10^{-6}	5.75×10^{-5}
2 (2,1)	1545	-.046%	-2.74×10^{-15}	6.30×10^{-5}
3 (3,1)	2139	-.064%	4.02×10^{-7}	5.44×10^{-5}
4 (4,1)	2971	-.089%	-4.90×10^{-15}	2.99×10^{-5}
5 (5,1)	4040	-.120%	-2.33×10^{-7}	3.82×10^{-5}
6 (1,2)	4397	-.130%	-1.15×10^{-17}	4.47×10^{-5}
7 (2,2)	4753	-.141%	5.07×10^{-14}	4.26×10^{-5}
8 (6,1)	5348	-.160%	-4.47×10^{-16}	1.10×10^{-4}
9 (3,2)	5348	-.160%	2.90×10^{-17}	1.08×10^{-4}
10 (4,2)	6179	-.185%	-7.22×10^{-12}	3.86×10^{-5}

Table 4.4: FEA validation results for a simply supported plate, $b/a = 1/4$.

Mode (m, n)	Exact ω_{mn} [Hz]	FEA ω_{mn} error	Mean χ_w error [mm]	STD χ_w error [mm]
1 (1,1)	2020	-.060%	-2.28×10^{-7}	3.06×10^{-5}
2 (2,1)	2377	-.071%	-3.56×10^{-14}	3.17×10^{-5}
3 (3,1)	2971	-.088%	6.57×10^{-7}	3.11×10^{-5}
4 (4,1)	3803	-.114%	1.36×10^{-14}	3.10×10^{-5}
5 (5,1)	4872	-.146%	5.18×10^{-8}	3.47×10^{-5}
6 (6,1)	6179	-.185%	-3.44×10^{-15}	4.37×10^{-5}
7 (1,2)	7724	-.232%	-1.31×10^{-12}	6.11×10^{-5}
8 (7,1)	7724	-.228%	1.23×10^{-7}	5.30×10^{-5}
9 (2,2)	8081	-.240%	-1.22×10^{-13}	6.88×10^{-5}
10 (3,2)	8675	-.259%	1.13×10^{-12}	6.33×10^{-5}

4.4.3 Radial Basis Function Interpolation Validation

The radial basis function interpolation of α_{ij} and β_{ij} described in section 4.4.1 was validated on the 1/3 simply-supported plate with the properties given in table 4.2. In order to test the interpolation on a nonuniform mesh, we use the mesh shown in figure 4.4 on page 161 to validate the interpolation. This mesh was automatically generated by the I-DEAS with a target element length of 2 mm, as used in the above validation. The interpolation support radius R was chosen to be 4 mm, or twice the automatic meshing routine's target element length. The accuracy of the interpolation was validated by calculating α_{ij} for the first five modes at evenly-distributed points on the plate and comparing the results to the exact solution. The points chosen for this comparison are the locations of the corner nodes (i.e., nodes 1, 3, 5, 7) of the elements of the 50×17 rectangular mesh used for the mode shape validation. In general, the points at which α_{ij} are compared *are not* nodes of the non-uniform mesh. As before, the FEA modes were scaled so that they have the same mean value of χ_w^2 over all sampling points as the exact solution. Figure 4.7 shows a typical $\alpha_{ij}(x, y)$ plotted on $0 < x \leq a$.

As in the previous section, the mean and standard deviations of α_{ij} error = $(\alpha_{ij})_{\text{exact}} - (\alpha_{ij})_{\text{RBF}}$ over the selected points are measures of the quality of the interpolation. Table 4.5 gives the validation results (the reported maximum $|\alpha_{ij}|$ is for the entire plate, not just the sampling points). For all modal combinations,

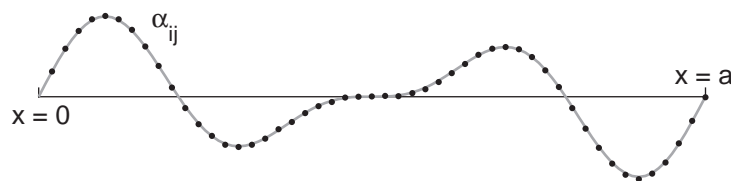


Figure 4.7: Graphical comparison of exact and approximate α_{ij} . Gray line is exact solution, dots are numerical solution using RBF approximations. α_{15} shown, calculated at $y = .3755b = 12.52$ mm.

Table 4.5: RBF interpolation validation results for a simply supported plate, $b/a = 1/3$.

i,j	$ \alpha_{ij} _{\max}$ [mm]	Mean α_{ij} error [mm]	STD α_{ij} error [mm]
1,1	49.3	-.0289	.0286
1,2	29.6	-.0228	.0388
1,3	30.6	-.00431	.0562
1,4	31.0	-.000532	.0728
1,5	31.1	.0239	.0844
2,2	197	-.0793	.0944
2,3	113	-.0523	.0947
2,4	59.2	-.0174	.116
2,5	74.8	.00300	.150
3,3	444	-.116	.142
3,4	199	-.0753	.170
3,5	140	-.0780	.244
4,4	790	-.0984	.279
4,5	349	-.0517	.264
5,5	1234	.463	.742

the mean error in α_{ij} is approximately a factor of 10^{-3} smaller than the respective maximum magnitude of α_{ij} ; the standard deviation of the error is similarly small. Note that the calculation of α_{ij} via RBF interpolation encompasses two approximations: first, the approximation of the FEM modes to the actual modes and second, the approximation of the RBF interpolation to the FEM modes. Even with these dual approximations, the calculated values of α_{ij} have small enough errors that the RBF interpolation method can be considered valid for this study.

4.4.4 Matrix Calculation Validation

As a final check of the numerical methods used for our approximations, we calculate the matrices \mathcal{C}_1 through \mathcal{E}_3 using the FEM modes and RBF interpolation and compare them with the exact integral values. We use again the 1/3 plate with properties given in table 4.2 and the nonuniform FEM mesh shown in figure 4.4;

the origin of the plate-fixed axes are coincident with the feathering axes, so that $x_\theta = x$ and $y_\theta = y$. The exact integrals were solved by symbolically evaluating Eqs. 4.6–4.12 using MATLAB’s Symbolic Toolbox functions and substituting the plate properties into the symbolic solutions. In contrast to the previous validation studies, the exact solutions are scaled to the FEM modes and not vice versa. The scaling factors were chosen to make the modal masses of the exact solution the same as the modal masses from the FEA, so that the \mathcal{E}_3 matrices are identical for the exact and FEM solutions.

Table 4.6 gives the exact and approximate FEM equation-of-motion matrices for the first five modes. The FEM matrices agree very well with the nonzero entries of the exact matrices. The FEM matrices do not accurately capture the matrix zeros, instead giving values that are one to four orders of magnitude smaller than the true nonzero entries. This will have the effect of introducing nonphysical couplings into the system. However, it is not clear that a general wing will have null entries

Table 4.6: Equation-of-motion matrices for simply supported plate, $b/a = 1/3$.

	Exact [mm ²]	FEM [mm ²]
\mathcal{C}_1	$\begin{bmatrix} 1.14 & .835 & .353 & -.171 & -.102 \\ & 4.85 & -2.35 & .627 & .297 \\ & & 11.0 & 3.46 & .900 \\ & \text{SYM.} & & 11.1 & -3.43 \\ & & & & 11.1 \end{bmatrix}$	$\begin{bmatrix} 1.14 & .837 & .352 & -.170 & -.103 \\ & 4.86 & -2.35 & .626 & .296 \\ & & 11.1 & 3.46 & .895 \\ & \text{SYM.} & & 11.1 & -3.44 \\ & & & & 11.1 \end{bmatrix}$
\mathcal{C}_2	$\begin{bmatrix} .309 & .278 & 0 & -5.68e-2 & 0 \\ & 1.24 & -.782 & 0 & 9.90e-2 \\ & & 2.78 & 1.15 & 0 \\ & \text{SYM.} & & 2.79 & -1.14 \\ & & & & 2.79 \end{bmatrix}$	$\begin{bmatrix} .310 & .279 & -1.77e-4 & -5.68e-2 & -2.13e-4 \\ & 1.24 & -.784 & -3.20e-4 & 9.91e-2 \\ & & 2.79 & 1.15 & -1.35e-3 \\ & \text{SYM.} & & 2.79 & -1.14 \\ & & & & 2.79 \end{bmatrix}$
\mathcal{D}_1	$\begin{bmatrix} 2.78 & -1.00 & 0 & 6.02e-2 & 0 \\ & 2.78 & 1.08 & 0 & -6.15e-2 \\ & & 2.78 & -.830 & 0 \\ & \text{SYM.} & & 1.57 & -.502 \\ & & & & 1.00 \end{bmatrix}$	$\begin{bmatrix} 2.78 & -1.00 & 8.52e-4 & 6.00e-2 & 1.16e-3 \\ & 2.79 & 1.08 & -3.48e-4 & -6.28e-2 \\ & & 2.78 & -.830 & -6.41e-4 \\ & \text{SYM.} & & 1.57 & -.502 \\ & & & & 1.00 \end{bmatrix}$
\mathcal{D}_2	$\begin{bmatrix} 1.14 & 0 & 0 & 0 & 0 \\ & 1.14 & 0 & 0 & 0 \\ & & 1.14 & 0 & 0 \\ & \text{SYM.} & & .644 & 0 \\ & & & & .413 \end{bmatrix}$	$\begin{bmatrix} 1.14 & 3.71e-4 & 2.74e-5 & -5.85e-5 & 2.76e-4 \\ & 1.14 & -5.09e-4 & -3.35e-4 & -4.39e-4 \\ & & 1.14 & 4.01e-5 & -5.51e-5 \\ & \text{SYM.} & & .644 & 1.94e-5 \\ & & & & .412 \end{bmatrix}$
\mathcal{E}_3	$\begin{bmatrix} .376 & & & & \\ & .376 & & & \\ & & .376 & & \\ & & & .212 & \\ & & & & .136 \end{bmatrix}$	$\begin{bmatrix} .376 & & & & \\ & .376 & & & \\ & & .376 & & \\ & & & .212 & \\ & & & & .136 \end{bmatrix}$

in these matrices—it is likely they arise because of the simple geometry we have chosen for the validation study. Since the nonzero matrix entries are captured accurately, we conclude this numerical method is valid with the understanding that there *may* be some small nonphysical couplings in a general system.

4.5 Non-dimensional Analysis

Now that we know we can accurately calculate the dimensional assumed-modes plate equation of motion via FEA, we can continue by rewriting it in non-dimensional form. As before, we introduce non-dimensional time $\tau = \omega t$ and non-dimensional prescribed flapping and feathering rotations $\hat{\phi}$ and $\hat{\theta}$:

$$\hat{\phi}(\tau) = \begin{cases} \phi(\frac{\tau}{\omega})/(\Phi/2) & \Phi \neq 0 \\ 0 & \Phi = 0 \end{cases}$$

$$\hat{\theta}(\tau) = \begin{cases} \theta(\frac{\tau}{\omega})/(\Theta/2) & \Theta \neq 0 \\ 0 & \Theta = 0 \end{cases}$$

For the plate case, it is not necessary to non-dimensionalize the equations in terms of the structural plate properties (i.e., mass, stiffness, etc.). The primary insight from non-dimensionalizing the beam equations was the effect of the beam’s non-rotating natural frequencies on the equations of motion. This effect can be easily determined from the results of the FEA in our plate model.

Note that we use a slightly different nomenclature for the plate modes, normalizing to the lowest natural frequency ω_1 instead of the lowest cantilever natural frequency ω_{cant} ; thus the representative non-dimensional stiffness for the plate model is ω_1/ω , the *normalized first natural frequency*. This change is reflective of the generality of the modes of the plate model, where “bending” and “torsion”

deformations need not be distinct.

Substituting the non-dimensional flapping and feathering rotations $\hat{\phi}$ and $\hat{\theta}$ into the the equation of motion Eq. 4.15 and dividing through by ω^2 gives

$$\begin{aligned} \mathcal{E}_3 \tilde{q} + \left[\frac{1}{\omega^2} \Lambda - \frac{\Phi}{2} \hat{\phi} \cos \theta (\mathcal{D}_1 - \mathcal{C}_2) + \frac{\Phi^2}{4} \hat{\phi}^2 \mathcal{C}_1 - \frac{\Phi^2}{4} \hat{\phi}^2 \sin^2 \theta \mathcal{E}_3 \right. \\ \left. + \frac{\Phi^2}{4} \hat{\phi}^2 \cos^2 \theta \mathcal{D}_2 - \frac{\Theta^2}{4} \hat{\theta}^2 (\mathcal{E}_3 - \mathcal{D}_2) - \frac{\Phi \Theta}{2} \hat{\phi} \hat{\theta} \sin \theta \mathcal{C}_2 \right] \tilde{q} \\ = \frac{\Phi}{2} \hat{\phi} \sin \theta \mathcal{B}_1 - \left[\frac{\Theta}{2} \hat{\theta} + \frac{\Phi^2}{4} \hat{\phi}^2 \sin \theta \cos \theta \right] \mathcal{B}_2 \quad (4.26) \end{aligned}$$

This equation can be fully non-dimensionalized by multiplying through by \mathcal{E}_3^{-1} . Recall that \mathcal{E}_3 is the diagonal modal mass matrix and Λ is the diagonal modal stiffness matrix, so that $\mathcal{E}_3^{-1} \Lambda$ is a diagonal matrix of the squared non-rotational frequencies of the structure:

$$\mathcal{E}_3^{-1} \Lambda = \begin{bmatrix} \omega_1^2 & & \\ & \ddots & \\ & & \omega_N^2 \end{bmatrix} \quad (4.27)$$

We continue multiplying Eq. 4.26 by \mathcal{E}_3^{-1} , using the relationship of Eq. 4.27. The result can be rearranged into the form

$$\begin{aligned} \tilde{q} + \left[(\omega_1/\omega)^2 \mathbf{K}_\omega - \Phi \hat{\phi} \cos(\theta) \mathbf{K}_{\phi c}^{**} + \Phi^2 \hat{\phi}^2 \mathbf{K}_{\phi^2}^{*2} - \Phi^2 \hat{\phi}^2 \sin^2(\theta) \mathbf{K}_{\phi^2 s^2}^{*2} \right. \\ \left. + \Phi^2 \hat{\phi}^2 \cos^2(\theta) \mathbf{K}_{\phi^2 c^2}^{*2} - \Theta^2 \hat{\theta}^2 \mathbf{K}_{\theta^2}^{*2} + \Phi \Theta \hat{\phi} \hat{\theta} \sin(\theta) \mathbf{K}_{\phi \theta s}^{*2} \right] \tilde{q} \\ = \Phi \hat{\phi} \sin \theta \tilde{F}_{\phi s}^{**} - \Theta \hat{\theta} \tilde{F}_{\theta}^{**} - \Phi^2 \hat{\phi}^2 \sin \theta \cos \theta \tilde{F}_{\phi^2 s c}^{*2} \quad (4.28) \end{aligned}$$

where the matrices are defined as

$$\begin{aligned}
\mathbf{K}_\omega &= \frac{1}{\omega_1^2} \begin{bmatrix} \omega_1^2 & & \\ & \ddots & \\ & & \omega_N^2 \end{bmatrix} \\
\mathbf{K}_{\phi c}^{**} &= \frac{1}{2} \boldsymbol{\mathcal{E}}_3^{-1} (\mathbf{D}_1 - \mathbf{C}_2) \\
\mathbf{K}_{\phi^2}^* &= \frac{1}{4} \boldsymbol{\mathcal{E}}_3^{-1} \mathbf{C}_1 \\
\mathbf{K}_{\phi^2 s^2}^* &= \frac{1}{4} \mathbf{I} \\
\mathbf{K}_{\phi^2 c^2}^* &= \frac{1}{4} \boldsymbol{\mathcal{E}}_3^{-1} \mathbf{D}_2 \\
\mathbf{K}_{\theta^2}^* &= \frac{1}{4} (\mathbf{I} - \boldsymbol{\mathcal{E}}_3^{-1} \mathbf{D}_2) \\
\mathbf{K}_{\phi \theta s}^{**} &= -\frac{1}{2} \boldsymbol{\mathcal{E}}_3^{-1} \mathbf{C}_2
\end{aligned}$$

and the forcing vectors are

$$\begin{aligned}
\tilde{\mathbf{F}}_{\phi s}^{**} &= \frac{1}{2} \boldsymbol{\mathcal{E}}_3^{-1} \underline{\mathbf{B}}_1 \\
\tilde{\mathbf{F}}_{\theta}^{**} &= \frac{1}{2} \boldsymbol{\mathcal{E}}_3^{-1} \underline{\mathbf{B}}_2 \\
\tilde{\mathbf{F}}_{\phi^2 sc}^* &= \frac{1}{4} \boldsymbol{\mathcal{E}}_3^{-1} \underline{\mathbf{B}}_2
\end{aligned}$$

We see that the non-dimensional plate equation of motion in Eq. 4.28 has the same form as the non-dimensional beam equation of motion in Eq. 2.75 on page 113, demonstrating their equivalence.

The matrix \mathbf{K}_ω is a determined solely from the natural frequencies of the system. In order to reduce numerical errors, \mathbf{K}_ω is calculated using the natural frequencies given by the FEA output, as opposed to solving $\boldsymbol{\mathcal{E}}_3^{-1} \boldsymbol{\Lambda}$. Likewise, the entries of $\boldsymbol{\mathcal{E}}_3$ are taken directly from the modal masses output by the FEA. As a check, however, the modal masses of $\boldsymbol{\mathcal{E}}_3$ are also calculated from the mode shapes

by the surface integral Eq. 4.12 to confirm that the FEA output is valid.

4.6 Representative Wing FEM

We use the representative wing developed for the beam analysis in section 2.2.2 as the model wing for the the plate analysis, so that the results can be directly compared. We use the physical properties of hawkmoth wings given by Combes, specifically a wing length of 52.2 mm and a uniform wing density of 0.5 mg/mm^3 . The feathering axis is coincident with the chordwise center of gravity. In keeping with our beam model, the chord has been chosen as 1/4 the wing length. Young's modulus has been selected so that the wing has a bending stiffness of approximately $EI_z = 1.09 \times 10^{-4} \text{ Nm}^2$, near the average for dorsal and ventral mean stiffnesses of *Manduca sexta* hawkmoths measured by Combes [127, p. 145]. We also use a Poisson's ratio of .495 as reported by Combes [127, p. 108]. All material properties are modeled as isotropic. Table 4.7 summarizes the wing

Table 4.7: Plate properties for representative wing FEM.

Property	Value
R	52.2 mm
c	13.05 mm
e_O	-9 mm
E	33 GPa
ν	.495
<u>Leading section</u>	
t	.1931 mm
ρ	.0966 mg/mm ²
Fraction of chord	42%
<u>Trailing section</u>	
t	.0350 mm
ρ	.0175 mg/mm ²
Fraction of chord	58%

properties.

The FEM was meshed using an automatic meshing routine with a target element length of $R/50$. The resulting mesh is shown in figure 4.8. This FEM is designated as the “straight-spar” wing. A cantilever boundary is applied at the root of the wing. The first six non-rotational modes are shown in figure 4.9. These are solely out-of-plane deformation modes. As asserted in the derivation of the plate equations, the wing is stiff in-plane so the deformations in the \underline{i} and \underline{j} directions are effectively zero—the maximum deflections in the \underline{i} and \underline{j} directions have magnitudes on the order of 10^{-14} times those in the \underline{k} direction for all modes.[†]

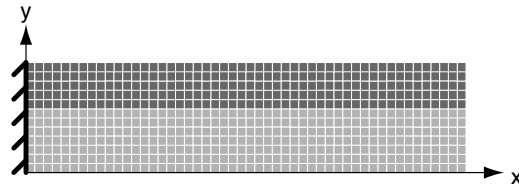


Figure 4.8: Planform view of FEM mesh of straight-spar wing. Thick leading elements are dark gray, thin trailing elements are light gray.

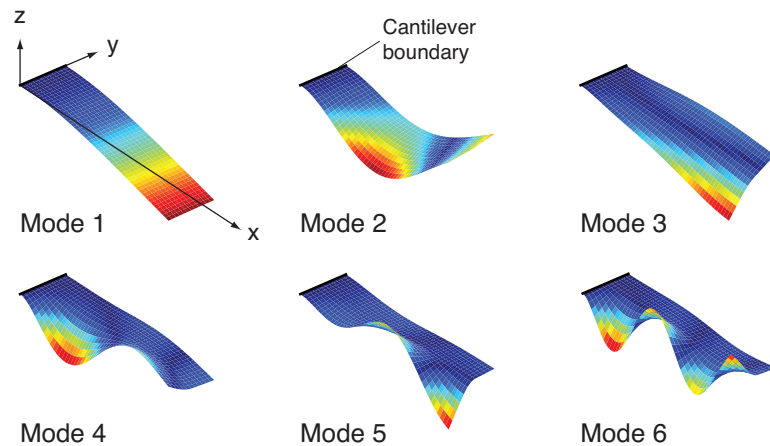


Figure 4.9: Normal modes of the straight-spar wing FEM. Element color is proportional to the magnitude of displacement at the element centroid.

[†]The FEM used to calculate the plate modes does not have any restraints limiting deformations to the out-of-plane direction. In contrast to the assumed-modes plate derivation of section 4.2, there is no *a priori* assumption that the FEM modes will not deform in the \underline{i} and \underline{j} directions. Rather, the normal-modes analysis simply does not identify any the deflections in the \underline{i} and \underline{j} directions.

The first mode shows no chordwise variation in deformations and reproduces the first bending mode of a slender cantilever beam. The second mode shows minor chordwise variations, but in shape approximates the second bending mode of a cantilever beam. The third mode, in contrast, is a torsional mode while the fourth, fifth and sixth modes are higher-order deformations of the trailing membrane.

4.6.1 Split-Spar Wing

In order to investigate the effects of structural layout and non-uniform spanwise structural properties, the straight-spar FEM was modified to create an alternate “split-spar” wing model, shown in figure 4.10. The thickened leading-edge elements in the straight-spar wing are divided into two equal-sized spars in the split-spar wing, one of which is angled backwards so as to intersect the trailing edge at the wing tip. This configuration approximates the trailing radial spars that are often incorporated into insect-like MAV wings (cf. Singh and Chopra’s wing shown in figure 1.33b). The weight and out-of-plane spanwise bending stiffness of the split-spar wing is identical to the straight-spar wing. The first six non-rotational modes of the split-spar wing as shown in figure 4.11. As with the straight-spar wing, the split-spar wing’s first mode is the first bending mode of a cantilever beam. Similarities can be seen between the second modes of the straight-spar and split-spar wings. The split-spar’s third and higher modes show complex couplings between bending and torsion.

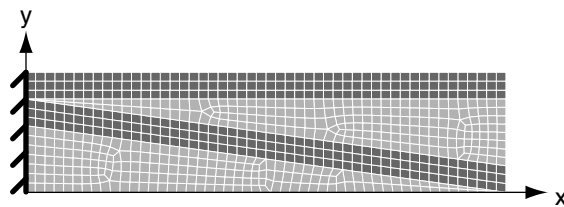


Figure 4.10: Planform view of FEM mesh of split-spar wing. Thick elements are dark gray, thin elements are light gray.

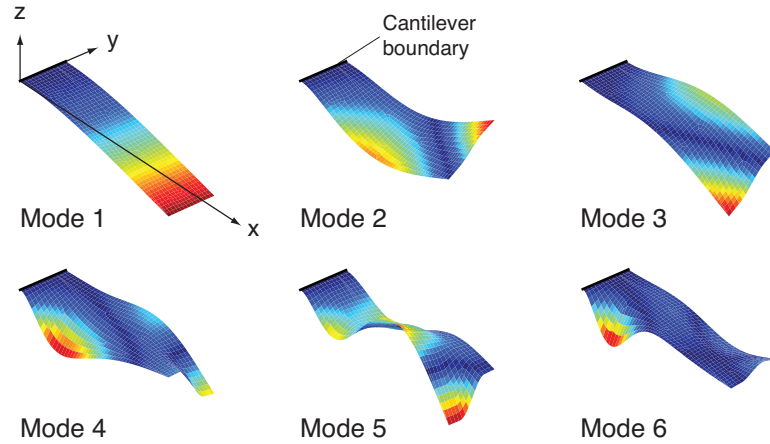


Figure 4.11: Normal modes of the split-spar wing FEM. Element color is proportional to the magnitude of displacement at the element centroid.

4.6.2 Natural Frequencies of FEM wings

A further comparison between the FEM models is performed by examining their modal natural frequencies in table 4.8. The natural frequencies of a comparable beam model are also reported. The beam frequencies were analytically calculated by for a uniform cantilever beam with EI_{z0} and m_0 properties calculated from the data of table 4.7. The third and fifth beam frequencies are torsion frequencies, calculated by assuming a uniform clamped beam with a first torsion frequency equal to $7.52\omega_1$. This value was chosen to replicate the non-dimensional torsion frequency of the straight-spar FEM wing. For all structural models, a non-dimensional frequency is also reported, measured in relation to each model's

Table 4.8: Natural frequencies of wing FEMs.

Mode	Straight-spar FEM		Split-spar FEM		Beam	
	ω_i [Hz]	ω_i/ω_1	ω_i [Hz]	ω_i/ω_1	ω_i [Hz]	ω_i/ω_1
1	85.6	1	85.4	1	83.5	1
2	511	5.97	520	6.09	523	6.27
3	644	7.52	543	6.35	628	7.52
4	1062	12.4	1343	15.7	1465	17.5
5	1201	14.0	1459	17.1	1884	22.6
6	1497	17.4	1964	23.0	2871	34.4

respective first natural frequency.

The first natural frequencies of the straight-spar FEM, split-spar FEM and analytical beam modes agree within 2.5% of each other. This similarity of natural frequencies, along with the absence of chordwise variations of deformations in the FEM modes, indicates that the first modes of both FEMs are essentially the same as the first cantilever beam mode. The second natural frequencies of the both FEMs are likewise close to the second beam frequency, though both FEMs show minor chordwise deformations and are not exactly equivalent to the corresponding beam mode.

It is interesting to compare the second and third modes of the FEM models. The third mode of the straight-spar FEM is torsion mode that is significantly stiffer than the second bending mode, evidenced by the 130 Hz difference between their natural frequencies. In contrast, the third mode of the split-spar beam is of comparable stiffness to the second mode (their natural frequencies about 20 Hz apart). The mode shapes appear qualitatively similar, as well, mirrored about the wing's midchord. While the straight-spar and split-spar wings are similar with respect to their lower modes, the splitting of the leading edge spar has a significant effect on the structural response for higher modes.

4.7 Stability of Plate Wings

Having derived the natural modes of the plate wings by use of finite element analysis, the stability of the plate wings is analyzed. Application of the stability analysis to the plate equation of motion (Eq. 4.28) proceeds exactly as before: Floquet analysis of the homogeneous state-space representation gives us a non-dimensional stability diagram. We first consider the simple case of a wing modeled by a single mode. Figure 4.12 compares the single-mode plate wing and beam wing stability diagrams for various feathering strokes. The plate-wing stability

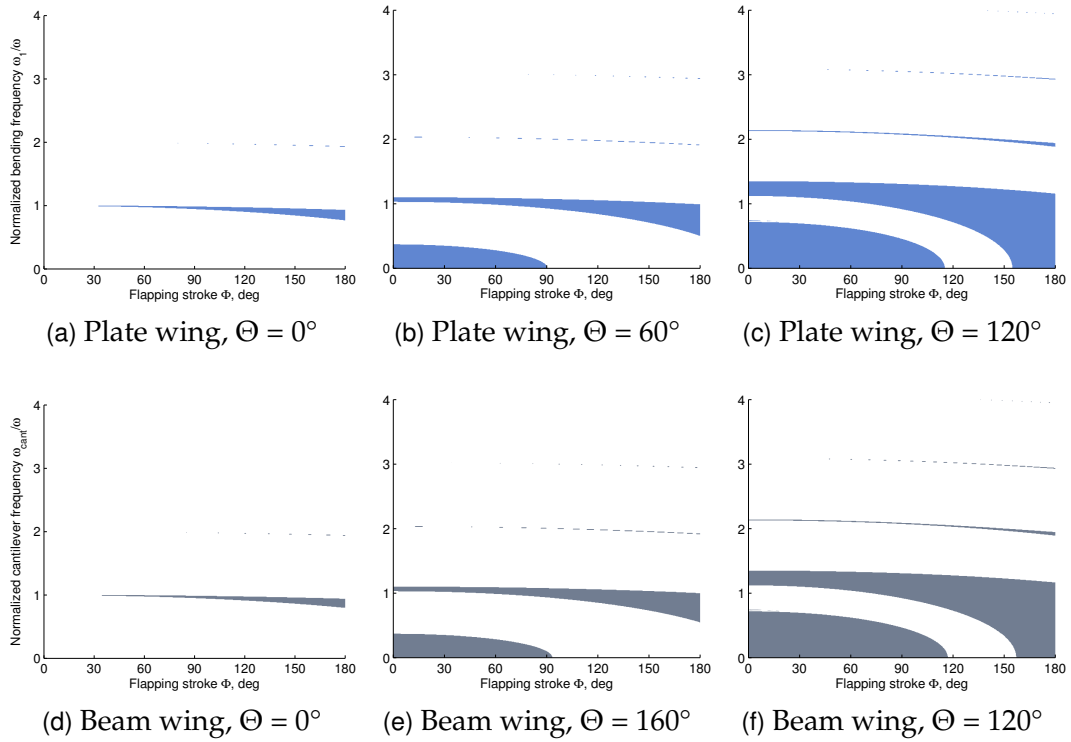


Figure 4.12: Comparison of single-mode stability diagrams of plate and beam assumed-modes models. The top row (blue) shows plate diagrams and the bottom row (gray) shows comparable beam diagrams.

diagram is generated using the first mode of the straight-spar wing. Due to the equivalence of the first modes of the straight-spar and split-spar wings, the single-mode stability diagram of each will be identical. In fact, the plate wing and beam wing stability diagram are also virtually identical for all feathering strokes, which is expected because of strong similarities of the first plate and beam modes.

The general resemblance of the plate and beam stability diagrams continues when higher modes are added, because of the dominant character of the first mode. Figure 4.13 compares plate and beam stability diagrams of systems with three modeled modes at various feathering strokes. For the three-mode diagrams, the straight-spar plate wing and split-spar plate wing are considered separately. As per the previous section, the beam models are calculated with a normalized torsion frequency of $\omega_{\text{tor}}/\omega_{\text{cant}} = 7.52$ to reflect the torsional stiffness of the straight-spar

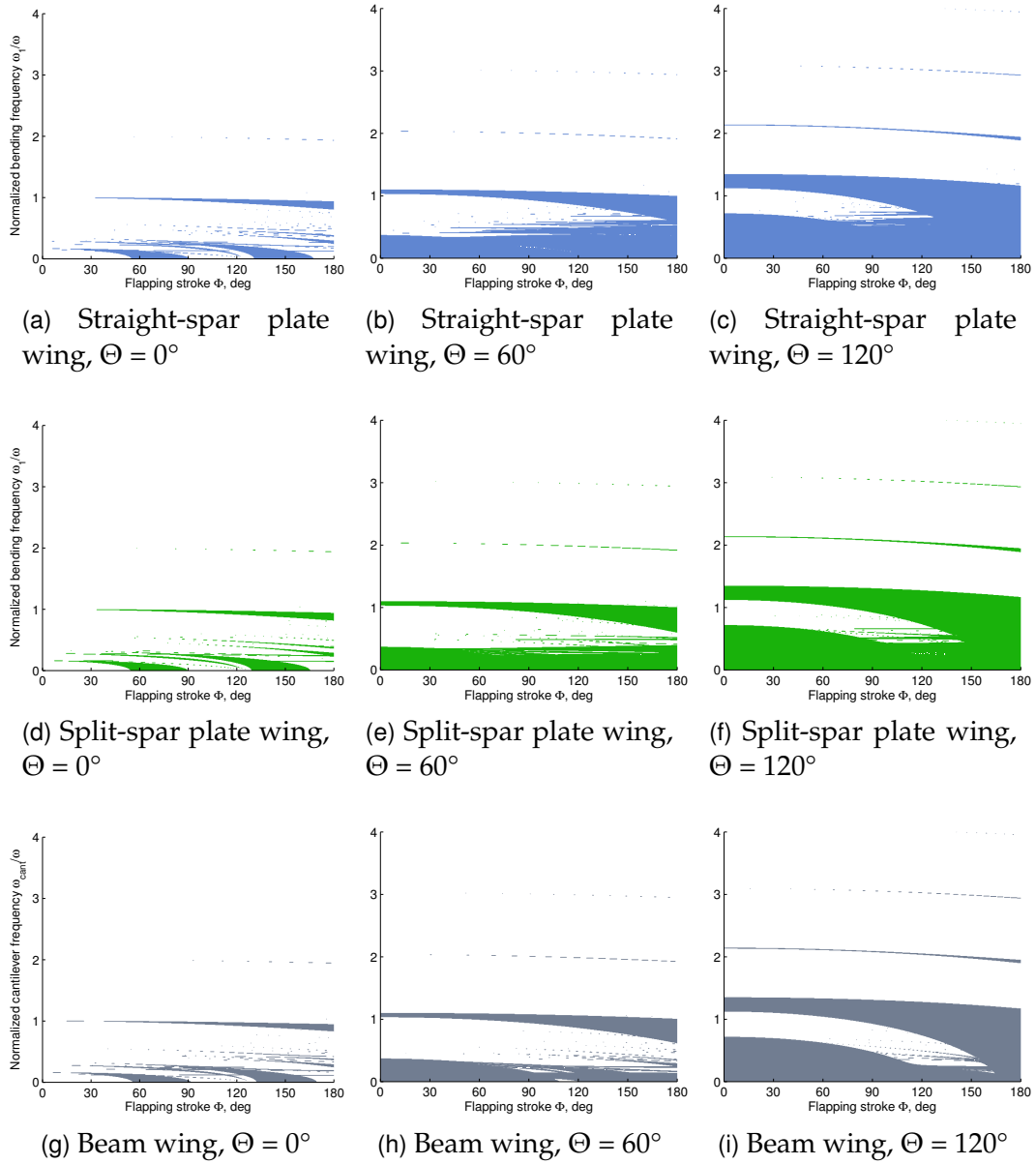


Figure 4.13: Comparison of three-mode stability diagrams of plate and beam assumed-modes models. The top row (blue) shows straight-spar plate diagrams, the middle row (green) shows split-spar plate diagrams and the bottom row (gray) shows beam diagrams.

plate wing model. The stability diagrams for both plate models and the beam model are very similar with no feathering rotation ($\Theta = 0^\circ$). At nonzero feathering strokes the straight-spar plate model shows greater regions of instability than the split-spar plate model, which in turn shows greater regions of instability than the comparable beam mode. However, these differences manifest at low normalized first natural frequencies, approximately $\omega_1/\omega < 2/3$. This range is below the thick horizontal spike associated with the first-mode instabilities, a region in which it is already inadvisable to operate an MAV. At greater values of ω_1/ω the beam and plate models remain remarkably similar.

From the stability analysis in chapter 3, we identified two trends in the beam-wing stability diagrams. The first trend is that the first-mode instability regions were dominant and persistent over the range of parameters considered in this dissertation. This trend appears to hold for the plate-wing analysis as well: the first-mode instability regions domination the stability diagrams. For the models considered in this chapter, the first mode of the plate models is nearly identical to the first mode of the beam model, resulting in strong similarities between the stability diagrams of the plate models with the beam modes in figures 4.12 and 4.13.

The second trend from the beam-wing stability analysis is that the effects of changes in system design parameters manifested as relatively minor differences in higher-mode instability regions at low values of $\omega_{\text{cant}}/\omega$ (typically $\omega_c/\omega < 2/3$). This trend also appears to hold for the plate wing in figure 4.13. The primary difference between the plate-wing diagrams and the beam-wing diagrams are somewhat larger unstable regions associated with these higher-mode instabilities of the plate models within this low- ω_1/ω bound.

We may conclude that the stability trends we have seen from parameteric variations of beam models in chapter 3 will be generally borne out if a more

complex plate model is used for the same analysis. From the view of a preliminary designer of a flapping-wing MAV, the additional effort in constructing a plate analysis—as opposed to a beam analysis—may be unwarranted for stability calculations. So long as the first assumed-mode of a beam model reasonably captures the first plate mode, the stability diagrams from both analyses should be similar overall. For use in examining a preliminary design configuration, it may be adequate to simply develop a beam model, with the understanding that regions of instability will likely be underpredicted at low $\omega_{\text{cant}}/\omega$, where the beam model would already show general operation is probably inadvisable.

Care should be taken for wings where the second (and possibly higher) natural frequencies are close to the first natural frequency, increasing the range of $\omega_{\text{cant}}/\omega$ where higher-order instabilities may appear. In such cases, a plate stability analysis would probably be advisable for preliminary design. Plate stability analysis would also be warranted for wing designs with first natural modes that show large chordwise variations in deflection, i.e., where the first mode cannot be adequately modeled using a beam representation.

4.8 Summary

The linear assumed-modes matrix equations of motion of a flapping wing were developed for a wing modeled as a thin plate undergoing elastic deformations. The equations of motion were developed by considering an assumed-modes model of a plate undergoing generalized large rigid-body motions and linear elastic deformations and simplifying for the case of insect-like flapping motion and out-of-plane bending deflections. The resulting dimensional flapping-wing plate equations of motion are equivalent to the flapping-wing beam equations developed earlier in this thesis.

The construction of the mass and stiffness matrices for the the assumed-

modes equations of motion require evaluations of surface and line integrals based on the assumed mode shapes of the plate wing. Assumed modes for use in the thin-plate analysis were calculated with a commercial FEA code. The necessary surface integrals were calculated from the FEA output are calculated with Gaussian quadrature over each plate element. Line integrals were calculated numerically, using integrands that are estimated from surrounding node points through the use of radial basis functions (RBFs). The output FEA mode shapes, RBF integrand estimations and equation-of-motion matrix calculations were validated against a simply-supported rectangular plate whose mode shapes are known exactly.

A rectangular wing FEM was modeled with a large thickened leading-edge spar, based on the “representative” insect wing model. A second rectangular wing FEM was developed in which the spar was split evenly into a leading-edge spar and a trailing radial spar. The mode shapes of both models were calculated and the Floquet stability analysis was applied to both. The results of the stability analysis of both wings show that the first bending mode dominates the stability response. The plate models’ stability plots were compared to a beam-wing stability plot. This comparison revealed that the plots for all three models were similar, except that the plate models show somewhat greater regions of instability at normalized natural frequencies less than one. This similarity suggests that beam models may be adequate for estimations of structural stability of flapping wings.

CHAPTER 5

PARAMETRIC STUDY OF AN AEROELASTIC FLAPPING WING

5.1 Introduction

The preceding chapters of this thesis have focused on the structural modeling and stability of a flapping wing system. Previous research has indicated that inertial loadings arising from wing flapping motions are the primary drivers of structural deformations in flapping wings, while aerodynamic forces play a secondary role. Therefore, aerodynamic forces have only been considered abstractly, as external force loads (derived for the equations of motion, but not included in any analysis) or as general system damping terms which may mitigate instabilities. However, the purpose of flapping wings on MAVs is the generation of aerodynamic forces. In this chapter, an aeroelastic flapping-wing analysis is used to perform a parametric study of the effect of structural design parameters on the lift generated by a flapping MAV wing.

5.2 Aeroelastic Model

The parametric study presented here uses an unsteady flapping-wing aeroelastic analysis developed and validated by Singh and Chopra [98]. Singh and Chopra's analysis is a loosely coupled aeroelastic analysis, meaning that the structural and aerodynamic portions of the analysis are not performed simultaneously.

Instead, separate structural and aerodynamic analyses are iteratively applied until convergence is attained. A brief overview of the analysis is given here. A more detailed explanation of the analysis can be found in Singh's dissertation [156].

The structural portion of the analysis models the wing as a plate subject to large rigid-body rotational motions (i.e., flapping and feathering rotations) and small, linear structural deformations.* The plate wing is represented as a finite element model (FEM) with a structured rectangular grid. The equations of motion for the structural analysis were derived using Hamilton's method by equating the variations of strain energy and kinetic energy within the plate. Modal reduction was applied to the FEM matrix equation to reduce the degrees of freedom of the system. Additional simplifications were made when the analysis was implemented in Fortran code [177]. Material and structural properties (Young's modulus, density, Poisson's ratio and thickness) were assumed to be constant within each element. The materials were also assumed to be isotropic. Since these simplifications were in place during the verification of the analysis, they are retained in the present analysis.

The aerodynamics of a flapping wing were analytically modeled using a quasi-steady thin airfoil theory that was augmented to include the effects of the attached leading-edge vortex (LEV) and the wing's wake. The conceptual framework for this method was proposed by Żbikowski as a combination of analyses originally developed for helicopters and delta-wing aircraft [96]. The unsteady aerodynamic modeling of pitching and plunging airfoils and of trailing and returning wakes are well-known from helicopter analysis (see [80, ch. 8]). The LEV was modeled by Polhamus' suction analogy which describes the effect of attached vortices on swept delta wings at high angles of attack [178]. Singh and Chopra implemented Żbikowski's framework and expanded it by including

*In contrast to the non-dimensional plate model presented in chapter 4 of this thesis, Singh and Chopra's model is fully dimensional.

pitching and plunging motions due to the structural deformations of the wing itself. Quasi-steady thin airfoil theory was used to calculate circulatory and noncirculatory (i.e., apparent mass) forces on the wing, including the effect of the wing's feathering rate, often called the "Kramer effect" or "rotational lift" in flapping-wing analyses. The quasi-steady lift also includes aerodynamic forces generated due to elastic deformation of the wing. The LEV was modeled by rotating the quasi-steady leading-edge suction force by 90° so that it acts normal to the wing, as per Polhamus' suction analogy. Unsteady wake aerodynamics were included with the Wagner and Küssner functions.

5.3 Baseline Wing

The baseline structural model for the parametric studies is Singh and Chopra's Wing III FEM, based on an aluminum-frame wing with a flexible mylar membrane that was used for experimental validation of the aeroelastic analysis [98]. A view of the finite element model is shown in figure 5.1 and the physical wing on which it was modeled is shown in figure 5.2. The FEM has a span of 9.28 cm, a maximum chord of 4.78 cm and a total area of 30.56 cm^2 . The flapping mechanism used in the experimental validation test had a 5.5-cm-long arm equipped with strain gauges,

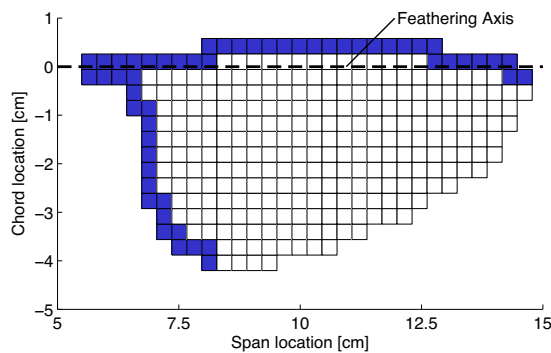


Figure 5.1: FEM of baseline wing. Colored elements are modeled as aluminum, white elements as mylar.

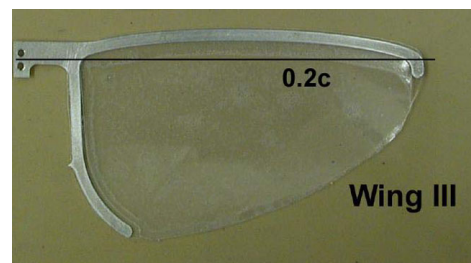


Figure 5.2: Physical model for baseline FEM.

causing a spanwise offset of the wing root. The elements of the FEM are modeled as either aluminum or mylar. All elements of a particular material are assumed to have identical properties, listed in table 5.1.

The mode shapes of the baseline FEM are calculated as part of the modal reduction of the structural model for use in the aeroelastic analysis. The first four mode shapes are drawn in figure 5.3. Mode one is the first bending mode of the wing and has a natural frequency of 36.7 Hz. Mode two is the first torsion mode, with a natural frequency of 85.0 Hz. The third and fourth modes are higher-order deformations of the mylar wing membrane

The input flapping angle ϕ and feathering angle θ for the parametric study are plotted in figure 5.4. Two sets of data are shown in the figure. The first are

Table 5.1: Structural properties for baseline wing elements.

	Aluminum	Mylar
E	60 GPa	7 GPa
ρ	2400 kg/m ³	1250 kg/m ³
ν	.33	.25
t	.0508 mm	.0104 mm

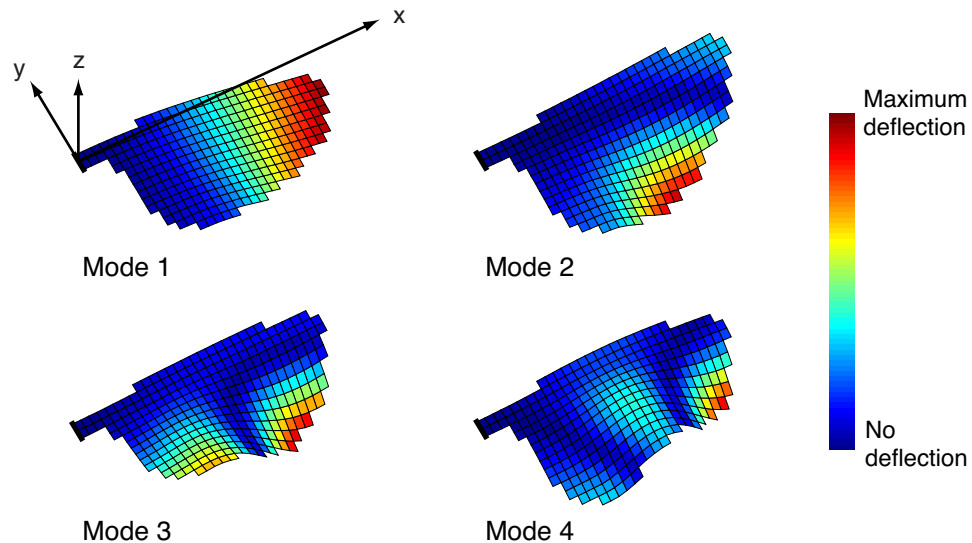


Figure 5.3: First four modes of the baseline FEM. Color shows the magnitude of out-of-plane deflection.

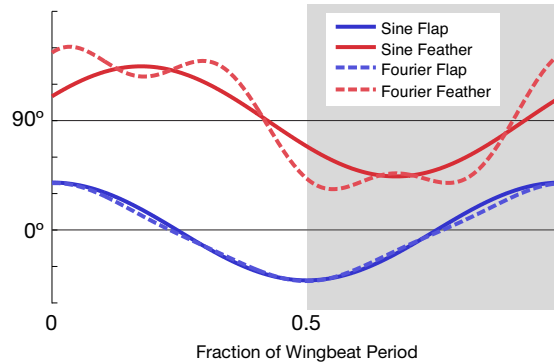


Figure 5.4: Input flapping motions and feathering motions for aeroelastic analysis. Solid lines are sinusoidal motions, dashed lines are the “Fourier series fit” from the Singh and Chopra’s validation exercise.

the pure sinusoidal functions. The stroke amplitudes of the sinusoids are selected as the nominal strokes in the validation study: a flapping stroke of $\Phi = 80^\circ$ and a feathering stroke of $\Theta = 90^\circ$. The second set of motions in figure 5.4 are Singh and Chopra’s “Fourier series fit” of the experimental flapping and feathering inputs that are used in the validation study [98, figure 41]. Note that the sinusoidal feathering input has a similar phase offset as the feathering of the Fourier series fit. The sinusoidal input motions are used for the majority of the parametric study for their simplicity and their applicability to generalized results, as opposed to the Fourier series fit, which represents the motions of a specific mechanism. The Fourier series fit is used in cases where the current analysis is compared to the original validation study.

The validity of the current implementation of the aeroelastic analysis was confirmed by performing a test case from Singh and Chopra’s validation study and comparing the results from the original and current analyses. The selected test case was the calculation of the bending moment at the wing root caused by flapping motion with a 9.07 Hz wingbeat frequency. Figure 5.5 plots the results from the validation exercise (originally reported in [98, figure 52a]) against the results from the current implementation. Both sets of data agree in both shape and

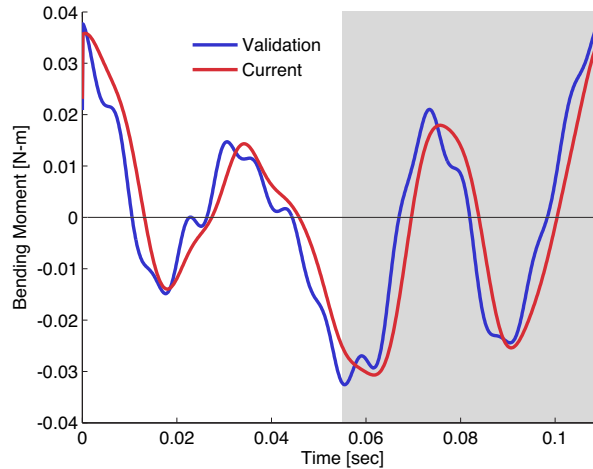


Figure 5.5: Comparison of calculated bending moments from validation exercise and current implementation, $\omega = 9.07$ Hz.

magnitude, giving confidence that the current implementation of the aeroelastic analysis is valid.

The lift forces generated by baseline wing while undergoing sinusoidal flap-ping motion are plotted in figure 5.6. The wingbeat frequency is $\omega = 9.07$ Hz, a speed typical of the flapping mechanism used in the validation exercise. The

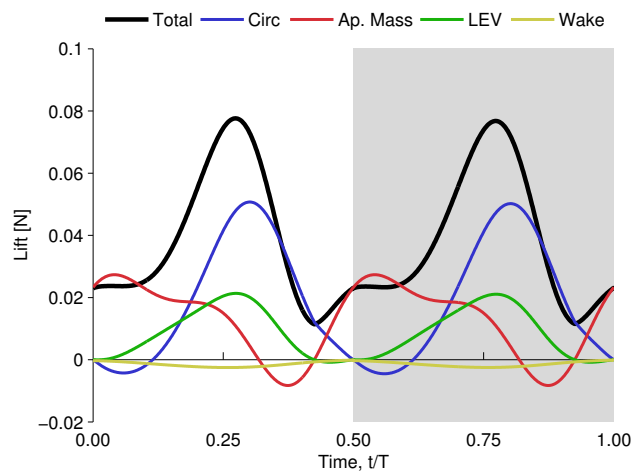


Figure 5.6: Total lift and lift components baseline wing subject to sinusoidal motion, $\omega = 9.07$ Hz. Components plotted are: circulatory loads (Circ), noncirculatory apparent-mass loads (Ap. Mass), leading-edge vortex suction (LEV) and wake losses (Wake).

flapping wing generates a mean thrust of .0385 N over one wingbeat, enough to lift 3.92 g. The equivalent rigid-wing lift is calculated by neglecting structural elasticity in the aeroelastic analysis. Subject to identical flapping motions, a rigid baseline wing generates a mean thrust of .0325 N. The elastic baseline wing generates 18% more thrust than an equivalent rigid wing, a significant improvement.

A breakdown of the mean thrust components is given in table 5.2. Almost half of the total thrust arises from circulatory loads, while apparent mass effects and the LEV account for roughly 30% and 20% of the loads, respectively. The lift deficit from the wake is relatively low at about 4% loss of lift. Note in figure 5.6 that the circulatory and LEV loads are greatest slightly after the middle of each half-stroke when the wing begins to pitch up relative to the flapping motion. In contrast, the added-mass loads are greatest at the beginning of each half-stroke. The effects complement each other to generate positive lift at all times during the wingbeat, despite circulatory and noncirculatory lift each producing negative lift at some point during each half-stroke.

Table 5.2: Mean values of lift components on baseline wing undergoing sinusoidal motion, $\omega = 9.07$ Hz.

Component	Mean lift	Percentage of total
Circulation	0.0186 N	48.3%
Apparent mass	0.0126 N	32.7%
LEV	0.0087 N	22.6%
Wake	-0.0014 N	-3.6%

5.4 Wing Planform Shape

As part of his morphological study of insect morphology, Ellington showed that the chord distribution of an insect wing can be generally approximated by a Beta distribution as a function of span [64]. Furthermore, the Beta distribution itself can be characterized as a function of a single variable, the spanwise location

of the wing's first moment of area (i.e., the wing's spanwise center of area). This simple approximation allows the generation of a series of arbitrary insect-like planforms for use in the parametric study.

Ellington reports that the wing chord c at a spanwise location x is given by the Beta distribution as

$$c(x) = x^{p-1} (R - x)^{q-1} / B, \quad 0 \leq x \leq R \quad (5.1)$$

where p and q are parameters derived from the spanwise moments of wing area and B acts as a scaling factor. The parameters p and q are

$$p = \hat{r}_1 \left(\frac{\hat{r}_1(1 - \hat{r}_1)}{\hat{r}_2^2 - \hat{r}_1^2} - 1 \right) \quad (5.2)$$

$$q = (1 - \hat{r}_1) \left(\frac{\hat{r}_1(1 - \hat{r}_1)}{\hat{r}_2^2 - \hat{r}_1^2} - 1 \right) \quad (5.3)$$

where \hat{r}_1 is the first spanwise moment of wing area and \hat{r}_2 is the second spanwise moment of wing area. These values are non-dimensionalized by the wing radius so, for example, a wing with $\hat{r}_1 = .50$ has a spanwise center of area at $.50R$. Ellington's experimental morphological study showed that the second moment of wing area is a strong function of the first moment, closely following the relation

$$\hat{r}_2 = 0.929 \hat{r}_1^{0.732} \quad (5.4)$$

Thus, an approximate biologically inspired chord distribution may be generated solely from the non-dimensional first moment of wing area \hat{r}_1 . These relationships are valid for the range of Ellington's experimental measurements, $0.42 \leq \hat{r}_1 \leq 0.56$.

The baseline wing, based on a fruit fly wing, has a first moment of area of $\hat{r}_1 = 0.47^\dagger$. Three additional biologically inspired FEM planforms were generated

[†]The three innermost columns of elements in the FEM, which represent the aluminum

from Ellington’s Beta distribution method for $\hat{r}_1 = 0.42, 0.51$ and 0.56 , spanning the range of Ellington’s measurements. The new FEM planforms use the same material properties as the baseline wing (see table 5.1) as well as the same wing length, mass, and area. The shape of the leading-edge spar has likewise been kept constant in all wings. Figure 5.7 compares all four planforms.

The four wings were subjected to sinusoidal flapping motion at a wingbeat frequency of $\omega = 9.07$ Hz. The predicted mean lift and a breakdown of the lift components are given in table 5.3. Mean lift increases as \hat{r}_1 increases, which is to say, as

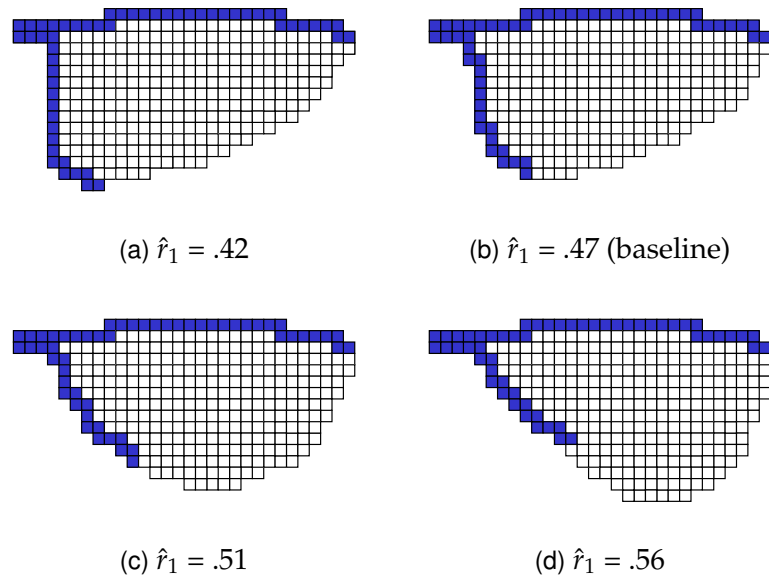


Figure 5.7: Biologically inspired wing FEMs of equal area and mass.

Table 5.3: Total lift and lift components of bioinspired wing planforms with different first moments of area \hat{r}_1 .

	$\hat{r}_1 = 0.42$	$\hat{r}_1 = 0.47$	$\hat{r}_1 = 0.51$	$\hat{r}_1 = 0.56$
Mean Lift	0.0338 N	0.0385 N	0.0423 N	0.0428 N
Circulation	49.4%	48.3%	49.6%	52.1%
Apparent Mass	31.7%	32.7%	32.2%	30.6%
LEV	23.1%	22.6%	22.7%	23.4%
Wake	-3.8%	-3.6%	-4.5%	-6.1%

connection spar, are not included in the first moment of area calculations of this or subsequent wings.

the wing area is biased more towards the wing tip. This relationship is expected: the outboard sections of rotating wings generate more lift than inboard sections, a result well-known from helicopter analysis. The proportional contributions of the separate lift components are relatively constant for all of the planforms and, indeed, the plots of the lift forces are quite similar, as seen in figure 5.8. Circulatory lift, for example, contributes approximately half of the total lift for all planforms.

The results of this planform study suggest that wings for MAVs should have planform areas biased towards the wing tip, with the goal of increasing lift. However, data in Ellington’s morphological survey of insect-like fliers [64] seems to support the opposite conclusion. Ellington’s measurements show that better fliers generally have wing planforms biased more towards the wing root.

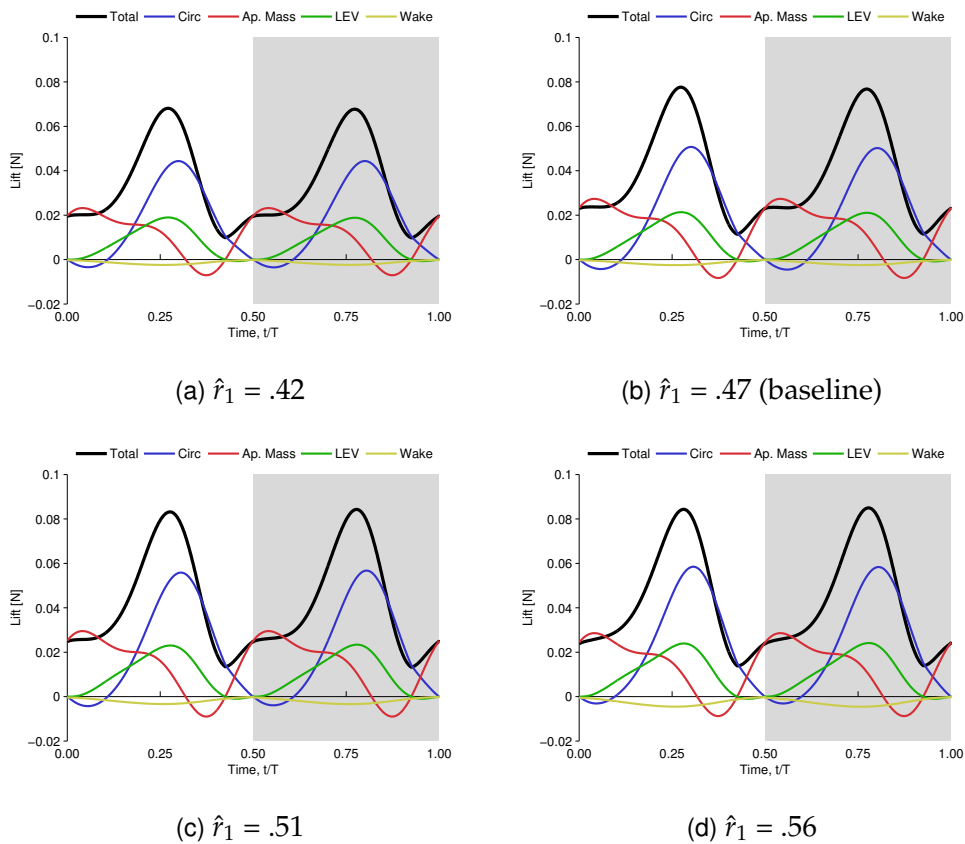


Figure 5.8: Time history of total lift and lift components of biologically inspired wing planforms, $\omega = 9.07$ Hz.

Honeybees, for example, typically have $\hat{r}_1 \approx .49$, while exceptional fliers like hawkmoths and hummingbirds have $\hat{r}_1 \leq .44$. In contrast, insects with $\hat{r}_1 > .54$ are typically poor fliers, such as craneflies and lacewings. This discrepancy implies that additional factors are influencing biological wing planforms that are not included in this analysis. One such factor is the possibility that inboard-biased planforms may be more efficient at generating lift (similar to blade taper for an optimum hovering helicopter rotor). Unfortunately, the aeroelastic analysis used in this study does not predict power requirements so system efficiency cannot be evaluated at this time. It is recommended that this discrepancy be examined in future research.

5.5 Material Thickness

The thickness of the materials used to construct the wing will have a significant effect on the structural response of the flexible wing, which in turn will change the thrust it generates. In order to characterize these effects, a parametric variation of the thickness of the aluminum frame and mylar membrane is performed. The thickness of the frame or the thickness of the membrane is varied from one-half to two times its baseline value while all other material properties are fixed at their baseline values (see table 5.1). Baseline sinusoidal flapping motion of frequency $\omega = 9.07$ Hz is used for all cases.

5.5.1 Wing Frame Thickness

The first parametric study varies the frame thickness. The frame is the primary structural component of the wing; in particular, the leading-edge spar is primarily responsible for the bending stiffness of the wing. The wing's first structural mode is the first bending mode, implying that bending flexibility plays

a key role in the gains in thrust experienced by an elastic wing over an equivalent rigid wing. We may thus expect a loss of wing thrust with a thicker frame, since a thicker, stiffer spar will resist beneficial deformations. Conversely, we may expect thrust gains with decreasing frame thickness. This expectation is generally borne out in the parametric study.

The results of the frame-thickness study are reported as non-dimensional values in table 5.4. The first value in the table is the predicted lift of the elastic wing non-dimensionalized by the lift of an equivalent rigid wing (as for the baseline wing, $L_{\text{rigid}} = .0325$ N for all cases). The second is the first natural frequency of the wing divided by the flapping frequency. Thicker frames have higher natural frequencies, indicating greater stiffness in bending. For the most part the results show the expected trend: for frame thicknesses of 0.9 times the baseline and greater, thicker wings are stiffer and produce less lift due to smaller beneficial deformations. Very stiff wings approach the rigid-wing value of lift.

Of note are the two wings with the thinnest frames, with 0.50 \times and 0.75 \times baseline frame thickness. These wings have relatively low stiffnesses and experience very large deformations when subjected to flapping motions. The aeroelastic analysis predicts wingtip deflections greater than 100% of the wing length for

Table 5.4: Results of parametric variation of flapping-wing frame thickness. Frame thickness is referenced to baseline frame thickness of 0.0508 mm. First natural frequency ω_1 is referenced to wingbeat frequency $\omega = 9.07$ Hz.

Frame thickness/ baseline thickness	L/L_{rigid}	ω_1/ω	Note
0.50	2.06	1.84	Violates small-deflection assumption
0.75	0.22	2.91	Violates small-deflection assumption
0.90	1.26	3.59	
1.00	1.18	4.04	
1.25	1.12	5.18	
1.50	1.08	6.29	
2.00	1.05	8.15	

both cases. Such excessive deformations violate the analysis' assumption of small deformations and linear strains, so these results are not strictly valid. However, it is surprising that the lift for the 0.75 \times -thickness case does not follow the expected trend of increased lift for decreased thickness, but instead produces nearly 80% less lift than the rigid-wing case.

This decrease in lift for the 0.75 \times -frame-thickness wing occurs because the natural frequency of the wing structure has been reduced such that the normalized first natural frequency ω_1/ω is near three. At $\omega_1/\omega \approx 3$, the flapping motion of the wing and the time-periodic stiffness of the flapping structure act together to increase structural deformations that are detrimental to lift production.

Experimental evidence of this phenomenon is found in Singh's measurements of flapping-wing lift. Figure 5.9 plots Singh's "high-frequency" lift measurements of Wing III as a function of ω_1/ω . The data were collected by flapping Wing III over a range of wingbeat frequencies ω . The upper bound of ω , and hence the lower bound of ω_1/ω , was limited by the performance of the flapping mechanism. Figure 5.9 shows that lift increases with decreasing ω_1/ω until ω_1/ω nears three, where the characteristic lift reduction is seen. Singh identifies the

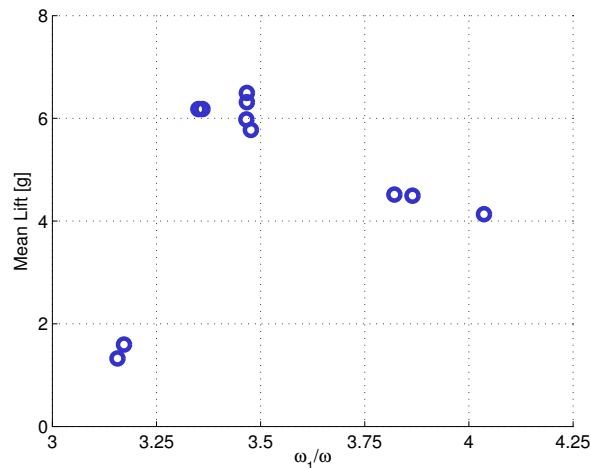


Figure 5.9: Experimental mean lift versus normalized first natural frequency for Singh's Wing III. Data originally reported in [156, figure 6.8].

cause of lift reduction a “large accelerations introduced by wing elasticity, [which] significantly [reduce] the non-circulatory contribution to the thrust.” The cause of these large elastic accelerations was not specifically identified. It is implied that the elastic deformations are a consequence of a high flapping frequency ω . In fact, the cause of the lift reduction is not related to the magnitude of the flapping frequency ω alone. It is related to the value of the normalized natural frequency ω_1/ω approaching a value of three.

Returning to the frame-thickness variation, we can see how the time-periodic stiffnesses of the wing act to excite a large structural response when $\omega_1/\omega \approx 3$. Figure 5.10 plots the variation of tip deflections for different frame thicknesses. The 0.75 \times -frame-thickness wing of figure 5.10b shows a pronounced 3-per-wingbeat (i.e., 3ω) response component, which is driving the increased elastic accelerations. This 3-per-wingbeat response is directly caused by this wing operating at $\omega_1/\omega \approx 3$. In contrast, the other wings which operate at higher or lower values of ω_1/ω do not have the large 3ω response. The mechanism by which $\omega_1/\omega \approx 3$ flapping motion drives large 3ω structural response is explained in complete detail later in section 5.6. For the moment, it is enough to note that this 3ω response is detrimental to lift production, resulting in the loss of mean lift for this case.

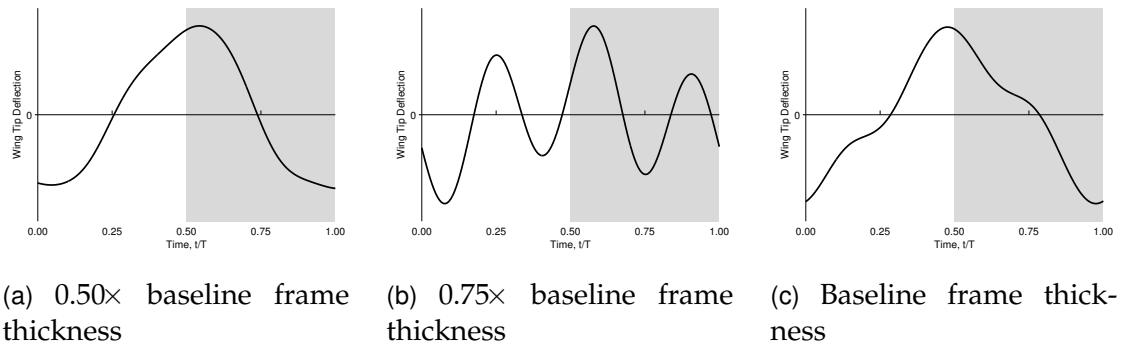


Figure 5.10: Comparison of tip deflections of wings with 0.50 to 1.00 \times baseline frame thickness. Units are not included because 0.50 \times and 0.75 \times cases violate small-deflection assumption, so the results are not strictly valid.

This detrimental loss of lift is illustrated in figure 5.11, which plots the predicted instantaneous lift over one wingbeat for frame thicknesses of $0.50\times$, $0.75\times$ and $1.00\times$ the baseline value. The plots for the $0.50\times$ and $1.00\times$ thicknesses are similar, showing positive lift over the entire stroke. The $0.75\times$ thickness case shows a significantly different lift history, where negative lift generation on both half-strokes results in a reduction of mean lift.

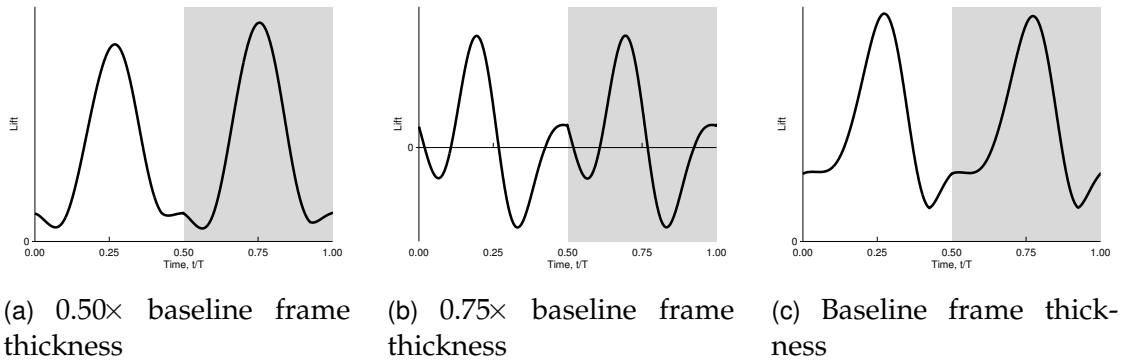


Figure 5.11: Comparison of lift variations of wings with 0.50 to $1.00\times$ baseline frame thickness. Units of lift are not included because $0.50\times$ and $0.75\times$ cases violate small-deflection assumption, so the results are not strictly valid.

5.5.2 Wing Membrane Thickness

The effect of wing membrane thickness on the wing's lift is somewhat more complicated than the effect of frame thickness (notwithstanding the anomalous $0.75\times$ frame thickness case). Variations of membrane thickness do not monotonically increase or decrease lift. In fact *all* of the thickness cases considered in the parametric study, whether using thicker or thinner membranes, have greater predicted lifts than the baseline case. This results can be understood by examining the wing membrane both as a structural stiffener and as a source of inertial loadings.

The results of the membrane-thickness study are reported in table 5.5. In comparison to the results of the frame-thickness study, the lift and first natural

Table 5.5: Results of parametric variation of flapping-wing membrane thickness. Membrane thickness is referenced to baseline membrane thickness of 0.0104 mm. First natural frequency ω_1 is referenced to wingbeat frequency $\omega = 9.07$ Hz.

Membrane thickness/ baseline thickness	L/L_{rigid}	ω_1/ω
0.50	1.29	4.07
0.75	1.19	4.16
1.00	1.18	4.04
1.25	1.20	3.92
1.50	1.21	3.82
2.00	1.23	3.68

frequency show relatively small variations with membrane thickness. But in contrast to the frame-thickness results, neither lift nor first natural frequency is a monotonic function of membrane thickness. This is due to two conflicting trends: the membrane’s contribution to the wing’s stiffness and its contribution to the wing’s mass. The wing membrane contributes somewhat to the overall stiffness of the wing, and for the 0.5 \times and 0.75 \times membrane thickness cases the effect is the same as seen for the frame thickness: a thinner membrane is more flexible, allowing larger beneficial deformations that increase lift. However, the membrane is not the wing’s primary structural element, so this trend does not continue for thicker membranes. Instead, as the membrane thickness increases further, its additional mass produces greater inertial loads in response to flapping motion. The increasing inertial loads drive increasing wing deformations in spite of the greater relative bending stiffness.

The trends of these two effects—the contribution of membrane mass versus the contribution of membrane stiffness—can be demonstrated by independently varying the mass and stiffness of the membrane elements through the parameters ρ and E . Membrane mass changes proportionally with wing thickness, so an equivalent mass variation is simulated by varying the membrane density $\rho \propto t$. The membrane’s bending stiffness EI is proportional to the cube of thickness, so

the equivalent stiffness variation is simulated by varying the Young's modulus $E \propto t^3$. Figure 5.12 plots the results of the variations of thickness, mass and stiffness. The independent effects of mass and stiffness are clear: as thickness increases, the increased bending stiffness acts to suppress lift-beneficial deformations while the increased mass acts to amplify them. When acting in concert, these opposed effects partially mitigate each other but act in total to increase lift when membrane thickness is increased *or* decreased.

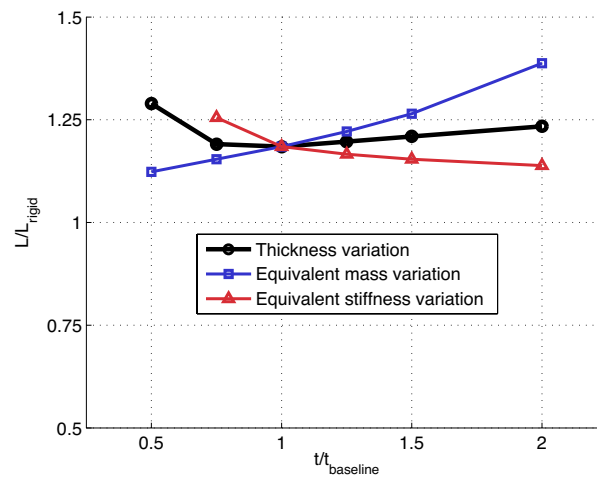


Figure 5.12: Effect of variation of membrane thickness and equivalent variations of mass and stiffness.

5.6 Forced Flapping at Odd Subharmonics of the the First Natural Frequency

In the frame-thickness parametric study of section 5.5.1 it was observed that reducing the wing's stiffness such that the first natural frequency ω_1 was approximately three times the wingbeat frequency ω , the structural response had a particularly large response with frequency 3ω . This response is a consequence of the time-periodic structural stiffness of the flapping wing system. The mechanism of this phenomenon can be demonstrated using the non-dimensional flapping-

wing beam equation of motion derived in chapter 2, which is given in Eq. 2.75. For this demonstration we will consider a beam wind with cantilever boundary conditions.

A number of initial simplifications are made for the sake of clarity. It is assumed that the beam wing is modeled by one bending mode, and all torsion modes are neglected. Note that for a single-mode cantilever beam, $K_\omega = 1$. Flapping motion is modeled as a pure cosine input, $\hat{\phi}(\tau) = \cos(\tau)$, while feathering angle is constant at $\hat{\theta} = \pi/2$ to fix the wing in a vertical orientation. Applying these simplifications to Eq. 2.75 results in the scalar differential equation

$$q_1^{**} + \left[(\omega_1/\omega)^2 + K\Phi^2 \sin^2(\tau) \right] q_1 = -F\Phi \cos(\tau) \quad (5.5)$$

Some notational changes are introduced in Eq. 5.5 with respect to Eq. 2.75 for convenience. The stiffness and forcing constants K and F in Eq. 5.5 are defined as

$$K \equiv \mathbf{K}_{\hat{\phi}^2}^* + \mathbf{K}_{\hat{\phi}^2 s^2}^* = \frac{\hat{\mathcal{T}}_{11}}{4\hat{\mathcal{C}}_{11}} - \frac{1}{4}$$

$$F \equiv \tilde{F}_{\hat{\phi}s}^{**} = \frac{\hat{F}_{\omega B1}}{2\hat{\mathcal{C}}_{11}}$$

and $\omega_1 \equiv \omega_{\text{cant}}$, the first cantilever natural frequency.

We assume that the solution of Eq. 5.5 is an infinite series of sinusoidal harmonics of the wingbeat frequency

$$q_1(\tau) = \sum_{n=0}^{\infty} \left[A_n \cos(n\tau) + B_n \sin(n\tau) \right] \quad (5.6)$$

where A_n and B_n are magnitudes which must be solved for. Substituting Eq. 5.6

into Eq. 5.5 (and noting $\sin^2(\tau) = \frac{1}{2} - \frac{1}{2} \cos(2\tau)$) results in the equation

$$\begin{aligned}
& - \sum_{n=0}^{\infty} \left[n^2 A_n \cos(n\tau) + n^2 B_n \sin(n\tau) \right] \\
& + \left[\left(\frac{\omega_1}{\omega} \right)^2 + \frac{K\Phi^2}{2} \right] \sum_{n=0}^{\infty} \left[A_n \cos(n\tau) + B_n \sin(n\tau) \right] \\
& - \underbrace{\frac{K\Phi^2}{2} \cos(2\tau) \sum_{n=0}^{\infty} \left[A_n \cos(n\tau) + B_n \sin(n\tau) \right]}_{\text{time-varying stiffness}} = -F\Phi \cos(\tau) \quad (5.7)
\end{aligned}$$

The time-varying stiffness term in Eq. 5.7 is the source of the coupling between harmonics. This coupling can be shown explicitly by expanding the products of the $\cos(2\tau)$ term with the harmonics in the infinite series:

$$\begin{aligned}
& \cos(2\tau) \sum_{n=0}^{\infty} \left[A_n \cos(n\tau) + B_n \sin(n\tau) \right] \\
& = \frac{1}{2} \sum_{n=0}^{\infty} \left[A_n \cos((n-2)\tau) + A_n \cos((n+2)\tau) \right. \\
& \quad \left. + B_n \sin((n-2)\tau) + B_n \sin((n+2)\tau) \right] \\
& = \frac{1}{2} \left\{ A_2 + (A_3 + A_1) \cos(\tau) + (B_3 - B_1) \sin(\tau) \right. \\
& \quad + (A_4 + 2A_0) \cos(2\tau) + B_4 \sin(2\tau) \\
& \quad \left. + \sum_{n=3}^{\infty} \left[(A_{n+2} + A_{n-2}) \cos(n\tau) + (B_{n+2} + B_{n-2}) \sin(n\tau) \right] \right\} \quad (5.8)
\end{aligned}$$

For the purposes of demonstration, we will now make a further simplification and assume that the structural response of the wing is comprised of only the first three harmonics, so $A_n = B_n = 0$ for $n \geq 4$. Using this assumption and the

relationship of Eq. 5.8, Eq. 5.7 is rewritten and simplified to give

$$\begin{aligned}
& -A_1 \cos(\tau) + \left(\frac{\omega_1}{\omega}\right)^2 A_1 \cos(\tau) + \frac{K\Phi^2}{4} (A_1 - A_3) \cos(\tau) - 9A_3 \cos(3\tau) \\
& + \left(\frac{\omega_1}{\omega}\right)^2 A_3 \cos(3\tau) + \frac{K\Phi^2}{2} \left(A_3 - \frac{1}{2}A_1\right) \cos(3\tau) = -F\Phi \cos(\tau) \quad (5.9)
\end{aligned}$$

The harmonics of the response can now be considered separately. We will look at the $\cos(\tau)$ terms in Eq. 5.9:

$$\underbrace{-A_1 \cos(\tau)}_{\text{mass}} + \underbrace{\left(\frac{\omega_1}{\omega}\right)^2 A_1 \cos(\tau)}_{\text{strain stiffness}} + \underbrace{\frac{K\Phi^2}{4} (A_1 - A_3) \cos(\tau)}_{\text{inertial stiffness}} = -F\Phi \cos(\tau) \quad (5.10)$$

The flapping motion drives the first harmonic response directly through the terms containing A_1 . Additionally, the time-periodic coupling in the inertial stiffness term drives the third harmonic response through the term containing A_3 .

Now consider $\cos(3\tau)$ terms in Eq. 5.9:

$$\underbrace{-9A_3 \cos(3\tau)}_{\text{mass}} + \underbrace{\left(\frac{\omega_1}{\omega}\right)^2 A_3 \cos(3\tau)}_{\text{strain stiffness}} + \underbrace{\frac{K\Phi^2}{2} \left(A_3 - \frac{1}{2}A_1\right) \cos(3\tau)}_{\text{inertial stiffness}} = 0 \quad (5.11)$$

If the wingbeat frequency ω is third subharmonic of the wing's natural frequency then $\omega_1/\omega = 3$ and the mass and strain stiffness contributions in Eq. 5.11 will cancel. The third harmonic magnitude A_3 will then be equal to one-half of A_1 . When the system is excited at the third subharmonic of ω_1 , the stiffness of the 3-per-wingbeat response becomes relatively small, causing the 3-per-wingbeat portion of the response to absorb energy through increased structural deformations.

For a general flapping wing system, the n -per-wingbeat response will lose stiffness when the wingbeat frequency is the n th subharmonic of the first bending frequency, when $\omega_1/\omega = n$. However, this loss of stiffness appears to be significant only when $\omega_1/\omega = 3$. For other values of n , the effect on the total

system response will be considerably less severe. The special significance of the $\omega_1/\omega = 3$ case can be understood by noting that wingbeat frequencies of $\omega_1/\omega = n$ will reduce the stiffness of the $n\omega$ structural response *only* with respect to the $(n - 2)\omega$ and $(n + 2)\omega$ response components. The structural response of the flapping wing is dominated by the 1-per-wingbeat response component, which can only significantly couple to the 3-per-wingbeat response component.

This effect is best understood with an example. We shall consider again the forced response of the scalar flapping-only system of Eq. 5.5 solved by the assumed harmonic response of Eq. 5.6. We assume the response is limited to the first five harmonics, so the modal response of the system is

$$q_1 = A_1 \cos(\tau) + A_3 \cos(3\tau) + A_5 \cos(5\tau)$$

and the magnitudes of the response components solve the matrix equation

$$\begin{bmatrix} \left(\frac{\omega_1}{\omega}\right)^2 + \frac{K\Phi^2}{4} - 1 & -\frac{K\Phi^2}{4} & 0 \\ -\frac{K\Phi^2}{4} & \left(\frac{\omega_1}{\omega}\right)^2 + \frac{K\Phi^2}{2} - 9 & -\frac{K\Phi^2}{4} \\ 0 & -\frac{K\Phi^2}{4} & \left(\frac{\omega_1}{\omega}\right)^2 + \frac{K\Phi^2}{2} - 25 \end{bmatrix} \begin{Bmatrix} A_1 \\ A_3 \\ A_5 \end{Bmatrix} = \begin{Bmatrix} -F\Phi \\ 0 \\ 0 \end{Bmatrix}$$

Furthermore, we will assume a uniform beam wing (for which $K = 0.048$) and flapping stroke $\Phi = 90^\circ$. Table 5.6 gives the relative magnitudes of the response components for several integer values of ω_1/ω . In general, the 5-per-wingbeat response A_5 is orders of magnitudes less than the 3-per-wingbeat response A_3 ,

Table 5.6: Frequency response components of a simplified flapping system for different normalized first natural frequencies.

$\omega_1/\omega = 2$	$\omega_1/\omega = 3$	$\omega_1/\omega = 4$	$\omega_1/\omega = 5$
$A_3 = -0.0060A_1$	$A_3 = 0.4995A_1$	$A_3 = 0.0042A_1$	$A_3 = 0.0018A_1$
$A_5 = -0.0014A_3$	$A_5 = -0.0019A_3$	$A_5 = -0.0033A_3$	$A_5 = 0.5000A_3$

which is itself orders of magnitudes less than the 1-per-wingbeat response A_1 . When $\omega_1/\omega = 3$ the 3-per-wingbeat response is nearly half of the 1-per-wingbeat response, an effect which will significantly alter the total response of the system. Likewise, when $\omega_1/\omega = 5$ the 5-per-wingbeat response is half of the 3-per-wingbeat response. While this represents a significant *relative* change in the 5-per-wingbeat response, both the 3-per-wingbeat and 5-per-wingbeat responses are still very small with respect to the dominant 1-per-wingbeat response.

5.7 Summary

A validated aeroelastic model of a flapping wing was used to perform a parametric study of flapping wing performance with changes of structural properties. The performance of the wings in this study are evaluated by the magnitude of the mean lift force over one flapping period. The baseline wing for this study is the physical wing and subsequent FEM used for the original validation of the aeroelastic model. The baseline wing is modeled on the planform of a fruit fly wing, and has an aluminum frame and a mylar membrane. Sinusoidal flapping and feathering motions are prescribed with flapping frequencies and amplitudes based on the original validation study. The inclusion of modeled deformations of the wing result in an 18% increase in mean lift in comparison with a rigid-wing case. Circulatory effects (including lift arising from wing deformations) account for nearly half of the mean lift, while LEV and apparent mass effects contribute approximately 20% and 30% of the mean lift, respectively.

The effect of wing planform shape on lift was analyzed. Planform geometries were generated using an empirical model of biological wing planforms parameterized by the radial center-of-area location. Wing FEMs were constructed with centers-of-area between 42% and 56% of wing radius and were designed to have the same mass and leading-edge spar geometry as the baseline wing. The

aeroelastic model indicates that total lift increases as the wing center-of-area is biased outboard. This trend is expected due to the greater relative airspeed (and hence, greater quasi-steady lift per unit chord) at the outer portions of the rotating wing. While the results of this parametric analysis suggest that outboard-biased wings are preferable for lift generation, the opposite trend is evident in nature: the strongest and most agile biological fliers have the the most inboard-biased wings. A possible explanation for this discrepancy may be that inboard-biased wings are more efficient in generating lift, but this cannot be confirmed with the current aeroelastic model, which does not predict power requirements. It is suggested that this discrepancy be studied as future research.

The effect of material thickness on lift was analyzed in two separate studies. The first study varied the thickness of the aluminum frame only. The aluminum frame includes the leading-edge spar, which is the primary structural member of the wing. For frame thicknesses of 90% of the baseline thickness and higher, lift decreases as frame thickness increases. As the frame thickness grows large, lift decreases to approach its rigid-wing value. This trend indicates that a thicker frame is more resistant to beneficial deformations. For frame thicknesses reduced to 75% and 50% of the baseline value, the wing experienced large deformations which invalidate the analysis. However, the 75% thickness cases showed an anomalous and significant decrease in lift, caused by a large and detrimental bending structural response at the $3/\text{rev}$ frequency. The flapping-wing structural model, which was developed in this dissertation, was used to show that the time-periodic stiffnesses of the system will couple together odd harmonic structural responses independently of even harmonic structural responses. For wingbeat frequencies near odd subharmonics of the bending frequency, these couplings can drive large structural motions due to decreased structural stiffnesses at the same frequency.

The second study of material thickness varied the thickness of the mylar membrane only. The magnitude of mean lift is less sensitive to changes in membrane thickness than it was to changes in frame thickness. However, the parametric study revealed that the mean lift generated by the wing increased when the membrane thickness was increased and *also* when it was decreased. This result is caused by two opposing trends. Increased membrane thickness will stiffen the wing, limiting lift-enhancing deformations, but simultaneously, increased membrane thickness increases the mass of wing wing, increasing inertial loads that drive lift-enhancing deformations. By coincidence, the former trend was dominant as membrane thickness was decreased from the baseline (lower thickness leads to lower stiffnessness and greater deformations), while the later was dominant as membrane thickness was increase (higher thickness leads to greater mass and greater deformations). These trends were numerically demonstrated by independently changing the mass and bending stiffness of the membrane. This non-monotonic effect of membrane thickness demonstrates the complexity of designing flexible wing structures for flapping wing flight.

CHAPTER 6

CONCLUDING REMARKS

In many ways, bio-inspired flapping-wing MAVs are unique aeronautical systems. Their mode of flight and their small size make them significantly unlike the airplanes and helicopters that form the basis of our current knowledge of aeronautical engineering. They offer a distinctive opportunity to learn directly from nature, to incorporate knowledge that is embodied in biological fliers. The possible benefits of bio-inspired MAVs are profound: tiny aerial robots with exceptional maneuverability, able to perform tasks in environments that are enclosed or otherwise inaccessible to conventional vehicles. Achieving this goal requires advances of our understanding of the complex functional processes of insect-like flight and the means to realize them in mechanical systems. This dissertation works toward a more complete understanding of insect-like flight by presenting an analytic study of flexible, flapping wing structures for normal hovering flight.

6.1 Summary and Conclusions

Bio-inspired flapping-wing flight is an attractive model for micro air vehicles because animals are existing, observable systems that demonstrate the feasibility of small-scale flight. The flapping-wing flight method used by birds and insects take advantage of novel aerodynamic phenomena to enhance lift at smaller scales. Bio-inspired flapping-wing flight is often subdivided into two broad regimes, bird-like flight and insect-like flight. Unsurprisingly, engineering knowledge about these two flapping-wing flight regimes is derived primarily from observations of

biological fliers. Based on such observations, bird-like flight appears to be the less attractive of the two with regard to MAV applications, for several reasons. First, bird-like flight is associated with high forward flight speeds, which is inappropriate for the autonomous operations in confined spaces to which MAVs are best suited. Second, almost all bird-like biological fliers exceed the desired dimensions of MAVs, some by orders of magnitude, which suggests that bird-like flight may not be optimized for MAV-scale flight. Third, all biological bird-like fliers have active musculature used to alter the shape of their wings on a per-wingbeat basis, suggesting that optimized bird-like flight requires complex and high-frequency morphing of the wings. Development and control of comparable small, fast actuators for MAV wings would be a challenge with current technology.

Insect-like flight suffers none of these drawbacks. Insect-like flight is characterized by hover capability and low-speed maneuverability, which is ideal for operation in confined spaces. Many of the largest and most maneuverable insect-like fliers, including hawkmoths and hummingbirds, are the same size as the MAV target, indicating that optimized insect-like flight is achievable at MAV scales. Finally, no biological insect-like flier has the ability to actively change the shape of its wing; this suggests that optimized insect-like flight can be achieved with fully-passive wing structures. Indeed, hummingbird evolution has resulted in *elimination* of the active wing control that is available to all other birds. This implies that the wing structures of insect-like MAVs can be optimized without the need for active on-wing actuation, significantly simplifying their construction.

While the construction of wings for insect-like MAVs may be relatively simple, their operation is not. Though they are not actively controlled, the wings of insect-like biological fliers are quite flexible and experience significant deformations due to the action of inertial and aerodynamic forces. These deformations include reversible twist and camber on up- and downstrokes, which are consistent

with lift-enhancing aerodynamics. Wing flexibility therefore appears to be important to insect-like flight.

Despite this apparent importance, wing flexibility is often neglected in quantitative analyses of insect-like flight in both the biological and engineering fields. Little useful data is available regarding the structural properties of insect wings, so it is difficult to deduce structural design strategies for bio-inspired MAVs. As such, wings for insect-like MAVs are often designed by experimental construction-and-evaluation methods, or by attempts to replicate the structural and geometric features of insect wings. The construction-and-evaluation approach can be scatter-shot and will likely not yield an optimized design, while replication of biological wings without an attendant understanding of their functionality may lead to incorporation of unnecessary structural features into MAV wings. Since biological information is not readily available, this dissertation presents an engineering model of a flexible flapping wing as a means of exploring and evaluating the structural dynamics of insect wings.

A flapping-wing structural analysis was developed that models the wing as a thin elastic beam undergoing small, linear deformations in out-of-plane bending, in-plane bending and torsion while subject to large, unsteady flapping and feathering rotational motions. This analysis was derived as an extension of existing helicopter blade analyses. The flapping wing analysis models cross-sectional properties of the wing, including cross-sectional mass, cross-sectional bending stiffness, center-of-gravity location, center-of-area location, location of wing feathering axis, polar mass radius of gyration and polar area radius of gyration. Since many of these properties have not been reported for either biological fliers or MAV wings, a simplified cross-sectional model was developed to estimate representative values. The inertial cross-sectional loadings of the wing were independently derived by two methods: first, by integration of forces acting on an infinitesimal volume of

the wing, and second, by consideration of various centrifugal, inertial and Coriolis forces acting on a cross-section. The two derivations were shown to be equivalent. An assumed-modes model of the wing was derived, which included a torsional spring at the wing root. This spring, which counteracts out-of-plane bending motions, was included to model the indirect flapping actuation method used by insects. MAV-type flapping actuations can be modeled by assuming an infinitely stiff torsional spring to recover cantilever boundary conditions. The assumed-modes equations of motion of the wing include time-varying stiffnesses which are functions of the velocities and accelerations of the flapping and feathering rotations.

The structural model was non-dimensionalized in time for the case of prescribed, periodic flapping and feathering motions. The non-dimensionalization of the constant, structural stiffness of the wing was facilitated by the definition of three natural frequencies, each characterizing a unique stiffness of the model:

1. The first natural bending frequency of the elastic, non-rotating wing when subject to cantilever boundary conditions, ω_{cant} . This characterizes the bending stiffness of the wing structure.
2. The first natural torsion frequency of the elastic, non-rotating wing when subject to cantilever boundary conditions, ω_{tor} . This characterizes the torsion stiffness of the wing structure.
3. The natural rotational frequency of the rigid wing when subject to pinned boundary conditions with a root spring, ω_{root} . This characterizes the stiffness of the root spring.

The non-dimensional equations of motion reveal that the constant strain stiffness and the time-periodic inertial stiffnesses of the flapping wing structure are both parameterized by the prescribed flapping and feathering motions. The constant

strain stiffness is parameterized by the *frequency* of the flapping motion while the time-periodic inertial stiffnesses are parameterized by the *amplitudes* of the flapping and feathering strokes. More specifically, the constant strain stiffness is parameterized by the ratio of a characteristic structural natural frequency to the flapping wingbeat frequency; the present analysis uses the “normalized cantilever frequency,” $\omega_{\text{cant}}/\omega$. The identification of the independent effects of wingbeat frequency and wingbeat amplitude on, respectively, the constant strain and time-periodic inertial stiffnesses of a flapping wing structure is an insight unique to this non-dimensionalized analytical model.

The non-dimensional parameterization of the flapping wing equations allows us to compare mechanical flapping-wing systems (MAVs and test stands) with biological fliers to assess the similarity of the systems. Current mechanical flapping devices typically have flapping amplitudes which are less than those of biological fliers, indicating that mechanical systems experience lower time-periodic stiffnesses. Also, current mechanical systems also tend to have rigid wings or low wingbeat frequencies, leading to greater $\omega_{\text{cant}}/\omega$ and hence greater constant stiffnesses than biological fliers. Therefore, current flapping-wing mechanisms are not structurally similar to flapping insect wings—the mechanical systems have greater constant stiffnesses and lesser time-periodic stiffnesses than biological fliers. Structural effects related to time-periodic stiffnesses on biological wings are expected to be greater than can be replicated on current mechanical models. Basic aerodynamic considerations indicate that lift developed by flapping wing mechanisms can be maximized by increasing wingbeat frequency and amplitude. This suggests that as future flapping-wing mechanisms improve, the balance of constant and time-periodic structural stiffnesses will tend to approach that of biological fliers.

One of the possible time-periodic effects that flapping wings may encounter

are parametric instabilities, unstable structural responses caused by the periodic variations of system stiffness parameters. The parametric stability of a system is a function of the magnitude of the system's constant and time-periodic stiffness. Parametric instabilities have not yet been observed in mechanical flapping systems. However, the dissimilarity between current mechanical and biological flapping systems means that current observations from mechanical systems may not be applicable to biological systems (nor to future mechanical systems which will be more similar to biological fliers). Using a simplified single-degree-of-freedom structural model, which was equivalent to the scalar Mathieu equation, a parametric stability diagram was developed as a function of two flapping-wing parameters: normalized cantilever frequency and flapping stroke amplitude. Parametric instabilities are shown to be unlikely for current mechanical flapping-wing systems, but are much more likely for the operational regions of current biological fliers. Therefore it is important for a designer to be aware of the possibility of parametric instabilities as future MAVs approach the wingbeat frequencies and amplitudes of biological fliers.

Further stability studies are presented for flapping-wing systems with single and multiple modal degrees-of-freedom; coupled and uncoupled assumed modes; and variations of feathering amplitude and structural design parameters. Stability diagrams were primarily generated through numerical Floquet analysis, though some of the simplest cases are solved exactly via transformation of Mathieu functions. For multi-mode systems, instability regions associated with individual modes were identified, as well as additional regions associated with the interaction between two or more modes. Instability regions associated with the first bending mode of the wing were dominant in every case examined in this dissertation. This first-bending-mode instability manifests most prominently as large unstable regions for normalized cantilever frequencies of $\omega_{\text{cant}}/\omega < 1$ to 1.5. Higher-

mode and coupled instability regions also tend to manifest in $\omega_{\text{cant}}/\omega < 1$, but are generally small compared to the first-bending-mode instability regions. Variations of structural design parameters cause minor changes in the higher-mode and coupled instability regions but do not alter the first-bending-mode instability. An exception is the root-spring stiffness, which can cause significant increases in the size of the instability regions, but only for soft springs (i.e., $\omega_{\text{root}} \leq \omega_{\text{cant}}$). The inclusion of linear damping in the structural model mitigates but does not eliminate parametric instabilities. Due to the dominance of the first bending mode in the stability diagrams, it appears that single-mode stability calculations may be sufficient for design studies to confirm the avoidance of possible parametric instabilities.

Having developed and analyzed a thin-beam structural model of a flapping wing the methodology is extended to a plate model of a flapping wing, which will better represent the low-aspect ratio wings typical of insect-like biological and mechanical systems. The flapping plate model is derived as a special case of a generalized assumed-modes model of a flexible plate undergoing large motions. The flapping-wing plate equation of motion has the same general form as the flapping-wing beam equation of motion. Therefore, the non-dimensionalization procedure and stability analysis developed for the thin-beam wing can be applied directly to the plate wing model. Mode shapes for complex plate geometries are calculated using finite element analysis. A procedure for numerically evaluating line integrals using radial basis functions is presented and validated as a means of calculating modal matrices. A plate-model equivalent of the thin-beam baseline wing is developed, along with a modified model with a more complex spar geometry. The stability diagrams for both plate wing models are calculated and compared with the equivalent thin-beam diagram. The flapping-wing plate stability diagrams are dominated by the first-mode instability regions,

while instability regions associated with higher modes tend to manifest in the range of $\omega_{\text{cant}}/\omega < 1$. The plate-wing stability diagrams are found to be very similar to the diagrams for the equivalent beam model. This similarity suggests that basic stability calculations may be performed with a beam-wing model, even for low-aspect ratio wings. Such a technique would seem particularly effective when the first mode of a plate wing is well-approximated by a beam bending mode, as is the case for the models presented here.

Finally, an aeroelastic flapping-wing analysis is applied to examine the effects of structural design parameters on lift generation. The aeroelastic analysis loosely couples an FEM-based structural model with an analytic unsteady aerodynamic analysis. The baseline wing for the structural parametric study is a frame-and-membrane wing, modeled from a fruit fly wing planform, that had been used for experimental validation of the aeroelastic analysis. An empirical model of biological insect wing planforms was used to generate a series of model wings of different planforms, which were parameterized by the wing's spanwise area centroid. Lift was found to increase as the wing's area was biased more outboard, suggesting that optimized wings should be designed with outboard-biased planforms. This trend is contrary to biological fliers—the strongest biological fliers tend to have the most inboard-biased wing planforms. It is speculated that inboard-biased wings may operate more efficiently but this theory cannot be tested with the current aeroelastic analysis, which has not been validated to predict power required. Parametric variation of the thickness of the wing frame indicates that increases in frame thickness lead to decreases in generated lift, due to the stiffer frame suppressing beneficial deformations. This finding demonstrates that wing flexibility can lead to gains in lift production. Parametric variation of the thickness of the membrane indicated increases in lift were possible by increasing or decreasing membrane thickness. This is the result of two opposing trends:

1) as membrane thickness is decreased the thinner wing is less stiff, allowing greater beneficial deformations, and 2) as membrane thickness is increased the thicker wing has more mass, so inertial loads increase and force greater beneficial deformations.

During the parametric study of the effect of membrane thickness, one particular case gives a unique result. In this case, the frame thickness was reduced by an amount that caused the wing's first natural frequency to be approximately three times greater than the wingbeat frequency, $\omega_1 = 3\omega$. In this case, the structural response of the wing showed a large 3/wingbeat component which caused a significant reduction in lift. This 3/wingbeat response was not observed in any other aeroelastic case in this dissertation. The thin-beam structural model was used to show that the time-periodic stiffnesses of the wing cause odd harmonics of the structural response to be coupled together. When the wingbeat frequency satisfies $\omega_1/\omega = 3$, the 3/wingbeat structural response experiences reduced stiffness, which is driven to large magnitude through the odd-harmonic structural coupling of the 1/wingbeat inertial loads. In this manner, the 3/wingbeat response that caused a significant loss of lift was analyzed using a purely structural model.

6.2 Contributions

- A thin-beam analytical assumed-modes structural model of a flexible, flapping insect wing is developed. The analysis is created to be compatible with analytical design studies and explicitly includes cross-sectional design parameters in its formulation. The model is presented in both dimensional and non-dimensional forms. Prior to this study, all models of flexible insect wings structures were FEM-based models, from which the effects of design parameters are not explicitly evident. This dissertation is the first to present a non-dimensional analysis of flapping wing structures.

- Non-dimensional structural similarity parameters are identified which characterize the magnitude of the constant, structural stiffness and the time-periodic inertial stiffness of the flapping wing system. These similarity parameters allow comparison of the structural similarity of biological and mechanical flapping-wing systems at different scales.
- A parametric stability analysis is developed for flapping wing structures. The analysis includes a stability diagram which characterizes a wing's parametric stability as a function of parameters characterizing the wing's constant strain stiffness and time-periodic inertial stiffness. Studies are presented that examine the effects of structural design parameters on parametric stability.
- The conceptual framework of non-dimensionalization and parametric stability analysis developed for the thin-beam wing is extended for flapping wings modeled as plates. Equivalences between the thin-beam model and plate model are identified for both the equations of motion and the stability analyses.
- Parametric studies of structural parameters' effects on lift production are presented, using a validated aeroelastic flapping wing model. Several unique observations are presented, including identification of harmonic structural couplings which may be detrimental to lift and the non-monotonic effect of membrane thickness on lift production. In general, the results confirm that beneficial structural deformations can increase lift of flapping wings.

6.3 Recommendations for Future Work

This dissertation has presented the development of structural models of flapping wings for use in designing MAVs, implemented these models to study

possible instabilities of MAV wings, and performed parametric studies of aeroelastic wing models. The study of flapping wing structures and aeroelastic effects is still in its early stages and provides numerous opportunities for continuing contributions to the field. Based on the research presented in this dissertation, the following future research tasks are recommended:

- The flapping-wing beam equations of motion presented in this dissertation can be extended to include a prescribed stroke deviation, the rotational wing motion perpendicular to the stroke plane. Stroke deviation is evident in biological flapping flight, but its purpose is not well understood. The framework that has been developed to derive the equations of motion will accommodate stroke deviation rotations in the same manner as flapping and feathering rotations. Inclusion of stroke deviation will allow more accurate representation and analysis of insect-like wing motions.
- Following this dissertation's methodology of extending Houbolt and Brooks' analysis of helicopter blades [162] to generate a linear structural model of a flapping wing, a nonlinear thin-beam flapping wing structural model should be developed based on the analysis of Hodges and Dowell [166]. The linear thin-beam flapping wing model created in this dissertation cannot be used to model large nonlinear wing deformations, and it does not include nonlinear coupling terms known from helicopter analyses of rotating beams. Large wing deformations are frequently observed in biological fliers and it seems likely that MAV wings will likewise exhibit large deformations as technology progresses, necessitating the development of appropriate analysis tools.
- An aerodynamic model can be integrated into the non-dimensional thin-beam flapping wing model to create a non-dimensional aeroelastic model. A quasi-steady aerodynamic model incorporating leading-edge vortex and

added-mass effects could be added to this dissertation's structural model through its external loading terms. These terms comprise the majority of the lift-generating effects on the wing, allowing the model to predict airloads for flapping wings. Non-dimensionalization of the aerodynamic terms through the methodology established in this dissertation should provide insight into key aeroelastic parameters.

- The two preceding recommendations, i.e., the development of a nonlinear structural model and application of a suitable aerodynamic model, can be applied to this dissertation's plate model as well as the beam model. Reformulation of the two-dimensional plate model to include spars (modeled as beam elements) will greatly enhance the ability to model the actual spar-and-membrane geometries of biological and MAV wings. A two-dimensional vortex-lattice aerodynamic model can be incorporated into the plate-wing model to derive a two-dimensional aeroelastic model.
- The parametric instabilities identified in this study for have not been experimentally observed in flapping-wing mechanisms. The prime difficulty in obtaining experimental confirmation of such stabilities are the limitations of current flapping mechanisms in generating the large-stroke, high-frequency flapping motions where instabilities are expected to be possible. It is anticipated that future improvements of flapping mechanisms towards such large-stroke, high-frequency motion will be necessary to attain increased lift. When these improved flapping mechanisms become available, experimental studies to confirm such instabilities should be performed.
- Regarding the parametric study of wing planform shape with an aeroelastic analysis, there exists a discrepancy between the results of parametric study and observations of nature. The parametric study suggests that better perfor-

mance (i.e., greater lift) is achieved with wing planforms biased toward the wing tip, however, all strong biological fliers have planforms biased toward the root. The universality of inboard-biased planforms on strong biological fliers suggests that this represents an optimized design, which would be beneficial for MAV designers to understand.

A hypothesis is put forward that inboard-biased wings may produce lift more efficiently than out-board biased wings. This theory cannot be tested at this time because the aeroelastic analysis used in this dissertation cannot predict power requirements. Testing this hypothesis would require the development and validation of an aeroelastic analysis that can predict power requirements.

- An experimental study to measure and record the material and structural properties of biological wings is necessary to fill large gaps in current knowledge. Representative measurements of bending and torsional stiffness, elastic axis location, cross-sectional area of inertia, wing mode shapes and wing natural frequencies are almost non-existent for insect-like biological fliers at the present time. This lack of knowledge hinders analysis and understanding of the function of flexible wings in insect-like flight. A systematic effort to generate this knowledge would benefit engineers developing bio-inspired MAVs as well as biologists studying insect-like flight.

APPENDIX A

NATURAL FREQUENCIES OF BEAM WINGS

A.1 Characteristic $(\lambda R)_{\gamma 1}$ of a Uniform Clamped-Free Beam

Presented is a demonstration that $\text{eig}(\widehat{\mathcal{A}}^{-1}\widehat{\mathcal{G}})_{\min} = (\lambda R)_{\gamma 1}^2$ for the case of a uniform clamped-free beam. $\widehat{\mathcal{A}}$ and $\widehat{\mathcal{G}}$ are given by

$$\begin{aligned}\widehat{\mathcal{A}}_{ij} &= \widehat{\mathcal{A}}_{ji} = \int_0^1 \hat{m} \hat{k}_m^2 \hat{\chi}_{\gamma i} \hat{\chi}_{\gamma j} d\xi \\ \widehat{\mathcal{G}}_{ij} &= \widehat{\mathcal{G}}_{ji} = \int_0^1 \widehat{GJ} \hat{\chi}'_{\gamma i} \hat{\chi}'_{\gamma j} d\xi\end{aligned}$$

For a uniform beam, $\hat{m} = \hat{k}_m^2 = \widehat{GJ} = 1$, and the exact i th mode shape for a clamped-free boundary is

$$\hat{\chi}_{\gamma i}(\xi) = \sin(\lambda R)_{\gamma i} \xi \quad (\text{A.1})$$

where $(\lambda R)_{\gamma i}$ solves

$$\cos(\lambda R)_{\gamma i} = 0 \quad (\text{A.2})$$

Since Eq. A.1 are the exact mode shapes, $\widehat{\mathcal{A}}$ and $\widehat{\mathcal{G}}$ will both be diagonal and the eigenvalues of $\widehat{\mathcal{A}}^{-1}\widehat{\mathcal{G}}$ will be the diagonal entries

$$\text{eig}(\widehat{\mathcal{A}}^{-1}\widehat{\mathcal{G}}) = \widehat{\mathcal{G}}_{ii} / \widehat{\mathcal{A}}_{ii}, \quad i = 1, \dots, N_\gamma$$

Now solve for $\widehat{\mathcal{A}}_{ii}$, noting that $\cos(\lambda R)_{\gamma i} = 0$ by definition from Eq. A.2:

$$\begin{aligned}\widehat{\mathcal{A}}_{ii} &= \int_0^1 \sin^2(\lambda R)_{\gamma i} \xi \, d\xi \\ &= \frac{1}{2} + \frac{\sin(\lambda R)_{\gamma i} \cos(\lambda R)_{\gamma i}}{(\lambda R)_{\gamma i}} \\ &= \frac{1}{2}\end{aligned}$$

Likewise,

$$\begin{aligned}\widehat{\mathcal{G}}_{ii} &= (\lambda R)_{\gamma i}^2 \int_0^1 \cos^2(\lambda R)_{\gamma i} \xi \, d\xi \\ &= (\lambda R)_{\gamma i}^2 \left[\frac{1}{2} - \frac{\sin(\lambda R)_{\gamma i} \cos(\lambda R)_{\gamma i}}{(\lambda R)_{\gamma i}} \right] \\ &= \frac{1}{2} (\lambda R)_{\gamma i}^2\end{aligned}$$

Therefore,

$$\text{eig}(\widehat{\mathcal{A}}^{-1} \widehat{\mathcal{G}}) = (\lambda R)_{\gamma i}^2, \quad i = 1, \dots, N_\gamma$$

and the minimum eigenvalue is $(\lambda R)_{\gamma 1}^2$ corresponding to the lowest natural torsion frequency.

A.2 Characteristic $(\lambda R)_{w1}$ of a Uniform Cantilever-Free Beam

Presented is a demonstration that $\text{eig}(\widehat{\mathcal{C}}^{-1} \widehat{\mathcal{H}})_{\min} = (\lambda R)_{w1}^4$ for the case of a uniform cantilever-free beam. $\widehat{\mathcal{C}}$ and $\widehat{\mathcal{H}}$ are given by

$$\begin{aligned}\widehat{\mathcal{C}}_{ij} &= \widehat{\mathcal{C}}_{ji} = \int_0^1 \hat{m} \hat{\chi}_{wi} \hat{\chi}_{wj} \, d\xi \\ \widehat{\mathcal{H}}_{ij} &= \widehat{\mathcal{H}}_{ji} = \int_0^1 \widehat{EI}_z \hat{\chi}_{wi}'' \hat{\chi}_{wj}'' \, d\xi\end{aligned}$$

For a uniform beam, $\hat{m} = \widehat{EI}_z = 1$, and the exact i th mode shape for a cantilever-free boundary is

$$\hat{\chi}_{wi}(\xi) = \sin(\lambda R)_{wi}\xi + \frac{\sin(\lambda R)_{wi}}{\sinh(\lambda R)_{wi}} \sinh(\lambda R)_{wi}\xi \quad (\text{A.3})$$

where $(\lambda R)_{wi}$ solves

$$\frac{\tan(\lambda R)_{wi}}{\tanh(\lambda R)_{wi}} - 1 = 0 \quad (\text{A.4})$$

As in appendix A.1, using the exact mode shapes of the system means that $\widehat{\mathcal{C}}$ and $\widehat{\mathcal{H}}$ are diagonal and

$$\text{eig}(\widehat{\mathcal{C}}^{-1}\widehat{\mathcal{H}}) = \widehat{\mathcal{H}}_{ii}/\widehat{\mathcal{C}}_{ii}, \quad i = 1, \dots, N_w$$

We now note that, $\widehat{\mathcal{C}}_{ii}$ is

$$\widehat{\mathcal{C}}_{ii} = \int_0^1 \left[\sin(\lambda R)_{wi}\xi + \frac{\sin(\lambda R)_{wi}}{\sinh(\lambda R)_{wi}} \sinh(\lambda R)_{wi}\xi \right]^2 d\xi$$

and $\widehat{\mathcal{H}}_{ii}$

$$\widehat{\mathcal{H}}_{ii} = (\lambda R)_{wi}^4 \int_0^1 \left[-\sin(\lambda R)_{wi}\xi + \frac{\sin(\lambda R)_{wi}}{\sinh(\lambda R)_{wi}} \sinh(\lambda R)_{wi}\xi \right]^2 d\xi$$

It is clear that $\widehat{\mathcal{H}}_{ii}/\widehat{\mathcal{C}}_{ii} = (\lambda R)_{wi}^4$ if the integrals in the above equations are equal. The only difference between the integrals is the sign of the leading term within the brackets, $\sin(\lambda R)_{wi}\xi$. Thus, the integrals in $\widehat{\mathcal{C}}_{ii}$ and $\widehat{\mathcal{H}}_{ii}$ will be the same if the interior product of the binomials,

$$2 \frac{\sin(\lambda R)_{wi}}{\sinh(\lambda R)_{wi}} \int_0^1 \sin(\lambda R)_{wi}\xi \sinh(\lambda R)_{wi}\xi d\xi$$

is zero. Evaluating the integral yields

$$\begin{aligned} \int_0^1 \sin(\lambda R)_{wi} \xi \sinh(\lambda R)_{wi} \xi d\xi &= \frac{\sin(\lambda R)_{wi} \cosh(\lambda R)_{wi} + \cos(\lambda R)_{wi} \sinh(\lambda R)_{wi}}{2(\lambda R)_{wi}} \\ &= \frac{\cos(\lambda R)_{wi} \sinh(\lambda R)_{wi}}{2(\lambda R)_{wi}} \left(\frac{\tan(\lambda R)_{wi}}{\tanh(\lambda R)_{wi}} - 1 \right) \\ &= 0 \end{aligned}$$

because the term in parentheses is zero by definition from Eq. A.4. It is confirmed that $\widehat{\mathcal{H}}_{ii}/\widehat{\mathcal{C}}_{ii} = (\lambda R)_{wi}^4$. Therefore,

$$\text{eig}(\widehat{\mathcal{C}}^{-1}\widehat{\mathcal{H}}) = (\lambda R)_{wi}^4, \quad i = 1, \dots, N_w$$

and the minimum eigenvalue is $(\lambda R)_{w1}^4$ corresponding to the lowest natural bending frequency of the cantilever-free beam.

A.3 Non-dimensional Mass Moment of Inertia of a Pinned, Uniform Rigid Beam

Presented is a demonstration that $\text{eig}(\widehat{\mathcal{C}}^{-1}\widehat{\mathcal{W}})_{\min} = 1/\bar{I}_b$ for the case of a pinned, uniform rigid beam. $\widehat{\mathcal{C}}$ and $\widehat{\mathcal{H}}$ are given by

$$\begin{aligned} \widehat{\mathcal{C}}_{ij} = \widehat{\mathcal{C}}_{ji} &= \int_0^1 \hat{m} \hat{\chi}_{wi} \hat{\chi}_{wj} d\xi \\ \widehat{\mathcal{W}}_{ij} = \widehat{\mathcal{W}}_{ji} &= \hat{\chi}'_{wi} \hat{\chi}'_{wj} \end{aligned}$$

and \bar{I}_b is

$$\bar{I}_b = \int_0^1 \hat{m} \xi^2 d\xi$$

For a uniform beam, $\hat{m} = 1$, and the rigid pinned beam only has a single mode shape

$$\hat{\chi}_{w1}(\xi) = \xi$$

Since there is only a single mode,

$$\text{eig}(\hat{\mathcal{C}}^{-1}\hat{\mathcal{W}})_{\min} = \text{eig}(\hat{\mathcal{W}}_{11}/\hat{\mathcal{C}}_{11})_{\min} = \hat{\mathcal{W}}_{11}/\hat{\mathcal{C}}_{11}$$

It is obvious that $\hat{\mathcal{W}}_{11} = 1$, and evaluating $\hat{\mathcal{C}}_{11}$ gives

$$\begin{aligned}\hat{\mathcal{C}}_{11} &= \int_0^1 \hat{m} \xi^2 d\xi \\ &= \bar{I}_b\end{aligned}$$

Thus, $\text{eig}(\hat{\mathcal{C}}^{-1}\hat{\mathcal{W}})_{\min} = 1/\bar{I}_b$.

APPENDIX B

DERIVATION OF ROOT-SPRING-FREE BENDING MODES OF A UNIFORM BEAM

For our modified Galerkin assumed-modes model to be valid, the assumed beam modes must satisfy the boundary conditions of the system, hence they must change in relation to the root spring stiffness k_{root} . In this dissertation, we use the exact bending modes of a uniform beam with the appropriate boundary conditions as our assumed mode shapes. As in the derivation of our non-dimensional model, we use the frequency ratio $\omega_{\text{root}}/\omega_{\text{cant}}$ as a measure of the root spring stiffness relative to the beam's bending stiffness, so that the non-dimensional modes $\hat{\chi}_w$ are given by a function $\hat{\chi}_w(\xi, \omega_{\text{root}}/\omega_{\text{cant}})$. The derivation of these mode shapes is presented here.

We consider a uniform beam supported by a pin with a root spring of stiffness k_{root} at $x = 0$ and free at $x = R$. In order to calculate the beam's modes, we must solve the following beam equation

$$EI w''''(x) - \omega^2 m w(x) = 0 \quad (\text{B.1})$$

over $0 \leq x \leq R$. The general solution for this equation is of the form

$$w(x) = A \sin \lambda x + B \cos \lambda x + C \sinh \lambda x + D \cosh \lambda x$$

subject to the boundary conditions

$$w(0) = 0$$

$$EI w''(0) = k_{\text{root}} w'(0)$$

$$EI w''(R) = 0$$

$$EI w'''(R) = 0$$

Note that as $k_{\text{root}} \rightarrow \infty$ the second boundary condition approaches $w'(0) = 0$. Conversely, as $k_{\text{root}} \rightarrow 0$ the second boundary condition approaches $w''(0) = 0$. These extremes are equivalent to the cantilever boundary condition and the pinned boundary condition, respectively, at $x = 0$.

For convenience, we introduce a change in variable $y = R - x$ to pose the solution of the beam equation as

$$w(y) = A \sin \lambda y + B \cos \lambda y + C \sinh \lambda y + D \cosh \lambda y \quad (\text{B.2})$$

subject to the boundary conditions

$$w(R) = 0 \quad (\text{B.3})$$

$$EI w''(R) = -k_{\text{root}} w'(R) \quad (\text{B.4})$$

$$EI w''(0) = 0 \quad (\text{B.5})$$

$$-EI w'''(0) = 0 \quad (\text{B.6})$$

Substituting Eq. B.2 into the moment boundary condition Eq. B.5 gives

$$\begin{aligned} 0 &= EI \lambda^2 (-A \sin 0 - B \cos 0 + C \sinh 0 + D \cosh 0) \\ &= EI \lambda^2 (-B + D) \end{aligned}$$

so that $D = B$. Likewise, substituting Eq. B.2 into the shear boundary condition Eq. B.6 gives

$$\begin{aligned} 0 &= -EI\lambda^3(-A \cos 0 + B \sin 0 + C \cosh 0 + D \sinh 0) \\ &= -EI\lambda^3(-A + C) \end{aligned}$$

so $C = A$. We now continue with the displacement boundary condition Eq. B.3. Evaluation of this boundary condition, noting the above equalities, gives

$$0 = A(\sin \lambda R + \sinh \lambda R) + B(\cos \lambda R + \cosh \lambda R)$$

Introducing the coefficient C_λ for notational convenience as

$$C_\lambda = \frac{\sin \lambda R + \sinh \lambda R}{\cos \lambda R + \cosh \lambda R}$$

we can write $B = -C_\lambda A$. The solution to the beam equation Eq. B.2 is rewritten as

$$w(y) = A \left[\sin \lambda y + \sinh \lambda y - C_\lambda (\cos \lambda y + \cosh \lambda y) \right] \quad (\text{B.7})$$

We can now solve for the modes' characteristic parameters λR by substituting Eq. B.7 into the root spring boundary condition Eq. B.4:

$$\begin{aligned} EI\lambda^2 A \left[-\sin \lambda R + \sinh \lambda R - C_\lambda (-\cos \lambda R + \cosh \lambda R) \right] = \\ -k_{\text{root}} \lambda A \left[\cos \lambda R + \cosh \lambda R - C_\lambda (-\sin \lambda R + \sinh \lambda R) \right] \end{aligned}$$

We now divide both sides by λA and manipulate the left hand side to yield an

explicit λR term:

$$\frac{EI}{R} \lambda R \left[-\sin \lambda R + \sinh \lambda R - C_\lambda (-\cos \lambda R + \cosh \lambda R) \right] = \\ -k_{\text{root}} \left[\cos \lambda R + \cosh \lambda R - C_\lambda (-\sin \lambda R + \sinh \lambda R) \right]$$

By substituting in the expression for C_λ and simplifying, this equation becomes

$$2 \frac{EI}{R} \lambda R \frac{\cos \lambda R \sinh \lambda R - \sin \lambda R \cosh \lambda R}{\cos \lambda R \cosh \lambda R} = -2 k_{\text{root}} \frac{1 + \cos \lambda R \cosh \lambda R}{\cos \lambda R \cosh \lambda R}$$

which is then further rearranged as

$$\lambda R (\cos \lambda R \sinh \lambda R - \sin \lambda R \cosh \lambda R) + \frac{k_{\text{root}} R}{EI} (1 + \cos \lambda R \cosh \lambda R) = 0$$

The above equation has no closed-form solution for the characteristic values of λR . Instead, λR must be solved numerically for each mode shape for a given root spring stiffness k_{root} . Using Eq. 2.67, the fraction $k_{\text{root}} R / EI_{z0}$ is calculated as a function of a user-defined value of $\omega_{\text{root}} / \omega_{\text{cant}}$:

$$\frac{k_{\text{root}} R}{EI_{z0}} = (\lambda R)_{\text{cant}}^4 \hat{I}_b \left(\frac{\omega_{\text{root}}}{\omega_{\text{cant}}} \right)^2$$

We now return to the beam solution in Eq. B.7, which is written as a function of y . We can rewrite this equation in terms of the non-dimensional length variable ξ by substituting

$$y = R - x = R(1 - \xi)$$

Since the magnitudes of the mode shapes are unimportant in relation to the

stability analysis, we set $A = 1$, resulting in

$$w(\xi) = \sin(\lambda R(1 - \xi)) + \sinh(\lambda R(1 - \xi)) - C_\lambda \left[\cos(\lambda R(1 - \xi)) + \cosh(\lambda R(1 - \xi)) \right]$$

The methodology for finding the mode shapes of a root-spring-free uniform beam is summarized as follows. First, select a value for the spring-frequency-to-first-bending-frequency ratio $\omega_{\text{root}}/\omega_{\text{cant}}$. Then, find the characteristic parameters λR for the mode shapes by numerically solving the equation

$$\lambda R (\cos \lambda R \sinh \lambda R - \sin \lambda R \cosh \lambda R) + (\lambda R)_{\text{cant}}^4 \hat{I}_b \left(\frac{\omega_{\text{root}}}{\omega_{\text{cant}}} \right)^2 (1 + \cos \lambda R \cosh \lambda R) = 0 \quad (\text{B.8})$$

Once λR is calculated for the desired number of modes, the mode shapes on $0 \leq \xi \leq 1$ are given by the equation

$$w(\xi) = \sin(\lambda R(1 - \xi)) + \sinh(\lambda R(1 - \xi)) - \frac{\sin \lambda R + \sinh \lambda R}{\cos \lambda R + \cosh \lambda R} \left[\cos(\lambda R(1 - \xi)) + \cosh(\lambda R(1 - \xi)) \right] \quad (\text{B.9})$$

Figure B.1 depicts some bending mode shapes of the beam as a function of decreasing $\omega_{\text{root}}/\omega_{\text{cant}}$. The first diagram, figure B.1a, shows the ideal cantilever case, which is equivalent to an infinitely stiff root spring. The last, figure B.1h, shows the ideal pinned case, which is equivalent to no root spring. Figures B.1b–B.1g show the modes as $\omega_{\text{root}}/\omega_{\text{cant}}$ decreases from 50 to 0.05; these mode shapes are intermediate between the cantilever and pinned case. Root spring frequency ratios of $\omega_{\text{root}}/\omega_{\text{cant}} > 50$ are generally equivalent to a cantilever boundary, while $\omega_{\text{root}}/\omega_{\text{cant}} < .05$ are generally equivalent to a pinned boundary.

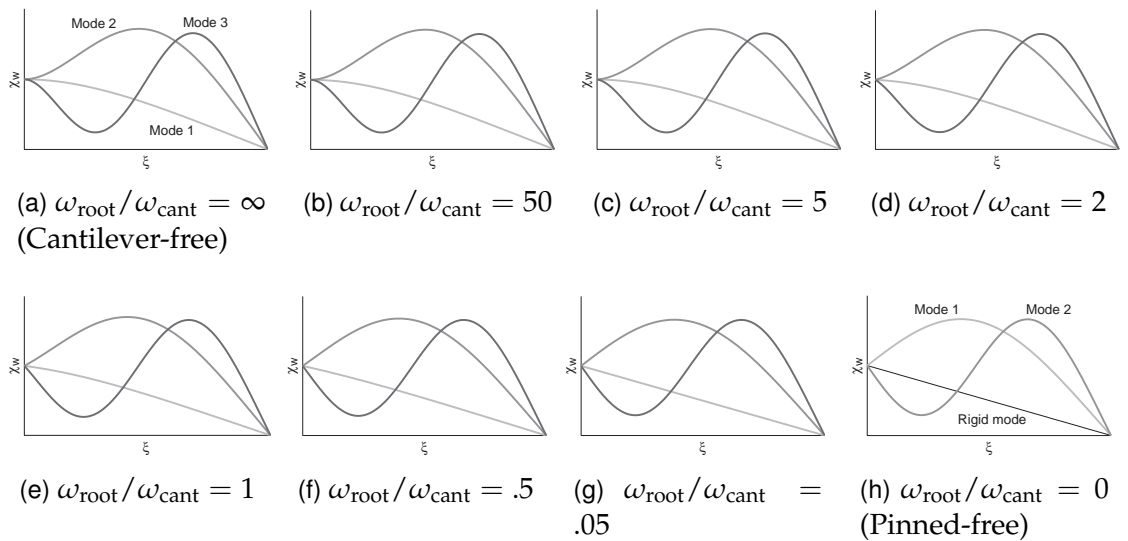


Figure B.1: Root-spring-free mode shapes of a uniform beam as a function of $\omega_{\text{root}}/\omega_{\text{cant}}$. First three bending modes are shown on all diagrams except for the pinned-free case, which shows rigid-body mode and first two bending modes. Modes scaled to a tip displacement of -1.

The most pronounced transition occurs in the range of $.5 < \omega_{\text{root}}/\omega_{\text{cant}} < 5$. Note that as the frequency ratio $\omega_{\text{root}}/\omega_{\text{cant}} \rightarrow 0$, the first root-spring-free mode approaches the pinned-free rigid-body mode, while the $(i + 1)$ th root-spring-free mode approaches the i th pinned-free bending mode.

Bibliography

- [1] James M. McMichael and Michael S. Francis, "Micro Air Vehicles—Toward a New Dimension in Flight," Tech. rep., Defense Advanced Research Projects Agency, Aug 7 1997. Available from: http://www.fas.org/irp/program/collect/docs/mav_auvsi.htm [cited Jun 4 2011].
- [2] Thomas J. Mueller and James D. DeLaurier, "An Overview of Micro Air Vehicle Aerodynamics," Mueller [179], chap. 1, pp. 1–10.
- [3] R. C. Michelson, "Novel Approaches to Miniature Flight Platforms," *Proceedings of the Institution of Mechanical Engineers, Part G: Journal of Aerospace Engineering*, vol. 218, no. 6, Dec 2004, pp. 363–373.
- [4] Joel M. Grasmeyer and Matthew J. Keennon, "Development of the Black Widow Micro Air Vehicle," Mueller [179], chap. 24, pp. 519–535.
- [5] Stephen J. Morris and Michael Holden, "Design of Micro Air Vehicles and Flight Test Validation," *Conference on Fixed, Flapping and Rotary Wing Vehicles at Very Low Reynolds Numbers*, Notre Dame, IN, Jun 5–7 2000.
- [6] J. Kellogg, C. Bovais, R. Foch, H. McFarlane, C. Sullivan, J. Dahlburg, J. Gardner, R. Ramamurti, D. Gordon-Spears, R. Hartley, B. Kamgar-Parsi, F. Pipitone, W. Spears, A. Sciambi and D. Snull, "The NRL Micro Tactical Expendable (MITE) Air Vehicle," *Aeronautical Journal*, vol. 106, no. 1062, Aug 2002, pp. 431–441.
- [7] P. G. Ifju, "Flexible-Wing-Based Micro Air Vehicles," C. H. M. Jenkins, ed., *Compliant Structures in Nature and Engineering*, chap. 8, WIT Press, Billerica, MA, 2005, pp. 171–191.
- [8] Wei Shyy, Peter Ifju and Dragos Vieru, "Membrane Wing-Based Micro Air Vehicles," *Transactions of the ASME: Applied Mechanics Reviews*, vol. 58, no. 4, Jul 2005, pp. 283–301.
- [9] Vijay Jagdale, Bhavani Sankar and Peter Ifju, "Modeling of Bendable MAV Wing Using Energy Method," *49th AIAA/ASME/ASCE/AHS/ASC Structures, Structural Dynamics & Materials Conference*, AIAA 2008-1790, Schaumburg, IL, Apr 7–10 2008.
- [10] Peter J. Kunz and Ilan Kroo, "Analysis and Design of Airfoils for Use at Ultra-Low Reynolds Numbers," Mueller [179], chap. 3, pp. 35–60.
- [11] J. L. Lin, C. Y. Wei and C. Y. Lin, "Aerodynamic Performance of Thin Wings at Low Reynolds Numbers," *Aircraft Engineering and Aerospace Technology*, vol. 79, no. 3, 2007, pp. 245–253.
- [12] Alain Pelletier and Thomas J. Mueller, "Low Reynolds Number Aerodynamics of Low-Aspect-Ratio Thin/Flat/Cambered-Plate Wings," *Journal of Aircraft*, vol. 37, no. 5, Sep–Oct 2000, pp. 825–832.
- [13] Michael S. Selig and James J. Guglielmo, "High-Lift Low Reynolds Number Airfoil Design," *Journal of Aircraft*, vol. 34, no. 1, Jan–Feb 1997, pp. 72–79.

- [14] Bret Stanford, Mujahid Abdulrahim, Rick Lind and Peter Ifju, "Investigation of Membrane Actuation for Roll Control of a Micro Air Vehicle," *Journal of Aircraft*, vol. 44, no. 3, May–Jun 2007, pp. 741–749.
- [15] R. M. Barrett, "Adaptive Aerostructures: Improving High Performance Subscale Military UAVs," *45th AIAA/ASME/ASCE/AHS/ASC Structures, Structural Dynamics & Materials Conference*, AIAA 2004-1886, Palm Springs, CA, Apr 19–22 2004.
- [16] Larry Lipera, Jason D. Colbourne, Mark B. Tischler, M. Hossein Mansur, Michael C. Rotkowitz and Paul Patangui, "The Micro Craft iSTAR Micro Air Vehicle: Control System Design and Testing," *Proceedings of the AHS 57th Annual Forum*, Washington, DC, May 9–11 2001, pp. 1998–2008.
- [17] Jayant Sirohi, Marat Tishchenko and Inderjit Chopra, "Design and Testing of a Micro-Aerial Vehicle with a Single Rotor and Turning Vanes," *AHS 61st Annual Forum Proceedings*, vol. 2, Grapevine, TX, Jun 1–3 2005, pp. 1957–1967.
- [18] Felipe Bohorquez, Paul Samuel, Jayant Sirohi, Daryll Pines, Lael Rudd and Ron Perel, "Design, Analysis and Hover Performance of a Rotary Wing Micro Air Vehicle," *Journal of the American Helicopter Society*, vol. 48, no. 2, Apr 2003, pp. 80–90.
- [19] Paul Samuel, Jayant Sirohi, Felipe Bohorquez and Ronald Couch, "Design and Testing of a Rotary Wing MAV with an Active Structure for Stability Control," *AHS 61st Annual Forum Proceedings*, vol. 2, Grapevine, TX, June 1–3 2005, pp. 1946–1956.
- [20] Epson Corporation, "Epson Develops World's Smallest Flying Microrobot," News release, Seiko Epson, Nov 17 2003. Available from: http://global.epson.com/newsroom/2003/news_20031118_2.html [cited Jun 4 2011].
- [21] Sara Black, "Composites Enable Micro Air Vehicle," *High-Performance Composites*, Sep 9 2008. Available from: <http://www.compositesworld.com/articles/composites-enable-micro-air-vehicle.aspx> [cited Jun 4 2011].
- [22] L. A. Young, E. W. Aiken, J. L. Johnson, R. Demblewski, J. Andrews and J. Klem, "New Concepts and Perspectives on Micro-Rotorcraft and Small Autonomous Rotary-Wing Vehicles," *20th AIAA Applied Aerodynamics Conference*, AIAA 2002-2816, St. Louis, MO, Jun 24–26 2002.
- [23] Ilan Kroo and Peter Kunz, "Mesoscale Flight and Miniature Rotorcraft Development," Mueller [179], chap. 23, pp. 503–517.
- [24] Aaron M. Harrington, Paul Samuel and Inderjit Chopra, "Optimal Design Study of a Micro Quad Rotor," *Proceedings of the AHS International Specialists' Meeting on Unmanned Rotorcraft and Network Centric Operations*, Tempe, AZ, Jan 25–27 2011.
- [25] Benjamin R. Hein and Inderjit Chopra, "Hover Performance of a Micro Air Vehicle: Rotors at Low Reynolds Number," *Journal of the American Helicopter Society*, vol. 52, no. 3, Jul 2007, pp. 254–262.
- [26] Joon W. Lim, Kenneth W. McAlister and Wayne Johnson, "Hover Performance Correlation for Full-Scale and Model-Scale Coaxial Rotors," *AHS 63rd Annual Forum Proceedings*, vol. 2, Virginia Beach, VA, May 1–3 2007, pp. 1106–1124.

- [27] Jeremy M. Nelson and Nikhil A. Koratkar, "Micro-Rotorcraft Performance Improvement Using Trailing-Edge Gurney Flaps," *AHS 60th Annual Forum Proceedings*, vol. 1, Baltimore, MD, Jun 7–10 2004, pp. 73–87.
- [28] Todd R. Quackenbush, Daniel A. Wachspress, Alexander H. Boschitsch and Christine L. Solomon, "Analytical and Experimental Micro Rotorcraft Design Studies," *AHS International Specialists' Meeting on Unmanned Rotorcraft*, Chandler, AZ, Jan 18–20 2005, pp. 505–521.
- [29] Jason L. Pereira and Inderjit Chopra, "Hover Tests of Micro Aerial Vehicle-Scale Shrouded Rotors, Part I: Performance Characteristics," *Journal of the American Helicopter Society*, vol. 54, no. 012001, Jan 2009.
- [30] Jason L. Pereira and Inderjit Chopra, "Hover Tests of Micro Aerial Vehicle-Scale Shrouded Rotors, Part II: Flow Field Measurements," *Journal of the American Helicopter Society*, vol. 54, no. 012002, Jan 2009.
- [31] Manikandan Ramasamy, Bradley Johnson and J. Gordon Leishman, "Toward Understanding the Aerodynamic Efficiency of a Hovering Micro-Rotor," *AHS International Specialists' Meeting on Unmanned Rotorcraft*, Phoenix, AZ, Jan 23–25 2007.
- [32] John J. Videler, *Avian Flight*, Oxford University Press, New York, NY, 2005.
- [33] Bret W. Tobalske, "Hovering and Intermittent Flight in Birds," *Bioinspiration and Biomimetics*, vol. 5, no. 045004, 2010.
- [34] Mike Baird, "mikebaird's photostream: birds," [online], Mar 15 2008. Available from: <http://www.flickr.com/photos/mikebaird/sets/72157594248796101/> [cited Jun 4 2011].
- [35] J. J. Videler, E. J. Stamhuis and G. D. E. Povel, "Leading-Edge Vortex Lifts Swifts," *Science*, vol. 306, no. 5703, Dec 10 2004, pp. 1960–1962.
- [36] Wei Shyy, Mats Berg and Daniel Ljungqvist, "Flapping and Flexible Wings for Biological and Micro Air Vehicles," *Progress in Aerospace Sciences*, vol. 35, no. 5, Jul 1999, pp. 455–505.
- [37] Ulla M. Lindhe Norberg, "Structure, Form, and Function of Flight in Engineering and the Living World," *Journal of Morphology*, vol. 252, no. 1, Apr 2002, pp. 52–81.
- [38] Rambod F. Larijani and James D. DeLaurier, "A Nonlinear Aeroelastic Model for the Study of Flapping Wing Flight," Mueller [179], chap. 18, pp. 399–428.
- [39] T. Nick Pornsin-Sirirak, Y. C. Tai, H. Nassef and C. M. Ho, "Titanium-Alloy MEMS Wing Technology for a Micro Air Vehicle Application," *Sensors and Actuators A: Physical*, vol. 89, no. 1–2, Mar 2001, pp. 95–103.
- [40] Beverly Beasley and Inderjit Chopra, "A Study of Planar and Nonplanar Membrane Wing Planforms for the Design of a Flapping-Wing Micro Air Vehicle," *AHS 62nd Annual Forum Proceedings*, vol. 2, Phoenix, AZ, May 9–11 2006, pp. 868–877.
- [41] James D. DeLaurier, "An Ornithopter Wing Design," *Canadian Aeronautics and Space Journal*, vol. 45, no. 2, Mar 1994, pp. 10–18.

- [42] James D. DeLaurier, "An Aerodynamic Model for Flapping-Wing Flight," *Aeronautical Journal*, vol. 97, no. 964, Apr 1993, pp. 125–130.
- [43] James D. DeLaurier, "The Development of an Efficient Ornothopter Wing," *Aeronautical Journal*, vol. 97, no. 965, May 1993, pp. 153–162.
- [44] Thomas J. Mueller and James D. DeLaurier, "Aerodynamics of Small Vehicles," *Annual Review of Fluid Dynamics*, vol. 35, 2003, pp. 89–111.
- [45] Nick Pornsin-Sirirak, Matthieu Liger, Yu-Chong Tai, Steve Ho and Chih-Ming Ho, "Flexible Parylene-Valved Skin for Adaptive Flow Control," *15th IEEE Annual International Conference on MEMS*, Las Vegas, NV, Jan 20–24 2002, pp. 101–104.
- [46] Dae-Kwan Kim and Jae-Hung Han, "Smart Flapping Wing Using Macro-Fiber Composite Actuators," Yuji Matsuzaki, ed., *Smart Structures and Materials 2006: Smart Structures and Integrated Systems, Proceedings of SPIE*, vol. 6173, Mar 16 2006, pp. 61730F-1–9.
- [47] "Entomopter Project," [online]. Available from: <http://angel-strike.com/entomopter/EntomopterProject.html> [cited Jun 4 2011].
- [48] Max F. Platzer, Kevin D. Jones, John Young and Joseph C. S. Lai, "Flapping-Wing Aerodynamics: Progress and Challenges," *AIAA Journal*, vol. 46, no. 9, Sep 2008, pp. 2136–2149.
- [49] Paul Marks, "In a Flap," *New Scientist*, vol. 166, no. 2244, Jun 24 2000, p. 7.
- [50] D. J. van Gerwen, M. M. Heiligers and Th. van Holten, "Ornicopter Yaw Control: Testing a Single Rotor Helicopter Without Reaction Torque," *45th AIAA Aerospace Sciences Meeting and Exhibit*, AIAA 2007-1253, Reno, NV, Jan 8–11 2007.
- [51] Brandon Fitchett and Inderjit Chopra, "A Biologically Inspired Flapping Rotor for Micro Air Vehicles," *AHS International Specialists' Meeting on Unmanned Rotorcraft*, Chandler, AZ, Jan 23–25 2007.
- [52] Evan R. Ulrich, Daryll J. Pines and Sean Humbert, "From Falling to Flying: The Path to Powered Flight of a Robotic Samara Nano Air Vehicle," *Bioinspiration and Biomimetics*, vol. 5, no. 045009, 2010.
- [53] Evan R. Ulrich, J. Sean Humbert and Daryll J. Pines, "Pitch and Heave Control of Robotic Samara Micro Air Vehicles," *Journal of Aircraft*, vol. 47, no. 4, Jul–Aug 2010, pp. 1290–1299.
- [54] Evan R. Ulrich, Imraan Faruque, Jared Grauer, Daryll J. Pines, Sean Humbert and Jr. James E. Hubbard, "Control Model for Robotic Samara: Dynamics About a Coordinanted Helical Turn," *Journal of Guidance, Control, and Dynamics*, vol. 33, no. 6, Nov–Dec 2010, pp. 1921–1926.
- [55] R. W. Prouty, "The Cyclogyro," *Vertiflite*, vol. 51, no. 2, Summer 2005, pp. 16–18.
- [56] Jayant Sirohi, Eric Parsons and Inderjit Chopra, "Hover Performance of a Cycloidal Rotor for a Micro Air Vehicle," *Journal of the American Helicopter Society*, vol. 52, no. 3, Jul 2007, pp. 263–279.

- [57] Gil Iosilevskii and Yuval Levy, "Experimental and Numerical Study of Cyclogiro Aerodynamics," *AIAA Journal*, vol. 44, no. 12, 2006, pp. 2866–2870.
- [58] Moble Benedict, Tejaswi Jarugumilli and Inderjit Chopra, "Design and Development of a Hover-Capable Cyclocopter MAV," *Proceedings of the 65th Annual Forum of the American Helicopter Society*, Grapevine, TX, May 27–29 2009.
- [59] Moble Benedict, Manikandan Ramasamy, Inderjit Chopra and J. Gordon Leishman, "Performance of a Cycloidal Rotor Concept for Micro Air Vehicle Applications," *Journal of the American Helicopter Society*, vol. 55, no. 022002, 2010.
- [60] Moble Benedict, Manikandan Ramasamy and Inderjit Chopra, "Improving the Aerodynamic Performance of Micro-Air-Vehicle-Scale Cycloidal Rotor: An Experimental Approach," *Journal of Aircraft*, vol. 47, no. 4, Jul–Aug 2010, pp. 1117–1125.
- [61] Moble Benedict, Tejaswi Jarugumilli and Inderjit Chopra, "Experimental Investigation of the Effect of Rotor Geometry and Blade Kinematics on the Performance of a MAV-Scale Cycloidal Rotor," *Proceedings of the AHS International Specialists' Meeting on Unmanned Rotorcraft and Network Centric Operations*, Tempe, AZ, Jan 25–27 2011.
- [62] Robin Wootton, "Insect Wings: The World's Smallest, Smartest Airfoils," *Biologist*, vol. 49, no. 3, Jun 2002, pp. 97–100.
- [63] Robert Dudley, *The Biomechanics of Insect Flight: Form, Function, Evolution*, Princeton University Press, Princeton, NJ, 2002.
- [64] C. P. Ellington, "The Aerodynamics of Hovering Insect Flight: II. Morphological Parameters," *Philosophical Transactions of the Royal Society of London B*, vol. 305, no. 1122, Feb 24 1984, pp. 17–40.
- [65] Crawford H. Greenewalt, *Hummingbirds*, Doubleday & Company, Garden City, NY, 1960.
- [66] Torkel Weis-Fogh, "Quick Estimates of Flight Fitness in Hovering Animals, Including Novel Mechanisms for Lift Production," *Journal of Experimental Biology*, vol. 59, no. 1, Aug 1973, pp. 169–230.
- [67] C. P. Ellington, "The Aerodynamics of Hovering Insect Flight: I. The Quasi-Steady Analysis," *Philosophical Transactions of the Royal Society of London B*, vol. 305, no. 1122, Feb 24 1984, pp. 1–15.
- [68] Don Baccus, "White-Lined Sphinx Moth, Foraging on Wild Mint, Great Basin NP, NV," [online], 1999. Available from: http://donb.photo.net/photo_cd/j/b44.html [cited Sep 12 2007].
- [69] Ryan Bushby, "Selasphorus rufus on Saltspring Island," [online], Apr 15 2007. This file is licensed under Creative Commons Attribution 2.5 License. Available from: http://en.wikipedia.org/wiki/Image:Selasphorus_rufus_on_Saltspring_Island.jpg [cited Jun 4 2011].
- [70] C. P. Ellington, "The Aerodynamics of Hovering Insect Flight: III. Kinematics," *Philosophical Transactions of the Royal Society of London B*, vol. 305, no. 1122, Feb 24 1984, pp. 41–78.

- [71] Peng Chai and David Millard, "Flight and Size Constraints: Hovering Performance of Large Hummingbirds Under Maximal Loading," *Journal of Experimental Biology*, vol. 200, no. 21, Nov 1 1997, pp. 2757–2763.
- [72] Z. Jane Wang, "The Role of Drag in Insect Hovering," *Journal of Experimental Biology*, vol. 207, no. 23, Nov 1 2004, pp. 4147–4155.
- [73] Sanjay P. Sane, "The Aerodynamics of Insect Flight," *Journal of Experimental Biology*, vol. 206, no. 23, Dec 1 2003, pp. 4191–4208.
- [74] C. P. Ellington, "The Aerodynamics of Hovering Insect Flight: IV. Aerodynamic Mechanisms," *Philosophical Transactions of the Royal Society of London B*, vol. 305, no. 1122, Feb 24 1984, pp. 79–113.
- [75] M. J. Lighthill, "On the Weis-Fogh Mechanism of Lift Generation," *Journal of Fluid Mechanics*, vol. 60, no. 1, Aug 1973, pp. 1–17.
- [76] T. Maxworthy, "Experiments on the Weis-Fogh Mechanism of Lift Generation by Insects in Hovering Flight: Part 1. Dynamics of the 'Fling'," *Journal of Fluid Mechanics*, vol. 93, no. 1, Jul 1979, pp. 47–63.
- [77] C. P. Ellington, "The Aerodynamics of Hovering Insect Flight: V. A Vortex Theory," *Philosophical Transactions of the Royal Society of London B*, vol. 305, no. 1122, Feb 24 1984, pp. 115–144.
- [78] C. P. Ellington, "The Aerodynamics of Hovering Insect Flight: VI. Lift and Power Requirements," *Philosophical Transactions of the Royal Society of London B*, vol. 305, no. 1122, Feb 24 1984, pp. 145–181.
- [79] S. A. Ansari, R. Żbikowski and K. Knowles, "Aerodynamic Modelling of Insect-Like Flapping Flight for Micro Air Vehicles," *Progress in Aerospace Sciences*, vol. 42, no. 2, Feb 2006, pp. 129–172.
- [80] J. Gordon Leishman, *Principles of Helicopter Aerodynamics*, Cambridge University Press, New York, NY, second edn., 2006.
- [81] Z. Jane Wang, "Dissecting Insect Flight," *Annual Review of Fluid Dynamics*, vol. 37, 2005, pp. 183–210.
- [82] Charles P. Ellington, Coen van den Berg, Alexander P. Willmott and Adrian L. R. Thomas, "Leading-Edge Vortices in Insect Flight," *Nature*, vol. 384, no. 6610, Dec 26 1996, pp. 626–630.
- [83] Coen van den Berg and Charles P. Ellington, "The Vortex Wake of a 'Hovering' Model Hawkmoth," *Philosophical Transactions of the Royal Society of London B*, vol. 352, no. 1351, Mar 29 1997, pp. 317–328.
- [84] James R. Usherwood and Charles P. Ellington, "The Aerodynamics of Revolving Wings: I. Model Hawkmoth Wings," *Journal of Experimental Biology*, vol. 205, no. 11, Jun 1 2002, pp. 1547–1564.

- [85] James M. Birch, William B. Dickson and Michael H. Dickinson, "Force Production and Flow Structure of the Leading Edge Vortex on Flapping Wings at High and Low Reynolds Numbers," *Journal of Experimental Biology*, vol. 207, no. 7, Mar 1 2004, pp. 1063–1072.
- [86] Michael H. Dickinson, "The Effects of Wing Rotation on Unsteady Aerodynamic Performance at Low Reynolds Numbers," *Journal of Experimental Biology*, vol. 192, no. 1, Jul 1 1994, pp. 179–206.
- [87] Michael H. Dickinson, Fritz-Olaf Lehmann and Sanjay P. Sane, "Wing Rotation and the Aerodynamic Basis of Insect Flight," *Science*, vol. 284, no. 5422, Jun 18 1999, pp. 1954–1960.
- [88] Ravi Ramamurti and William Sandberg, "A Three-Dimensional Computational Study of the Aerodynamic Mechanisms of Insect Flight," *Journal of Experimental Biology*, vol. 205, no. 10, May 15 2002, pp. 1507–1518.
- [89] Mao Sun and Jian Tang, "Unsteady Aerodynamic Force Generation by a Model Fruit Fly Wing in Flapping Motion," *Journal of Experimental Biology*, vol. 205, no. 1, Jan 1 2002, pp. 55–70.
- [90] James M. Birch and Michael H. Dickinson, "The Influence of Wing–Wake Interactions on the Production of Aerodynamic Forces in Flapping Flight," *Journal of Experimental Biology*, vol. 206, no. 13, Jul 1 2003, pp. 1063–1072.
- [91] Matthew J. Tarascio, Manikandan Ramasamy, Inderjit Chopra and J. Gordon Leishman, "Flow Visualization of Micro Air Vehicle Scaled Insect-Based Flapping Wings." *Journal of Aircraft*, vol. 42, no. 2, Mar–Apr 2005, pp. 385–390.
- [92] Sanjay P. Sane and Michael H. Dickinson, "The Aerodynamic Effects of Wing Rotation and a Revised Quasi-Steady Model of Flapping Flight," *Journal of Experimental Biology*, vol. 205, no. 8, Apr 15 2002, pp. 1087–1096.
- [93] Michael J. C. Smith, Peter J. Wilkin and Marc H. Williams, "The Advantages of an Unsteady Panel Method in Modelling the Aerodynamic Forces on Rigid Flapping Wings," *Journal of Experimental Biology*, vol. 199, no. 5, May 1 1996, pp. 1073–1083.
- [94] Michael J. C. Smith, "Simulating Moth Wing Aerodynamics: Towards the Development of Flapping-Wing Technology," *AIAA Journal*, vol. 34, no. 7, Jul 1996, pp. 1348–1355.
- [95] H. Liu and K. Kawachi, "A Numerical Study of Insect Flight," *Journal of Computational Physics*, vol. 146, no. 1, Oct 10 1998, pp. 124–156.
- [96] Rafał Żbikowski, "On Aerodynamic Modelling of an Insect-like Flapping Wing in Hover for Micro Air Vehicles," *Philosophical Transactions of the Royal Society of London A*, vol. 360, no. 1791, Feb 15 2002, pp. 273–290.
- [97] R. Żbikowski, K. Knowles, C. B. Pedersen and C. Galiński, "Some Aeromechanical Aspects of Insect-like Flapping Wings in Hover," *Proceedings of the Institution of Mechanical Engineers, Part G: Journal of Aerospace Engineering*, vol. 218, no. 6, Dec 2004, pp. 389–398.

- [98] Beerinder Singh and Inderjit Chopra, "Insect-Based Hover-Capable Flapping Wings for Micro Air Vehicles: Experiments and Analysis," *AIAA Journal*, vol. 46, no. 9, Sep 2008, pp. 2115–2135.
- [99] S. A. Ansari, R. Żbikowski and K. Knowles, "Non-Linear Unsteady Aerodynamic Model for Insect-Like Flapping Wings in the Hover. Part 1: Methodology and Analysis," *Proceedings of the Institution of Mechanical Engineers, Part G: Journal of Aerospace Engineering*, vol. 220, no. 2, Apr 2006, pp. 61–83.
- [100] Robin J. Wootton, "Support and Deformability in Insect Wings," *Journal of Zoology*, vol. 193, no. 4, Apr 1981, pp. 447–468.
- [101] Dmitry L. Grodnitsky, *Form and Function of Insect Wings: The Evolution of Biological Structures*, Johns Hopkins University Press, Baltimore, MD, 1999.
- [102] R. J. Wootton, "Functional Morphology of Insect Wings," *Annual Review of Entomology*, vol. 37, 1992, pp. 113–140.
- [103] R. J. Wootton, R. C. Herbert, P. G. Young and K. E. Evans, "Approaches to the Structural Modelling of Insect Wings," *Philosophical Transactions of the Royal Society of London B*, vol. 358, no. 1437, Sep 29 2003, pp. 1577–1587.
- [104] Christopher J. C. Rees, "Form and Function in Corrugated Insect Wings," *Nature*, vol. 256, no. 5514, Jul 17 1975, pp. 200–203.
- [105] Robin J. Wootton, "Function, Homology and Terminology Insect Wings," *Systematic Entomology*, vol. 4, 1979, pp. 81–92.
- [106] Robert Sanders, "University of California, Berkeley News Release: Photos of Robofly," [online], Jun 15 1999. Available from: <http://berkeley.edu/news/media/releases/99legacy/6-15-1999pix.html> [cited Jun 4 2011].
- [107] Douglas L. Altshuler, William B. Dickson, Jason T. Vance, Stephen P. Roberts and Michael H. Dickinson, "Short-Amplitude High-Frequency Wing Strokes Determine the Aerodynamics of Honeybee Flight," *Proceedings of the National Academy of Sciences of the United States of America*, vol. 102, no. 50, Dec 13 2005, pp. 18213–18218.
- [108] Fritz-Olaf Lehmann, Sanjay P. Sane and Michael Dickinson, "The Aerodynamic Effects of Wing–Wing Interaction in Flapping Insect Wings," *Journal of Experimental Biology*, vol. 208, no. 16, Aug 15 2005, pp. 3075–3092.
- [109] Steven N. Fry, Rosalyn Sayaman and Michael H. Dickinson, "The Aerodynamics of Hovering Flight in *Drosophila*," *Journal of Experimental Biology*, vol. 208, no. 12, Jun 15 2005, pp. 2303–2318.
- [110] Mao Sun and Jiang Hao Wu, "Aerodynamic Force Generation and Power Requirements in Forward Flight in a Fruit Fly with Modeled Wing Motion," *Journal of Experimental Biology*, vol. 206, no. 17, Sep 1 2003, pp. 3065–3083.
- [111] S. A. Ansari, R. Żbikowski and K. Knowles, "Non-Linear Unsteady Aerodynamic Model for Insect-Like Flapping Wings in the Hover. Part 2: Implementation and Validation," *Proceedings of the Institution of Mechanical Engineers, Part G: Journal of Aerospace Engineering*, vol. 220, no. 3, Jun 2006, pp. 169–186.

- [112] G. R. Spedding and T. Maxworthy, "The Generation of Circulation and Lift in a Rigid Two-Dimensional Fling," *Journal of Fluid Mechanics*, vol. 165, Apr 1986, pp. 247–272.
- [113] Shigeru Sunada, Keiji Kawachi, Isao Watanabe and Akira Azuma, "Fundamental Analysis of Three-Dimensional 'Near Fling'," *Journal of Experimental Biology*, vol. 183, no. 1, Oct 1 1993, pp. 217–248.
- [114] Z. Jane Wang, "Two Dimensional Mechanism for Insect Hovering," *Physical Review Letters*, vol. 85, no. 10, Sep 4 2000, pp. 2216–2219.
- [115] Coen van den Berg and Charles P. Ellington, "The Three-Dimensional Leading-Edge Vortex of a 'Hovering' Model Hawkmoth," *Philosophical Transactions of the Royal Society of London B*, vol. 352, no. 1351, Mar 29 1997, pp. 329–340.
- [116] Hao Liu, Charles P. Ellington, Keiji Kawachi, Coen van den Berg and Alexander P. Willmott, "A Computational Fluid Dynamic Study of Hawkmoth Hovering," *Journal of Experimental Biology*, vol. 201, no. 4, Feb 15 1998, pp. 461–477.
- [117] Michael J. C. Smith, "Leading-Edge Effects with Moth Wing Aerodynamics: Towards the Development of Flapping-Wing Technology," *14th AIAA Applied Aerodynamics Conference*, AIAA 1996-2511, New Orleans, LA, Jun 17–20 1996.
- [118] John D. Anderson, Jr., *Introduction to Flight*, McGraw-Hill, New York, NY, fourth edn., 2000.
- [119] A. Roland Ennos, "The Importance of Torsion in the Design of Insect Wings," *Journal of Experimental Biology*, vol. 140, no. 1, Nov 1 1988, pp. 137–160.
- [120] D. J. S. Newman and R. J. Wootton, "An Approach to the Mechanics of Pleating in Dragonfly Wings," *Journal of Experimental Biology*, vol. 125, no. 1, Sep 1 1986, pp. 361–372.
- [121] Shigeru Sunada, Lijiang Zeng and Keiji Kawachi, "The Relationship Between Dragonfly Wing Structure and Torsional Deformation," *Journal of Theoretical Biology*, vol. 193, no. 1, Jul 7 1998, pp. 39–45.
- [122] R. J. Wootton, K. E. Evans, R. Herbert and C. W. Smith, "The Hind Wing of the Desert Locust (*Schistocerca gregaria* Forskål): I. Functional Morphology and Mode of Operation," *Journal of Experimental Biology*, vol. 203, no. 19, Oct 1 2000, pp. 2921–2931.
- [123] R. Åke Norberg, "The Pterostigma of Insect Wings an Inertial Regulator of Pitch," *Journal of Comparative Physiology*, vol. 81, no. 1, 1972, pp. 9–22.
- [124] Laitche, "Image:Ischnura senegalensis October 2007.jpg," [online], Oct 5 2007. Available from: http://commons.wikimedia.org/wiki/Image:Ischnura_senegalensis_October_2007.jpg [cited Jun 4 2011].
- [125] S. A. Combes and T. L. Daniel, "Flexural Stiffness in Insect Wings: I. Scaling and the Influence of Wing Venation," *Journal of Experimental Biology*, vol. 206, no. 17, Sep 1 2003, pp. 2979–2987.

- [126] S. A. Combes and T. L. Daniel, "Flexural Stiffness in Insect Wings: II. Spatial Distribution and Dynamic Wing Bending," *Journal of Experimental Biology*, vol. 206, no. 17, Sep 1 2003, pp. 2989–2997.
- [127] Stacey A. Combes, *Wing Flexibility and Design for Animal Flight*, Ph.D. thesis, University of Washington, Jul 12 2002.
- [128] A. Roland Ennos, "The Inertial Cause of Wing Rotation in *Diptera*," *Journal of Experimental Biology*, vol. 140, no. 1, Nov 1 1988, pp. 161–169.
- [129] C. W. Smith, R. Herbert, R. J. Wootton and K. E. Evans, "The Hind Wing of the Desert Locust (*Schistocerca gregaria* Forskål): II. Mechanical Properties and Functioning of the Membrane," *Journal of Experimental Biology*, vol. 203, no. 19, Oct 1 2000, pp. 2933–2943.
- [130] R. Herbert, P. G. Young, C. W. Smith, R. J. Wootton and K. E. Evans, "The Hind Wing of the Desert Locust (*Schistocerca gregaria* Forskål): III. A Finite Element Analysis of a Deployable Structure," *Journal of Experimental Biology*, vol. 203, no. 19, Oct 1 2000, pp. 2945–2955.
- [131] S. A. Combes and T. L. Daniel, "Into Thin Air: Contributions of Aerodynamic and Inertial-Elastic Forces to Wing Bending in the Hawkmoth *Manduca sexta*," *Journal of Experimental Biology*, vol. 206, no. 17, Sep 1 2003, pp. 2999–3006.
- [132] A. M. Mountcastle and T. L. Daniel, "Vortexlet Models of Flapping Flexible Wings Show Tuning for Force Production and Control," *Bioinspiration and Biomimetics*, vol. 5, no. 045005, 2010.
- [133] Benjamin Thiria and Ramiro Godoy-Diana, "How Wing Compliance Drives the Efficiency of Self-Propelled Flapping Flyers," *Physical Review E*, vol. 82, Jul 2010, p. 015303.
- [134] Robert K. Josephson, Jean G. Malamud and Darrell R. Stokes, "Asynchronous Muscle: A Primer," *Journal of Experimental Biology*, vol. 203, 2000, pp. 2713–2722.
- [135] Douglas R. Warrick, Bret W. Tobalske and Donald R. Powers, "Aerodynamics of the Hovering Hummingbird," *Nature*, vol. 435, no. 7045, Jun 23 2005, pp. 1094–1097.
- [136] Patrick Zdunich, Derek Bilyk, Marc MacMaster, David Loewen, James DeLaurier, Roy Kornbluh, Tom Low, Scott Stanford and Dennis Holeman, "Development and Testing of the *Mentor* Flapping-Wing Micro Air Vehicle," *Journal of Aircraft*, vol. 44, no. 5, Sep–Oct 2007, pp. 1701–1711.
- [137] Robert J. Wood, "The First Takeoff of a Biologically Inspired At-Scale Robotic Insect," *IEEE Transactions on Robotics*, vol. 24, no. 2, Apr 2008, pp. 341–347.
- [138] AeroVironment, "AeroVironment Develops World's First Fully Operational Life-Size Hummingbird-Like Unmanned Aircraft for DARPA," Press release, AeroVironment, Feb 17 2011. Available from: http://www.avinc.com/resources/press_release/aerovironment_develops_worlds_first_fully_operational_life-size_hummingbird [cited Oct 18 2011].

- [139] AeroVironment, "DARPA Awards AeroVironment Phase II Contract Extension for Nano Air Vehicle Development Program," Press release, AeroVironment, Jun 30 2009. Available from: <http://www.avinc.com/downloads/NAVPRLongDARPAV4.doc.pdf> [cited Oct 18 2011].
- [140] Martin Sitti, "Piezoelectrically Actuated Four-Bar Mechanism with Two Flexible Links for Micromechanical Flying Insect Thorax," *IEEE/ASME Transactions on Mechatronics*, vol. 8, no. 1, Mar 2003, pp. 26–36.
- [141] R. J. Wood, S. Avadhanula, M. Menon and R. S. Fearing, "Microrobotics Using Composite Materials: The Micromechanical Flying Insect Thorax," *Proceedings of the IEEE International Conference on Robotics and Automation*, vol. 2, Taipei, Taiwan, Sep 14–19 2003, pp. 1842–1849.
- [142] S. Avadhanula, R. J. Wood, E. Steltz, J. Yan and R. S. Fearing, "Lift Force Improvements for the Micromechanical Flying Insect," *IEEE International Conference on Intelligent Robots and Systems*, vol. 2, Las Vegas, NV, Oct 27–31 2003, pp. 1350–1356.
- [143] E. Steltz, S. Avadhanula and R. S. Fearing, "High Lift Force with 275 Hz Wing Beat MFI," *Proceedings of the 2007 IEEE/RSJ International Conference on Intelligent Robots and Systems*, San Diego, CA, Oct 29–Nov 2 2007, pp. 3987–3992.
- [144] R. J. Wood, S. Avadhanula, R. Sahai, E. Steltz and R. S. Fearing, "Microrobot Design Using Fiber Reinforced Composites," *Journal of Mechanical Design, Transactions of the ASME*, vol. 130, no. 5, May 2008.
- [145] R. S. Fearing, "Micromechanical Flying Insect (MFI) Project," [online]. Available from: <http://robotics.eecs.berkeley.edu/~ronf/MFI/> [cited Jun 4 2011].
- [146] David L. Raney and Eric C. Slominski, "Mechanization and Control Concepts for Biologically Inspired Micro Air Vehicles," *Journal of Aircraft*, vol. 41, no. 6, Nov–Dec 2004, pp. 1257–1265.
- [147] Rafał Żbikowski, Cezary Galiński and Christopher B. Pedersen, "Four-Bar Linkage Mechanism for Insectlike Flapping Wings in Hover: Concept and an Outline of Its Realization," *Transactions of the ASME: Journal of Mechanical Design*, vol. 127, no. 4, Jul 2005, pp. 817–824.
- [148] Cezary Galiński and Rafał Żbikowski, "Materials Challenges in the Design of an Insect-Like Flapping Wing Mechanism Based on a Four-Bar Linkage," *Materials and Design*, vol. 28, no. 3, 2007, pp. 783–796.
- [149] S. K. Banala and S. K. Agrawal, "Design and Optimization of a Mechanism for Out of Plane Insect Wing Like Motion With Twist," *Transactions of the ASME: Journal of Mechanical Design*, vol. 127, no. 4, Aug 2005.
- [150] Sean H. McIntosh, Sunil K. Agawal and Zaeem Khan, "Design of a Mechanism for Biaxial Rotation of a Wing for a Hovering Vehicle," *IEEE/ASME Transactions on Mechatronics*, vol. 11, no. 2, Apr 2006, pp. 145–153.

- [151] Viet-Quoc Nguyen, M. Syaifuddin, H. C. Park, D. Y. Byun, N. S. Goo and K. J. Yoon, "Characteristics of an Insect-Mimicking Flapping System Actuated by a Unimorph Piezoceramic Actuator," *Journal of Intelligent Material Systems and Structures*, vol. 19, no. 10, Oct 2008, pp. 1185–1193.
- [152] J. K. Shang, S. A. Combes, B. M. Finio and R. J. Wood, "Artificial Insect Wings of Diverse Morphology for Flapping-Wing Micro Air Vehicles," *Bioinspiration and Biomimetics*, vol. 4, no. 036002, 2009.
- [153] Hiroto Tanaka, Kiyoshi Matsumoto and Isao Shimoyama, "Fabrication of a Three-Dimensional Insect-Wing Model by Micromolding of Thermosetting Resin with a Thin Elastomeric Mold," *Journal of Micromechanics and Microengineering*, vol. 17, no. 12, 2007, pp. 2485–2490.
- [154] Hiroto Tanaka and Robert J. Wood, "Fabrication of Currugated Artificial Insect Wings Using Laser Micromachined Molds," *Journal of Micromechanics and Microengineering*, vol. 20, no. 7, 2010, p. 075008.
- [155] Derek John Bilyk, *The Development of Flapping Wings for a Hovering Micro Air Vehicle*, Master's thesis, University of Toronto, Toronto, Canada, 2000.
- [156] Beerinder Singh, *Dynamics and Aeroelasticity of Hover Capable Flapping Wings: Experiments and Analysis*, Ph.D. thesis, University of Maryland, College Park, MD, 2006.
- [157] W. Shyy, H. Aono, S. K. Chimakurthi, P. Trizila, C.-K. Kang, C. E. S. Cesnik and H. Liu, "Recent Progress in Flapping Wing Aerodynamics and Aeroelasticity," *Progress in Aerospace Sciences*, vol. 46, no. 7, Oct 2010, pp. 284–327.
- [158] Hikaru Aono, Satish Kumar and Chimakurthi, Carlos E. S. Cesnik, Hao Liu and Wei Shyy, "Computational Modeling of Spanwise Flexibility Effects on Flapping Wing Aerodynamics," *47th AIAA Aerospace Sciences Meeting*, AIAA 2009-1270, Orlando, FL, Jan 5–8 2009.
- [159] Satish Kumar Chimakurthi, Jian Tang, Rafael Palacios, Carlos E. S. Cesnik and Wei Shyy, "Computational Aeroelasticity Framework for Analyzing Flapping Wing Micro Air Vehicles," *AIAA Journal*, vol. 47, no. 8, 2009, pp. 1865–1878.
- [160] Christopher T. Orlowski and Anouck R. Girard, "Modeling and Simulation of Nonlinear Dynamics of Flapping Wing Micro Air Vehicles," *AIAA Journal*, vol. 49, no. 5, May 2011, pp. 969–981.
- [161] Nicholas C. Rosenfeld and Norman M. Wereley, "Time-Periodic Stability of a Flapping Insect Wing Structure in Hover," *Journal of Aircraft*, vol. 46, no. 2, Mar–Apr 2009.
- [162] John C. Houbolt and George W. Brooks, "Differential Equations of Motion for Combined Flapwise Bending, Chordwise Bending, and Torsion of Twisted Nonuniform Rotor Blades," Report No. 1346, NACA, 1958.
- [163] Wayne Johnson, *Helicopter Theory*, Dover Publications, Mineola, NY, 1994.

- [164] A. Roland Ennos, "Inertial and Aerodynamic Torques on the Wings of *Diptera* in Flight," *Journal of Experimental Biology*, vol. 142, no. 1, Mar 1 1989, pp. 87–95.
- [165] Donald L. Kunz, "Survey and Comparison of Engineering Beam Theories for Helicopter Rotor Blades," *Journal of Aircraft*, vol. 31, no. 3, May–Jun 1994, pp. 473–479.
- [166] D. H. Hodges and E. H. Dowell, "Nonlinear Equations of Motion for the Elastic Bending and Torsion of Twisted Nonuniform Rotor Blades," Technical Note TN-D-7818, NASA, 1974.
- [167] Leonard Meirovitch, *Fundamentals of Vibrations*, McGraw-Hill, New York, NY, 2001.
- [168] Alexander P. Willmott and Charles P. Ellington, "The Mechanics of Flight in the Hawkmoth *Manduca sexta*: I. Kinematics of Hovering and Forward Flight," *Journal of Experimental Biology*, vol. 200, no. 21, Nov 1 1997, pp. 2705–2722.
- [169] Sanjay P. Sane and Michael H. Dickinson, "The Control of Flight Force by a Flapping Wing: Lift and Drag Production," *Journal of Experimental Biology*, vol. 204, no. 15, Aug 1 2001, pp. 2607–2626.
- [170] J. A. Richards, *Analysis of Periodically Time-Varying Systems*, Springer-Verlag, New York, NY, 1983.
- [171] J. P. Dormand and P. J. Prince, "A Family of Embedded Runge–Kutta Formulae," *Journal of Computational and Applied Mathematics*, vol. 6, no. 1, Mar 1980, pp. 19–26.
- [172] A. K. Banerjee and T. R. Kane, "Dynamics of a Plate in Large Overall Motion," *Transactions of the ASME: Journal of Applied Mechanics*, vol. 56, no. 4, Dec 1989, pp. 887–892.
- [173] UGS PLM Solutions, "Element Library: Thin Shell - Parabolic Quadrilateral," *I-DEAS Help Library Bookshelf*, 2004.
- [174] S. N. Atluri, Z. D. Han and A. M. Rajendran, "A New Implementation of the Meshless Finite Volume Method, Through the MLPG "Mixed" Approach," *Computer Modeling in Engineering & Sciences*, vol. 6, no. 6, Dec 2004, pp. 491–513.
- [175] M. A. Golberg, C. S. Chen and H. Bowman, "Some Recent Results and Proposals for the Use of Radial Basis Functions in the BEM," *Engineering Analysis with Boundary Elements*, vol. 23, no. 4, Apr 1999, pp. 285–296.
- [176] Arthur W. Leissa, "Vibration of Plates," Tech. Rep. NASA-SP-160, NASA, 1969.
- [177] Beerinder Singh, "Aeroelastic Analysis Source Code," transmitted via personal correspondence, Oct 4 2009.
- [178] Edward C. Polhamus, "A Concept of the Vortex Lift of Sharp-Edge Delta Wings Based on a Leading-Edge-Suction Analogy," Technical Note TN D-3767, NASA, Dec 1966.
- [179] Thomas J. Mueller, ed., *Fixed and Flapping Wing Aerodynamics for Micro Air Vehicle Applications*, AIAA, Reston, VA, 2001.